Numerical and Experimental Investigations of the Noise and Performance Characteristics of a Radial Fan with Forward-Curved Blades

vorgelegt von
M.Sc.
Manoochehr Darvish
geboren in Teheran (Iran)

von der Fakultät V - Verkehrs- und Maschinensysteme
der Technischen Universität Berlin
zur Erlangung des akademischen Grades

Doktor der Ingenieurwissenschaften

- Dr.-Ing.-

genehmigte Dissertation

Promotionsausschuss:

Vorsitzender: Prof. Dr. rer. nat. Lars Enghardt
Gutachter: Prof. Dr.-Ing. Christian Oliver Paschereit
Gutachter: Prof. Dr.-Ing. Stefan Frank

Tag der wissenschaftliche Aussprache: 26. März 2015

Berlin 2015
D83

Preface

I would like to express my sincere gratitude to Prof. Dr. Christian Oliver Paschereit for his support and guidance. His great insight that originates from his vast experience and expertise in the field helped me to steer my thesis toward completion. I am grateful for the chance he gave me to graduate from the Technical University of Berlin.

I am greatly indebted to Prof. Dr.-Ing. Stefan Frank for his endless support and enthusiasm. He has been the most influential professor of my life. Attending his CFD lecture in 2008 at HTW-Berlin completely changed my perception of Mechanical Engineering. Indeed, writing this thesis would not be possible without his supervision and mentoring. I have learned many lifelong lessons from him, and it has been a true honor for me to work with him during the past years.

I am most grateful to our CD-Adapco colleagues, Fred Mendonça from the London office, Stephan Caro from the Lyon office, and Harsh Khatri from the Nuremberg office for their generous support and continuous commitment, particularly during the last year of my Ph.D.

I would also like to thank all of the developers of the computer programs that are available under a free license, and everyone who is engaged with open-source projects. I have greatly benefited from, and enjoyed working with, some of these programs during my research activities. This thesis is written in LaTeX on a laptop powered by GNU/Linux. I have extensively used Python Matplotlib library, Paraview, Inkscape and Gimp throughout my work.

I would not be able to pursue my study without the unconditional love and support of my family. My father is my role model in life and the sample of a true engineer in my mind; it was undoubtedly because of him that I always wanted to become an engineer. My mother's love and kindness are limitless. She has helped me throughout my life to take many first steps. I have always admired her ambition and outstanding character.

Finally, I would like to dedicate this work to my dear wife, Hajar, since I cannot thank her enough in a line or two. Doing Ph.D. was a challenging, yet wonderful journey we started together a few years ago, and it has been all because of her endless love, support and patience that we are finishing it together.

Abstract

Forward-Curved (FC) blade fans are widely used in the automotive industry as well as in HVAC applications. This is due to the fact that FC fans have the smallest dimensions for any given ventilation task. However, the downside is that their efficiency is relatively poor and the prediction of the performance curve is still a major challenge. Although FC fans generate comparatively a lower level of noise, there is still a great potential to enhance their acoustic comfort.

The main focus of this thesis is on investigation of the noise characteristics of a FC fan which demands an in-depth knowledge of its aerodynamic characteristics. The experimental noise measurements are performed by using the in-duct method in accordance with DIN/ISO 5136. Furthermore, a major part of the thesis is devoted to numerical simulations and computational methods. A wide range of turbulence modeling approaches including Reynolds Averaged Navier-Stokes (RANS) and Large Eddy Simulation (LES) are investigated on numerical grids with total cell counts ranging from twelve to one hundred million.

The numerical results obtained are compared against the experimental measurements, and the ability of the performed simulations to predict the tonal and broadband noise components of the fan is investigated. Numerical and experimental data is in very good agreement with each other. Furthermore, the simulation results helped to gain a better understanding of the underlying noise generation mechanisms, and to shed light on the role of different fan components in noise generated.

The effects of changing the number of blades and the blade's outlet angle are numerically investigated. It is shown that changing the number of blades significantly affects the tonal noise level of the fan. However, changing the blade's outlet angle appears to be less effective. Reducing the noise level of the fan through a phase-shift generation at the cut-off (volute tongue) is also extensively investigated. It is shown, how stepped tongues help to generate a phase-shift and affect tonal noise level of the fan. The design parameters dominating the phase-shift generation capabilities of the stepped tongues are also addressed, and their effects are investigated by performing experimental measurements and numerical simulations.

It is assumed that the findings of this thesis are not only valid for FC fans, but mostly can be applied to other radial fan types.

Zusammenfassung

Radialventilatoren mit vorwärts gekrümmten Schaufeln, so genannte Trommelläufer-Ventilatoren, sind in der Automobilindustrie sowie in der Heizungs-, Klima- und Lüftungstechnik weit verbreitet. Ihr Vorteil liegt in den kleinen Abmessungen begründet. Nachteilig sind jedoch der relativ geringe Wirkungsgrad und die Schwierigkeit, die Kennlinie vorherzusagen. Trommelläufer erzeugen ein vergleichsweise niedriges Geräuschniveau, dennoch weisen sie ein großes Potenzial für akustische Verbesserungen auf.
Der Schwerpunkt dieser Arbeit liegt auf der Untersuchung des Geräuschverhaltens eines Trommelläufer-Ventilators. Dies setzt eine detaillierte Kenntnis seiner Aerodynamik voraus. Die experimentellen Schallpegelmessungen werden mit der Kanalmethode nach DIN 5136 durchgeführt. Darüber hinaus ist ein Großteil der Arbeit den numerischen Methoden gewidmet. Hierzu ist eine große Bandbreite verschiedener Turbulenzmethoden untersucht worden, welche die Reynolds Averaged Navier-Stokes (RANS) und die Large Eddy Simulation (LES) einschließt. Die hierfür erzeugten numerischen Gitter weisen eine Zellanzahl zwischen zwölf und einhundert Millionen auf.
Die erzielten numerischen Daten werden mit den experimentellen Messungen evaluiert. Des Weiteren wird untersucht, in wieweit sich die durchgeführten Simulationen eignen, die tonalen und breitbandigen Geräuschanteile vorherzusagen. Dabei kann eine große qualitative und quantitative Übereinstimmung zwischen numerischen und experimentellen Daten festgestellt werden. Die Simulationsergebnisse helfen, ein besseres Verständnis der zugrunde liegenden Mechanismen der Geräuscherzeugung zu erlangen. Dabei ist auch die Bedeutung der verschiedenen Ventilator-Komponenten bei der Schallerzeugung beleuchtet worden.
Die Auswirkung unterschiedlicher Schaufelzahlen und des Schaufelaustrittswinkels ist numerisch analysiert worden. Es zeigt sich, dass beide Maßnahmen den tonalen Schallpegel beeinflussen. Die Veränderung des Schaufelaustrittswinkels scheint im Vergleich zur Änderung der Schaufelzahl jedoch weit weniger bedeutsam zu sein. Die Verminderung des Geräuschpegels durch Erzeugung einer Phasen-Verschiebung an der Gehäusezunge ist detailliert untersucht worden. Es wird gezeigt, wie die Phasen-Verschiebung mit Hilfe von gestuften Zungen erzeugt werden kann und wie diese die tonalen Geräuschanteile beeinflusst. Dabei sind die konstruktiven Möglichkeiten zur Erzeugung von Phasenverschiebungen durch experimentelle und numerische Parameterstudien analysiert worden. Es ist anzunehmen, dass die Ergebnisse dieser Arbeit nicht nur für Trommelläufer gelten, sondern weitgehend auch auf andere Radial-Ventilatoren übertragen werden können.

Contents

Nomenclature

Abbreviations

BC	Backward-Curved
BEM	Boundary Element Method
BEP	Best Efficiency Point
BPF	Blade Passing Frequency
CAA	Computational Aeroacoustics
CFD	Computational Fluid Dynamics
CFF	Cross-Flow Fan
DDES	Delayed Detached Eddy Simulation
DES	Detached Eddy Simulation
DNS	Direct Numerical Simulation
FC	Forward-Curved
FT	Fourier Transform
FW-H	Ffowcs Williams-Hawkings
GIS	Grid-Induced Separation
HVAC	Heating, Ventilation and Air Conditioning
IDDES	Improved Delayed Detached Eddy Simulation
LDA	Laser Doppler Anemometry
LEE	Linearized Euler Equations
LES	Large Eddy Simulation

MRF	Moving Reference Frame
MSD	Modelled Stress Depletion
NWM	Near Wall Modelling
NWR	Near Wall Resolution
PIV	Particle Image Velocimetry
PSD	Power Spectral Density
PTV	Particle Tracking Velocimetry
RANS	Reynolds-Averaged Navier-Stokes
RBM	Rigid Body Motion
rmp	Rotations per Minute
rms	Root-Mean-Square
S-A	Spalart-Allmaras
SGS	Subgird Scale
SIL	Sound Intensity Level
SPL	Sound Pressure Level
SST	Shear Stress Transport
St	Strouhal Number
TCN	Tip Clearance Noise
TKE	Turbulent Kinetic Energy
TS	Time-Step
VLES	Very Large Eddy Simulation
WALE	Wall Adopting Local Eddy
WMLES	Wall-Modelled Large Eddy Simulation

Greek Symbols

β_1	Blade inlet angle
β_2	Blade outlet angle

Δ	Cell size, Grid filter width
δ	Non-dimensional diameter
ϵ	Turbulent dissipation rate
η	Efficiency
κ	Gas constant (thermodynamic ratio of specific heats)
λ	wavelength
μ	Molecular viscosity coefficient
μ_T	Eddy (or turbulent) viscosity
ν	Kinematic viscosity
ω	Angular frequency
ϕ_n	Phase angle of the nth harmonic in a complex wave
ψ	Pressure coefficient
ρ	Density
ρ_w	Density at the wall
σ	Non-dimensional speed
σ	Standard deviation
τ	Shear stress, Time interval of measurement
τ_w	Wall shear stress
φ	Flow coefficient

Mathematical Symbols

$\delta(f)$	Dirac delta function of f
δ_{ij}	Kronecker delta function
∇	Spatial differential operator
$\overline{S}_{ij}$	Mean strain-rate tensor
Π_{ij}	Stress tensor
$\Box^2$	Wave operator

τ_{ij}	Shear stress in j direction on a face normal to i axis
dS	Element of surface area
$H(f)$	Heaviside function of f
T_{ij}	Lighthill stress tensor

Latin Symbols

$\dot{V}$	Flow rate
$\overline{L_{pi}}$	Time-averaged SPL of different microphones
a_i	Coefficient value used for calculating $C_{3,4}$
A_n	Amplitude of the nth harmonic in a complex wave
b	Impeller width
C	Combined frequency response correction of the sampling-tube microphones
c	Speed of sound
c_1	Absolute velocity at leading edge
c_2	Absolute velocity at trailing edge
C_1	Free field microphone response correction
C_2	Frequency response correction of the microphone shield
$C_{3,4}$	Mean flow velocity-modal correction of the microphone shield
C_n	Complex amplitude of the nth harmonic in a complex wave
c_p	Specific heat at constant pressure
c_v	Specific heat at constant volume
D	Diameter of the measurement duct
d_1	Inner impeller diameter
d_2	Outer impeller diameter
E	Modulus of elasticity (Young's modulus)
e	Internal energy
E_t	Total energy

f	Force, Frequency
f_c	Center frequency of the octave interval
f_l	Frequency of the lower edge of the octave interval
f_u	Frequency of the upper edge of the octave interval
h	Enthalpy
I	Sound Intensity
I_0	Reference Sound Intensity $= 10^{-12}\,W/m^2$
k	Coefficient of thermal conductivity, Turbulent kinetic energy
l_0	Reference length (=1 m referring to DIN 5136) used for calculating the length of the transition duct
L_{eq}	Energy-equivalent continuous sound level
l_k	Kolmogorov length
l_{min}	Minimum length of transition duct in DIN 5136
l_{mix}	Prandtl's empirical mixing length
L_{p1}	SPL measured with a microphone in sampling tube for calculating the frequency response correction
L_{p2}	SPL measured with a microphone (without sampling tube) placed at the reference position for calculating the frequency response correction
L_p	Sound pressure level
L_w	Sound power level
N	Number of microphones
n	Rotational speed (revolutions per second)
p	Pressure
p_0	Reference pressure $= 20\,\mu Pa$
Q	Heat
q	Heat transfer
R	Gas constant

r	Distance from the source in the Lighthill's analogy
r_a	Pressure reflection coefficient
S	Duct cross-sectional area, Surface area surrounding a point source for defining the sound power
S_l	Larger area for calculating the minimum length of transition duct in DIN 5136
S_s	Smaller area for calculating the minimum length of transition duct in DIN 5136
St	Strouhal number
T	Absolute temperature, Period of a single cycle
t_k	Kolmogorov time
U	Mean flow velocity
u^*	Shear (or reference) velocity
u^+	Dimensionless velocity
u_1	Blade speed at leading edge
u_2	Blade speed at trailing edge
v_k	Kolmogorov velocity
v_n	Local normal velocity of the surface in FW-H equation
w_1	Relative velocity at leading edge
w_2	Relative velocity at trailing edge
W_0	Reference sound power = $10^{-12}\,W$
y	Normal distance from the cell centroid to the adjacent wall
y^*	Dimensionless wall distance
z	Number of blades

List of Figures

List of Tables

Chapter 1

Introduction

1.1 Background

The radial fan with forward-curved (FC) blades, also called the Squirrel cage fan or Sirocco fan, was invented by Samuel Cleland Davidson in 1898. Sirocco is the name of a hot wind that blows across the north African desert. He developed Sirocco fans in order to improve the system of tea manufacturing in the company which he inherited after his father's death. He used Sirocco fans in his tea dryers with the aim of generating positive pressure inside tea dryers and improve the tea drying technique. This is perhaps the main reason that he selected the name of a hot African wind for this fan [1]. Sirocco fans were later extensively used in the ventilation of ships. The Royal Victoria Hospital at Belfast was also ventilated by means of Sirocco fans [2].

According to the assessment of B. Eck [3, 4], the original Sirocco impeller had the following dimensions:

$$d_1/d_2 = 0.875;\ b = 0.6\,d_2;\ \beta_1 = 64^\circ;\ \beta_2 = 158^\circ,\ z = 54$$

Forward-curved blade fans have been the subject of various studies, although for almost 100 years the impeller design has not significantly changed and even the impellers used today in the modern FC fans are very similar to the primary design (Fig. 1.1). The complex structure of the flow inside the FC fans, in spite of their simple design, as well as their wide range of applications, provide an interesting case of research.

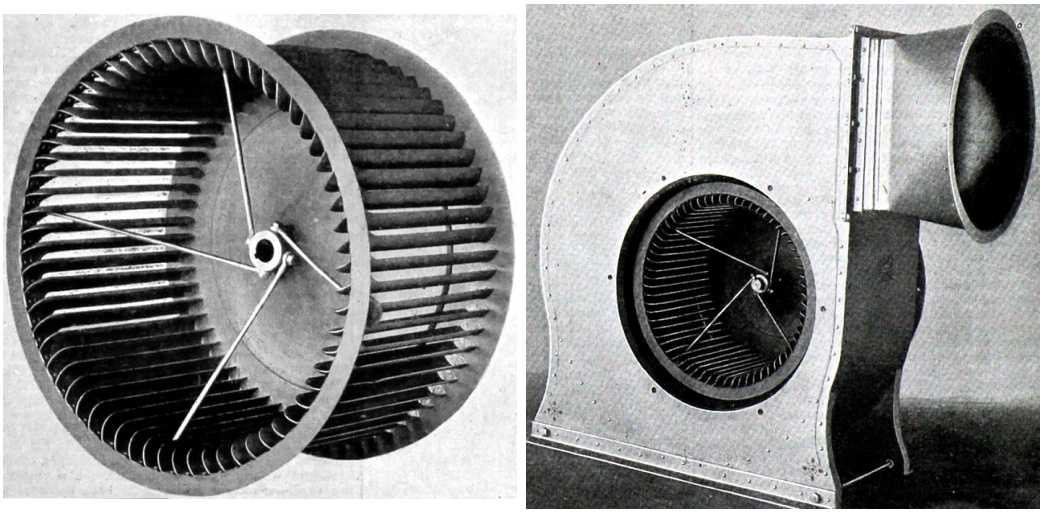

Figure 1.1: The original Sirocco fan designed by Samuel Cleland Davidson; photos from the website of British industrial history (http://www.gracesguide.co.uk).

Like many other fan types, previous studies of FC fans can be divided into different specific categories. The early works were all based on experimental measurements with the aim of understanding the flow field inside the fan as well as its characteristics. However, once the numerical methods became mature enough and technological advancements in the computer industry provided enough power to perform high-fidelity numerical simulations, the numerical methods became more and more involved in the research studies. Nowadays, numerical simulations play an important role in the engineering of fans and have become an inseparable part of the product development process. With this in mind, the previous studies about the forward-curved blade fans can be divided into different categories:

- Obtaining the characteristic curves of the fan through performing experimental measurements or numerical simulations.
- Measurement and visualization of the flow field inside the fan by conducting experimental measurements and comparing with the numerical predictions.
- Measuring the noise generated by the fan and detecting the noise sources.
- Predicting the noise of the fan by performing numerical simulations.
- Investigating the effects of different design parameters on noise and performance of the fan.

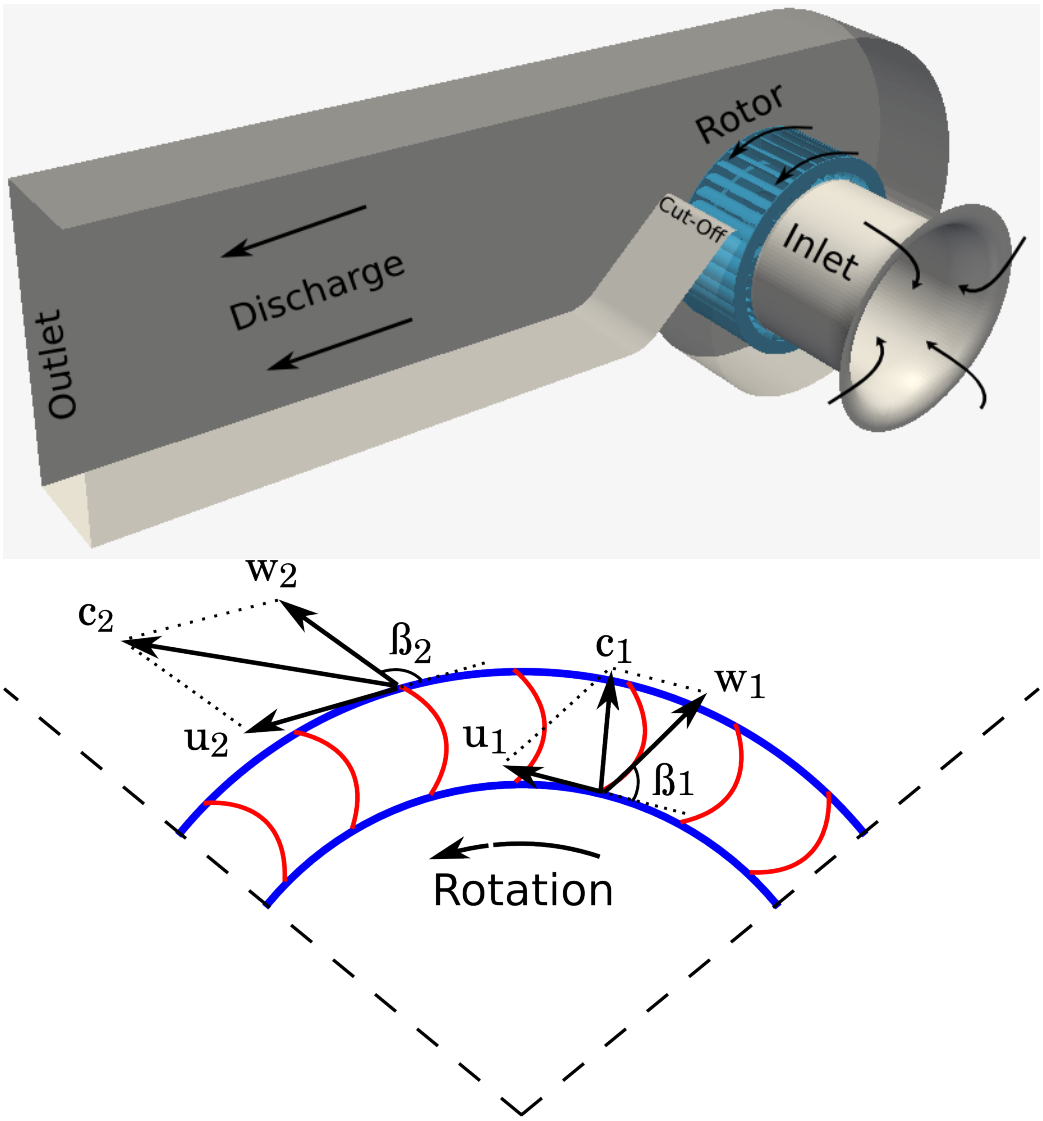

Figure 1.2: Conventional Forward-Curved blade fan design (top); schematic illustration of the theoretical inlet and outlet velocity diagrams in FC fans (bottom).

1.2 Literature Review & State-of-the-Art

One of the famous experimental studies of FC fans is the research work of Roth et al. (1979) [5]. Different FC fans were tested in their work with the aim of finding an optimum design for this type of fan. They found out the

optimum inlet and outlet impeller angles (see Fig. 1.2), i.e. $\beta_1 \approx 80^\circ$ and $\beta_2 \geqslant 150^\circ$, the optimum number of blades, i.e. between 35 and 45 blades for an impeller with the ratio of 0.8 between its inner and outer diameters.

Raj and Swim (1981) [6], used hot wire measurements and visualization techniques to investigate the flow field of a 48 blade FC fan. Their results show that the flow inside FC fan is highly turbulent and completely three-dimensional. Moreover, the inlet flow was found to fill only 3/4 of the blade span. The shroud end of the rotor was an inactive or separated region, while a jet-wake pattern occurred at the blade exit in the active flow region.

Montazerin et al. (2000) [7, 8] investigated the effects of inlet induced flow on the performance of FC fans. Their study focused on two different inlet geometries, i.e. outward and inward nozzles. In addition to the inlet geometry, the effects of some inlet parameters, e.g. the spacing between the inlet nozzle and the impeller as well as the ratio between the impeller diameter and the inlet diameter (by changing the shroud width) were investigated in their study. Their results show that the fan with an outward inlet is less sensitive to the gap spacing between the impeller and the inlet. They concluded that higher flow coefficients can be achieved when the inlet diameter is equal to the shroud inner diameter. Furthermore, when the inlet diameter is larger than the shroud inner diameter, the shroud surface blocks the inlet flow and causes further flow separation and loss in the rotor. In their study, the outward inlet could produce a comparable performance with the inward inlet, but the flow given to the volute and the blade loading were more uniform for the outward inlet type. Bayomi et al. (2006) [9] investigated the influence of inlet straighteners on the performance of centrifugal fans. According to their results, inlet straighteners have positive effects on the performance and noise of centrifugal fans with backward-curved blades and radial blades, but it is not a useful method for centrifugal fans with forward-curved blades.

Some authors have studied the slip factor models in forward-curved blade fans. Montazerin et al. (2001) [10] conducted experimental measurements by means of Laser Doppler Anemometry (LDA) to calculate the slip factor and investigate the effects of some geometrical parameters. They concluded that the outward flow leaving the impeller, hence the slip factor, is not only affected by the parameters related to the blades, but also it varies with the change of the volute spread angle. Gou et al. (2003) [11] developed an improved slip factor model, and a correction method for a forward-curved blade fan. They validated their calculations by comparing the results with the solutions obtained from steady and unsteady CFD simulations. They

concluded that their method is more applicable to FC fans with uniform flow within the blade passages, since the predictions of their model were in good agreement with the area-averaged slip factor, rather than with the mass-averaged values. In order to improve their slip factor model, they introduced some corrections factors which took into account the viscous effects, e.g. blockage in the rotor passages. Consequently, by using the correction factors, their model predictions became similar to the mass-averaged CFD results.

The flow inside forward-curved blade fans has gained a lot of attention, and there is a body of research on this topic. Many authors have performed experimental and/or numerical studies to gain a better understanding of the flow field inside the FC fans. Denger et al. (1990) [12] conducted experimental flow measurements by mounting the fan in a transparent acrylic glass water tank. Dye visualization technique and Particle Tracing (also called Tracking) Velocimetry (PTV) method were used to quantify the flow field inside the fan. Their measurement results show an extensive blade passage flow separation, re-entrant flow structure at the cut-off, rotating stall, and location dependent blade loading.
Tsurusaki et al (1997) [13] performed experimental and numerical investigations on the flow field inside a cross-flow fan (CFF). The experimental measurements were conducted by using PTV method. Their numerical method was based on two dimensional random walk model analysis. The random walk model was used to define the vorticity diffusion effect for non-convective and axis-symmetric flow. They used a probability function model to estimate the existence of a vortex within a circle of desired radius and angular band. Their model assumed the vortex location to be a function of circulation of point vortices, elapsed time after shedding of a vortex from blade, and the effective kinematic viscosity of the fluid. Their results show a close correlation between the numerical and experimental streamlines. They concluded that at high flow rates, the work done by the impeller in the through-flow region is significantly larger than the work done in the recirculating region, and it decreases as the flow rate decreases. Also, an eccentric vortex, transfers its kinetic energy to the through-flow, and the amount of energy transferred increases as the flow rate decreases. Klemm et al. (2003) [14] studied the effect of casing design on the performance of cross-flow fans by means of 2-dimensional PIV measurements and 2-dimensional unsteady RANS (URANS) numerical simulations. According to the characteristic curves in their study, the numerical simulation could only predict a very limited part of the experimental curve, which is an evidence that the 2-dimensional numerical simulation was not able to reliably predict the characteristics of the fan. The comparison of their numerical and experimental results show that the numerical predictions could provide a

basic overview of the experimental flow fields. They concluded that in order to accurately capture the flow inside cross-flow fans their numerical method needs to be improved. Klemm et al. (2006) [15] studied the flow field inside a forward-curved blade fan by means of PIV measurements and numerical simulations. They performed 3-dimensional URANS simulations on a relatively coarse numerical grid for a simplified model as a test case. They achieved good agreement between the numerical and experimental characteristic curves, but the flow field comparison showed non-negligible differences in some areas. They related the mentioned discrepancy to the coarseness of the grid in those areas. They continued the study by performing numerical simulations and experimental measurements for the real geometry (without simplifications). They refined the mesh in the second part of the study, but on contrary, made the time-step coarser (analogous to one blade channel per time-step) to reduce the simulation time. According to the characteristic curves, they could only obtain accurate numerical results at high flow rates, whereas in the lower range, there is a significant difference between the numerical and experimental characteristic curves. They related this discrepancy to the limited number of cells used in their numerical simulation. Apparently, not only their grid was relatively coarse (even in the second part), but also their time-step, i.e. one blade passage per time-step, was very coarse and can be another source of discrepancy in their results. However, they achieved to capture some flow separation structures in the blade passages as well as the in spiral housing.

Velarde-Suárez et al. (2006) [16] numerically investigated the flow inside a forward-curved blade fan. They achieved to capture the flow separation between the blade passages as well as a strong pressure fluctuating pattern at the cut-off, which they associated with the tonal noise generation. They also concluded that the unsteady forces over the blades produce an unbalance on the impeller which can be the source of vibration and mechanical noise.
Rezaei Niya et al. (2006) [17] investigated forward-curved blade fans with half-cone (non-cylindrical) rotors. They tested five different conical rotors with the angles in the range of -10° to 10°. They measured the flow inside the fans by means of 2-dimensional Laser Doppler Anemometer. They concluded that rotors with positive cone angles (in which the diameter of the rotor on the shroud side is larger than on the hub side) can be more efficient for the same head (pressure rise), and rotors with negative cone angles can produce higher pressure rise for the same efficiency. They also related the efficiency of the fan to the velocity profile, and concluded that when the flow exits the rotor earlier, it travels longer inside the volute, and therefore the fan becomes less efficient. Kitadume et al. (2007) [18] studied the effect of casing on the performance of FC fans by performing 3-dimensional Stereoscopic PIV

(SPIV). They achieved capturing the velocity distribution inside two scroll housing models, as well as the interaction between the outflow of impeller, and the flow in the casing, at different volute angles. They concluded that the decrease of the cross sectional area, which is caused by the decrease of volute angle, generates a strong spiral flow that affects the outlet flow of impeller, and causes a considerable pressure coefficient drop. Jung et al. (2008) [19] performed 3-dimensional URANS simulations to investigate the unsteady flow behavior inside a FC fan. They also performed a parametric study to investigate the effect of impeller width, and the cut-off location on the efficiency of the fan. The focus of their study was more on interpretation of different numerical results, but the study suffers from the lack of detailed comparison of the experimental and numerical results. They concluded that the efficiency of the fan becomes higher when the impeller width is greater, and the cut-off location has only a small influence on the fan efficiency.

Fukutomi et al. (2008) [20] investigated the performance and the internal flow of FC fans with contra-rotating blades. In order to do so, they settled a smaller impeller inside a bigger impeller, and rotated the impellers in two different directions, i.e. one in clockwise and the other one in counter clockwise direction. They tested two different impeller sizes inside the outer impeller. However, all of the impellers employed had unconventional number of blades; the inner impellers had 50 and 70 blades, while the outer impeller had 80 blades. However, there is no explanation given for the large number of blades selected for the impellers. Their measurement results show that it is possible to obtain higher pressure rise by using contra-rotating fans (by up to 2.5 times higher depending on the operating point), but at the expense of considerable efficiency reduction. Their results also show that the size of the inner impeller has a small influence on the characteristics of the contra-rotating fans. Accordingly, a larger inner rotor diameter could be effective to increase the discharge pressure of the fan. Their results also show that the flow outlet angle in a contra-rotating fan is smaller than in a simple FC fan, and the Best Efficiency Point (BEP) of the fan is shifted towards higher flow rates.
Stuchlik et al. (2010) [21] performed 2-dimensional PIV measurement as well as 3-dimensional RANS simulations to study the flow field inside a FC fan. They used the PIV results to verify the quality of their numerical simulations. There is a close correlation between the experimental and numerical results in their study, in terms of both the characteristic curves and the flow fields. They numerically investigated the influence of different number of impeller blades as well as different blades shape on the performance of the fan. They concluded that it is possible to reduce the flow separation between

the impeller blades by using the shaped blades, but it is not a beneficial method across the whole operating range of the fan. Moreover, their obtained results show that although using the shaped blades leads to pressure rise and efficiency enhancement at the BEP of the fan, but both of them will be reduced at the higher flow rates comparing to the normal blade shapes. They concluded that increasing the number of blades together with using the shaped blades leads to higher pressure rise and better efficiency across the whole operating range of the fan, especially in the overload range. Stuchlik et al. (2011) [22] also comprehensively investigated the characteristics of FC fans. Their study includes both experimental measurements and numerical simulations (RANS and URANS). They measured the performance curves of different FC fan designs on a chamber test-rig, and also conducted PIV measurements to obtain the flow field inside the fan, by means of which they validated their obtained numerical results. Like Roth et al. [5], they were also intended to establish relations between different design parameters and maximum attainable efficiency of the fan. They concluded that using an eccentric rotor position positively affects the pressure rise in the throttle range of the fan (i.e., flow-rates less than the flow-rate of the BEP), but deteriorates both the pressure rise and the static efficiency of the fan in the overload range (i.e., flow-rates higher than the flow-rate of the BEP).

Frank et al. (2012) [23] performed 2-, and 3-dimensional PIV measurements as well as RANS simulations to study the flow field inside a FC fan. The comparisons made between the characteristic curves and the velocity fields show good agreement between the experimental and numerical results in their study. They concluded that although performing 3-dimensional PIV measurement helps to gain a better understating and a more accurate representation of the flow field inside the fan, it is a formidable task to perform such a measurement, and a 2-dimensional study is completely sufficient most of the time. They continued the study by performing numerical simulations of an industrial FC fan model. Performing numerical simulations helped them to modify the model to inhibit the re-entrant flow near the cut-off as well as the flow separation zone downstream of the cut-off, and consequently improve the performance of the fan. Darvish et al. (2012) [24] investigated the influence of different turbulence models and cell shapes on the accuracy of the numerical predictions in the simulations performed for a FC fan. This numerical study can be considered as the second part or the completion of the experimental study conducted by Frank et al. [23]. They tested different numerical grids including one full structured hexahedral grid and three unstructured grids generated by means of polyhedral cells and trimmed cells (i.e., hexahedral cells which are trimmed at the edges). They found out that by using unstructured

grids, it is possible to achieve high quality results which are comparable to those can be obtained from a structured grid. They also investigated three different turbulence models, i.e., Realizable $k-\epsilon$, Shear Stress Transport (SST) $k-\omega$ and Spalart-Allmaras model. Their study includes comparison of the experimental and numerical characteristic curves as well as the velocity fields (i.e., 2-, 3-dimensional PIV results vs. numerical predictions). They introduced the SST $k-\omega$ as the best model in this comparison, since it could reliably predict the characteristic curves and also the flow field inside the fan. They also concluded that the steady-state simulations being performed by using Moving Reference Frame (MRF, also called Frozen Rotor) are capable of predicting the characteristics of the fan at the BEP and also in the overload range, but in the throttle range the unsteady simulations being performed by means of Rigid Body Motion (RBM) method would be more accurate. Stuchlik (2013) [25] comprehensively investigated the secondary flow patterns at ten different locations in the scroll housing and in the discharge of a FC fan at different operating points by performing numerical simulations. According to his results, fan benefits from the secondary flow at the best efficiency point of the fan and also near its best point in the throttle range. Due to the recirculation zones on both sides of the impeller (near the shroud and the hub), the flow through the impeller is axially uniform that leads to a better aerodynamic performance of the fan. However, increasing the flow rate, makes the separation zone on the hub side bigger, and on the shroud side smaller, as a result of which the corresponding uniformity fades away. The numerically captured flow patterns show the presence of the secondary flow in discharge of the fan across the whole operating range. His results show that the flow inside the FC fans, even in the discharge, can be highly turbulent and completely three dimensional.

The noise characteristics of radial fans have also been the subject of numerous experimental and numerical studies. Moreland (1974) [26] investigated the sound power spectrum of forward-curved fans. In his study, the enhancement of the sound power at certain frequencies was related to the acoustical resonances in the blower housing. He quantified the housing effects by performing experimental measurements for two configurations, i.e. with housing (housed) and without housing (unhoused). In order to make sure that the spectral peaks were only related to the housing geometry, he performed the sound measurements for three different fan speeds and noticed that the enhancements were independent of the fan speed. He developed also a theoretical model to calculate the resonance frequency of the housing. The results of his theoretical model for the lowest resonance frequency (i.e., Helmholtz frequency) matched the experimental results accurately. His experimental results show that the

peaks diminish from the spectral curves when operating the fan without housing at a constant rotating speed. Neise (1976) [27], extensively commented on this study and rejected the concept of comparing housed and unhoused fans. Neise substantiated his claim by performing some measurements and showed that the unhoused forward-curved fan has completely different characteristics, hence it is not meaningful to compare the mentioned configurations in view of acoustical effects.

Leist et al. (1979) [5] addressed the effects of some geometrical modifications on the noise of FC fans. Different design parameters like rotational speed of the fan, number of blades, inlet and outlet impeller angles and the volume of the scroll housing were investigated and their influences on the noise of the fan were addressed. Their results show that increasing the rotational speed of the fan leads to a higher level of noise. Moreover, they tested three different blade inlet angles of 30°, 50° and 80° for an impeller, with 40 blades and an outlet angle of 170°, which operated at the constant rotational speed of 840 rpm. They concluded that increasing the blades inlet angle leads to the reduction of the broadband noise, because the flow separation on the suction side of the blades becomes smaller. However, the impeller with the inlet angle of 50° had the highest level of tonal noise among the others. Moreover, three blade outlet angles of 120°, 150° and 170° for an impeller with the inlet angle of 80° with the aforementioned number of blades and the rotational speed were tested in their study. They concluded that the impeller with the outlet angle of 150° has the maximum level of tonal noise and both reducing or increasing this outlet angle leads to the reduction of sound power level at the blade passing frequency. They also investigated the effect of changing the number of impeller blades, and tested four impellers with 20, 40, 60 and 80 blades. Inlet and outlet angles were identical for all of the impellers and equal to $\beta_1 \approx 80°$ and $\beta_2 \approx 150°$. Their results show that increasing the number of blades leads to a considerable reduction in the sound power level at the corresponding blade passage frequencies. Particularly, the difference between the sound power levels of the impellers with 20 and 40 blades was very significant. They concluded that changing the number of blades has only negligible influence on the broadband noise of the fan. They also tested two parameters related to the stator geometry, first the impeller-tongue clearance, and second the volume of the scroll housing. In this part of their study, the impeller had 40 blades with the angles of $\beta_1 \approx 90°$ and $\beta_2 \approx 170°$. They concluded that increasing the clearance leads to sound power reduction at all of the operating points. Moreover, their results show that changing the stator volume, while keeping the width of the stator constant, at the same blade passage frequency and the operating point affects the sound pressure level by up to 10 dB.

The literature survey provided by Neise (1979) [28] about the noise reduction methods in centrifugal fans is perhaps the most acknowledged work in this field. According to his literature survey, diminishing the cut-off effects by increasing the clearance between the impeller and the cut-off in a backward-curved blade fan was one of the earliest methods presented in the book of Eck (1962) [3]. However, increasing the clearance leads to a reduction of efficiency and is likely to deteriorate the performance of the fan [29,30].

Holste and Neise (1992) [31] investigated the standardized measurement procedures, i.e. free field or enveloping surface method over a reflecting plane, reverberation room method, and in-duct method for determination of the sound power radiated from a fan inlet or outlet. They conducted experimental measurements for six industrial fans of different designs including a forward-curved blade fan. Their results show a very good agreement between the results of the free field and the reverberation room method in the frequency range above 80 Hz. They concluded that both methods are equally well suited for the determination of the sound power radiated from an unducted fan inlet or outlet. In the frequency region of plane wave sound propagation, owing to the reflection of the sound waves at the inlet or outlet, in-duct method yielded higher sound levels than the other two methods. Their study shows that the acoustic loading also affects the noise level of the fan. They noticed that removing the anechoic duct on the inlet side reduces the total sound power, while such effect was not apparent on the outlet side. In the frequency range of higher order mode sound propagation, the in-duct sound power results were lower than the other methods. The difference was frequency-dependent and on average equal to 3 dB on the inlet side and 5 dB on the outlet. They could not find the definite source of this discrepancy, but suggested that the modal correction factor as well as the velocity correction factor, which were based on extrapolated experimental data should be re-examined.
Velarde-Suárez et al. (2008) [32] investigated the influence of increasing the distance between impeller and cut-off. Their results show a reduction of sound pressure level at the BPF of the fan and also reduction of pressure rise and flow rate. In order to compensate the performance reductions mentioned, they bent the cut-off tip by 30°, and concluded that the slight bend of the volute tongue leads to a tonal noise reduction, without affecting the performance.
Reducing the tonal noise by inclining either the cut-off geometry or the rotor blades is another method mentioned in [28]. Embleton (1963) [33] investigated the properties of double inlet impellers with 20° inclined rotor blades in the range of 400-800 rpm. Embleton reported a 9 to 12 dB sound pressure level reduction at the blade passage frequency (BPF) and at half of this frequency.

However, as Neise mentioned in his literature survey, the study suffers the lack of measurement results at a constant flow rate. Accordingly, a higher broadband noise level should be expected from the model with the inclined blades when a given flow rate is considered [28]. Lyons et al. (1963) [34] investigated the effects of inclined tongue in a fan with a relatively small impeller geometry (outer diameter of 101.6 mm and axial length of 63.5 mm). The maximum sound reduction they measured was equal to 10 dB for a sharp cut-off located close to the impeller. Other geometrical parameters regarding the test case, e.g. the inclination angle is not given in the reference [28]. Datong et al. (2009) [35] also investigated the effects of inclined tongues on an industrial FC fan with an unusual shape. The FC fan in their study had large diameters (i.e., outlet diameter of 630 mm and inlet diameter of 240 mm) and the inlet and outlet blade widths (i.e., 110 mm and 57 mm) similar to the conventional design of backward-curved blade fans, in which the inlet width is greater than the outlet width. Their experimental results show a sound pressure level reduction at the BPF, and a negligible effect on the broadband noise. Yeow (1966) [36] suggested that splitting the cut-off into two halves, and separating them by half a blade-to-blade circumferential distance is a useful method to reduce the tonal noise. However, Yeow did not conduct any measurement to investigate the actual noise reduction ability of this method [28].
Petrov et al. (1970) [37–39] used transition meshes (similar to the woven screen used in a sifter) at the leading edges and the trailing edges of a radial fan with radial-tip blades, meaning that the intake part of the blades were forward-curved, and the trailing edges were terminated radially [28]. The mesh near the inner circumference was meant to improve the mean flow and the turbulence in the impeller ducts by shifting the point of flow separation towards the blade trailing edges. The mesh around the impeller (near the outer circumference) was to smooth the rotor outlet velocity field and create a smaller turbulence scale [28]. Although this method was useful to reduce the sound pressure by 4-9 dB in different frequency ranges depending on the size of the mesh on the woven screen, it decreased the fan efficiency by up to 15%. They reported that, the transition meshes generally reduce noise, most effectively when the mean flow conditions in the impeller ducts were poor. Thus, the use of meshes was primarily recommended for the impellers with large regions of flow separation [28].

Using tandem bladed impellers is another method to reduce the noise of FC fans. The main idea is to use the pressure difference between the two sides of the blades and transfer energy to the area of flow separation on the blades suction side. However, the effectiveness of this method is reported to

be negligible [30]. Another method to reduce the noise of FC fans presented in is to use punched blades. In this method, the blades near their leading edge are punched, in order to inhibit the flow separation on the suction side. The numerical study conducted by Saeki et al. (1997) [40] confirmed the effectiveness of this method [30]. Another successful method is the active source cancellation by using resonators [41, 42] or loudspeakers [43] developed by Neise and Koopmann et al. (1980). Although, using this methods helped to reduce the tonal noise of a backward-curved fan, it has a notable shortcoming, i.e. assembling the mentioned add-on devices on the fan makes it massive and bulky, which is not favorable.
Gérard et al. (2012) [44] investigated the feasibility of tonal noise control in a backward-curved centrifugal fan by means of flow control obstructions. In their study, the flow control obstruction was located such that the secondary radiated noise was of equal magnitude, but in opposite phase compared to the primary noise. Their in-duct experimental measurements for 7-,8- and 9-lobed inlet obstructions approved the feasibility of this method to control the tonal noise generation of the fan.

There is also a continuously growing body of research on the role of computational methods and numerical simulations in predicting the noise characteristics of different fan types. However, due to the limited computational power in the past, most of the earlier simulations were performed on simplified geometries by means of RANS turbulence models. Jeon (2003) [45] used discrete vortex method (DVM) to calculate the flow field inside a backward-curved radial fan and obtain its tonal noise. According to the results shown in the paper, there is consistency between the numerical tonal noise predictions and the experimental measurements. Jeon continued the study with numerically testing the variations of some design parameters, and concluded that the clearance between the impeller and the cut-off has the highest influence on the tonal noise of the fan. Caro et al. (2005) [46] investigated the use of the variational formulation of the Lighthill's analogy on a real automotive HVAC blower. They conducted the CFD simulations by using Detached Eddy Simulations with three variations of the Navier-Stokes equations: i) incompressible flow (density is constant and acoustic wave speed is infinite), ii) pseudo compressible flow (small density variations are accounted for in the continuity equation and acoustic wave speed is equal to a certain value), iii) isentropic flow (density is a function of pressure only and the acoustic waves propagate at the proper sound speed). For the CAA part of the study, they employed the commercially available software Actran/LA. In order to validate the simulation results, they also conducted experimental measurements in a semi-anechoic room, and measured the noise of the fan

by using four microphones (one microphone upstream of the inlet, and three downstream of the outlet). Their first attempt included a coarse mesh for both CFD and CAA parts and the quality of the results were not satisfying. They used more refined numerical grids for both CFD and CAA, which could successfully improve quality of the results. However, they concluded that the mesh refinement was not enough in neither of the performed simulations, and the future works must contain high-resolution numerical grids.
Sorguven et al. (2007) [47, 48] performed large eddy simulation (LES) of a FC fan and calculated the acoustic sources by means of boundary element method (BEM). Although the mesh resolution used in their study was coarse for a large eddy simulation, their simulation results could predict the experimental curve up to the frequency of 2 kHz.

Velarde-Suárez et al. (2007) [49] performed URANS simulations to obtain the pressure fluctuations inside the volute of a FC fan. Their numerical results show a similar pattern to the experimental measurement results at the BPF of the fan. Khelladi et al. (2008) [50] conducted URANS CFD simulations to study the impeller-diffuser interaction of a backward-curved fan. The pressure fluctuations recorded at the impeller-diffuser interface was similar to their experimental results. Moreover, they used the force and the velocity fluctuations on the impeller as the input data for the calculation of the far field acoustic pressure using the Ffowcs Williams and Hawkings equation (FW-H), and calculated the contribution of the monopole and dipole sources. Mao et al. (2008) [51] used 2-dimensional URANS simulations and BEM to predict the tonal noise radiated from a large centrifugal fan with FC blades. Considering the tonal noise of the fan, their numerical result show a similar pattern to the experimental result recorded in a hemi-anechoic chamber. They concluded that the major source of tonal noise is in the vicinity of the volute tongue, and performing LES is necessary to accurately obtain the scattering effects of the rotating blades and the volute casing. Lee et al. (2010) [52] performed URANS simulations and used BEM method to predict and reduce the tonal noise of a backward-curved radial fan in a household refrigerator. Their obtained sound pressure level results could predict the experimental trend with approximately 5 dBA difference. They continued by conducting parametric study to qualitatively assess the effects of some chosen design parameters on the tonal noise of the fan. They achieved to reduce the tonal noise of the fan up to 3 dB by 40% increasing the cut-off clearance. Heo et al. (2011) [53] performed URANS simulations to obtain the near field fluctuations of a backward-curved radial fan, and BEM to predict the noise of the fan. Based on the numerical results, they designed new S-shaped blades, which reduced the overall noise of the fan by up to 2.2 dBA.

1.3 Scope and Objectives of the Thesis

Investigating the noise and performance characteristics of a radial fan with Forward-Curved (FC) blades is the main objective of this thesis. The noise generated by the fan is experimentally measured at different operating points. Moreover, numerical modeling is extensively used to achieve an in-depth representation of the flow field inside the fan. This thesis is aimed at pursuing the following objectives:

- Performing the experimental measurements and providing a basis for verification of the numerical simulations.
- Investigating the noise generation mechanisms of the FC fan by means of numerical and experimental methods.
- Studying the reliability and effectiveness of different turbulence modeling approaches in predicting the noise of the fan.
- Investigating the effects of geometrical modifications on the noise and aerodynamic performance of the fan.

In order to investigate the noise characteristics of the fan, experimental measurements are performed using the in-duct method according to DIN ISO 5136. This study gives an overview as well as a detailed description of different components of the in-duct method. Moreover, within the scope of this thesis, various numerical grids are generated to comprehensively investigate different turbulence modeling approaches. The numerical simulations are carried out using Reynolds Averaged Navier-Stokes (RANS), Detached Eddy Simulation (DES), and Large Eddy Simulation (LES) methods. The numerical results obtained are quantitatively and qualitatively compared against the experimental data. This study examines the effectiveness of the aforementioned turbulence modeling approaches from different aspects, and delves into their conceptual differences.
In this study, numerical simulation helps to investigate the effects of changing the number of impeller blades, and the blade's outlet angle on the noise generated by the fan as well as on the aerodynamic performance of the fan. Investigating the effectiveness of the stepped tongues is also within the scope of this thesis. This part of the study aims to answer the questions whether or not:

- It is possible to generate a destructive phase shift at the cut-off?
- It is feasible to reduce the tonal noise of the fan through a phase-shift generation?

1.4 Radial Fans with Forward-Curved Blades

Forward-curved (FC) radial fans are capable of delivering considerably more air volume and producing higher static pressures than many other radial fan types of the same size and speed. However, this gain in the FC fans is at the expense of their lower efficiencies. Equation 1.1 can be used to obtain the efficiency of a fan.

$$\eta_{t,st} = \frac{p_{t,st} \cdot \dot{V}}{M \cdot 2\pi n} \tag{1.1}$$

$$p_{st} = p_{outlet} - p_{inlet} \quad ; \quad p_t = p_{st} + \frac{\rho v^2}{2} \tag{1.2}$$

where $\dot{V}$ is the volumetric airflow, M is torque, v is the outlet velocity, ρ is density, and n is the impeller rotating speed. Total efficiency of the fan (η_t) should be obtained by using the total pressure definition (p_t), while using the static pressure definition (p_{st}) yields obtaining the static efficiency of the fan (η_{st}). Figure 1.3 illustrates the six commonly used blade shapes in radial fans and the approximate maximum attainable efficiency of each type.

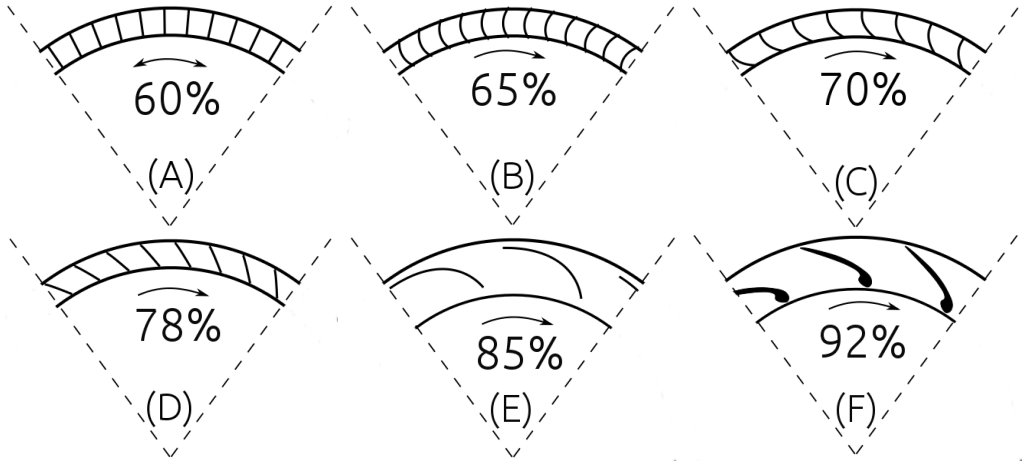

Figure 1.3: Six blade shapes commonly used in radial fans with the approximate maximum efficiency attainable for each type according to [29]; (A) Radial blades, (B) Forward-Curved blades, (C) Radial-Tip blades, (D) Backward-Inclined blades, (E) Backward-Curved blades, (F) Backward-Inclined Airfoil blades.

In the FC fans, it is the flow deflection which has a strong influence on the performance as well as the flow pattern, unlike the other radial fans where

the centrifugal force is the predominant factor. Moreover, in the FC fans, the relative velocity at the trailing edge of the blades (w_2) is in the direction of the rotation, in contrast to the BC fans, that the relative velocity is against the rotating direction (compare Figures 1.2 & 1.4). Compared to the FC fans, backward-inclined and backward-curved fans have fewer passages of greater area that are inclined away from the direction of rotation. This produces a non-overloading characteristics which makes these fan types ideal for the applications where the flow rate vary greatly with time [54].

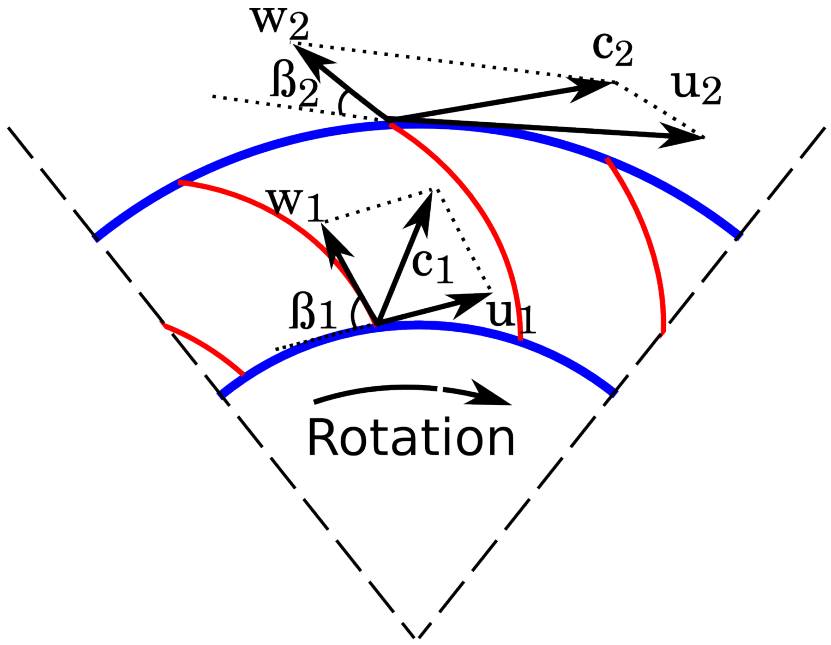

Figure 1.4: Schematic illustration of the inlet and outlet velocity diagrams in Backward-Curved fans

The FC fan is not part of the Cordier curve [55, 56], but it can be found on a separate band below the main curve. Cordier curve is a mean experience curve fitted through a scatter plot and only serves as an indication of the suitable machine type to select for a given application. This curve categorizes the best turbomachines at their BEP according to their non-dimensional speeds and diameters. Non-dimensional speed (σ) and diameter (δ) as well as two other related parameters, i.e., Flow coefficient (φ) and Pressure coefficient (ψ) can be defined as follows [3, 30, 55]:

$$\sigma = \frac{\varphi^{1/2}}{\psi^{3/4}} \tag{1.3}$$

$$\delta = \frac{\psi^{1/4}}{\varphi^{1/2}} \tag{1.4}$$

$$\varphi = \frac{4\dot{V}}{\pi^2 D^3 n} \tag{1.5}$$

$$\psi = \frac{2\Delta p}{\pi^2 \varrho D^2 n^2} \tag{1.6}$$

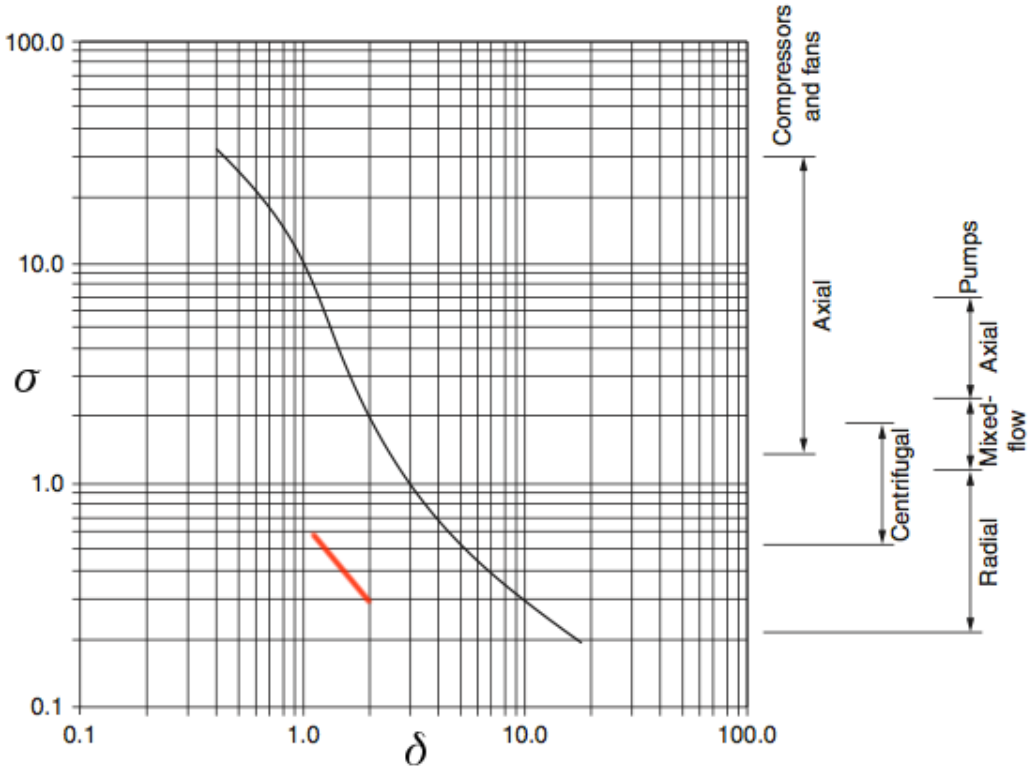

Figure 1.5: Cordier diagram showing empirical relationship between non-dimensional speed and diameter. The red line indicates where the FC fans stand on the diagram (modified after [57]).

The static pressure curve of the FC fan (Fig. 1.6) has a dip which represents a potential stall region and in some installations may cause unstable operations [29]. Moreover, the pressure curve of a FC fan is steeper than other radial fan types (refer to [3]), which makes it difficult to accurately adjust the flow rate of this fan type. As a result, the FC fan is not suitable for the applications where the close adjustment of the flow rate is required.

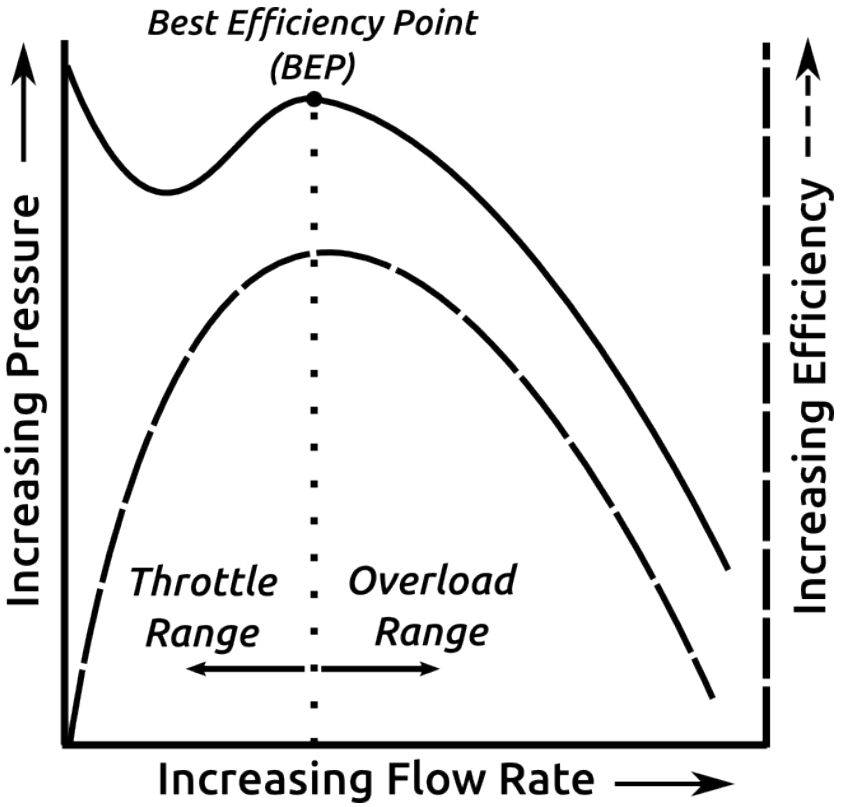

Figure 1.6: Schematic characteristic curve of a FC fan.

The defining characteristics of turbulent flow completely match the flow condition inside the FC fans and give us an approximate picture of it. The flow field inside a FC fan is three-dimensional, time dependent and has some rotational flow structures. This means that the flow inside the fan is completely turbulent, and it is valid across the entire operating range of the fan. The complexity of the flow inside the FC fans stems from the inevitable flow separation zones. Even at the BEP, where the fan has a comparatively steady operation, the flow separation zones are inherent in the flow field. Although some of the mentioned separation zones are relatively small in size, they are large enough to affect aerodynamic performance and decrease the efficiency of the fan. One of the most important flow separations is found in the impeller passages (Fig. 1.7). The formation of this separation zone is due to the inertia of the air particles occupying the space between the blades, which may partially or thoroughly stall the flow passages.
The blade angles are very wide in the FC fans in order to obtain a large air volume. At the leading edge, owing to the wide blade angle β_1, the relative airflow hits the corresponding edge at an unfavorable angle, far from any

tangential condition. The blade angle β_2 at the trailing edge is even wider, which results in a large and almost circumferential absolute air velocity c_2 at the blade tip; c_2 is greater than the tip speed (i.e., the velocity of the blade tip itself), and this is a result of the scooping action of the blades.
The main reason for the lower efficiency of FC fans is that the airflow through the blade channels has to sharply change its direction through an angle which is more than in other radial fan types. The air stream can hardly follow the strong curvature of the blades, tangential conditions no longer prevail, and the flow is far from smooth [29].

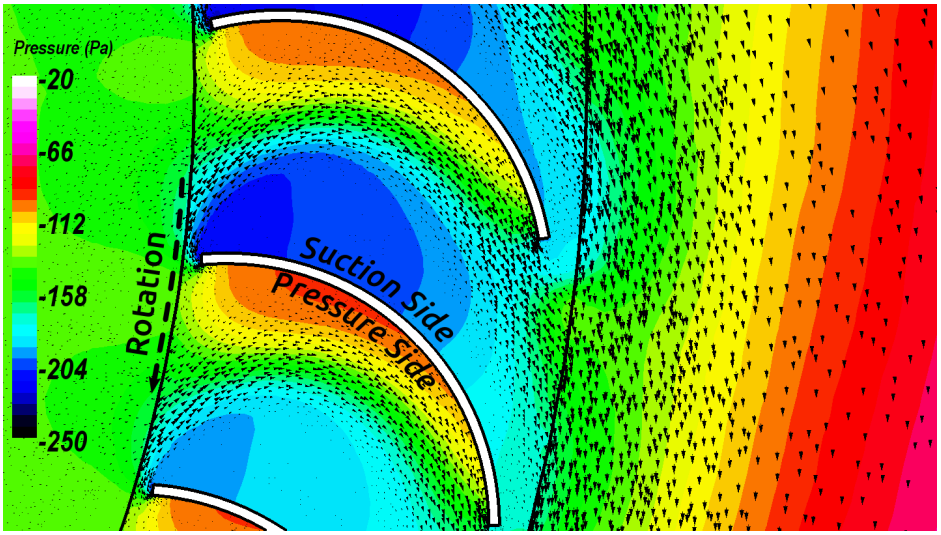

Figure 1.7: Flow separation between the blades in a FC fan. The vectors show relative velocity and the contour represents pressure distribution in a RANS CFD simulation.

The area downstream of the volute tongue (cut-off) is another spot in the FC fans where flow recirculation might take place. This form of flow separation is more prevalent at higher flow rates. Once the velocity becomes high enough, the flow detaches from the surface of the cut-off and at some distance further, as the flow hits the housing surface, reattachment takes place (Fig. 1.8). This is a pattern similar to the typical flow field in a backward-facing step channel [58].
The area above the impeller blades in a FC fan can be divided into active and inactive zones (Fig. 1.9). Detachment of the tangential inlet flow leads to the generation of a flow separation zone between the inlet nozzle and the shroud, which consequently leads to little (if any) flow through this part of the impeller (i.e., the inactive zone).

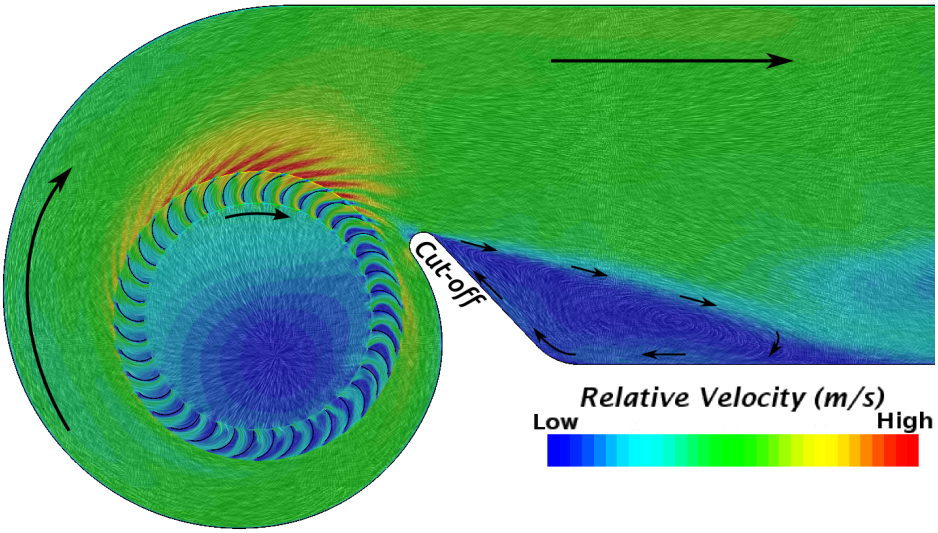

Figure 1.8: The flow separation zone downstream of the cut-off. The figure is captured on a mid-section plane in a transient CFD simulation at an operating point in the overload range.

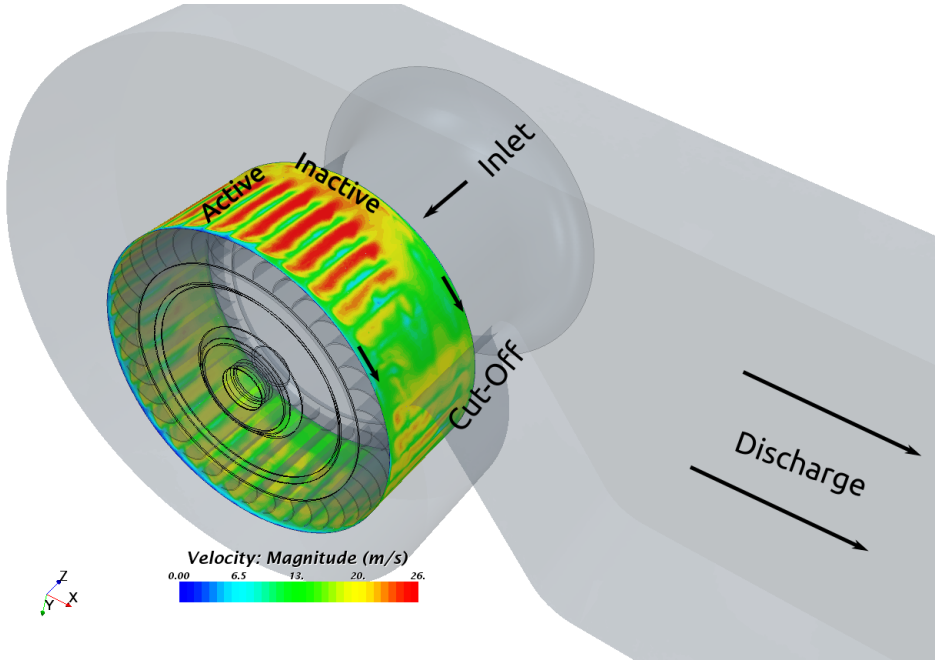

Figure 1.9: Formation of the active and inactive zones above the impeller blades of a FC fan. The result is obtained from a transient CFD simulation at the BEP of the fan.

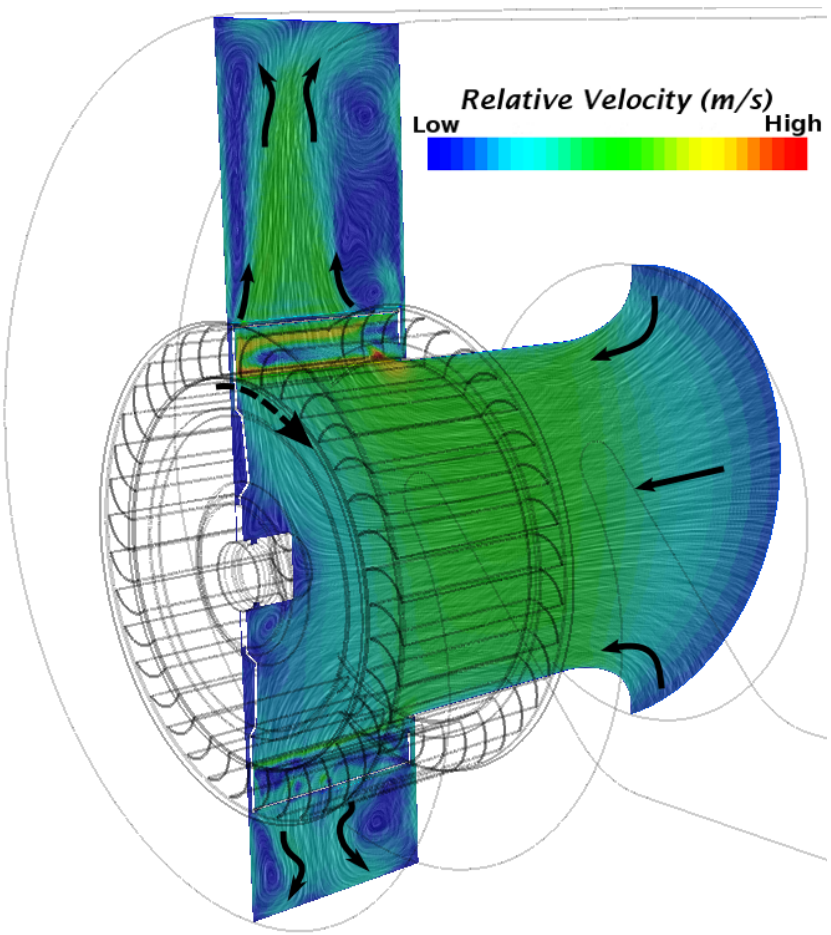

Figure 1.10: Illustration of the secondary vortex flow inside the volute of a FC fan. The result is obtained from a transient CFD simulation at the BEP of the fan.

The inactive zone may cover by upto 1/3 of the impeller width [59]. The secondary flow pattern (or secondary vortex flow), which develops within the volute and distorts the primary flow (Fig. 1.10), is believed to be partially a consequence of the near inlet separation and the inactive zone. The flow induced by the rotation of the fan is the other factor which contributes to the generation of the secondary flow pattern in the volute.
Another flow separation zone (not shown here), which makes a re-entrant flow through the rotor, might be developed near the cut-off. This reverse flow is most prevalent in the throttle range and can be inhibited to a great extent by modifying the design of the fan (refer to [23]).

1.5 Noise Generation in FC Fans

The FC fans can run at about half the speed needed to operate many other radial fan types in comparable range of air volume and static pressure. For example, at a same rotational speed and flow rate, FC fans are capable of producing static pressure 2.5 times higher than backward-inclined and radial-tip radial fans [29]. The lower rotating speed of the FC fans makes their operation comparatively quiet; in fact there is no other fan type, which can be as quiet as the FC fan at a same pressure condition [3].
Like many other fan types, the noise of the FC fans can be divided into two components, i.e. tonal noise and broadband noise. The tonal noise (the harmonic part) is caused by the interaction between the mean air flow leaving the impeller and the fan casing. The main source region can be located at the volute cut-off which is nearest to the rotating impeller blades. Very close to the rotor, the mean velocity profile with respect to the circumferential direction exposes sharp minima and maxima due to the blade wakes. This non-uniformity of the velocity profile (Fig. 1.11) produces strong pressure fluctuations at the cut-off which result in an effective sound radiation illustrated as spikes centered at the Blade Passage Frequency (BPF) and its harmonics [28, 60]. In a psychoacoustic study [61], the ability of tonal noise control from an automotive fan to enhance acoustic comfort inside and outside the vehicle has been proven. Jury testing (composed of 20 occidental persons) proved that even if the loudness difference is low between two sounds with and without tonal noise control, the perception difference can be significant if the tonality difference is large [44]. The BPF of a fan can be calculated using the rotational speed of the fan (n in rev/s) and the number of blades (z) according to Eq. 1.7.

$$BPF = z \times n = \frac{z \times rpm}{60} \tag{1.7}$$

The broadband noise arises from sources that are random in nature and can be of two types. One contribution originates from the fluctuations of the aerodynamic forces on the blade, while the second contribution arises from turbulent flow in the blade wakes [28, 30]. At low Mach numbers, it is generally the force fluctuation source (the dipole sources) that dominates the spectrum [62] (further details in Section 3.2.2). There are two sources of force fluctuations. The first arises from the shedding of vorticity at the trailing edge which generates noise as the tight eddies of air leave the impeller and introduces surface pressure fluctuations on the blade. The second is generated when the blades move through turbulent flow. The turbulence causes random

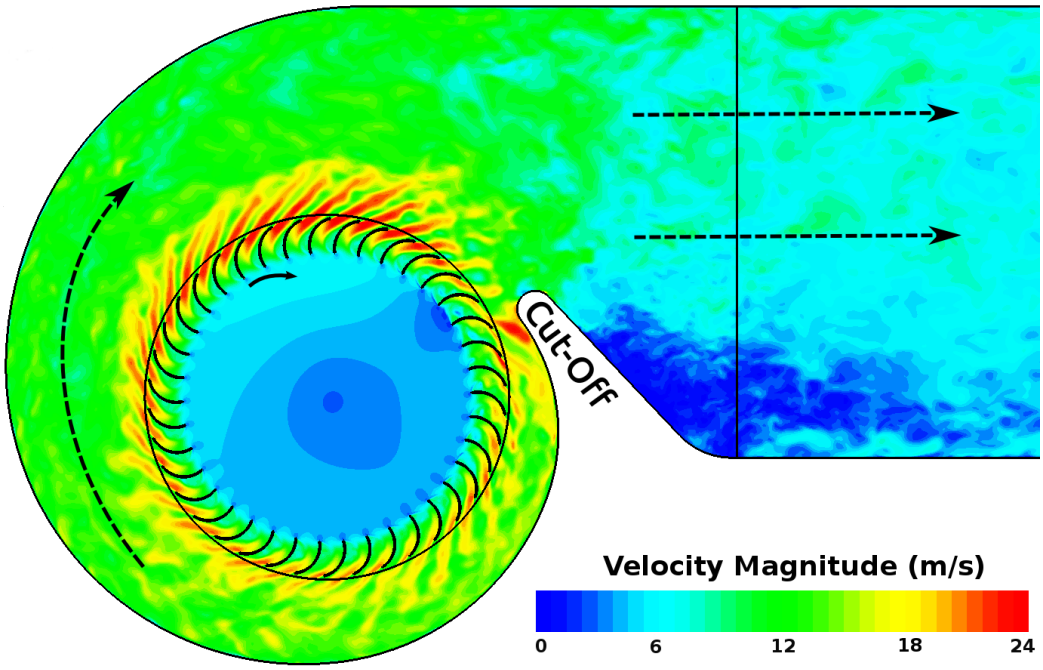

Figure 1.11: Instantaneous velocity field in a FC fan captured on a mid-section plane from a Detached Eddy Simulation at BEP of the fan (i.e., 450 m^3/h).

variations in the incidence of flow, relative to the blade, hence creating random pressure loadings and force fluctuations. If a body is in non-turbulent flow the vortex shedding is periodic which forms the well-known Karman street [28,60]. Figure 1.12 shows the instantaneous pressure fluctuations (i.e., $p' = p - \overline{p}$) in a FC fan. Higher pressure fluctuation is apparent in the flow between the blade passages as well as the flow leaving the impeller, especially in the vicinity of the cut-off.

Strouhal number is the non-dimensional parameter related to the BPF and can be defined using impeller diameter, blade tip speed and the number of blades according to Eq. 1.8 [30].

$$St = \frac{f \cdot d_2}{u_2} \frac{\pi}{z} = \frac{f}{BPF} \tag{1.8}$$

Therefore, $St = 1$ represents the BPF and $St = 2$ its first harmonic, respectively. Strouhal number is likely to be important in unsteady, oscillating flow problems and represents a measure of the ratio of inertial forces due to the unsteadiness of the flow (local acceleration, Eq. 1.9) to the inertial forces due to changes in velocity from point to point in the flow field (convective

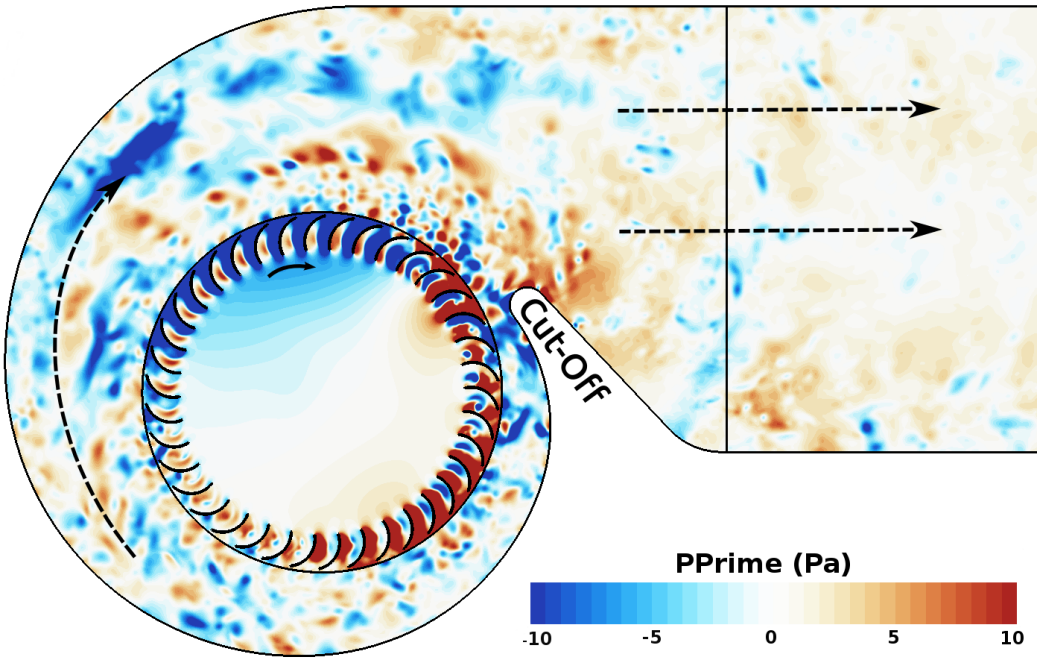

Figure 1.12: Instantaneous pressure fluctuations ($p' = p - \overline{p}$) in a FC fan captured on a mid-section plane from a Detached Eddy Simulation at the BEP of the fan.

acceleration, Eq. 1.9) [63].

$$\underbrace{\frac{D\overrightarrow{v}}{Dt}}_{\substack{\text{Substantial (Material)}\\ \text{acceleration}}} = \underbrace{\frac{\partial\overrightarrow{v}}{\partial t}}_{\substack{\text{Temporal (Local)}\\ \text{acceleration}}} + \underbrace{(\overrightarrow{v}\cdot\nabla)\ \overrightarrow{v}}_{\substack{\text{Convective}\\ \text{acceleration}}} \tag{1.9}$$

∇ is the spatial differential operator (nabla, del): $\nabla = i\,\frac{\partial}{\partial x} + j\,\frac{\partial}{\partial y} + k\,\frac{\partial}{\partial z}$.

1.6 Generation and Propagation of Sound

The phenomenon of sound in a fluid essentially involves time-dependent changes of density, with which are associated time-dependent changes of pressure, temperature and positions of the fluid particles [64]. The observed sound incident at a point has two main distinguishing attributes: *timbre* and *loudness*. The physical quantity for loudness is sound pressure and the quantity for timbre is frequency, measured in cycles per second, or Hertz.

$$f = \frac{1}{T} = \frac{\omega}{2\pi} \tag{1.10}$$

The frequency range of technical interest covers more than the range that is audible by the human ear, which is referred to as hearing level. The human hearing starts at about 16 Hz and ranges up to 16 kHz [1] [65]. Noise conveys the definition of unwanted sound in the audible range [59]. The sound out of this range is frequency-wise inaudible, with the frequencies lower than 16 Hz defined as infrasonic and above 16 kHz as ultrasonic. The value of 16 kHz refers to a healthy human being who is about of 20 years old. The upper limit decreases at the rate of 1 kHz per decade as the person gets older [65]. The hearing acuity can be permanently lost as the results of sustained exposure to loud sounds, e.g. loud rock concert or heavy equipment.

Sound, since it is a phenomenon incarnating the nature of waves, may contain only one frequency in the case of a pure steady-state sine wave, or many frequency components as in the case of noise generated by a construction machinery [59]. The purest type of sound wave can be presented by a sine function (Fig. 1.13) where the abscissa represents the elapsed time and the ordinate represents the displacement of the molecules of the propagation medium or the deviation of pressure, density, or the aggregate speed of the disturbed molecules from the quiescent (undisturbed) state of the propagation medium. When the ordinate represents the pressure difference from the quiescent pressure, the upper portions of the sine wave would then represent the compressive states and the lower portions the rarefaction phases of the propagation [59].

A wave motion can be described as a phenomenon by which a particle is distributed such that it collides with adjacent particles and imparts momentum to them. After collision, the particles oscillate about their equilibrium positions without advancing in any particular direction, i.e. there is no net transport of particles in the medium. The disturbance, however, propagates through the medium at a speed which is a characteristic of the medium, the kinematics of the disturbance, and any external body forces on the medium [66]. Sound travels far more rapidly in solids than it does in gases. At a temperature of 20 °C sound moves at the rate of approximately 344 m/s through air at the normal atmospheric pressure of 101 kPa. Sound velocities are also greater in liquids than in gases, but remain less in order of magnitude than those for solids. For an ideal gas the velocity c of a sound wave may be computed according to Eq. 1.11.

[1] In some literature this range is defined as 20 Hz-20 kHz (e.g. [59])

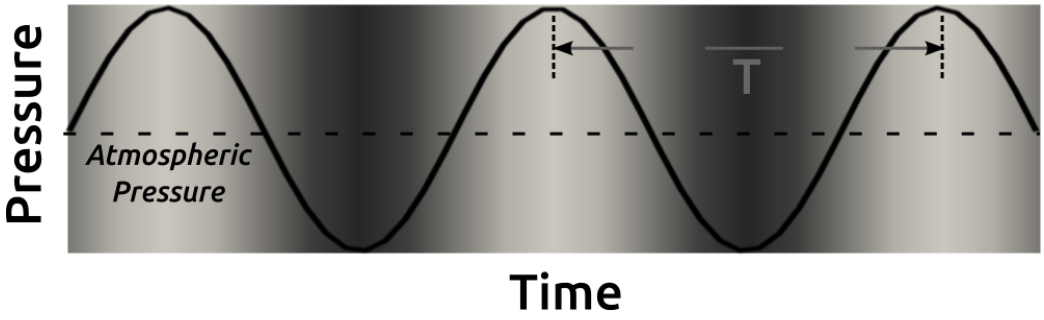

Figure 1.13: An instantaneous view of the compressed (above the atmospheric pressure) and rarefied regions (below the atmospheric pressure) of a sound wave in air.

$$c = \sqrt{\frac{\kappa\, p}{\rho}} = \sqrt{\kappa\, R\, T} \tag{1.11}$$

where κ (= 1.4) is the ratio of the specific heat of air at constant pressure to that at constant volume (c_p/c_v), p is the quiescent gas pressure, ρ is the density of the gas, R is the gas constant, and T is the absolute temperature of the gas. The wavelength λ can be established as being the peak-to-peak distance between two successive waves or the distance a wave travels to complete one cycle.

$$\lambda = \frac{c}{f} \tag{1.12}$$

A simple relation such as Eq. 1.11 does not exist for acoustic velocity in liquids, but the propagation velocity does depend on the temperature of the liquid, and to a lesser degree, on the pressure. For a solid the propagation speed [1] is a function of Young's modulus (or modulus of elasticity) of the material and the material density [59].

The concept of simple sinusoidal waves lacks specificity to be of practical value in noise control, but all complex periodic waveforms are combinations of several harmonically related sine waves (Fig. 1.14). The shape of a complex waveform depends upon the relative amplitudes of the various harmonics and the position in time of each individual component with respect to the others [67].

[1] $c = \sqrt{\frac{E}{\rho}}$

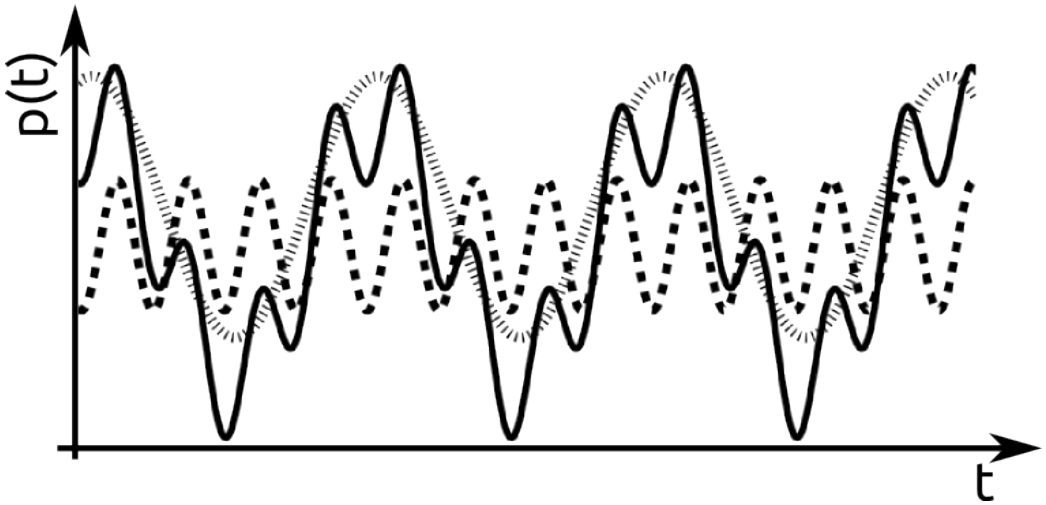

Figure 1.14: Breaking a complex wave (solid line) into harmonically related sinusoidal waves.

In Fig. 1.14, a complex waveform resolves into a sum of harmonically related waves. Sound pressure waves radiating from pumps, gears, and other rotating machinery are usually complex and periodic, with distinguishable discrete tones or pure tones. These sinusoidal waves can be broken down or synthesized into simple sinusoidal terms. In the analysis of the noise emanating from rotating machinery, there are often several harmonics present with frequencies which are integer-ordered multiples of the fundamental frequency [59]. If one of the harmonic components is shifted slightly in time, the shape of the waveform is changed, although the frequency composition remains the same. Obviously a record of the time locations of the various harmonic components is required to completely describe the complex waveform. This information is noted as the phase of the individual components [67]. The general equation of $p(t)$ in Fig. 1.14 can be written according to Eq. 1.13 [59].

$$\begin{aligned} p(t) &= A_1 sin(\omega\, t + \phi_1) + A_2 sin(2\omega\, t + \phi_2) + A_3 sin(3\omega\, t + \phi_3) + \\ &\ldots + A_n sin(n\omega\, t + \phi_n) = \sum_{i=1}^{n} A_n sin(n\omega\, t + \phi_n) = \sum_{i=1}^{n} C_n e^{i\omega\, t} \end{aligned} \tag{1.13}$$

where
A_n: Amplitude of the *nth* harmonic
ϕ_n: Phase angle of the *nth* harmonic
C_n: Complex amplitude of the *nth* harmonic

Under *in-phase* condition, the waves start from zero at $t = 0$. If another

sine wave of identical frequency is delayed by 90°, its time relationship to the first one is a quarter wave late. A half-wave late would be 180° and so on. This is called an *out-phase* condition [68]. *Phase-shift* expresses in degrees the fraction of a period or wavelength by which a single-frequency component is shifted in the time domain [67]. When two or more sound waves become superimposed upon each other, they combine in a linear manner, i.e. their amplitudes add algebraically at any point in space and time. The superposition generally results in a complex wave that can be synthesized into basic sinusoidal spectrum components [59].

1.7 Dimensions of Sound

In a normally propagating sound wave, energy is required to move the air particles; they must be pushed or pulled against the elasticity of the air, causing the incremental rises and falls in pressure. Doubling the displacement doubles the pressure change, and this requires double the force. Because the work done is the product of force times distance and both are doubled, the energy in a sound wave is therefore proportional to the square of the particle displacement amplitude or, in more practical terms, to the square of the sound pressure amplitude [67].

Sound energy spreads outward from the source in the three dimensions of space, in addition to those of amplitude and time. The energy of such a sound field is usually described in terms of the energy flow through an imaginary surface. The sound energy transmitted per unit of time is called *sound power*. The sound power passing through a unit area of a surface perpendicular to a specified direction is called the *sound intensity*. Because intensity is a measure of energy flow, it also is proportional to the square of the sound pressure amplitude [67].

The human ear can generally perceive sound pressures over the range from about 20 µPa up to about 200 Pa [69]. Because the range of typical acoustic pressures is so large, it is convenient to work with a relative measurement scale rather than an absolute scale. These scales are expressed using logarithms to compress the dynamic range. This is based on *bel*, which represents a ratio of 10:1 in sound intensity or sound power. A difference of 10 dB therefore corresponds to a factor of 10 difference in sound intensity or sound power [67]. A simple way to measure the degree of disturbance from the the equilibrium or quiescent pressure value is to square the values of the sound pressure disturbance over a period of time, thereby eliminating the counter-effects of

negative and positive disturbances by rendering them always positive. The root-mean-square sound pressure p_{rms} can be defined by Eq. 1.14 [59].

$$p_{rms} = \sqrt{(p)^2} = \sqrt{\frac{\int_0^\tau p^2 \, dt}{\int_0^\tau dt}} \tag{1.14}$$

where τ is the time interval of measurement and p instantaneous pressure.

1.7.1 Octave and One-Third Octave Bands

In some cases, high spectral resolution is not required. Therefore, for analytical purposes, the audio range of frequencies are divided into 10 standard intervals, namely octave bands, with center frequencies f_c = 31.5, 63, 125, 250, and 500 Hz, and 1, 2, 4, 8, and 16 kHz. An octave is defined as a 2:1 ratio of two frequencies [59, 65] :

$$f_u = 2f_l \quad \text{and} \quad f_c = \sqrt{f_l f_u} \tag{1.15}$$

where
f_u = frequency of the upper edge of the octave interval
f_l = frequency of the lower edge of the octave interval
f_c = center frequency of the octave interval

One-third octave bands are formed by subdividing each octave band into three parts. The successive center frequencies increase in intervals by cube root of 2, and the upper and lower frequencies are related to the center frequency according to Eq. 1.16 [59].

$$f_u = \sqrt[3]{2} f_l \quad \text{and} \quad f_l = \frac{f_c}{\sqrt[6]{2}} \quad \text{and} \quad f_u = \sqrt[6]{2}\, f_c \tag{1.16}$$

The ratio of the bandwidth $(f_u - f_l)$ to the center frequency (f_c) is equal to $1/\sqrt{2}$ for the octave bands, and $\sqrt[6]{2} - \ ^{-6}\sqrt{2}$ for the one-third octave bands.

1.7.2 Sound Intensity and Power

The sound power radiated by a point source can be defined as:

$$W = \int_S I \cdot dS \tag{1.17}$$

where I is the sound intensity, dS element of surface area and S surface

area surrounding source. In a free field, far from the influence of reflecting objects, sound from a point source is propagated spherically and uniformly in all directions (Fig. 1.15). Therefore, sound power is related to intensity by Eq. 1.18.

$$I = \frac{W}{S} = \frac{W}{4\pi\, r^2} \tag{1.18}$$

All of sound power passing through the small square area S1 (in Fig. 1.15) also passes through surface areas S2, S3 and S4. But, the sound intensity decreases as the sound passes through the greater areas, due to the geometric spreading of the sound energy. Equation 1.18 constitutes the inverse-square law of sound propagation, which accounts for the fact that sound becomes weaker as it travels in open space away from the source, even if viscous effects of medium are disregarded [59, 68]. Sound power level (L_w) and Sound Intensity Level (SIL) [69] can be defined as:

$$L_w = 10\, log(\frac{W}{W_0}) \tag{1.19}$$

$$SIL = 10\, log(\frac{I}{I_0}) \tag{1.20}$$

$W_0 = 10^{-12}\, W$ and $I_0 = 10^{-12}\, W/m^2$ represent the reference power [1] and the reference intensity corresponding to the threshold of perception in the frequency domain where the ear sensitivity is maximum (approximately 1 kHz) [71].

1.7.3 Sound Pressure Level

The sound pressure as portrayed by the oscillation of the pressure above and below the atmospheric pressure is detected by normal human ear at levels as low as approximately 20 µPa. The scale which defines the relationship between the level of the sound and the reference level, is called Sound Pressure Level (SPL) [59].

$$L_p = SPL = 10\ \log(\frac{p_{rms}}{p_0})^2 = 20\ \log(\frac{p_{rms}}{p_0}) \tag{1.21}$$

From the context of Eq. 1.21 it can be established that the doubling of a root-mean-square pressure corresponds to approximately 6 dB in the SPL. Most Sound Pressure Levels do not arise from single sources, nor do they

[1] The reference power is defined as $W_0 = 10^{-13}\, W$ in some literature (e.g. [70])

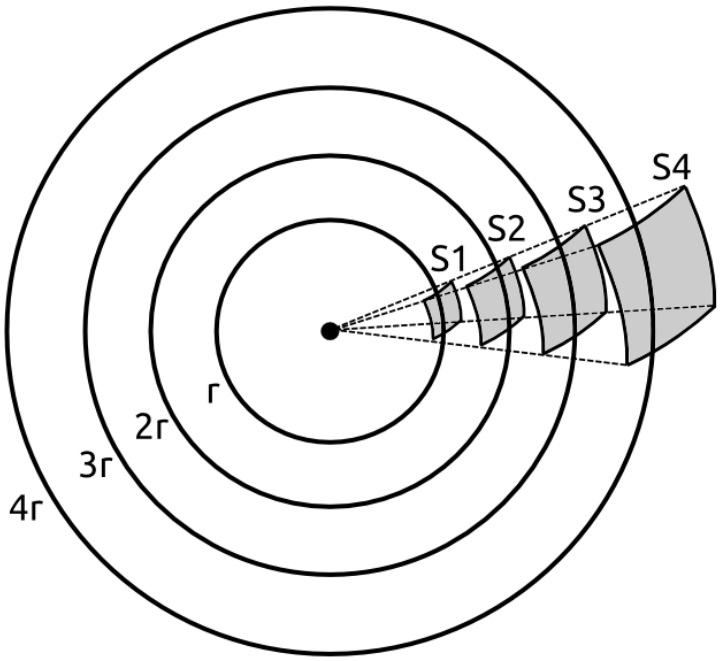

Figure 1.15: Spherical propagation of sound from a point source; the intensity of sound is inversely proportional to the square of the distance from the point source (reproduced from [68]).

remain constant in time. Mathematical procedures must be used to add, subtract, and average decibels. From the definition of Eq. 1.21 it is apparent that decibels from single-noise sources do not add or subtract directly. If we wish to add sound pressure levels L_{p1}, L_{p2}, L_{p3},...,L_{pn}, we need to obtain the antilogs of these sound pressure levels to convert them into squares of rms pressures which can then be added directly to yield the square of total rms pressure, that in turn yields the total dB. In terms of sound pressure levels, the total SPL can be calculated according to Eq. 1.22 [59].

$$L_{pt} = 10 \log \left[\sum_{i=1}^{n} \log^{-1} \left(\frac{L_{pi}}{10} \right) \right] = 10 \log \left(\sum_{i=1}^{n} 10^{L_{pi}/10} \right) \tag{1.22}$$

1.8 Perception of Sound

Human perception of loudness depends on the frequency of a sound. A noise having most of its energy concentrated in the middle of the audio spectrum (e.g., in the region of 1 kHz) is perceived as being louder than noise of equal energy but concentrated either in the low-frequency region (e.g. 40 Hz) or

in the high- frequency region (near 15 kHz) [59]. In order to emulate human hearing, sound level meters usually offer a selection of frequency weighting networks, namely, A, B and C.

A-weighting network, for instance, assigns to each frequency a "*weight*" that is related to the sensitivity of the ear at that frequency [72]. Network selection is based on the general level of sounds to be measured (background noise, jet engines, and so on). For example [68]:

- A-weighting network to be used for SPLs of 20 to 55 dB
- B-weighting network to be used for SPLs of 55 to 85 dB
- C-weighting network to be used for SPLs of 85 to 140 dB

However, the B and C weightings often do not correspond to human perception. The A weighting is more commonly used. Sound level that is measured for example with A-weighting is reported in terms of dB(A) or simply dBA rather than the generic decibel dB. The A-weighted SPL at frequency f can be calculated according to Eq. 1.23 [73].

$$A(f) = 10log\left[\frac{f_4^2 f^4}{(f^2+f_1^2)(f^2+f_2^2)^{0.5}(f^2+f_3^2)^{0.5}(f^2+f_4^2)}\right]^2 dB \qquad (1.23)$$

where $f_1 = 20.6\,Hz$, $f_2 = 107.7\,Hz$, $f_3 = 737.9\,Hz$, and $f_4 = 12194\,Hz$.

A(1000) is equal to approximately -2 dB; therefore, in order to normalize the function so that the frequency response becomes 0 dB at $f = 1000\,Hz$, a 2 dB should be added to the values obtaining from Eq. 1.23. Figure 1.16 depicts the frequency response of the weighting networks.

The family of equal-loudness contours (Fig. 1.17) has been adopted as an international standard (DIN ISO 226 [74]). Each equal-loudness contour is identified by its value at the reference frequency of 1 kHz, and the term, loudness level in phons, is thus defined. For example, the equal-loudness contour passing through 40 dB sound pressure level at 1 kHz is called the 40-phon contour. Similarly, the 100-phon contour passes through 100 dB at 1 kHz. The line of each contour shows how sound pressure level must be varied at different frequencies to sound equally loud as the 1 kHz reference loudness of 40 phons. These data are for pure tones and do not apply directly to music and other audio signals. The phone is a unit of physical loudness

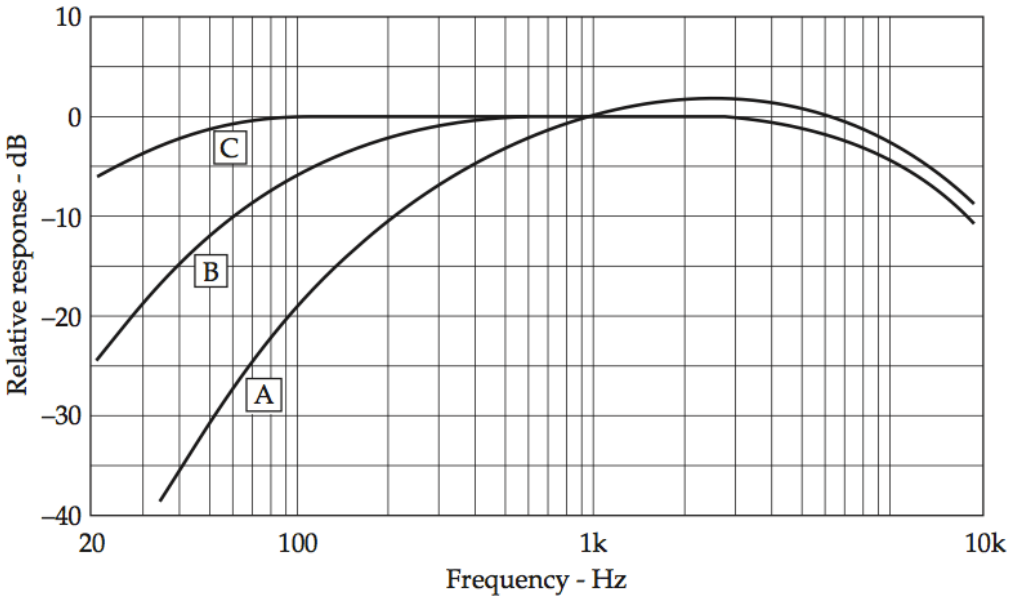

Figure 1.16: Frequency responses for different weighting networks [68].

level that is referenced to a Sound Pressure Level at 1 kHz. This is useful, but it tells us little about human reaction to loudness of sound. Therefore, a subjective unit of loudness is needed which estimates the loudness of a sound. The experimental measurements revealed that for a 10 dB increase in sound pressure level, the average person reports that loudness is doubled. Therefore, the so called unit "*sone*" is established for subjective loudness which defines the loudness of a sound (not its loudness level). One sone is defined as the loudness experienced by a person listening to a 1 kHz tone of 40 phone loudness level. A sound of 2 sones (i.e., 50 phone at 1 kHz) is twice as loud and 0.5 sone (i.e., 30 phone at 1 kHz) half as loud [68].

The shapes of the equal-loudness contours contain subjective information because they were obtained by a subjective comparison of the loudness of a tone to its loudness at 1 kHz. These contours (Fig. 1.17) reveal the relative lack of sensitivity of the ear to bass tones, especially at lower sound levels. Inverting these curves give the frequency response of the ear in terms of loudness level. For example, a Sound Pressure Level of 30 dB yields a loudness level of 30 phons at 1 kHz, but it requires a Sound Pressure Level of 58 dB more to sound equally loud at 20 Hz.
The threshold of hearing, represents the level at each frequency where sounds are just barely audible. The curve also shows that human ears are most

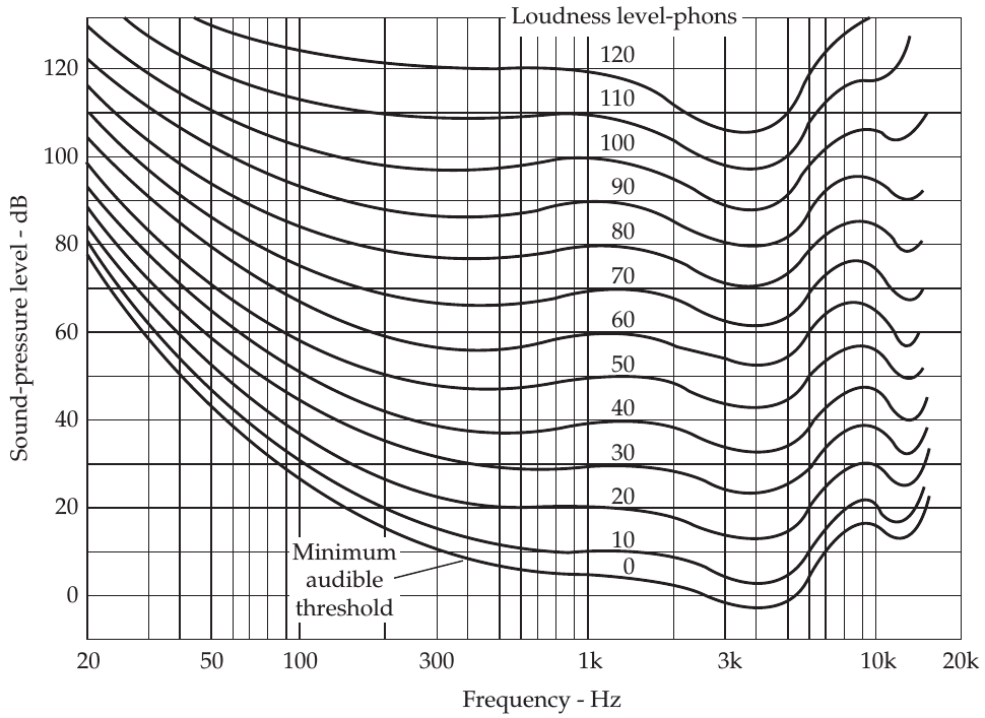

Figure 1.17: Equal-loudness contours of the human ear for pure tones [68].

sensitive around 3 kHz. Another way to state this is that around 3 kHz; a lower-level sound elicits a greater threshold response than higher or lower frequencies. The ear canal (auditory canal) has an average diameter of about 0.7 cm and length of about 2.5 cm [68]. By considering the ear canal as a cylinder pipe closed at one end (by eardrum), the resonance frequency of this tube (i.e., $f = c/4L$ [59]) is approximately equal to 3400 Hz. At this most sensitive region, a sound pressure level defined as 0 dB can just barely be heard by a person of average hearing acuity. The reference level of pressure of 20 µPa was selected to establish this 0 dB level. The threshold of feeling (120-phone contour), represents the level at each frequency at which a tickling sensation is felt in the ears. At 3 kHz, this occurs at a Sound Pressure Level of about 110 dB. Further increase in level results in an increase in feeling until a sensation of pain is produced. The threshold tickling is a warning that the sound is becoming dangerously loud and that ear damage is either imminent or has already taken place. Between the threshold of hearing and the threshold of feeling is the area of audibility. This area has two dimensions; the vertical range of Sound Pressure Level and the horizontal range of frequencies that the ear can perceive. All the sounds that humans experience must be of such a frequency and level as to fall within this auditory area [68].

Chapter 2

Experimental Measurements

2.1 Experimental Setup

The radial fan under consideration has an impeller with 38 forward-curved blades, and is manufactured by Punker GmbH [75]. The performance characteristics of the fan are obtained from the measurements performed on a chamber test rig in accordance with DIN/ISO 5801 [76]. The performance data, such as pressure rise, shaft power and static efficiency, are collected for a range of flow rates [22]. An electrical motor is used to drive the fan at 1000 rpm. Figure 2.1 shows the sketch of the reference model and Tab. 2.1 lists some of the important dimensions of the fan. More detailed illustrations can be found in the Appendix. Considering the optimum FC fan design parameters, including the ratio between the outer and inner diameters, number of blades etc. reported in different previous studies, e.g. [5], the FC fan under investigation enjoys an optimum design.

The sound measurements are performed by using the in-duct method in accordance with DIN/ISO 5136 [77]. The volute tongue (cut-off) is screwed to the housing, making it easy to remove the cut-off geometry and replace it with another one. In order to investigate the effects of the cut-off geometries on the noise characteristics of the fan, different volute tongues such as stepped tongues are designed, prototyped, and tested on the rig. Each cut-off geometry is designated by a straightforward serial number following the format shown in Fig. 2.2. The abbreviation '*LHLH*', which is only relevant in the case of stepped tongues (i.e., phase-shift tongues), denotes the relative position of each segment, from the hub side toward the shroud side (L stands for low and H for high). The first number represents the inclination of the cut-off geometry, or the circumferential difference in the heights of the segments for

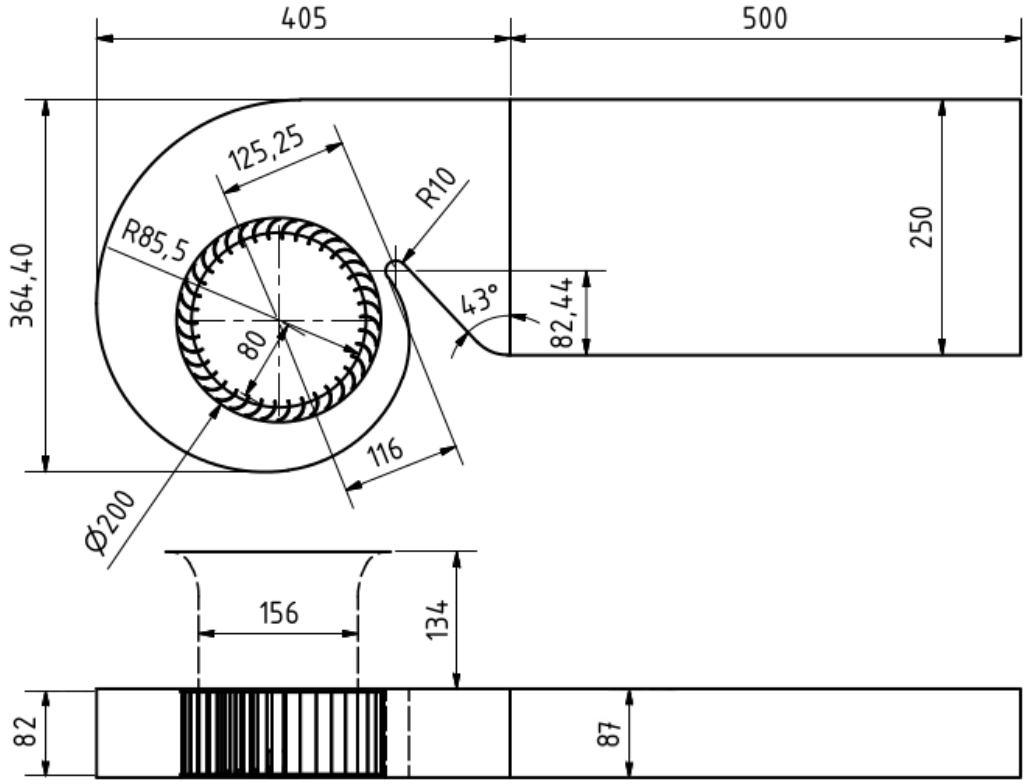

Figure 2.1: Geometrical dimensions and parameters of the reference fan.

stepped tongues; 0 means the cut-off is not inclined, 8.25 mm represents half a blade-to-blade spacing and 16.5 mm one blade-to-blade spacing (i.e., one rotor passage). The second number denotes the radius of the tongue and the third number represents the minimum distance between impeller and cut-off (clearance).

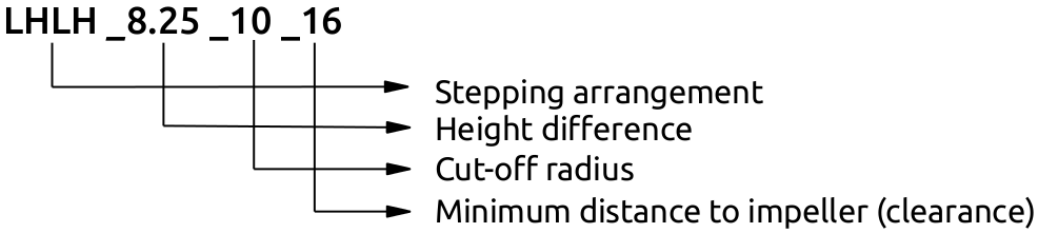

Figure 2.2: Description of the serial numbers assigned to cut-off geometries.

According to the given description, the original cut-off geometry (i.e., reference cut-off) shown in Fig. 2.3 is termed 0_10_16.

Table 2.1: Dimensions of the reference FC fan model.

Parameter	Dimension (mm)
Impeller inlet diameter	160
Impeller outlet diameter	200
Impeller width	82
Blade width	80
Blade arc radius	15
Blade thickness	0.6
Blade arc length	25
Volute width	87
Volute tongue (cut-off) radius	10
Impeller-tongue distance (clearance)	16
Inlet nozzle diameter	156
Inlet nozzle length	134
Blade inlet angle	77.3°
Blade outlet angle	165.4°
Volute opening angle	7°
Cut-off angle	23°
Number of blades	38

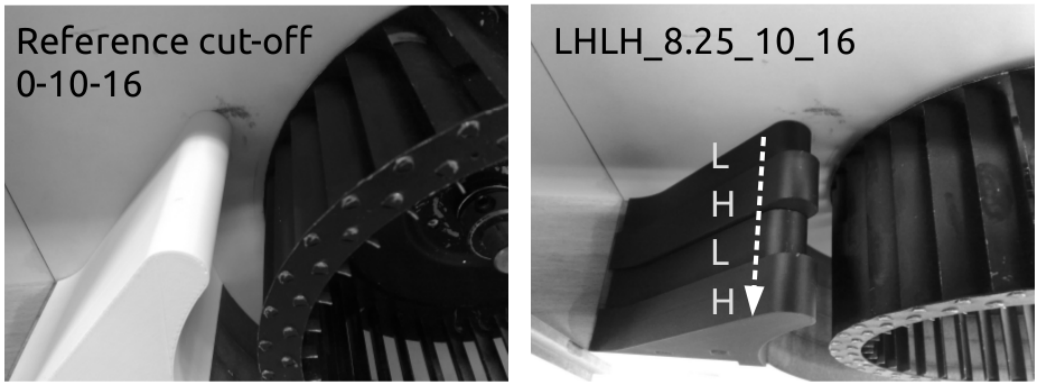

Figure 2.3: The reference cut-off (left) alongside with the stepped tongue LHLH_8.25_10_16 (right).

2.2 In-Duct Method

The in-duct method helps to overcome most of the following difficulties arising when one attempts to determine the sound power of an air moving device radiated into a duct connected to it [78]:

- The sound power generated by an acoustic source depends on its acoustic load, i.e. the acoustic impedance presented to its inlet and outlet side.
- The sound power propagating from the source down the duct is reflected at duct discontinuities and/or the duct end.
- Above a certain frequency, the sound pressure in the duct is not uniform over the duct cross-section but depends on the transverse position.
- The microphone in the flow duct is exposed not only to the sound pressures to be measured but also to the unsteady pressures associated with the turbulent flow.
- In a practical measurement situation, it is difficult to decide whether or not the microphone signal is contaminated by the turbulent flow pressures (even when a windscreen is used).

For performing the sound measurements, the fan is placed in a semi-anechoic room (Fig. 2.4) while its outlet is terminated by means of a two-sided non-reflective (anechoic) termination (Fig. 2.6). The operating point of the fan is determined by using a Prandtl Tube (Pitot-Static Tube) installed in the fan discharge and a throttle unit connected to the outlet of the anechoic termination. The setup is calibrated on a chamber test rig priori to the sound measurements. A maximum flow rate of approximately $550\,\mathrm{m}^3/\mathrm{h}$ can be reached at 1000 rpm when conducting a sound measurement for the reference model.
The anechoic termination should prevent the formation of the axial standing waves, and as a result, the sound measurement becomes independent of the axial location [78]. In cases where the duct is not properly terminated or ends abruptly, sound from the fan travels along the duct and gets reflected at the open end. Within the duct, the resulting sound pressure is a combination of the direct and the reflected noise. At some positions in the duct the pressures will be reinforced while at others they will cancel so that the in-duct sound pressure level becomes a function of axial location in the duct [79].
An anechoic termination consists of three basic elements; an expansion section, a body, and a throttle plate in the case of an outlet side termination (like in this study) or a further set of tapers in the case of an inlet side

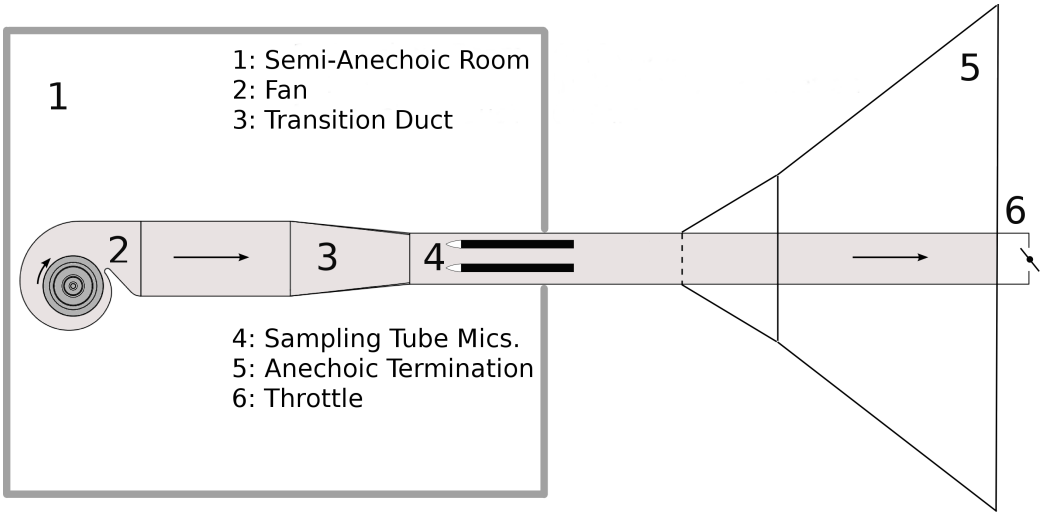

Figure 2.4: Schematic illustration of the test rig used for the noise measurements according to the so called in-duct method (DIN/ISO 5136).

termination. The throttle unit helps to adjust the flow rate of the fan and bring it to a desired operating point. The role of the expansion section is to provide a gradual change in the duct impedance, acting as an acoustical transformer between the test duct and the terminator body. The acoustic impedance, at any surface is the ratio of the area-averaged acoustic pressure to the effective volume velocity through the surface [79]. The impedance of the transformation section should be such that the reflection coefficient does not exceed the specified limits.

The reflection coefficient can be defined as the ratio of the reflected sound pressure to the incident sound pressure. The sound pressure reflection coefficient, occurring in the duct as a result of the standing wave formed by the incident and the reflected plane waves, at each center frequency of the frequency bands starting from 50 Hz upto the band containing the cut-on frequency can be calculated using Eq. 2.1 [77, 79].

For a well designed anechoic termination, the pressure reflection coefficient decays monotonically with frequency in the plane wave frequency range. The reflection coefficients of the higher acoustic modes are highest close to their cut-on frequencies with again a monotonic decrease with frequency [78].

The cut-on frequency specifies the range up to which the sound propagation is in the form of plane-wave (see Fig. 2.5). For a duct with circular cross-

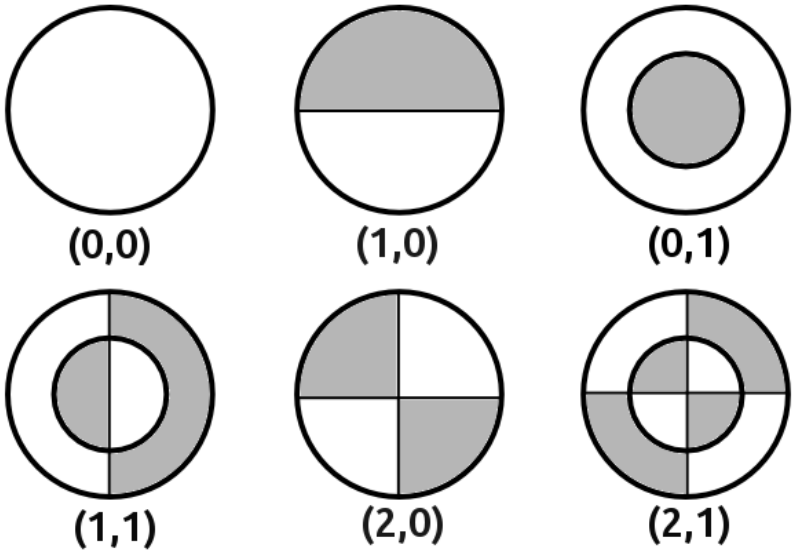

Figure 2.5: Pressure distribution in a circular duct from lower to higher order modes (reproduced from [64, 80]).

section, the cut-on frequency of the first cross mode can be calculated using Eq. 2.2 [77, 79].

$$r_a = \frac{10^{\left(\frac{Lp_{max} - Lp_{min}}{20}\right)} - 1}{10^{\left(\frac{Lp_{max} - Lp_{min}}{20}\right)} + 1} \tag{2.1}$$

$$f_{cut\text{-}on} = 0.586 \frac{c}{D} \sqrt{1 - \left(\frac{U}{c}\right)^2} \tag{2.2}$$

The role of the terminator body is to absorb or to radiate away from the test duct, much of the acoustic energy transmitted to it through the transformation section, so that very little is reflected back into the test duct. Since the expansion section has to be an efficient transmitter of sound energy from the test duct to the terminator it follows that it will also be efficient in the reverse direction [79].

The anechoic-termination (shown in Fig. 2.6) is constructed according to the norm proposals and its performance is evaluated according to the standard procedure given in DIN/ISO 5136 [81, 82].

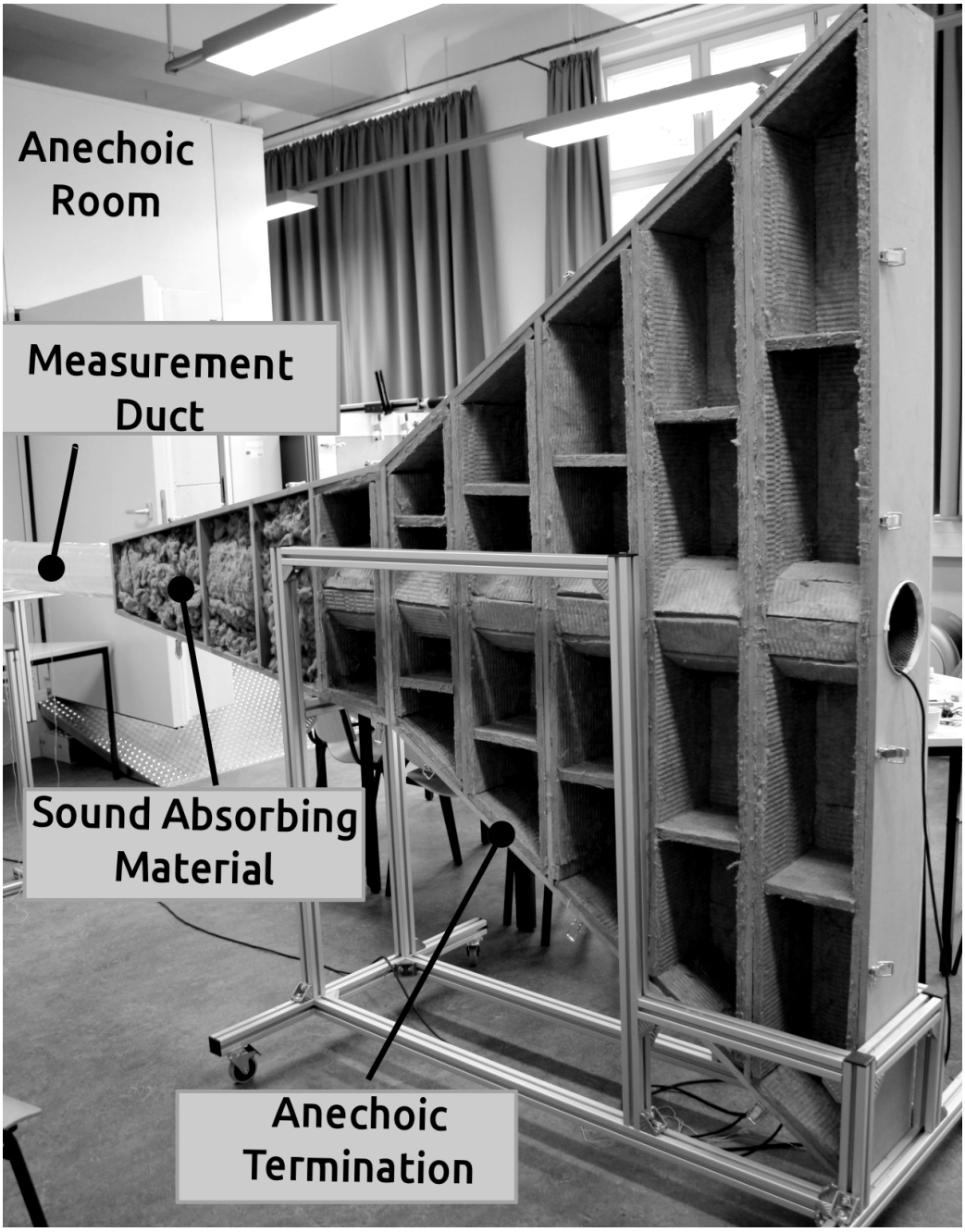

Figure 2.6: An image of the anechoic termination used for the sound measurements in the Laboratory of Thermo & Fluid Dynamics at HTW Berlin. The anechoic termination is connected to the fan outlet through a measurement duct. The expansion section is filled with a sound absorbing material (e.g., mineral wool).

The Measurement duct, which connects the fan outlet (through a transition duct) to the anechoic termination, has a diameter of 170 mm. Therefore, according to Eq. 2.2, the experimental results are influenced by the effects of modes beginning from approximately 1172 Hz at the BEP of the fan (i.e., 450 m^3/h).
Sound radiated from the outlet of the fan is measured upto 5000 Hz by using three high precision microphones installed in the measurement duct. The microphones are manufactured by Microtech Gefell GmbH and are applicable in the range of 10 Hz to 40 kHz with the maximum SPL upto 158 dB [83]. The microphones are calibrated by means of a Brüel & Kjær sound calibrator (Type 4231) with a reference sound pressure level of 94 dB. The calibration accuracy is ±0.2 dB according to the device manufacturer [84].

The measurements are performed by using turbulence screen microphones (also called slit-tube microphones [78]) shown in Fig. 2.7. Equipping the microphones with slit-tube wind screens helps to suppress the effect of the turbulence induced pressure fluctuations on the microphone. These fluctuations can mask acoustic signals recorded by a simple in-flow microphone even if protected by a forebody such as nose cone. Owing to the design of the slit-tube microphone, it must be installed parallel to the duct-axis and pointed into the wind to avoid flow separation and excessive flow noise [85, 86].

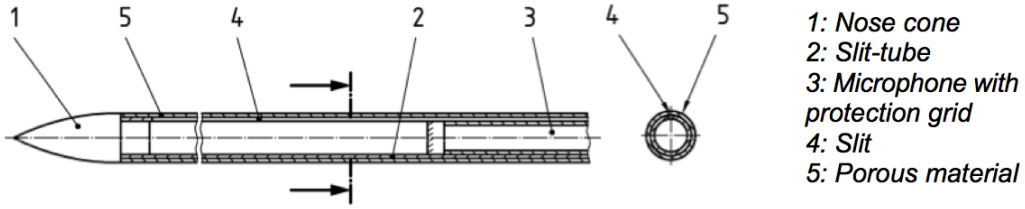

Figure 2.7: Schematic illustration of a slit-tube windscreen for 0.5-inch microphones [77, 78].

As shown in Fig. 2.4, the fan outlet is connected to the measurement duct through a transition duct. It is well known that abrupt changes in cross-section involve sound reflections as well as changes in acoustic loading [78]. In order to avoid the reflections, the transition duct should be designed according to the suggested guidelines, and its length should be calculated based on Eq. 2.3. l_0 is the reference length which is equal to 1 m. Besides, for aerodynamic reasons the valley angle of the transition duct should not exceed 15° [77].

$$\frac{l_{min}}{l_0} = \frac{S_l}{S_s} - 1 \tag{2.3}$$

As mentioned earlier, the measurement duct has a diameter of 170 mm, which makes the cross-section area of the duct approximately equal to the cross-section area of fan outlet. Therefore, the length of the transition duct is not an influential parameter herein.

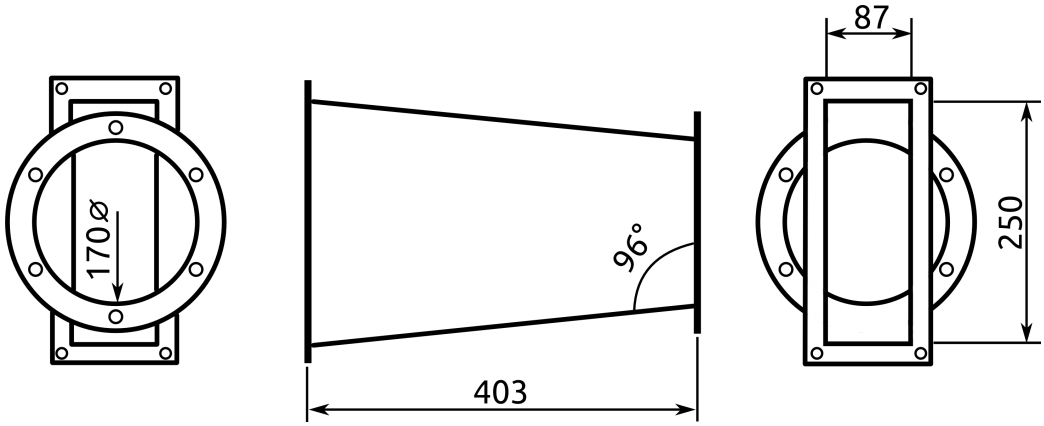

Figure 2.8: Dimensions of the transition duct that connects the fan outlet to the measurement duct (reproduced from [81, 82]).

Only when the sound wavelength is large compared with the cross dimension of a duct is the sound pressure uniform over the cross-section. If sound reflections from duct discontinuities are absent, acoustic pressure p and acoustic particle velocity v are related by the plane wave relation $p/v = \rho\, c$. The determination of sound power transmitted in a duct of cross-sectional area S without flow is given by $P = \overline{pv}S$, where the overbar indicates time-averaging. In logarithmic form, the so-called plane wave formula can be defined according to Eq. 2.4 [78].

$$L_w = L_p + 10\, log(S/S_0) - 10\, log\,[\rho\, c/(\rho\, c)_0] \tag{2.4}$$

where $S_0 = 1\,\mathrm{m}^2$ and $(\rho\, c)_0 \cong 408\,\mathrm{N\,s/m}^3$ are the usual reference values.

In the frequency region where higher order acoustic modes can propagate, the sound pressure amplitude varies over the duct cross-section, and determination of the duct sound power requires integration of the sound intensity over the cross-section. Equation 2.5, for instance, is valid for the no-flow case [78].

$$P = \int_S \overline{pv}\,\mathrm{d}S \tag{2.5}$$

As shown in Fig. 2.5, distribution of sound intensity is non-uniform in the presence of higher order modes. In the case of a circular pipe, a practical approach to sound power determination is to use multiple microphones distributed radially across the cross-section of the duct (Fig. 2.9). For a directional sensor like a microphone equipped with slit-tube, the optimum radial position is closer to the pipe wall, where the mode amplitudes are generally larger, to compensate for the microphone directivity [78, 87].

For a slit-tube microphone with 400 mm effective length the relative radial position of the microphone from the duct axis is $2r/d = 0.8$ for pipe diameters between $0.15 \leqslant d \leqslant 0.5\,\mathrm{m}$ and $2r/d = 0.65$ for $0.5 \leqslant d \leqslant 2\,\mathrm{m}$ [77, 78, 87].

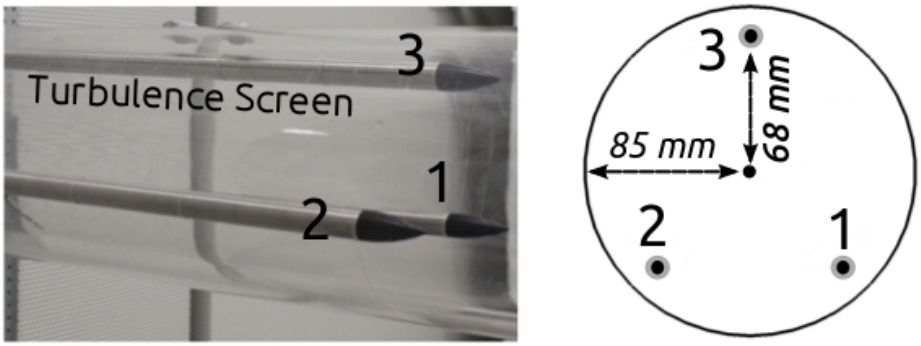

Figure 2.9: Distribution of the slit-tube microphones in the measurement duct calculated according to DIN 5136.

The average sound pressure level recorded by three microphones shown in Fig. 2.9 is calculated according to Eq. 2.6 [77].

$$\overline{L_p} = 10\,log\left[\frac{1}{N}\sum_{i=1}^{N} 10^{0.1L_{pi}}\right]\,dB + C \tag{2.6}$$

where C is the combined frequency response correction of the sampling-tube microphone to be calculated according to Eq. 2.7 [77].

$$C = C_1 + C_2 + C_{3,4} \tag{2.7}$$

C_1 is the free field microphone response correction which shall be taken from the microphone manufacturer's data sheets (see Appendix A.6), C_2 is the frequency response correction of the microphone shield, and $C_{3,4}$ is the combination of C_3 & C_4. The former is defined as the flow velocity correction

which accounts for the change in the frequency response of the microphone shield as a result of superimposed flow [78] and the latter is defined as the modal frequency correction which accounts for the directivity characteristics of the microphone with the turbulence screen in the view of the propagation angles of the higher order duct modes [31].

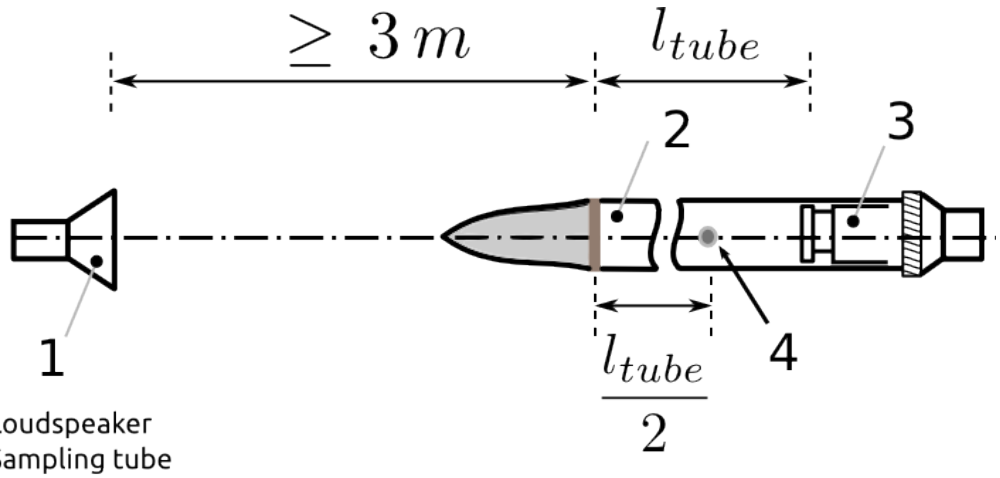

Figure 2.10: Illustration of the reference microphone position to calculate the frequency response correction $C_2 = L_{p2} - L_{p1}$; l_{tube} is the length of the slit (reproduced from [77]).

The frequency response correction C_2 for the a slit-tube microphone can be defined as the difference between the sound pressure level measured with the microphone equipped with the sampling tube and the sound pressure level measured at the same position with the same microphone without the slit-tube according to Fig. 2.10 [77].

Values for the mean flow velocity-modal correction of the microphone shield $C_{3,4}$ can be calculated according to Eq. 2.8 [77], where U is the mean flow velocity ($U < 0$ for the inlet duct and $U > 0$ for the outlet duct) and a_i is the coefficient value given in DIN 5136 (see Appendix A.8).

$$C_{3,4}(U) = \sum_{i=0}^{10} a_i U^i \tag{2.8}$$

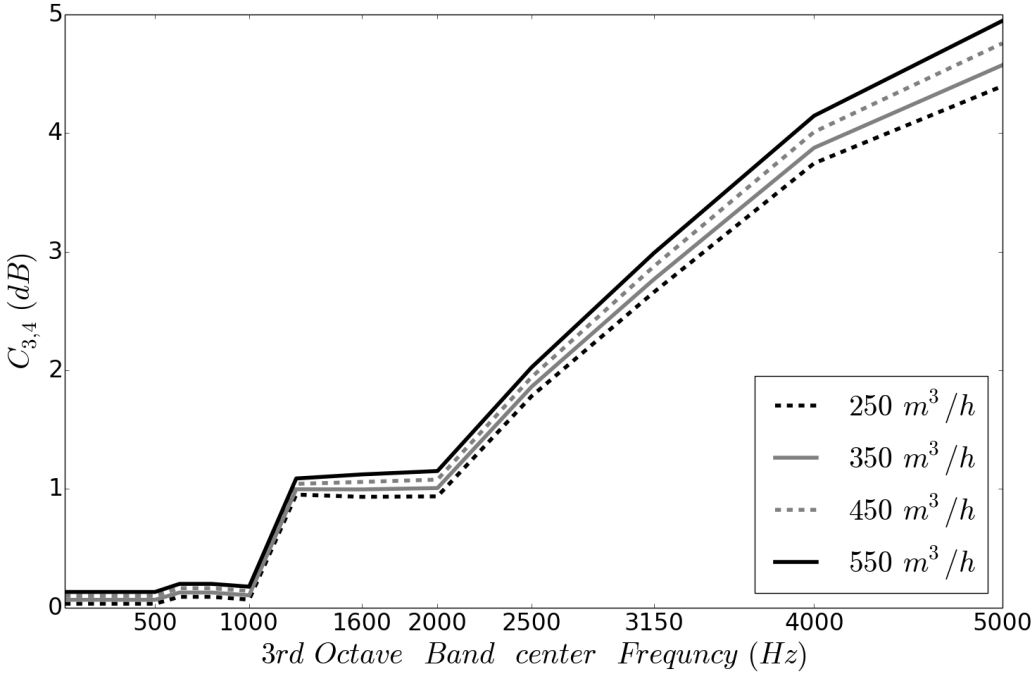

Figure 2.11: Combined flow velocity and modal correction $C_{3,4}$ calculated for the turbulence screen and different flow rates.

2.3 Reproducibility of the In-Duct Method Measurements

Table 2.2 presents a detailed comparison between the standard deviations of free field method [88], reverberation room methods [89, 90], and in-duct method [77] all applied to fans [78].

The information given in this table reflect the cumulative effects of all causes of measurement uncertainty such as source location, end reflections, duct transitions, instrument calibration, sound pressure to sound power computing and sampling errors. By assuming the statistical interdependency between the uncertainties, the combined standard deviation can be calculated according to Eq. 2.9 [87].

$$\sigma = \sqrt{\sigma_1^2 + \sigma_2^2 + \sigma_3^2 + \cdots + \sigma_n^2} \tag{2.9}$$

Table 2.2: Estimated standard deviations of reproducibility of sound power levels according to various ISO-standards [78].

f (Hz)	ISO 3743-1	ISO 3743-2	ISO 3744	ISO 5136
50	-	-	5	3.5
63	-	-	5	3
80	-	-	5	2.5
100	3	5	3	2.5
125	3	5	3	2
163	3	5	3	2
200	2	3	2	2
250	2	3	2	2
315	2	3	2	2
400	1.5	2	1.5	2
500	1.5	2	1.5	2
630	1.5	2	1.5	2
⋮	⋮	⋮	⋮	⋮
3150	1.5	2	1.5	2
4000	1.5	2	1.5	2
5000	1.5	2	1.5	2.5
6300	2.5	3	2.5	3
8000	2.5	3	2.5	3.5
10000	2.5	3	2.5	4

The standard deviations reported are those which would be expected if the measurement of a single fan were repeated in many different laboratories. They do not include variations in the sound power radiated by the fan itself caused for example by changes in the mounting arrangements [77].

ISO 3743-1 & 2 are applicable only for octave bands between 125 and 8000 Hz, while ISO 3744 and ISO 5136 are for one-third octave bands in the range 50 - 10000 Hz. Up to 315 Hz, the in-duct method yields the best accuracy and is only slightly worse than the free field method up to 4000 Hz [78].

2.4 Experimental Signal Processing

The experimental signals are processed using the commercially available program SAMURAI [91]. Each single measurement involves 10 repetitions, each

taking 35 s. The final result of each measurement, calculated by digital signal processor according to Eq. 2.10, is the average energy-equivalent continuous sound level L_{eq} of the corresponding repetitions.

$$L_{eq} = 10log\left(\frac{1}{T}\int_0^T \frac{p^2(t)}{p_0^2}\right)\,dt = 10log\left(\frac{1}{T}\int_0^T 10^{L(t)/10}\right)\,dt \qquad (2.10)$$

where $p^2(t)$ indicates the mean square (time-varying) sound pressure and $L(t)$, the level gradient over time [59, 65].

Table 2.3, presents the settings used for the signal processing of the experimental measurements. Using the parameters given in this table, the signal processor converts the recorded sound signals into the spectral results with a frequency resolution of approximately 0.8 Hz.

Table 2.3: Settings used for processing the experimental signals in SAMURAI environment.

General Settings	
Duration of measurement	35 s
Frequency range	0-10 kHz
Number of repetitions	10
FFT	
Sampling rate	25.6 kHz
Number of lines	12801
Window	Hanning (Hann)
Averaging mode	Exponential
Exp. time[1]	0.64 s
Delta time[2]	1.28 s
1/3 Octave	
Lower band	50 Hz
Upper band	5 kHz
Averaging mode	Fast
Delta time	0.12 s

[1]The time constant for exponential averaging [91]
[2]The time interval for data storage [91]

Chapter 3

Numerical Simulations

Computational Fluid Dynamics (CFD) and Computational Aeroacoustics (CAA) simulations are performed to numerically predict the aeroacoustical characteristics of the fan. The commercially available CFD package STAR-CCM+ is used for performing the numerical simulations as well as numerical grid generations. The grids employed consist of several million cells (volume elements) in the range of approximately 12.5 million to 100 million. In the performed simulations the influence of different boundary-conditions and time-steps are evaluated and addressed. The performance of different turbulence models and methods including Unsteady Reynolds-Averaged Navier-Stokes (URANS), Detached Eddy Simulation (DES) and Large Eddy Simulation (LES) are investigated.

Due to the complex nature of sound as well as the variety of sound sources, it has not been possible so far to introduce a single CAA method which is capable of reliably predicting the noise generated in all cases. As a result, there are several approaches available for predicting the noise and the following are some of the common methods which are practical to solve the everyday engineering problems [92]:

Direct methods can be considered the most accurate approach for CAA and are comparable to Direct Numerical Simulation (DNS) in the CFD field. The compressible Euler or Navier-Stokes equations are solved in the domain of interest for the unsteady combined flow and acoustic field from the aerodynamic effective area down to the far field observer. They do not include any modeling of sound and thus do not suffer from any modeling or approximation errors (except for the turbulence modeling). The main drawback of these methods is that they require tremendous computational resources,

especially in the case of small Mach number flows. Moreover, space and time resolution requirements for the aerodynamic data combined with the large distance up to an observer in the far field increases the number of cells in the numerical grid while demanding very small time steps. Direct methods are generally attractive because the well-known CFD packages promise to provide aerodynamic and aeroacoustic data at the same time. Sometimes they work surprisingly well, mostly in the cases that the difference between the aerodynamics and aeroacoustics are negligible. However, they sometimes completely fail, since the basic requirements for CFD and CAA might be too different.

Hybrid method is used in many successful aeroacoustic tools. In this method, sound generation is decoupled from sound transport. Therefore, most of the time, a CFD package is required which solves the governing equations and provides information about the sound sources in the near field. The CAA package inherits the near field solution from the CFD package by means of which it is able to compute the sound propagation (transport). Two transport methods are available to be used by a CAA solver:

- Computational transport methods are similar to a CFD computation, in the sense that they solve some partial differential equations from the source (near field) up to the observer (far field). Usually computational transport methods solve simple equations such as the Linearized Euler Equations (LEE). Since the equations are simpler, the grids are not as demanding as CFD grids and the advanced discretization schemes are often not required. The computational costs can grow tremendously in the case that the observer is far away from the source, because the numerical grid should cover all the space between the source and the receiver.

- Analytical transport techniques employ an integrated form of the relevant acoustic propagation equation, which is either Kirchhoff's surface integral or the Ffowcs Williams-Hawkings (FW-H) equation. The sound pressure at an observer at a specific point in time is computed by an integration of source term along a surface, which is either a physical surface or a virtual surface surrounding the source.

3.1 Governing Equations

3.1.1 Conservation Laws

In the Eulerian description of fluid mechanics the field variables, such as pressure, density, momentum, and energy, are considered to be continuous functions of the spatial coordinates x, y, z and of time t [59]. In three dimensional space velocity has three components, and at least two thermodynamic variables are needed to establish the equation of state (Eq. 3.1 for an ideal gas). In order to obtain the mentioned field variables six independent equations are needed. The following conservation laws can be used to determine the dynamical behaviour of a fluid.

1. Conservation of Mass (Eq. 3.3)
2. Conservation of Momentum (Eq. 3.4)
3. Conservation of Energy (Eq. 3.8)

The conservation of mass supplies one equation; the conservation of momentum supplies three equations along the three principle axes; the conservation of energy supplies the fifth equation; and the equation of state constitutes the sixth equation [59, 93]. Temperature in the equation of state can be obtained from the caloric equation of state (Eq. 3.2) [94].

$$\frac{p}{\rho} = RT \tag{3.1}$$

$$e = c_v T \qquad h = c_p T \tag{3.2}$$

$$\frac{\partial \rho}{\partial t} + \nabla . (\rho \, \overrightarrow{v}) \; = 0 \tag{3.3}$$

The conservation of momentum or shortly the momentum equation (Eq. 3.4) is based on Newton's second law which states that the rate of change of momentum of a fluid particle equals the sum of forces acting on the particle. There are two kinds of forces acting on fluid particles (or control volumes) [94, 95]:

- External volume or body forces which act directly on the volumetric mass of the fluid element, such as gravitational, buoyancy, Coriolis or centrifugal forces.

- Surface forces which act directly on the surface of the control volume, and result from two sources (a) the pressure distribution imposed by the outside fluid surrounding the volume and (b) the shear and normal stress distributions, resulting from the friction between the fluid and the surface of the volume.

$$\rho \frac{D\overrightarrow{v}}{Dt} = \rho \overrightarrow{f} + \nabla \cdot \Pi_{ij} \tag{3.4}$$

The first term on the right-hand side of Eq. 3.4 is the body force per unit volume, while the second term represents the surfaces force per unit volume. Π_{ij} is the stress tensor which for a Newtonian fluid can be written as follows:

$$\Pi_{ij} = -p\,\delta_{ij} + \underbrace{\mu\left[\left(\frac{\partial v_i}{\partial x_j} + \frac{\partial v_j}{\partial x_i}\right) - \frac{2}{3}\delta_{ij}\,\frac{\partial v_k}{\partial x_k}\right]}_{\tau_{ij}} \tag{3.5}$$

In Eq. 3.5, δ_{ij} is the Kronecker delta function ($\delta_{ij} = 1$ if $i = j$ and $\delta_{ij} = 0$ if $i \neq j$), and μ is dynamic viscosity (also called coefficient of viscosity) [96]. The second term on the right-hand side of Eq. 3.5 is the viscous stress tensor τ_{ij}. For a Newtonian fluid the components of the viscous stress tensor are given by [93, 96]:

$$\tau_{xx} = -\frac{2}{3}\,\mu\,(\nabla\,.\,\overrightarrow{v}) + 2\mu\frac{\partial v_x}{\partial x} \tag{3.6a}$$

$$\tau_{yy} = -\frac{2}{3}\,\mu\,(\nabla\,.\,\overrightarrow{v}) + 2\mu\frac{\partial v_y}{\partial y} \tag{3.6b}$$

$$\tau_{zz} = -\frac{2}{3}\,\mu\,(\nabla\,.\,\overrightarrow{v}) + 2\mu\frac{\partial v_z}{\partial z} \tag{3.6c}$$

$$\tau_{xy} = \tau_{yx} = \mu\left(\frac{\partial v_y}{\partial x} + \frac{\partial v_x}{\partial y}\right) \tag{3.6d}$$

$$\tau_{xz} = \tau_{zx} = \mu\left(\frac{\partial v_z}{\partial x} + \frac{\partial v_x}{\partial z}\right) \tag{3.6e}$$

$$\tau_{yz} = \tau_{zy} = \mu\left(\frac{\partial v_z}{\partial y} + \frac{\partial v_y}{\partial z}\right) \tag{3.6f}$$

Substituting the above equations in Eq. 3.4 yields the Navier-Stokes equations in conservation form:

$$\frac{\partial(\rho v_x)}{\partial t} + \nabla \cdot (\rho v_x \overrightarrow{v}) = -\frac{\partial p}{\partial x} + \frac{\partial \tau_{xx}}{\partial x} + \frac{\partial \tau_{yx}}{\partial y} + \frac{\partial \tau_{zx}}{\partial z} + \rho f_x \tag{3.7a}$$

$$\frac{\partial(\rho v_y)}{\partial t} + \nabla \cdot (\rho v_y \overrightarrow{v}) = -\frac{\partial p}{\partial y} + \frac{\partial \tau_{xy}}{\partial x} + \frac{\partial \tau_{yy}}{\partial y} + \frac{\partial \tau_{zy}}{\partial z} + \rho f_y \tag{3.7b}$$

$$\frac{\partial(\rho v_z)}{\partial t} + \nabla \cdot (\rho v_z \overrightarrow{v}) = -\frac{\partial p}{\partial z} + \frac{\partial \tau_{xz}}{\partial x} + \frac{\partial \tau_{yz}}{\partial y} + \frac{\partial \tau_{zz}}{\partial z} + \rho f_z \tag{3.7c}$$

The conservation of energy is derived from the first law of thermodynamics, which states that the rate of change of energy of a fluid particle is equal to the sum of the rate of heat addition to the fluid particle and the rate of work done on the particle [97].

$$\underbrace{\frac{\partial E_t}{\partial t} + \nabla \cdot E_t \overrightarrow{v}}_{\substack{\text{Rate of change of energy} \\ \text{inside the fluid element}}} = \underbrace{\frac{\partial Q}{\partial t} - \nabla \cdot \overrightarrow{q}}_{\substack{\text{Net flux of heat} \\ \text{into the element}}} + \underbrace{\rho \overrightarrow{f} \cdot \overrightarrow{v} + \nabla \cdot (\Pi_{ij} \cdot \overrightarrow{v})}_{\substack{\text{Rate of working} \\ \text{done on the element}}} \tag{3.8}$$

Equation 3.8 is the conservation of energy written in terms of total energy [96]. The total energy of a fluid element per unit mass is the sum of its internal energy per unit mass, e, and its kinetic energy per unit mass, $v^2/2$.

Equation 3.9 defines the rate of change of energy of a fluid particle in terms of its total energy in conservation form [93].

$$\rho \frac{D}{Dt}\left(e + \frac{v^2}{2}\right) dx\, dy\, dz \tag{3.9}$$

The net flux of heat into the element originates from two sources, i.e. volumetric heating such as absorption or emission of radiation, and heat transfer across the surface due to temperature gradients (thermal conduction).

$$\left[\rho \dot{q} - \left(\frac{\partial \dot{q}_x}{\partial x} + \frac{\partial \dot{q}_y}{\partial y} + \frac{\partial \dot{q}_z}{\partial z}\right)\right] dx\, dy\, dz \tag{3.10}$$

According to Fourier's law, heat transfer by thermal conduction is proportional to the local temperature gradient [93, 96].

$$\dot{q}_x = -k\frac{\partial T}{\partial x} \qquad \dot{q}_y = -k\frac{\partial T}{\partial y} \qquad \dot{q}_z = -k\frac{\partial T}{\partial z} \tag{3.11}$$

And lastly, the net rate of work done on the moving fluid element due to body and surface forces can be written as follows [93]:

$$\rho\left(\overrightarrow{f}\cdot\overrightarrow{v}\right)\,dx\,dy\,dz+\left[-\nabla\cdot(p\,\overrightarrow{v})+\frac{\partial(v_x\tau_{xx})}{\partial x}+\frac{\partial(v_x\tau_{yx})}{\partial y}\right.$$
$$+\frac{\partial(v_x\tau_{zx})}{\partial z}+\frac{\partial(v_y\tau_{xy})}{\partial x}+\frac{\partial(v_y\tau_{yy})}{\partial y}+\frac{\partial(v_y\tau_{zy})}{\partial z} \qquad (3.12)$$
$$\left.+\frac{\partial(v_z\tau_{xz})}{\partial x}+\frac{\partial(v_z\tau_{yz})}{\partial y}+\frac{\partial(v_z\tau_{zz})}{\partial z}\right]dx\,dy\,dz$$

3.2 Incorporation of the Acoustic Equations

In order to obtain the acoustic equations based on the conservation laws, the following assumptions should be made [59, 80]:

1. The unperturbed fluid has definite values of pressure, density, temperature, and velocity, all of which are assumed to be time independent and denoted by the subscript 0. The quiescent density ρ_0 also does not vary in space.

2. The passage of an acoustic signal through the fluid results in small perturbations of pressure, temperature, density, and velocity. These perturbations are expressed as:

$$p'=p-p_0\quad;\quad\rho'=\rho-\rho_0\quad;\quad T'=T-T_0\quad;\quad\overrightarrow{v}'=\overrightarrow{v} \qquad (3.13)$$

   The unperturbed velocity ($\overrightarrow{v}_0$) is set to zero. Also, $p'\ll p_0$, $\rho'\ll\rho_0$ and $T'\ll T_0$.

3. The transmission of the sound through the fluid results in low values of spatial temperature gradients at audio frequencies, resulting in almost no heat transfer between warmer and cooler regions of the plane wave. Thus the ongoing thermodynamics process may be considered an adiabatic process (at ultrasonic frequencies there is virtually no time for heat transfer to occur).

In an adiabatic process involving ideal gas the following equation is valid:

$$p\,\rho^{-\kappa}=constant\;\Rightarrow\;\frac{dp'}{p_0}=\kappa\,\frac{d\rho'}{\rho_0} \qquad (3.14)$$

Differentiating the above expression with respect to time leads to:

$$\frac{1}{p_0}\frac{\partial p'}{\partial t} = \frac{\kappa}{\rho_0}\frac{\partial \rho'}{\partial t} \tag{3.15}$$

By replacing $\frac{\partial \rho'}{\partial t}$ from the continuity equation (Eq. 3.3), and then differentiating the resulting equation with respect to time the following equation can be obtained:

$$\frac{\partial^2 p'}{\partial t^2} = \kappa\, p_0 \left[\frac{-\partial}{\partial t}(\nabla \cdot \overrightarrow{v})\right] \tag{3.16}$$

For inviscid flow ($\mu = 0$) the momentum equation (Eq. 3.4) yields Euler's equation:

$$\rho \frac{D\overrightarrow{v}}{Dt} = -\nabla p \tag{3.17}$$

Differentiating Euler's equation by space and discarding the second-order velocity terms leads to:

$$\rho_0 \frac{\partial}{\partial t}(\nabla \cdot \overrightarrow{v}) = -\nabla^2 p' \tag{3.18}$$

Finally, by equating the cross-differential terms in Eq. 3.16 & 3.18 to each other, the three dimensional wave equation can be defined as follows:

$$\nabla^2 p' = \frac{1}{c^2}\frac{\partial^2 p'}{\partial t^2} \tag{3.19}$$

c is the speed of sound which is previously defined for ideal gases in Eq. 1.11. Alternatively, Eq. 3.19 can be written in terms of velocity or density, by eliminating p' in favour of $\overrightarrow{v}$ or ρ':

$$\nabla^2 \overrightarrow{v} = \frac{1}{c^2}\frac{\partial^2 \overrightarrow{v}}{\partial t^2} \tag{3.20}$$

$$\nabla^2 \rho' = \frac{1}{c^2}\frac{\partial^2 \rho'}{\partial t^2} \tag{3.21}$$

One of the simplest general solutions to Eq. 3.19 can be written in the form of one dimensional progressive waves [59, 70, 98]:

$$p'(x,t) = F(t - \frac{x}{c}) + G(t + \frac{x}{c}) = Ae^{i(\omega t - kx)} + Be^{i(\omega t + kx)} \tag{3.22}$$

The first part $F(x - ct)$ represents a wave of arbitrary shape traveling in the positive x-direction with velocity c (an outgoing wave), and the second part $G(x + ct)$ represents a wave also of arbitrary shape traveling in the negative x-direction with velocity c (a backward traveling wave). In complex exponential form, $k = \omega/c$ is the wave number, and A and B are arbitrary constants (real or complex) to be evaluated by initial conditions.

3.2.1 Lighthill's Acoustic Analogy

The theory of aerodynamic sound developed by Lighthill [99] is the rearrangement of the continuity and momentum equations into an exact, inhomogeneous wave equation whose source terms are important only within the turbulent region [100]. In the Lighthill's analogy, it is assumed that the listener is surrounded by a quiescent reference fluid (p_0, ρ_0, c_0 uniformly constant and $v_0 = 0$) in which the small acoustic perturbations are accurately described by the homogeneous wave equation [92].

$$\frac{\partial^2 \rho'}{\partial t^2} - c_0^2 \nabla^2 \rho' = \frac{\partial^2 T_{ij}}{\partial x_i \partial x_j} \tag{3.23}$$

Equation 3.23 is the Lighthill equation, and T_{ij} is the Lighthill stress tensor given by [80, 100]:

$$T_{ij} = \rho\, v_i v_j - \tau_{ij} + \delta_{ij}(p' - c_0^2 \rho') \tag{3.24}$$

In order to obtain the right-hand side of Eq. 3.23 and compute the Lighthill stress tensor in the near field, transient CFD simulation should be performed. The general solution to Eq. 3.23 for an unbounded medium can be written as [99]:

$$\rho'(\overrightarrow{x}, t) = \frac{1}{4\pi c_0^2} \frac{\partial^2}{\partial x_i \partial x_j} \int_V \frac{T_{ij}(\overrightarrow{y}, t - |\overrightarrow{x} - \overrightarrow{y}|/c_0)}{|\overrightarrow{x} - \overrightarrow{y}|}\, d\overrightarrow{y} \tag{3.25}$$

It follows that when the flow is known, it is possible by means of Eq. 3.25 to evaluate the sound generated [62].

3.2.2 Curle's Analogy

Solid boundaries might well play an important role in the sound production in certain cases, even when they remain rigid. Curle extended the solution of the Lighthill equation by taking the presence of stationary reflective solid surfaces into account [101]. In addition to the volume integral (Eq. 3.25), Curle's solution has a surface integral which represents the contribution of the solid boundaries. Therefore, in Curle's solution, the sound field is composed of the sound generated by a volume distribution of quadrupoles and by a surface distribution of dipoles. Solid boundaries can contribute to sound production in two ways [62]:

1. The sound generated by the quadrupoles of Lighthill's theory will be reflected and diffracted by the solid boundaries.

2. The quadrupoles will no longer be distributed over the whole of space, but only throughout the region external to the solid boundaries, and it seems that there might be a resultant distribution of dipoles (or even sources) at the boundaries. Dipoles are specially likely, since they correspond to externally applied forces, and such forces are present between the fluid and the solid boundary.

Equation 3.26 is the simplified Curle surface integral as adopted in STAR-CCM+ [102].

$$\rho'(\overrightarrow{x},t) = \frac{1}{4\pi c_0^3}\int_S \left[\frac{(\overrightarrow{x}-\overrightarrow{y})}{r^2}\frac{\partial p}{\partial t}\left(\overrightarrow{y},t-\frac{r}{c_0}\right)\right]\overrightarrow{n}\,dS\,(\overrightarrow{y}) \tag{3.26}$$

where $t-\dfrac{r}{c_0}$ is the emission time, p is the surface pressure, ρ' is density perturbations, and $r=|\overrightarrow{x}-\overrightarrow{y}|$ is the distance from the source. This equation is valid when presuming $|\overrightarrow{x}| \gg \lambda$ [62].

The solution of Eq. 3.26 along with the relation $p' = c_0^2\,\rho'$, which is valid for an adiabatic process involving an ideal-gas, can be used to compute the local acoustic power. In STAR-CCM+, the Curle acoustic model can be used in combination with two-equation RANS turbulence models. RANS models are responsible of providing turbulence time scale, turbulence length scale and wall shear stress necessary to compute the mean-square time derivative of the source surface pressure [102].

3.2.3 Ffowcs Williams–Hawkings Equation

The Ffowcs Williams-Hawkings (FW-H) equation is a further development of the Lighthill's acoustic analogy to include the effects of general types of surfaces and motions. Using the mathematical theory of distributions (also known as generalized functions), it is possible to rearrange the continuity equation and the momentum equations into the form of an inhomogeneous wave equation with two surface source terms (monopole and dipole) and a volume source term (quadrupole). Although the quadrupole source contribution is insignificant in many subsonic applications, substantially more computational resources are needed for volume integration when the quadrupole source is required [103, 104].

The moving surface is described by $f(\overrightarrow{x},t) = 0$ such that $\nabla f = \overrightarrow{n}$; $\overrightarrow{n}$

is the unit outward normal. Equation 3.27 is the original impermeable FW-H equation as proposed in [105]:

$$\left(\frac{\partial^2}{\partial t^2} - c^2\,\frac{\partial^2}{\partial x_i^2}\right)(\,\overline{\rho-\rho_0}\,) = \frac{\partial^2 \overline{T_{ij}}}{\partial x_i \partial x_j} - \frac{\partial}{\partial x_i}\left[[(p-p_0)\delta_{ij}]\delta(f)\frac{\partial f}{\partial x_j}\right] + \frac{\partial}{\partial t}\left[\rho_0 v_i\,\delta(f)\frac{\partial f}{\partial x_i}\right] \tag{3.27}$$

where v_i is the local velocity of the body in the direction normal to the surface implicitly defined by $f = 0$, p is the local gage pressure on the surface and $\delta(f)$ is the Dirac delta function ($= 0$ except for $f = 0$). Moreover, $\overline{\rho - \rho_0}$ is the generalized density perturbation, and $\overline{T_{ij}}$ is the generalized Lighthill stress tensor that is equal to the Lighthill stress tensor outside any surfaces, and is zero within them. In Eq 3.27, it is assumed that the viscous term is a negligible source of sound, hence the stress tensor is reduced to $(p-p_0)\delta_{ij}$ [104].

The three source terms in the FW-H equation each have a physical meaning, which is helpful in understanding the noise generation. The thickness noise (monopole source) is determined completely by the geometry and kinematics of the body. The loading noise (dipole source) is generated by the force that acts on the fluid as a result of the presence of the body. The quadrupole source term accounts for non-linear effects (e.g., noise generated by shocks, vorticity, and turbulence in the flow field) [103]. The FW-H acoustic model is suitable for predicting the propagation of sound in the free space, and it does not include effects such as sound reflections, refraction, or material property change [102]. Equation 3.27 can be written in a compact form by exploiting the wave operator (also called D'Alembertian operator), $\Box^2$, and the Heaviside function, $H(f)$ [101, 104, 106, 107]:

$$\Box^2\, p' = \underbrace{\frac{\partial}{\partial t}[\rho_0 v_n\,\delta(f)]}_{\substack{\text{monopole or}\\ \text{thickness source}}} - \underbrace{\frac{\partial}{\partial x_i}[(p-p_0)n_i\,\delta(f)]}_{\substack{\text{dipole or}\\ \text{loading source}}} + \underbrace{\frac{\partial^2}{\partial x_i \partial x_j}[H(f)T_{ij}]}_{\substack{\text{quadrupole or}\\ \text{volume source}}} \tag{3.28}$$

where v_n is the local normal velocity of the surface ($v_n = v_i n_i$). Also, $\rho - \rho_0$ on the left hand-side of Eq. 3.27 is converted into p' using the relation $p' = c^2(\rho - \rho_0)$. The Heaviside function is $H(f) = 0$ for $f < 0$, and $H(f) = 1$ for $f > 0$, which reminds that the volume source only exists in the exterior of the surface [104]. The wave operator can be defined as:

$$\Box^2 = \frac{1}{c^2}\frac{\partial^2}{\partial t^2} - \nabla^2 \tag{3.29}$$

In STAR-CCM+, the FW-H formulation is coded based on Farassat's Formulation 1A . For the exact formulation refer to [102–104, 106, 107].

3.3 Turbulence Modeling

Turbulence modeling is still one of the major concerns of CFD after several decades. Due to the complexity of the flow on the one hand, and the inevitability of making assumptions and simplifications (e.g., averaging) on the other hand, it is not possible to introduce a single turbulence model which reliably predicts all kinds of turbulent flows. For instance, a particular model might perfectly work in the case of attached boundary layers, and completely fail for separated flows. An ideal model should introduce the minimum amount of complexity while capturing the essence of the relevant physics. Furthermore, an important consequence of closing the governing equations with turbulence models is that the solutions are no longer exact representations of physical problems implied by the boundary conditions, and the uncertainties associated with the assumptions have to be appraised, usually by comparison with experiments [95, 108, 109]. The complex nature of turbulence caused some of the scientists studying it to give exciting descriptions about it. For example, Bradshaw inspires the whole phenomenon of turbulence as being unrigorous and probably invented by the Devil on the seventh day of Creation [110].

Turbulence is a natural phenomenon in fluids that occurs when velocity gradients are high, resulting in disturbances in the flow domain as a function of space and time. The outstanding feature of a turbulent flow, contrary to a laminar flow, is that the molecules move in a chaotic fashion along complex irregular paths. The strong chaotic motion causes the viscous layers of the fluid to mix together intensely. Because of the increased momentum and energy exchange between the molecules and solid walls, turbulent flows lead at the same conditions to higher skin friction and heat transfer as compared to laminar flows [95, 100].

There are different principal classes of turbulence models with each of them being further divided into different subcategories. The main distinction between turbulence models is whether turbulence properties are related directly to the mean flow or obtained from transport equations [111].

Direct Numerical Simulation (DNS)

The most accurate approach to turbulence simulation is to solve the Navier-Stokes equations without averaging or approximating other than numerical discretizations whose error can be estimated and controlled. It is also the simplest approach from the conceptual point of view [112]. Despite all the advantages that can be listed for DNS, there are some serious impediments to perform such simulation. Direct solution of the flow equations is very difficult because of the wide range of length and time scales caused by the appearance of eddies in a turbulent flow [97]. To resolve a turbulent flow by DNS requires that all relevant length scales be resolved from the smallest eddies to scales on the order of the physical dimensions of the problem domain. The computations need to be 3D even if the time mean aspects of the flow are 2D, and the time steps must be small enough that the time-scale motion can be resolved in a time-accurate manner even if the flow is steady in a time-mean sense [96].

A valid simulation must also capture all the kinetic energy dissipation. This occurs on the smallest scales (Kolmogorov scales Eq. 3.30), the ones on which viscosity is active, so the size of the grid must be no larger than a viscously determined scale, called the Kolmogorov scale (Eq. 3.30a). Such requirements place great demands on computer resources, and only relatively simple flows at low-to-moderate Reynolds numbers can be computed directly with present-day machines [112, 113]. However, further research has shown that some of the DNS requirements suggested in most of the literature are sometimes too stringent. For instance, the direct numerical simulations conducted by Moin and Mahesh show very good agreement with experimental results even though the Kolmogorov lengthscale was not resolved. As noted in the corresponding study, it appears that the relevant requirement to obtain reliable first and second order statistics is that the resolution be fine enough to accurately capture most of the dissipation. Consequently, in some cases, the smallest resolved lengthscale is required to be a factor of the Kolmogorov lengthscale, and not necessarily equal to it [114].

In addition to spatial discretization, boundary conditions and temporal discretization can be sources of numerical issues in DNS. For complex geometries, like most of the engineering geometries, it is not affordable to satisfy the DNS requirements. This is the reason why DNS is still confined to simple geometries and research activities. However, DNS results, alongside with the experimental results, play a cardinal role in the assessment of the simpler turbulence models. Many researchers developing turbulence models have

verified the performance of their proposing models through comparing results obtained with DNS results (e.g., [115, 116]).

$$l_k \equiv (\nu^3/\epsilon)^{1/4} \tag{3.30a}$$

$$t_k \equiv (\nu/\epsilon)^{1/2} \tag{3.30b}$$

$$v_k \equiv (\nu\,\epsilon)^{1/4} \tag{3.30c}$$

Reynolds Averaged Navier-Stokes (RANS) Equations

In Reynolds-averaged approaches to turbulence, any variable ϕ is decomposed into the sum of its mean quantity $\overline{\phi}$ and its fluctuation about the mean value ϕ':

$$\phi(x,t) = \overline{\phi}(x,t) + \phi'(x,t) \tag{3.31}$$

Therefore, in Reynolds Averaged Navier-Stokes models the focus is on the mean flow and the effects of turbulence on the mean flow properties [100, 112]. The mean values are obtained by averaging procedures. The three most pertinent averaging methods in turbulence research are the time average, the spatial average and the ensemble average. Time averaging is suitable for stationary turbulence, i.e. a turbulent flow that, on average does not vary with time. Spatial averaging is appropriate for homogeneous turbulence, which is a turbulent flow that, on the average, is uniform in all directions. Ensemble averaging is the most general type of averaging, which is appropriate for unsteady turbulent flows. The number of members of the ensemble N must be large enough to eliminate the effects of the fluctuations. For turbulence that is both steady and homogeneous, it can be assumed that these three averages are all equal. In cases where the density is not constant, it is advisable to apply both mass-weighted or Favre decomposition and Reynolds averaging. The most convenient way is to apply Reynolds averaging for density and pressure and Favre averaging for other quantities such as velocity [95, 112, 117] (refer to Appendix A.10 for the averaging formulations).

Applying the averaging procedures to the governing equations leads to the arising of some additional terms, e.g., Reynolds stresses, turbulent heat flux, turbulent diffusion flux, etc. [118]. In order to be able to compute turbulent flows with the RANS equations it is necessary to develop turbulence models to predict the Reynolds stresses and the scalar transport terms and close the system of mean flow equations. The Reynolds stresses, which appear as unknowns in the Reynolds equations, are determined by turbulence models

either via the turbulent viscosity hypothesis (Boussinesq hypothesis) or more directly from modelled Reynolds-stress transport equations. Boussinesq hypothesis assumes a linear relationship between the turbulent shear stress and the mean strain-rate (similar to laminar flow), with the proportionality factor in this relationship being defined as eddy (or turbulent) viscosity [96, 108].

$$-\rho\,\overline{v_i' v_j'} = 2\mu_T \overline{S}_{ij} - \rho\frac{2k}{3}\delta ij \tag{3.32}$$

where $\rho\,\overline{v_i' v_j'}$ is the Reynolds stress tensor and represents the transfer of momentum due to turbulent fluctuations, k is the turbulent kinetic energy per unit mass (Eq. 3.33), $\overline{S}_{ij}$ is the mean strain-rate tensor (Eq. 3.34), and μ_T is eddy viscosity. Unlike the molecular viscosity, turbulent viscosity represents no physical characteristic of the fluid, but it is the function of the local flow conditions [95–97, 113].

$$k = \frac{1}{2}\,\overline{v'_i v'_i} = \frac{1}{2}\,(\overline{v'_x v'_x} + \overline{v'_y v'_y} + \overline{v'_z v'_z}) \tag{3.33}$$

$$\overline{S}_{ij} = \frac{1}{2}\left(\frac{\partial \overline{v}_i}{\partial x_j} + \frac{\partial \overline{v}_j}{\partial x_i}\right) - \frac{1}{3}\frac{\partial \overline{v}_k}{\partial x_k}\delta_{ij} \tag{3.34}$$

The most common RANS turbulence models are classified on the basis of the number of additional transport equations that need to be solved along with the RANS flow equations.The turbulence models which use the Boussinesq hypothesis are referred to as eddy viscosity models, and the models which do not rely upon this hypothesis and derive exact equations for Reynolds stress are called Reynolds stress or stress-equation models [96, 97].

Zero-equation (algebraic) models invariably utilize the Boussinesq assumption to compute the Reynolds stress tensor as the product of eddy viscosity and the mean strain-rate tensor. Prandtl suggested one of the most successful algebraic models, which is based on the mixing-length hypothesis to calculate the eddy viscosity. For 2D and 3D thin boundary layers, Prandtl's mixing length formula can be interpreted as follows [96, 100]:

$$\text{2-Dimensional}: \mu_T = \rho\, l_{mix}^2 \left(\frac{\partial \overline{v}_x}{\partial y}\right)^2 \tag{3.35a}$$

$$\text{3-Dimensional}: \mu_T = \rho\, l_{mix}^2 \left[\left(\frac{\partial \overline{v}_x}{\partial y}\right)^2 + \left(\frac{\partial \overline{v}_z}{\partial y}\right)^2\right]^{0.5} \tag{3.35b}$$

where l_{mix} is the Prandtl's empirical mixing length.

Prandtl postulated further that for flows near solid boundaries the mixing length is proportional to distance from the surface [108]. However, the mixing length is a flow dependent variable that should be derived according to the type of the flow being considered, wall boundary layer, jet, wake, etc. In the log-law zone of Fig. 3.1, the appropriate approximation of the mixing length is $l_{mix} = \kappa\, y$, with $\kappa = 0.41$ being defined as the von Kármán constant [96, 113]. In the buffer zone, the mentioned expression should be multiplied by the Van Driest damping function (refer to [119]).

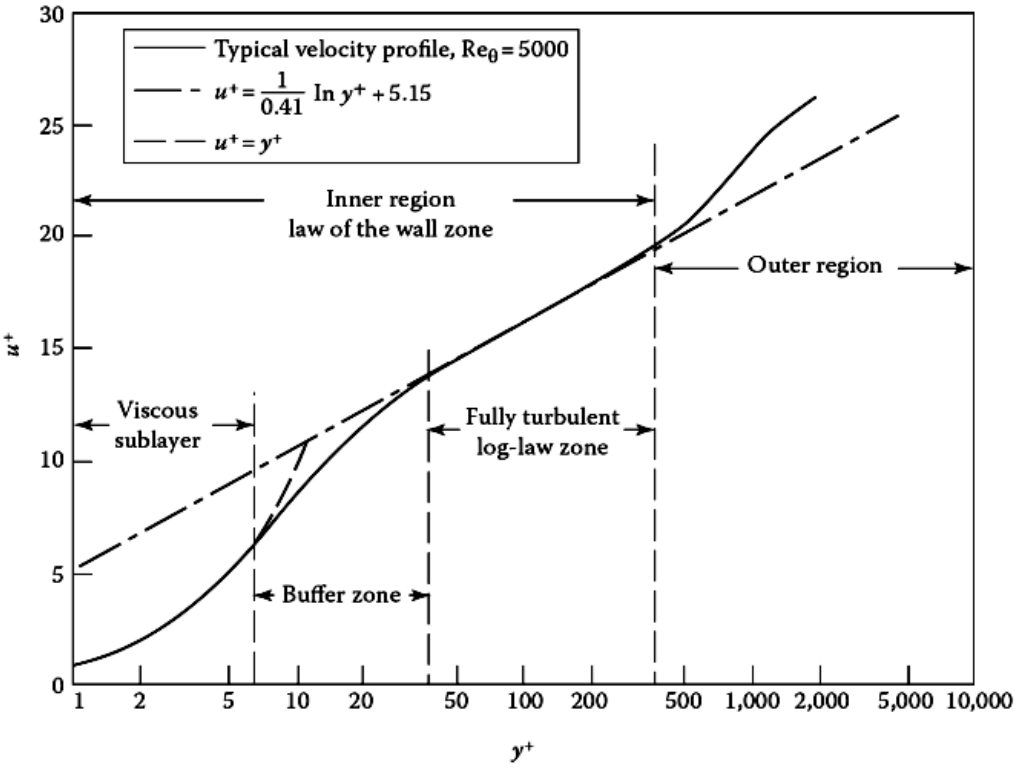

Figure 3.1: Turbulent boundary layer for a typical incompressible flow over a smooth flat plate showing various layers [96].

The parameter y^+ is the dimensionless wall distance which according to Eq. 3.36 is a function of the reference velocity u^* (also called shear velocity) and y, i.e. the normal distance from the cell centroid to the wall in wall-adjacent cells [97, 102].

$$y^+ = \frac{yu^*}{\nu} \tag{3.36}$$

The shear velocity u^* is a function of the instantaneous wall shear stress and density at the wall (Eq. 3.37). Moreover, in Fig. 3.1, u^+ is the dimensionless velocity, which is defined as the ratio of the local velocity to the shear velocity [96]. The definition of the shear velocity becomes different from Eq. 3.37 when using wall treatment models in the simulation (refer to [102] for more information).

$$u^* = \sqrt{\frac{\tau_w}{\rho_w}} \tag{3.37}$$

Despite all the benefits that the Prandtl mixing length model offers, one of which is its simplicity, it has some serious weaknesses. One obvious shortcoming of the algebraic models that evaluate eddy viscosity based on the Prandtl mixing length model is that $\mu_T = 0$ whenever the terms between the parentheses in Eq. 3.35 becomes zero. For example, considering the flow in a pipe, this means that the eddy viscosity would be zero at the centreline of the pipe (which is not true). The shortcomings of the Prandtl mixing length model was the main motivation behind the development of the other turbulence models which determine the eddy viscosity more accurately.

The Spalart-Allmaras (S-A) [120] is the most well-known one-equation eddy viscosity model, while $k-\epsilon$ [115] [1] and $k-\omega$ [108] models (and their derivatives) are the most employed two-equation eddy viscosity models. One-equation models are incomplete as they relate the turbulence length scale to some typical flow dimension. By contrast, two-equation models provide an equation for the turbulence length scale or its equivalent and are able to predict properties of a given turbulent flow with no prior knowledge of the turbulence structure [108]. The Spalart-Allmaras turbulence model uses a semi-empirical transport equation for eddy viscosity. This model was calibrated using the results for 2D mixing layers, wakes and flat plate boundary layers. Being local is one of the favourable numerical features of S-A model; this means that the equation at one point does not depend on the solution at other points. Therefore, in addition to structured multi-block grids, it can be readily implemented on unstructured grids [95, 109]. The original model was developed primarily for the aerospace industry [102], and its performance is verified in various benchmark studies (e.g., [121]). The exact formulation of the S-A model can be found in [122].

The most popular and widely used two equation model is perhaps the $k - \epsilon$ turbulence model. This model is based on the solution of the equations for

[1] This reference is not the earliest work related to $k - \epsilon$ model but it is the most acknowledged study according to [108].

the turbulent kinetic energy k and turbulent dissipation rate ϵ. This model requires the addition of the so called damping function to stay valid through the viscous sublayer [95, 108]. The standard form of the $k-\epsilon$ model, namely the standard $k-\epsilon$, has given reasonably good results for free-shear-layer flows with relatively small pressure gradients. For wall bounded flows, the model gives good agreement with experimental results for zero and small mean pressure gradients, but is less accurate for large adverse pressure gradients. This model requires the use of fine grid spacing near solid walls to be able to accurately capture the profiles of the turbulent kinetic energy and its dissipation [112, 121].

Realizable $k-\epsilon$ [116, 123] is one of the more successful developments of the standard $k-\epsilon$ model. The inability of many of the existing $k-\epsilon$ models to provide correct near-wall behaviour of the eddy-viscosity was one of the main motivations behind developing the realizable $k-\epsilon$ model.
This model contains a new equation for the turbulence dissipation rate as well as a critical coefficient of the model. Unlike the standard model, the model coefficient c_μ ($= 0.09$ in the standard model [102]) is not a constant anymore in the realizable model, but it is expressed as a function of mean flow and turbulence properties. This allows the model to satisfy certain mathematical constraints on the normal stresses consistent with the physics of turbulence. The concept of a variable model coefficient is also consistent with experimental observations in boundary layers. As a result, the realizable $k-\epsilon$ model is substantially better than the standard $k-\epsilon$ model for many applications, and can generally be relied upon to give answers that are at least as accurate [102].

$k-\omega$ turbulence model is another two-equation model, which is the most prominent alternative to the $k-\epsilon$ model. In the $k-\epsilon$ model the kinematic eddy viscosity is expressed as the product of a velocity scale $\sqrt{k}$, and a length scale, i.e. $k^{3/2}/\epsilon$ [97]. In the $k-\omega$ model, convective transport equations are solved for the turbulent kinetic energy and its specific dissipation rate, i.e., $\omega = \epsilon/k$ (also called turbulence frequency [97]).
The $k-\omega$ model of Wilcox (standard $k-\omega$) has proven to be superior in numerical stability to the $k-\epsilon$ model primarily in the viscous sublayer near the wall. Unlike any other two-equation model, $k-\omega$ does not involve wall-damping functions. In free-shear layer and adverse-pressure-gradient boundary layer flows, the results of the $k-\omega$ model are sensitive to small free stream values of ω. This translates into extreme sensitivity to inlet boundary conditions for internal flows, a problem that does not exist for the $k-\epsilon$ model [102, 121].

Shear Stress Transport (SST) $k-\omega$ [124] is developed to overcome the mentioned sensitivity of the standard $k-\omega$ model. The two major features of SST model are a zonal weighting of model coefficients and a limitation on the growth of the eddy viscosity in rapidly strained flows. The zonal modeling uses the standard $k-\omega$ near solid walls and the standard $k-\epsilon$ near boundary layer edges and in free shear layers. This switching is achieved by a blending function of the model coefficients. The SST model also modifies the turbulent eddy viscosity function to improve the prediction of separated flows [109, 121]. A comparison between the abilities of the Spalart-Allmaras, Realizable $k-\epsilon$, and SST $k-\omega$ turbulence models to predict aerodynamic characteristics of the FC fan under investigation can be found in [24, 125].

Large Eddy Simulation (LES)

LES is based on the observation that the small turbulent structures are more universal in character than the large eddies. Therefore, the idea is to compute the contributions of the large, energy-carrying structures to momentum and energy transfer and to model the effects of the small structures, which are not resolved by the numerical scheme [95]. In other words, the LES strategy is to resolve most of the turbulent kinetic energy k of the flow, while modeling most of the dissipation ϵ. This distinction can be drawn considering the fact that k is determined by the large scales of motion and ϵ by the small scales [126, 127].

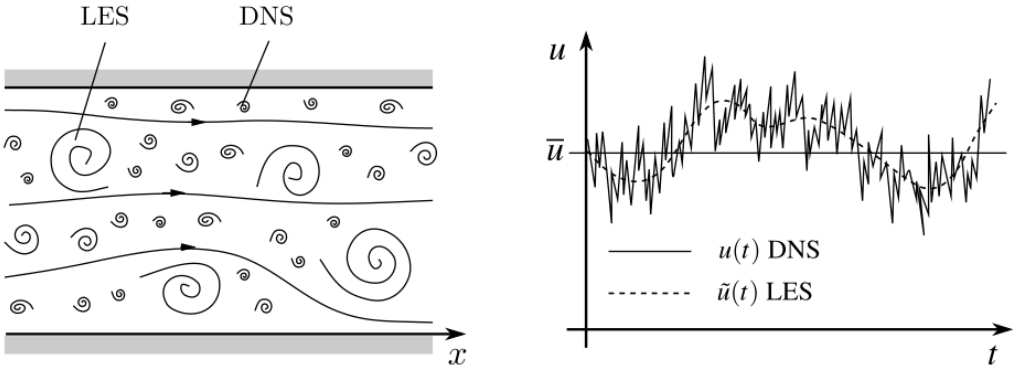

Figure 3.2: Schematic comparison of DNS and LES; representation of turbulent motion (left) and time-dependent velocity fluctuations at a point (right) [112].

As mentioned above, performing direct numerical simulations are computationally expensive and still only applicable to simple cases. In LES, the dynamics of the larger scale motions (which are affected by the flow geometry

and are not universal) are computed explicitly, whereas the influence of the smaller scales (which have more a universal character) being represented by simple models. Thus, compared with DNS, the vast computational cost of explicitly representing the small-scale motions is avoided [113]. In general, DNS is the preferred method whenever it is feasible, because it is a more accurate approach. LES is the preferred method for flows in which the Reynolds number is too high or the geometry is too complex to allow the application of DNS.

There are four conceptual steps in LES [112, 113]:

- A filtering operation is defined to decompose the velocity $v(x,t)$ into the sum of a filtered (or resolved) component $\overline{v}(x,t)$ and a residual (or subgrid-scale, SGS) component $v'(x,t)$. The filtered velocity field which is three-dimensional and time-dependent represents the motion of the large eddies. Every filter has a length scale Δ associated with it, eddies of size larger than Δ are large eddies while those smaller than Δ are small eddies, i.e., the ones that need to be modeled.

- The equations for the evolution of the filtered velocity field are derived from the Navier-Stokes equations. These equations are of the standard form, with the momentum equation containing the residual stress tensor (or SGS stress tensor) that arises from the residual motion.

- Closure is obtained by modeling the residual-stress tensor, most simply by an eddy viscosity model.

- The modeled filter equations are solved numerically for $\overline{v}(x,t)$, which provides an approximation to the large-scale motions in one realization of the turbulent flow.

There are important distinctions between the variants of LES (Tab. 3.1). Considering the flow remote from walls, a distinction should be made between large eddy simulation and very large eddy simulation (VLES). In LES, the filtered velocity field accounts for the bulk (80%) of the turbulent kinetic energy everywhere in the flow field. In VLES, the grid and filter are too large to resolve the energy-containing motions, and instead a substantial fraction of the energy resides in the residual motions. Although VLES is performed on coarser grids, and therefore is less expensive, the simulation is more strongly dependent on the modeling of the residual motions. In practice, the fraction of energy resolved is seldom estimated, so that it is not always clear whether a particular simulation is LES or VLES [113].

Table 3.1: Resolution in DNS and some variations of LES [113].

Model	Acronym	Resolution
Direct Numerical Simulation	DNS	Turbulent motions of all scales are fully resolved
Large Eddy Simulation with near-wall resolution	LES-NWR	The filter and grid are sufficiently fine to resolve 80% of the energy everywhere
Large Eddy Simulation with near-wall modeling	LES-NWM	The filter and grid are sufficiently fine to resolve 80% of the energy remote from the wall, but not in the near-wall region
Very Large Eddy Simulation	VLES	The filter and grid are too coarse to resolve 80% of the energy

As mentioned above, LES always uses a subgrid scale model to compute part of the flow. In STAR-CCM+, there are two SGS models available, viz. Smagorinsky and WALE (Wall Adopting Local Eddy) [102]. The Smagorinsky SGS model is the most basic and commonly used model, upon which many other advanced models are based. Despite being a relatively successful model, its use is highly discouraged for a number of reasons [128]:

1. The Smagorinsky SGS tends to be overly dissipative.

2. The Smagorinsky eddy viscosity model constant has been accurately validated only for the simple flow of decaying turbulence. This same value for the model constant is often applied for complex flows, while its correctness remains questionable.

3. The model does not allow the eddy viscosity to vanish in near wall regions, which requires employing an ad hoc damping function.

WALE subgrid scale model uses a novel form of the velocity gradient tensor in its formulation. Its advantage is that it does not need any form of near-wall damping, so it is more suited to large-scale parallel computation on complex geometries. This model appears to be less sensitive to the model coefficient than the Smagorinsky model. Nevertheless, similar to the Smagorinsky model, it suffers from the limitation that the model coefficient is not universal [102].

In comparison to RANS turbulence models, LES requires high grid resolution not only in the wall normal direction, but also in the streamwise, and in the cross-flow direction (spanwise) [95]. However, LES is still computationally considerably cheaper than DNS. Table 3.2 presents the mesh requirements for performing wall-resolved LES (LES-NWR) in comparison with DNS both applied to a "flat-plate-like" configuration with a homogeneous spanwise direction.

Table 3.2: Mesh resolution requirements for performing LES and DNS [128].

Method	Streamwise direction	Wall normal direction	Cross-flow direction
LES	$50 \leq \Delta x^+ \leq 150$	$\Delta y^+ \leq 1$	$15 \leq \Delta z^+ \leq 40$
DNS	$10 \leq \Delta x^+ \leq 20$	$\Delta y^+ \leq 1$	$5 \leq \Delta z^+ \leq 10$

It is possible to calculate the corresponding x^+, y^+, and z^+ values when using a structured grid to simulate a simple flow that moves in a definite direction, e.g. channel flow. However, when simulating more complex flows on unstructured grids, where the axes defining the streamwise and cross-flow direction trade place as the flow direction changes, calculating the corresponding dimensionless distances is indeed troublesome, if not completely impossible.

In LES-NWM, the modelling of the near-wall layer introduces several sources of error. The three main ones are the inaccuracy of the wall-layer modelling assumptions, the incapability of the SGS models in the near-wall region, and the increased numerical errors that appear when the resolution becomes marginal, or the grid is suddenly refined near a solid boundary. These errors interact with each other, but a global treatment is difficult [129].

Detached Eddy Simulation (DES)

Detached Eddy Simulation (DES) is a hybrid modeling approach that combines features of RANS and LES. The first DES model was proposed in 1997 [130], and is usually referred to as DES97 in the literature. It was created to address the challenge of high-Reynolds number and massively separated flows. This model was aimed to be a cost-effective and plausibly accurate solution to those cases that performing a whole-domain LES, due to its computational cost, is nearly impossible. DES models are set up so that boundary layers and irrotational flow regions are solved using a base RANS closure model (Spalart-Allmaras or SST turbulence model). However,

the model is essentially modified so that, if the grid is fine enough, it will emulate a basic LES subgrid scale model in detached flow regions and regions of massive separation [102]. In other words, detached eddy simulation, models the attached eddies and resolves the detached ones [130]. Switching between Spalart-Allmaras RANS and LES regions is achieved by using a Smagorinsky-like SGS model in DES97. In order to do so, a new definition for the length-scale is given and the distance to the nearest wall d was replaced with $\tilde{d}$, which is dependent on the filter size :

$$\tilde{d} \equiv min(d, C_{DES}\Delta) \tag{3.38}$$

where Δ is a measure of local grid spacing taken as the largest distance between the cell center under consideration and the cell centers of the neighbouring cells, i.e. $\Delta \equiv max(\Delta x, \Delta y, \Delta z)$. C_{DES} is the adjustable model constant which is of order 1. Near a solid surface the wall-parallel grid spacings determine Δ and are larger than the distance to the wall d. Thus, within the boundary where $d \leq \Delta$ boundary layer properties are predicted using the S-A RANS model. Away from the wall where $\Delta \leq d$, the model changes its behaviour to LES [130, 131].

A key weakness in the DES97 formulation was identified, which can be attributed to strong influence of the local grid resolution in the simple DES97 length scale formulation. When the wall-tangential grid resolution in the boundary layer becomes fine (i.e., of the order of the boundary layer thickness), the RANS-LES interface moves inside the boundary layer. This causes a phenomenon known as "Modelled Stress Depletion" (MSD), whereby the modelled turbulent stresses drop strongly below RANS levels without sufficient grid resolution to support a viable LES above the interface. The result is a significant underprediction of skin friction, which in strong cases can lead to spurious prediction of flow separation, known as "Grid-Induced Separation" (GIS) [132, 133].

Figure 3.3 shows the roots of these problems, with three levels of grid density in a boundary layer. The first level matches the initial vision of DES; it is a boundary layer grid, with the wall-parallel spacing in excess of the boundary layer thickness, which allows full RANS function. The third level matches the needs of LES in the outer layer and thus of the extended use of DES as a wall model: the grid spacing in all directions is much smaller than boundary layer thickness. The second level is the troublesome one: small enough for the eddy viscosity to be affected by the DES limiter but not small enough to support accurate LES content.

Modelled Stress Depletion occurs if the grid is gradually refined starting from grid 1 (in Fig 3.3), typically when a user is justifiably seeking grid convergence, or when geometry features demand a fine wall-parallel grid. It also occurs when a boundary layer thickens and nears separation. Thus, over an airfoil, a gird which is suitable for DES at one angle of attack may be troublesome at another angle of attack. Figure 3.4 is a visualization of Grid-Induced Separation on an airfoil. The RANS solution is steady and quite accurate, whereas the DES solution suffers from an early separation [132]. It can be argued that the Grid-Induced Separation could be avoided by coarsening the mesh in the lateral direction, but this demands knowing the flow direction prior to the grid generation, which is of course not possible in the case of complex three-dimensional simulations [134]. DES shortcomings are not limited to only what mentioned here; the reader is referred to [132, 134, 135] for more information.

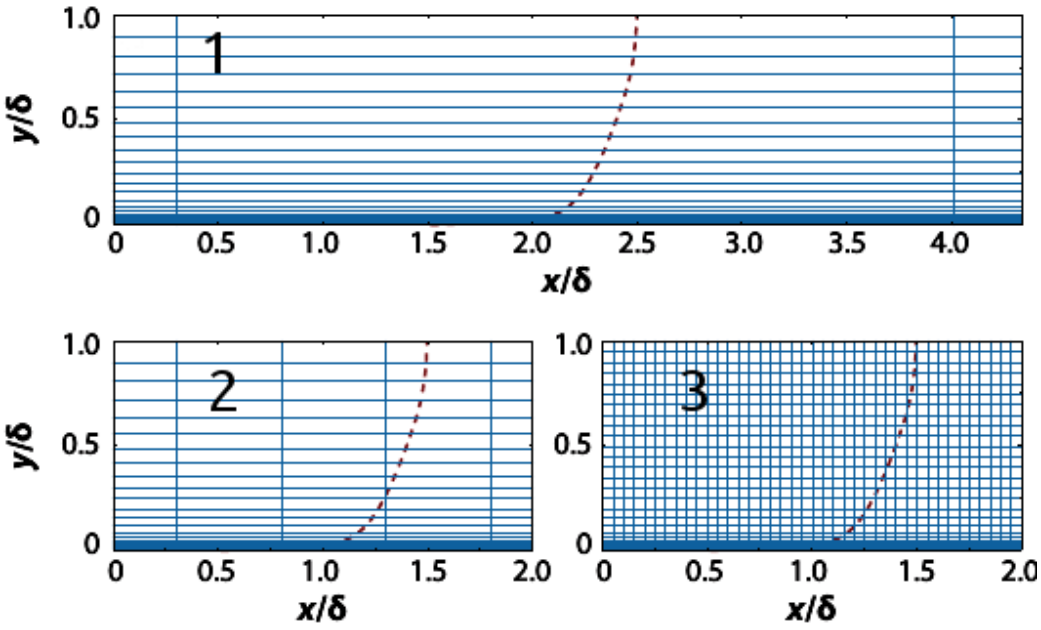

Figure 3.3: Representation of the velocity profile (dashed line) for three grid refinement densities in a boundary layer. The second level of refinement is troublesome in DES [132, 136].

Different remedies have been proposed to overcome the shortcomings of the original DES model mentioned above. One of the effective proposals suggests employing a shield function to disable the DES limiter and maintain RANS operation throughout the boundary layer. This detection device depends on the eddy viscosity, so that the limiter now depends on the solution.

In 2006, the first revision of DES was published [136], which included a generic formulation for a shield function as well as a new definition for $\tilde{d}$ to protect against Modelled Stress Depletion. This model is called "Delayed Detached-Eddy Simulation" DDES and is likely to be the new standard version of DES [132, 133].

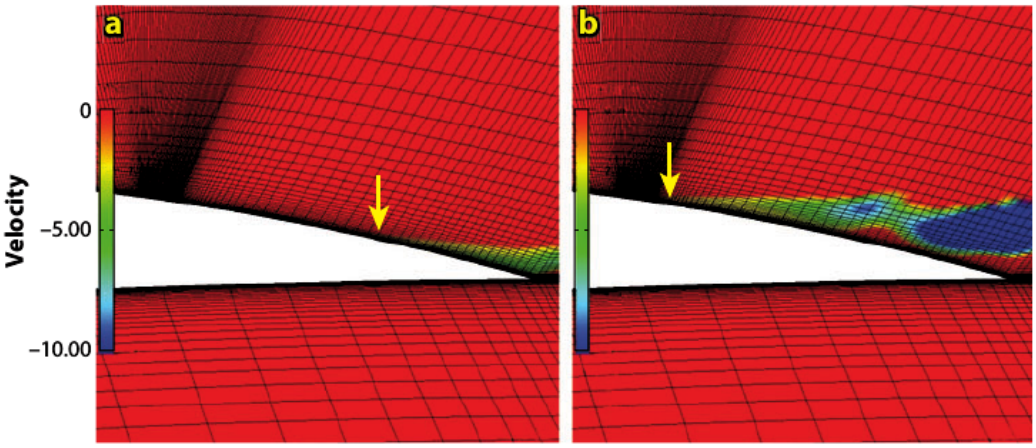

Figure 3.4: Velocity contours over an airfoil: (a) RANS and (b) DES. Arrow indicates the separation point, and DES suffers from a premature separation [132, 134].

The more ambitious version of Delayed Detached-Eddy Simulation (DDES) is the "Improved Detached-Eddy Simulation" IDDES, which is in fact a combination of DDES and Wall-Modelled LES (WMLES) [137]. This approach aims at resolving log-layer mismatch (i.e, another weakness of DES97 as well as DDES) in addition to the Modelled Stress Depletion. It defines a new subgrid length-scale Δ, which includes the wall distance and not only the local spacing of the grid. This modification tends to depress Δ near the wall and give it a steep variation, which stimulates instabilities, boosting the resolved Reynolds stress [132]. Moreover, the Improved Detached-Eddy Simulation behaviour depends on the local flow conditions so that when the inflow conditions do not have any turbulent content the IDDES shows a DDES like functionality, but when the simulation has turbulent inflow and the grid is fine enough to resolve boundary layer dominant eddies, IDDES reduces to Wall-Modelled LES in which most of the flow is resolved except near the wall.

The blending of Delayed Detached-Eddy Simulation and Wall-Modelled LES branches is achieved by means of a hybrid length scale which is a function of

the blending function as well as the RANS and the LES length scales; more details about the Improved Detached-Eddy Simulation formulations as well as its performance comparison with DNS and LES can be found in [137].

3.4 Simulations Setup

Since noise in fluids is fundamentally related to time-dependent pressure fluctuations, numerical simulations need to be of transient or unsteady mode. This allows molding impeller rotation by moving the mesh components, i.e, cells, vertices etc. Steady-state simulations which can be performed by means of Moving Reference Frame (MRF) method (also called frozen-rotor), can only be used for preliminary assessments. In this study, for each case, first a steady-state RANS simulation is performed by using MRF method, and after obtaining converged results, the simulation is switched to the transient mode and the simulation is continued by using Rigid Body Motion (RBM) method. Two different methods are used in this study to predict the noise of the fan.

I. A set of probes is used to monitor pressure in the discharge of the fan (Fig. 3.5) and to capture the fluctuations necessary for obtaining the noise and conducting spectral analysis. Time Fourier transform is then applied to convert time-accurate pressure data into frequency domain signal representing the noise of the fan. This is a practical and straightforward method, since most of the time it is feasible to monitor pressure in the simulation environment. However, the corresponding pressure monitors are completely exposed to the effects of boundary conditions, and as will be shown in the next section, the accuracy of the results highly depends on defining suitable boundary conditions.

II. A Ffowcs Williams-Hawkings (FW-H) receiver is placed near the outlet of the fan. The receiver records time-resolved data from the assigned impermeable (solid) surfaces. In this study, the quadrupole (volume) source is neglected in FW-H model due to the difficulties associated with defining the permeable surfaces (refer to [107] for more information). Moreover, since the flow inside the fan is completely subsonic, it is believed that the dipole source should be of greater importance. However, neglecting the volume (quadrupole) source in the FW-H method can lead to underestimation of the noise predicted, especially in the higher frequency range.

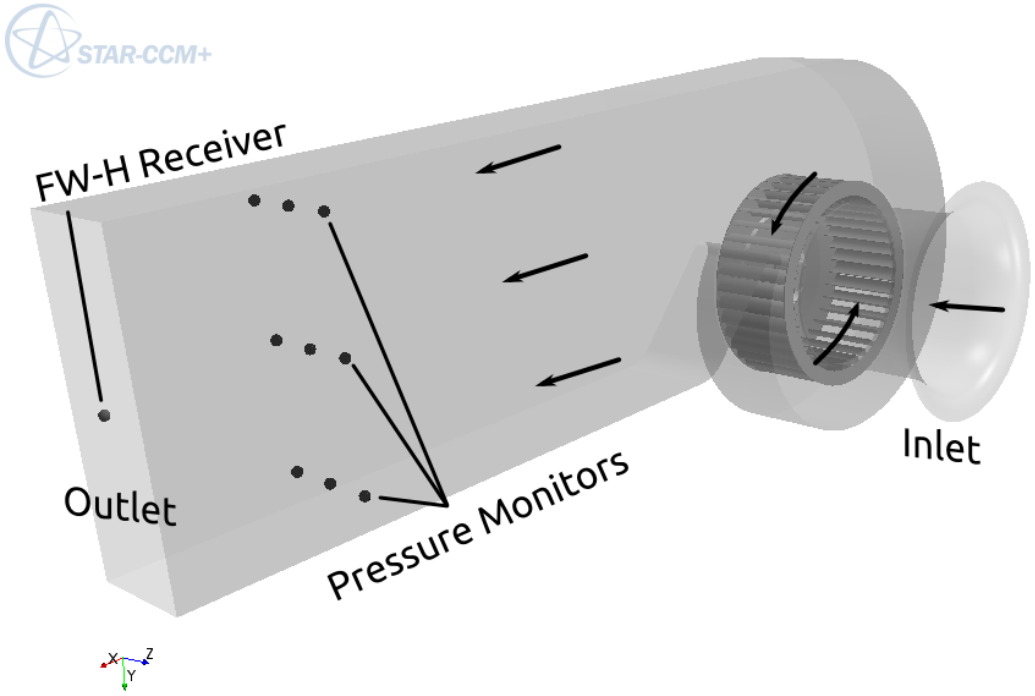

Figure 3.5: The noise radiated from the fan is predicted using the pressure monitors defined in the discharge of the fan as well as the FW-H monitor defined near the outlet.

3.4.1 Boundary Conditions

The inlet and outlet boundary conditions are exposed to pressure reflections. These reflections are not of great importance from the aerodynamic point of view most of the time; therefore, it is not necessary to consider them in most of the CFD simulations. However, in aeroacoustic simulations, pressure reflections at the boundary conditions are known to contaminate the signals that are being recorded by the monitors. The non-reflective boundary condition (also called free-stream boundary condition [102]) helps to avoid pressure reflections at the inlet and outlet of a CFD domain. Using the free-stream boundary condition demands having a priori knowledge about some of the flow parameters, e.g., Mach number, pressure, and temperature at the corresponding boundaries.

In order to estimate the flow parameters mentioned, the simulations should be first started using more common boundary conditions which can be set based on the available experimental data, e.g. mass flow rate for inlet condition and relative pressure for outlet condition. The necessary parameters should

be monitored in the first run, and once the solution is converged, they can be used for setting the free-stream boundary conditions. However, using the corresponding boundary conditions might negligibly change the operating point of the fan, since pressure, velocity, and temperature will be calculated according to the free-stream governing equations (refer to [102]).
The non-reflective boundary uses extrapolation conditions which requires the derivative of all quantities in the direction normal to the boundary be zero. For unsteady simulations this condition should be replaced by an unsteady convective condition (Eq. 3.39).

$$\frac{\partial \phi}{\partial t} + v \frac{\partial \phi}{\partial n} = 0 \tag{3.39}$$

In Eq. 3.39 ϕ is any of the dependent variables and v is a velocity that is independent of location on the outflow surface and is chosen so that overall conservation is maintained, i.e. it is the velocity required to make the outflow mass flux equal to the incoming mass flux. This condition avoids the problem caused by pressure perturbations being reflected off the outflow boundary back to the interior of the domain [112].

Figure 3.6 illustrates a comparison between the velocities in the x direction (normal to the boundary) of a reflective (relative pressure) and a non-reflective (free-stream) conditions applied to the fan outlet. Figure 3.7 helps to acknowledge the importance of boundary conditions in CAA simulations. This figure illustrates a comparison between the spectral results obtained from simulations performed with different boundary conditions, i.e. reflective and non-reflective. It can be clearly seen that some spurious peaks exist in the result obtained from the simulation with the reflective boundary conditions. Moreover, the harmonic sound of the fan at BPF (633 Hz) is only well captured in the non-reflective simulation, while a clear peak at the corresponding frequency is not noticeable in the other simulation result.

3.4.2 Time-Step

In a transient simulation, it is time-step Δt which governs the advancement of the solution and the rate at which the transient data is stored from $t = 0$ up to the defined stopping time. Physics of the problem and complexity of the flow play a defining role in choosing a time-step size. In general, when the flow is complex, a small time-step with a sufficient number of inner iterations should be used to make sure that all the necessary flow details are well captured. Through a previously conducted study, it is concluded that a time-step that corresponds to a 3.6° rotation of impeller, is sufficient to reliably obtain the

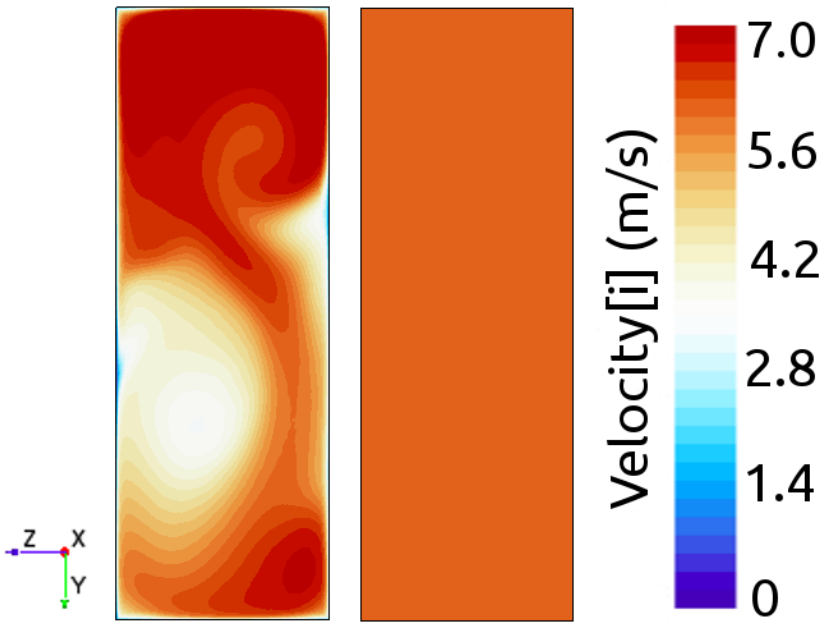

Figure 3.6: Comparison between the x-component of the outlet velocities in a reflective (left) and non-reflective (right) boundary conditions.

characteristic curves of the radial fan under investigation [22]. Moreover, the accuracy of the CFD flow field is verified through a point to point comparison with the experimental PIV results. It is found out that a time-step that corresponds to a 1.5° rotation of impeller is small enough for accurately capturing the flow field inside the fan [24]. However, when noise prediction is the purpose of simulation, choosing a proper time-step becomes even more crucial. In fact, time-step directly affects the accuracy of the results as well as the range of the predictions.

In a CAA simulation the requisite time-step should at least satisfy the Nyquist sampling criterion, which suggests the maximum frequency resolvable in a time-based simulation is half the inverse of the time-step, $f_{max} = 1/2\Delta t$ [64]. In addition to the Nyquist sampling criterion, some more conservative guidelines can be found in the literature. According to [102], following criteria can be used to evaluate a correct time-step in an aeroacoustics simulation:

- Convective Courant number should be equal to 1 on average in the zone of interest. Since convective Courant number is the ratio of the physical time-step to the mesh convective time scale, this value implies that the fluid moves by about one cell per time-step.

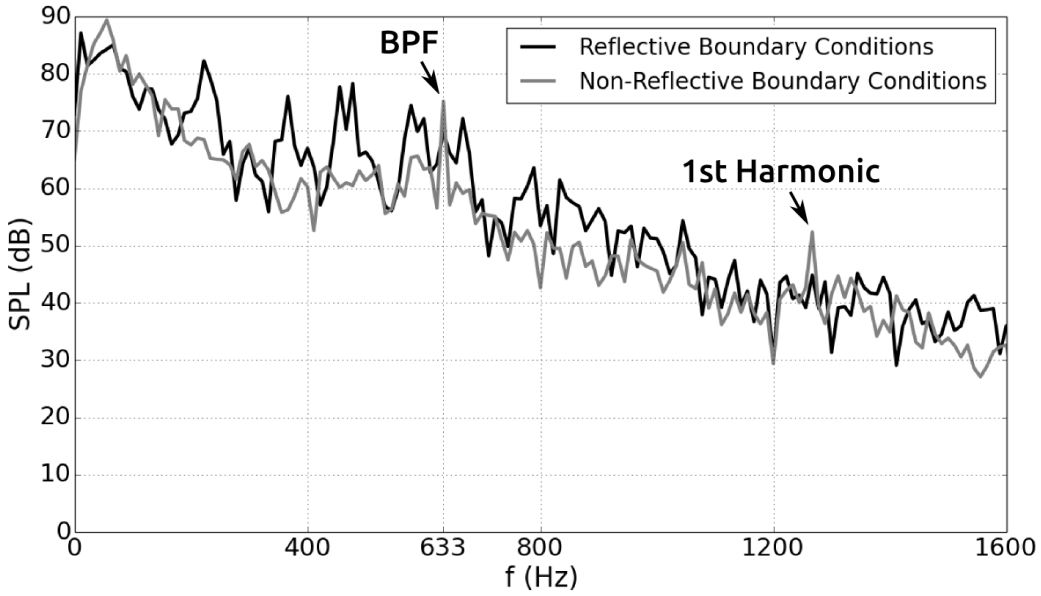

Figure 3.7: The effects of the boundary conditions on the quality of the sound predictions. The contamination caused by the the reflective boundary conditions is evident and the tonal noise of the fan at 633 Hz is not properly resolved.

- Maximum resolvable frequency can be used to estimate time-step. The recommendation is to resolve 10 points in the wave at the maximum frequency of interest. For instance, in order to obtain 10 points at 1000 Hz, time-step size should be 10 000 Hz, or 1×10^{-4} s.
- Local Strouhal shedding can also be used to estimate the requisite time-step size, in cases where empirical data is available to estimate the Strouhal number based on the physics of the problem, e.g. flow around a cylinder.

The smallest value obtained from the above criteria should be suitable to be used in a CAA simulation. However, the second criterion appears to be more practical, and is the method which is employed in some of the previous studies for estimating the size of time-step [92, 138, 139].

It is self-explanatory that using a small time-step increases the total simulation time. A practical way to save time and avoid prolonged simulations is to start the unsteady simulations using coarser time-steps and to make it gradually smaller after adequate advancement in the solution. For example, in turbo-machinery simulations, this procedure can be repeated after every some

rotations of the rotor. Simulation results approve that a considerable amount of time can be saved by using this method, without affecting the accuracy of the final results [140]. In this study, transient simulations are performed for 8 complete rotations of impeller, and time-step is changed after every two rotations according to Tab. 3.3. The smallest time-step, i.e. 4.1667×10^{-5} s corresponds to 0.25° rotation of impeller and resolves 10 points at 2400 Hz. Each physical time-step is solved with 10 inner (internal) iterations, resulting in at least two orders of magnitude reduction in the residuals (see Fig. 3.8).

Table 3.3: Summary of the time-steps employed in this study and their corresponding number of points in a wave at 2400 Hz.

Time-step (s)	Impeller rotation (degree)	Number of points at 2400 Hz	Time-steps/blade passage (Reference impeller)
16.667 e-5	1.00	2.4	9
12.450 e-5	0.75	3	12
8.3334 e-5	0.50	5	18
4.1667 e-5	0.25	10	38

3.4.3 Discretization

Discretization is approximating the differential equations by a system of algebraic equations for the variables at some set of discrete locations in space and time. The spatial discretization divides the solution domain into a finite number of subdomains (elements or cells) [112]. There are three methodologies that can be used to perform the spatial discretization of a domain, i.e. finite difference, finite element, and finite volume [95].
The algebraic equations can be obtained on an organized (structured) or an unorganized (unstructured) distribution of points or cells [141]. A cell is an ordered collection of faces that defines a closed volume in space; the faces of a cell should not intersect each other, except where they touch along the common edges. A face comprises an ordered collection of vertices which are defined by position vectors and connected to each other through feature curves [102]. There are different advantages and disadvantages associated with structured and unstructured grids. The order inherent in the structured grid is its most important advantage. Such an order in the grid structure allows to accurately access the neighboring nodes by adding or subtracting an integer value to or from a node integer (i,j,k). The same structure can be used to store the flow variables in the computer memory.

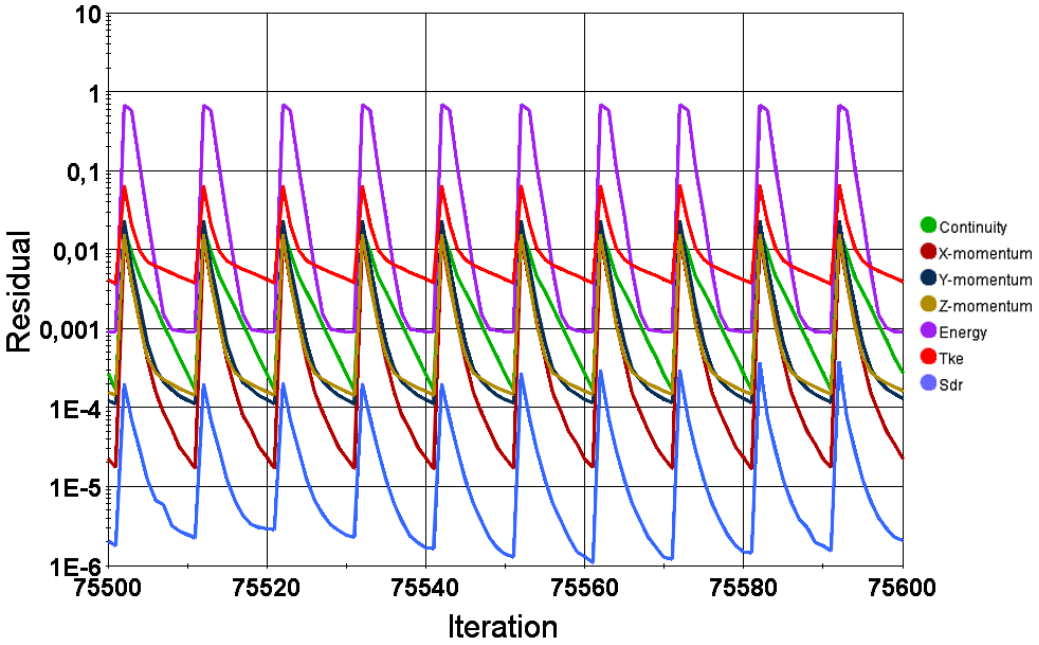

Figure 3.8: Normalized simulation residuals vs. the iteration count in a Detached Eddy Simulation performed on a grid with 12.5 million cell. Using 10 inner iterations per time-step helps to achieve at least two order of magnitude reduction in the residuals.

The neighbor connectivity between the vertices (nodes) simplifies programming, and the matrix of the algebraic equation system also benefits from this well-ordered structure [95, 112].
Nevertheless, generating a structured grid for a complex geometry can be a formidable and time-consuming task. The main reason is the inflexibility of this method that demands intensive settings and preparations. Moreover, structured grid generators generally suffer from lack of zonal refining capabilities. In many cases the complexity of the flow varies along the domain from one part to another; therefore, in some parts of the domain, e.g. high gradient regions [141], the mesh resolution needs to be higher in order to be able to capture all necessary flow details. This demands some special treatments to change the concentration of cells in those regions, which in a structured grid may lead to undesired changes as well as increase in the number of cells in some other parts of the grid. However, this problem can be solved to some extent by splitting the domain into different blocks (subdivisions) and using the multi-block techniques.
Unstructured grids, on the other hand, do not suffer from disadvantages mentioned for the structured grids. Thanks to a collection of cell shapes

that comes with most of the unstructured mesh generators, every geometry can easily be discretized through a semi-automatic procedure. This means that a user should only define the required parameters such as surface size, refinement level, number of points, surface growth rate etc. without being obliged to define the entire structure of the grid. As a result, unstructured grid generation is not only a faster procedure, but also easier. However, due to the lack of an organized distribution, the matrix of the algebraic equation system does not have a regular structure; therefore, the solver is usually slower than those for structured grids.

The main issue related to the unstructured grids arises near the wall boundaries, especially in cases where an accurate prediction of the near wall flow is desired. Moreover, different turbulence models demand different near wall mesh resolutions, and some are only practical in a definite range of y^+ values. From this point of view, not every cell shape is suitable near wall in the viscous sublayer of a turbulent boundary layer. This difficulty can be overcome in the unstructured grids by using several layers of orthogonal cells (called prism-layers [102]) near the wall boundaries. The core mesh can be then generated upon the subsurface of the last layer of the prism cells. Figure 3.9 illustrates a planar cut through a channel which is meshed differently in the wall normal direction. From left to right, the first mesh is only composed of hexahedral cells without featuring any prism-layer near the wall and represents $y^+ = 200$. Both the second and the third grids have several layers of prism cells near the wall, yet with different refinement levels and thickness ratios. The second mesh has $y^+ = 40$, and the third mesh $y^+ = 10$. The wall y^+ could easily be further reduced by adding more prism-layers and/or changing the thickness ratio between the layers.

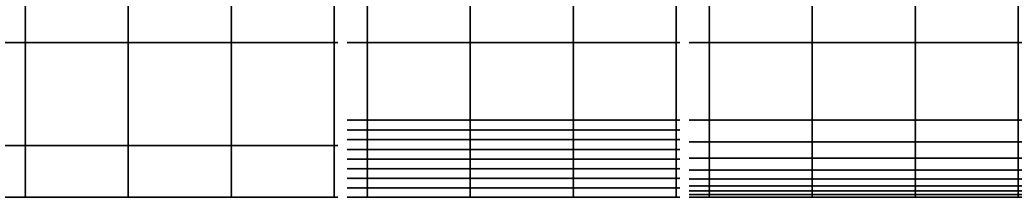

Figure 3.9: Three different near wall mesh resolutions in a 1 m long channel. Air enters the channel with a velocity of 15 m/s. The mesh on the left represents $y^+ = 200$, the mesh in the middle $y^+ = 40$, and the mesh on the right $y^+ = 10$.

Aeroacoustic simulations demand very accurate numerical grids. Due to the complex nature of sound and the variety of sound sources as well as

computational methods, it is not easily possible to evaluate suitability of a numerical grid for a CAA simulation. There are, however, some general guidelines, which can be taken into account when generating a mesh, but since most of them are aimed to cover a broad range of simulation cases, they might be seen as being too general. For instance, it is recommended that the grids should be as far as possible orthogonal and isotropic (featuring unit aspect ratio) [92]. The cubic cells (hexahedral cells) which are being used in structured grids are the best example of orthogonal cells. The inherent difficulties of generating fully structured grids are mentioned above. Trimmed cells have similar geometries to the cubic cells, and can be employed as an alternative to the hexahedral cells. However, due to the shape of the trimmed cells, it is very likely to have skewed cells in highly curved and very thin boundaries, e.g. fan blades.

Keeping the aspect ratio equal to one in the whole domain notoriously increases the number of cells which is not desirable most of the time, specifically in the industrial environments, the goal is to keep the number of cells as low as possible to avoid protracted simulations.
Another difficulty stems from the nature of sound and its propagation. Sound is a transient and time-dependent phenomenon which demands performing time-accurate (transient) simulations. Therefore, the standard mesh verification measures, which are based on the steady-state results and are useful in general CFD cases, are not useful for verifying the suitability of a grid for CAA simulation. However, there are some methods which help to gain a priori knowledge about the gird resolution and its potential for sound prediction. Mesh frequency cutoff [102], for example, is an analysis based on local turbulent fluctuations in a steady RANS simulation, which helps to assess the mesh in advance of a transient calculation to find out whether the grid generated has sufficient resolution to capture the necessary turbulent flow structures in the frequency range of interest. In the case of an isotropic grid, the mesh frequency cutoff can be defined as a function of the cell size (Δ) and the local turbulent kinetic energy (k).

$$f_{MC} = \frac{\sqrt{\frac{2}{3}k}}{2\Delta} \tag{3.40}$$

Because this measure is derived from a steady-state solution, some limitations are inherent. The frequencies associated with time-varying, large-scale motions such as vortex shedding, which convect through the mesh, will not be accounted for. Instead, its usefulness is to approximate the frequencies of the

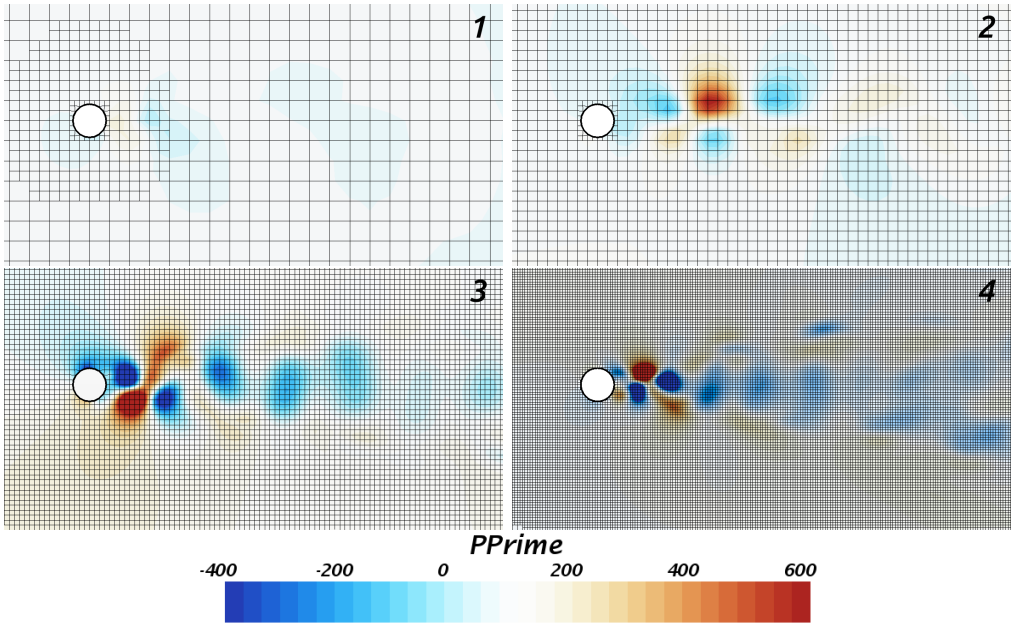

Figure 3.10: The potential of different grids to capture the near field turbulent fluctuations of the flow created by a cylinder geometry. Only grids 3 & 4 are capable of providing an acceptable representation of the pressure fluctuations.

turbulence scales modeled in RANS that become resolved in LES. In other words, this test is more relevant for the broadband and less so for narrowband excitations [139].

A standard criterion that is suggested in [102] and qualified in several previous studies (e.g. [138, 142]), is to generate and refine the mesh so that it resolves 20 cells per the smallest acoustic wavelength of interest. Such a grid resolution is sufficient for second-order space and time discretization [102,142].

Figure 3.10 illustrates four refinement levels of a mesh covering a cylinder geometry and its wake region. The time-step employed and the total simulation time are identical in all of the cases. As the contours qualitatively show, only two grids can accurately capture the near field turbulent fluctuations. The first mesh is completely unable to represent the corresponding pressure fluctuations, while the second mesh provides only an obscure representation. Time-dependent nature of sound is not the only difficulty that makes a priori grid assessment troublesome. In many cases, the generation of sound is related to the flow structures which are not merely dependent on the mean flow characteristics. This means that RANS simulations are in many cases not

enough for sound predictions, and more sophisticated turbulence approaches, e.g. LES should be employed. Generally, grid generation for LES and DES is a perplexing problem, and unless for the simplest flow, grid-independent solutions can not be obtained. Particularly, the non-monotonic response of DES to grid refinement and its shortcomings associated with the ambitious grids [132] (as addressed in section 3.3) makes the problem even more severe.

Keeping the mentioned points in mind, generating the first grid and performing the first transient simulation is just the start of a time-consuming and iterative procedure to find an optimum grid configuration. Such a grid should be able to reliably capture all the necessary physical details and the essence of the flow. As always, the challenge is to increase the solution accuracy while keeping the simulation time as short as possible. Transient simulation results are of the essence to assess the suitability of a mesh for CAA simulations and help the user to improve the mesh quality and tailor it so that a promising sound prediction becomes feasible.

Spatial Discretization of the Fan Geometry

The fan geometry is spatially discretized by means of polyhedral and trimmed cells in STAR-CCM+. Trimmed cells are hexahedral cells which are trimmed at their edges to properly conform with the original geometry of the boundaries. The suitability of the cell shapes used in this study are extensively validated for three-dimensional fan simulations [24, 125] as well as other rotating machines [92, 142, 143]. It is already shown that an unstructured grid consisted of approximately 4 million cells, with a proportion of 60% of the cells in the rotating region and 40% in the stationary region, is capable of predicting the characteristics of the fan in terms of both aerodynamic performance and the flow field inside the fan. The corresponding results are comparable to those of a complete structured grid with a comparable cell concentration in the mentioned regions [22, 24, 125]. However, such a grid is still too coarse for aeroacoustic simulations, and using it yields significantly underpredicted results due to the lack of required spatial resolution [140].
In this study, in order to find a mesh that is suitable for aeroacoustic simulations, several grids are generated and the simulation results are compared against the experimental measurements. The coarsest grid, which is used in URANS and DES, consists of 12.5 million polyhedral cells with 65% of the cells in the rotating region and the remaining 35% in the stationary region. The intermediate grid, which is employed for URANS, DES, and LES has 26.5 million polyhedral cells with approximately an identical cell concentration level in both regions, i.e. 50% in the rotating region and 50% in the stationary

region. The 12.5 million and the 26.5 million cell models have an identical topology concerning the boundary distribution and the placement of the interfaces. Three interfaces connecting the rotating region to the stationary region. The interfaces are of internal type with in-place topology. As can be seen in Fig. 3.11, two of the interfaces cover the area above and below the impeller blades, while the third interface, which is in the form of a small ring, covers the area between the impeller hub and the stator wall.

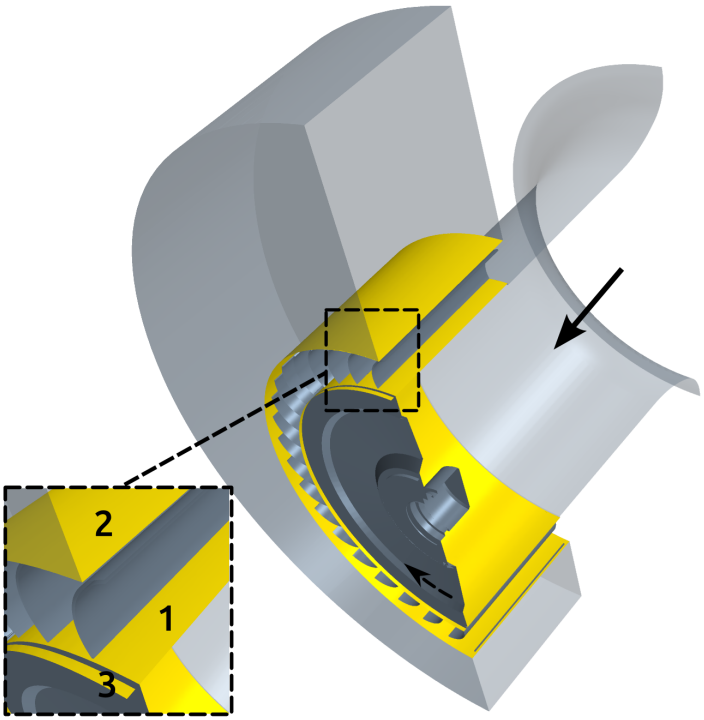

Figure 3.11: The placement of the CFD interfaces (yellow surfaces) relative to the impeller blades; the geometry is sliced and some of the boundaries are hidden for the sake of simplicity.

The most refined mesh, which consists of approximately 102 million polyhedral and trimmed cells, is used for performing DES and LES. The polyhedral cells are used in the rotating region and constitute 30% of the total count. The remaining 70% are trimmed cells which are used in the stationary region. The interface above the impeller blades is also present in this model, while the other two interfaces are moved in order to have a better control on the distribution of the cells. One interface is defined at the end of the inlet nozzle and the other one between the volute and the discharge of the fan.

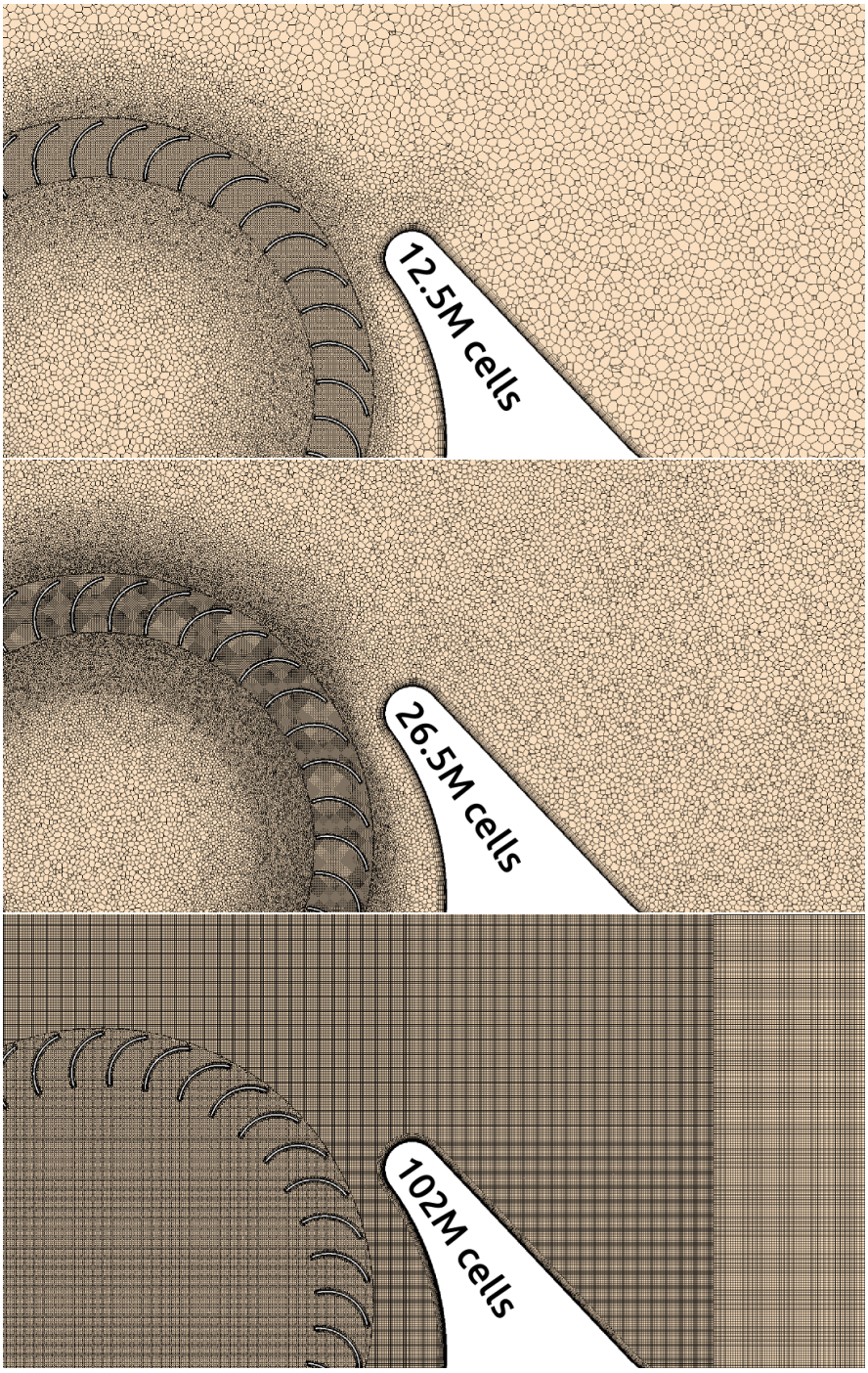

Figure 3.12: Three numerical grids which are used in the CFD simulations. The first mesh (top) has 12.5 million polyhedral cells, the second mesh (middle) has 26.5 million polyhedral cells, and the third mesh (bottom) has 102 million polyhedral & trimmed cells.

As can be seen in Fig. 3.12, trimmed cells covering the volute geometry are more refined than the cells covering the discharge. The distribution of trimmed cells is strictly controlled so that, except near the interfaces, the grid ubiquitously has unit volume change, meaning that the volume of each cell is equal to the volume of its neighbors. In the same figure, it is also evident that a special attention is paid to the distribution of the cells covering the area above the impeller blades (near the interface). Sound predictions obtained from different mesh models manifested the importance of the grid quality near the impeller blades. Therefore, having a smooth transition between the regions is vital, since it helps to accurately transfer the unsteady flow leaving the impeller to the other region. Moreover, the mesh quality in the corresponding area directly affects the noise predictions of hybrid CAA methods (refer to [140] for more information). Considering even the smallest time-step in Tab. 3.3, the convective courant number is equal to one around the impeller in all of the models. This value implies that the fluid moves by about one cell per time-step.

Generating several layers of prism cells near the solid walls helped to reduce the wall y^+ values so that all of the grids feature low-Reynolds wall resolutions (Fig. 3.13). Accordingly, for 12.5M and 26.5M models, in the rotating region $y^+ \leq 2$ and reduces to approximately 1 on the blades; whilst, in the stationary region $y^+ \leq 5$. For the most refined mesh, i.e. 102M model, $y^+ \leq 1$ in the whole domain.

Table 3.4: Detailed summary of the unstructured grids generated for simulations; numbers are in million.

Grid Component	Rotor	Stator	Total
Cells	8.1	4.4	12.5
	13.5	13.0	26.5
	32.3	69.7	102.0
Nodes	32.7	22.2	54.9
	63.0	68.3	131.3
	126	72.0	198.0
Interior faces	43.3	27.0	70.3
	78.8	82.5	161.3
	172.0	209.0	381.0

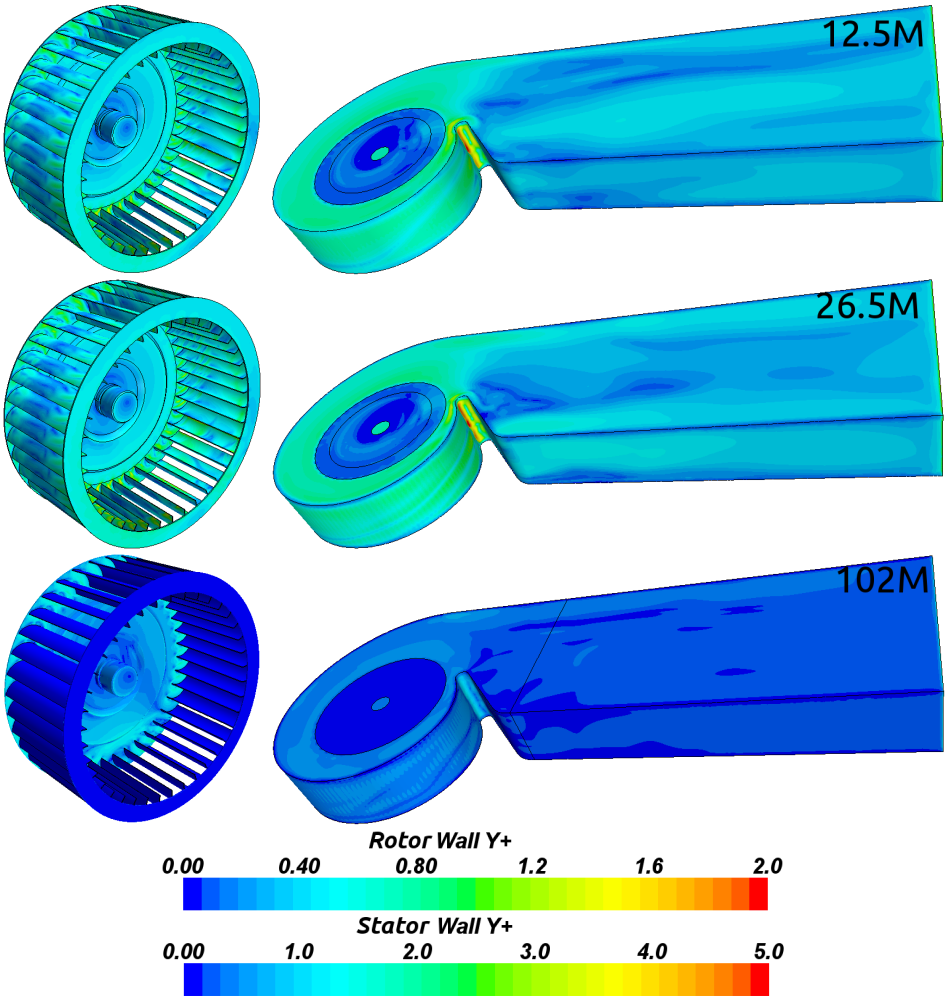

Figure 3.13: Near wall resolutions of the numerical grids.

3.4.4 Numerical Signal Processing

The results obtained from the pressure-monitors as well as the FW-H monitor are analyzed using STAR-CCM+ signal processor through applying a time Fourier Transform (FT). STAR-CCM+ converts finite time-signals into the frequency-domain by using the following equation [102]:

$$FT_t[h(x;t)] = \int_{-T/2}^{T/2} h(x;t)e^{-i\omega t}dt = g(x;\omega;t) \quad \forall\omega \in \left[-\frac{m\pi}{T}, \frac{m\pi}{T}\right] \quad (3.41)$$

where m is the number of sampling points, t is time, and ω is angular frequency. The function $h(x;t)$ is periodic in time (or altered to be periodic). Every CFD simulation has a stopping condition and therefore the sampled signals

being obtained from the simulation have finite lengths. Keeping this in mind, spectral leakage, which is a result of discontinuity in time-domain signal, is inherent in the processed simulation results. In order to suppress the effects of discontinuities, time signals should be multiplied by a window function, whose amplitude tapers smoothly and gradually toward zero at both ends [144]. There are different window functions which fulfill the mentioned requirement, e.g. Hamming, Hanning (Hann), Blackman etc. The magnitude of the time Fourier Transformed of a window provides two important characteristics about it. One is the width of the window's main lobe and the other is the strength of its side lobes. These characteristics help to select a window function with respect to the form of the signal being processed and the aim of signal processing. A narrow main lobe allows for a better resolution, and low side lobes improve the smoothing of the estimated spectrum [145]. According to Eq. 3.42 the Hanning window (also called Hann or raised cosine [146]) has a zero value and slope at each end, thus renders a gradual transition over the discontinuity of data [59]. The Hanning window is the most commonly applied window function to broadband random signals [64, 147].

$$w(n) = cos^2\left(\frac{n\pi}{N}\right) = 0.5 + 0.5\,cos\left(\frac{2\pi n}{N}\right) \quad \text{for:} \quad \frac{-(N-1)}{2} \leq n \leq \frac{(N-1)}{2} \tag{3.42}$$

Figure 3.14 clearly shows the effect of windowing on the spectral results obtained from signals with two different lengths. The long signal is 35 s and the short signal is the first 0.4 s of the long signal. Accordingly, the effect of windowing on the long signal is only apparent in the higher frequency range (starting from 7 kHz), while for the short signal, it is noticeable that the window function affects also the lower frequencies. Moreover, the trend of the short signal becomes closer to the long signal after applying the Hanning window. The difference in the sound pressure levels of the short signals is due to the spectral leakage.

The unequal lengths of the numerical and experimental signals is another point should be taken into account when analyzing the signals. The experimental signals are usually longer than the numerical signals, since it is computationally not affordable to prolong the simulations to equalize the lengths of corresponding signals. As a result, due to different lengths, the numerical and experimental signals have different energy levels. In order to ensure that Power Spectral Density (PSD, Eq. 3.45) is conserved the signals should be normalized to a selected signal length. The normalization procedure

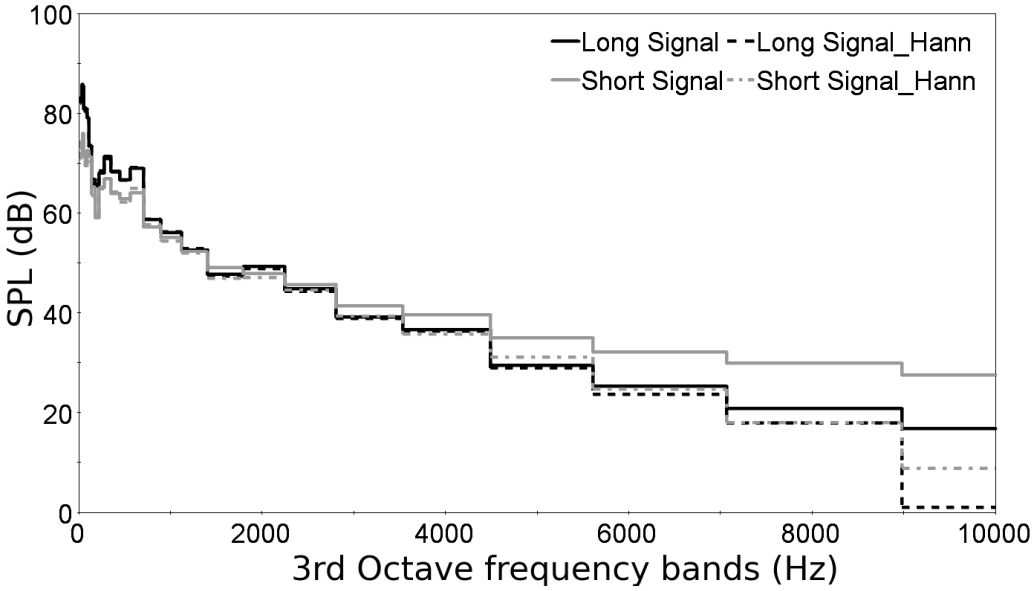

Figure 3.14: The effect of applying the Hanning window function on signals with different lengths. The long signal is 35 s and the short one is the first 0.4 s of the long signal.

should be performed according to Eq. 3.43.

$$\mid FT_t[h(x;t)] \mid_1 \sqrt{T_1} = \mid FT_t[h(x;t)] \mid_2 \sqrt{T_2} \tag{3.43}$$

where T_1 is the block length of the first signal and T_2 is the block length of the normalized signal. In terms of sound pressure level (SPL), Eq. 3.43 becomes converted into:

$$SPL_2 = SPL_1 + 10\,log\left(\frac{T_1}{T_2}\right) \tag{3.44}$$

Based on the processed measurement results, it is found out that the experimental signal processor (SAMURAI) normalizes the signals over 1.28 s. For this reason, the numerical signals are also normalized to the same value.

For periodic signals, the power spectrum not only provides information about the frequency components of a signal, but also the distribution of the power of the signal over different frequencies, i.e. the strength of these frequency components [148].

$$PSD = \frac{1}{2\pi}\int_{-\infty}^{+\infty} R(\tau)e^{-i\omega\tau}\,d\tau \tag{3.45}$$

In Eq 3.45, τ is the time interval between measurements, t is time, ω is radial frequency, and $R(\tau)$ is the auto-correlation function (Eq. 3.46).

$$R(\tau) = \lim_{T\to\infty} \left(\frac{1}{T} \int_0^T p(t)\, p(t+\tau) dt \right) \tag{3.46}$$

The temporal auto-correlation function $R(\tau)$ describes, on the average, the way in which the instantaneous value of function $p(t)$ depends on previous values [59, 67].

Experimental and numerical signals in this study are processed using two different programs, i.e. SAMURAI and STAR-CCM+. These programs presumably use different algorithms for calculating the Fourier Transform; therefore, it is vital to take into account the ensuing differences and their effects on the final results. In order to do so, a recorded signal is first analyzed with SAMURAI, and then imported into STAR-CCM+ and processed again therein by following the same settings used in the first step. Figure 3.15 shows the result of this comparison; a difference level of 2-4 dB is apparent in the results obtained. The difference level is equal to 0.8 dB at the BPF of the fan (i.e., 633 Hz). The corresponding difference in the levels should be taken into account when comparing the numerical and experimental results.

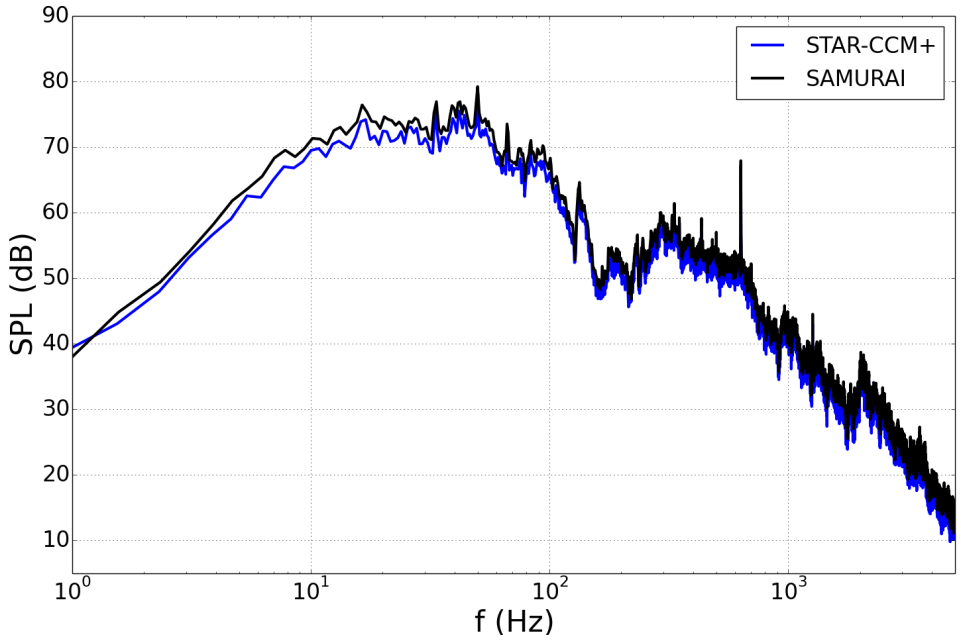

Figure 3.15: Difference in the resulting sound pressure levels of a reference signal processed by SAMURAI and STAR-CCM+; a difference of 2-4 dB is apparent in the results.

Chapter 4

Results and Discussion

4.1 Experimental Results of the Reference Model

4.1.1 Characteristic Curves

The performance curves of the reference fan (Fig 2.1) obtained from chamber test-rig measurements are shown in Fig. 4.1. For both performance and noise measurements, the rotational speed of the fan is fixed to 1000 rpm. Torque measurements are performed by using a high precision torque sensor[1] with metering capacity of 0...2 N.m, and the uncertainty of 0.2% . The mechanical losses are taken into account by measuring the torque without the fan wheel at the nominal speed for each operating point (for more information refer to [22]).

As already remarked in Section 1.4, FC fans often have an unstable range appearing as a dip on the static pressure curve. The approximate instability range of the fan under investigation is $100 \leq \dot{V} \leq 250$. The best efficiency point of the fan (BEP) is around the flow rate of 450 m^3/h; at this flow rate the fan shows a relatively steady operation. Torque of the fan continuously increases as flow rate increases, and overloads in the low-pressure range. At free delivery, torque is approximately more than twice the value in the range of maximum efficiency. Although FC fans are not built to operate at or near the free delivery condition, the observing trend in the torque curve can be considered as a serious disadvantage, which sometimes demands an oversized motor to have a safe operation at any condition [29].

[1] Manufactured by Kistler Instrumente AG

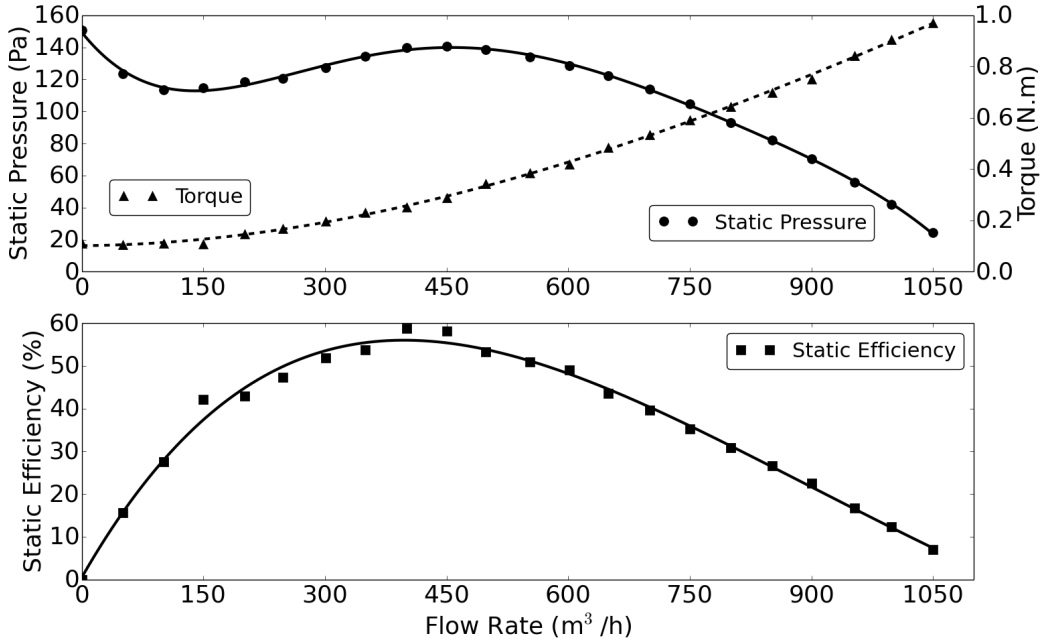

Figure 4.1: Characteristic curves of the reference fan obtained from chamber test-rig measurements; data from [22, 149].

Therefore, as can be seen in Fig. 4.1, the permissible operating range of FC fan is limited to the left by the instability region and to the right by the excessive torque values.

4.1.2 Noise Measurement Results

Figure 4.2 shows the average results of 24 single measurements performed for the reference model during 12 days. As already explained, each single measurement is the average of 10 sequential noise measurements, each taking 35 s. The measurement results provide a good basis to justify the repeatability of the measurements and help to estimate the standard deviation. Considering the broadband noise of the fan, the standard deviation is less than 1 dB across the entire operating range. However, the standard deviation becomes flow rate dependent and indicates higher values at the blade passing frequency and its harmonics (see Tab. 4.1).

The spectrogram of the reference fan is illustrated in Fig 4.3. It is clearly observable that sound pressure level of the fan increases with the increase of flow rate; this is completely in agreement with the results of Leist et al. [5]. Moreover, thanks to the optimum design of the fan, it operates quietly at

least at the flow rates measured. Sound pressure level of the fan is less than 40 dB in the range of 3-4 kHz, in which the human ear is very sensitive. As a basis for comparison, 40 dB corresponds to the noise level in a quite room (e.g., library) [59, 67].

The increase in the sound pressure level of the fan with the increase of flow rate can be explained with respect to the velocity diagram above the impeller blades (near the trailing edge).
Figure 4.4 shows the numerical velocity magnitude captured near the blade tip (2 mm above the trailing edge) at different operating points. According to this figure, increasing the flow rate leads to the increment of absolute velocity, and produces higher velocity fluctuations and pressure perturbations.

Contrary to the general belief that a fan has its minimum sound level near its best efficiency point [29], the experimental results obtained show that at a fixed rotational speed, the sound level of the FC fan under investigation is directly proportional to the flow rate.

There are some spurious peaks noticeable in the measurement results, especially in the low frequency range. The source of the spikes in the sound pressure results are not exactly known, but the high frequency resolution of the experimental results (i.e., $\Delta f \approx 0.8$ Hz) is for sure the reason that the spikes can be noticed in the spectra, and they disappear as the frequency resolution increases sixfold.

Although the contamination caused by the mentioned peaks is easy to identify and does not yield misinterpretation of the results, additional measurements are performed to delve into the source of these spurious peaks.

Table 4.1: Sound pressure level of the reference fan at the blade passing frequency (633 Hz) and its first harmonic (1266 Hz) at different operating points.

Flow rate (m^3/h)	SPL at BPF (dB)	SPL at 1^{st} Harmonic (dB)
250	50.5 ± 1.5	33.5 ± 0.4
350	63.5 ± 1.8	39.5 ± 1.9
450	64.5 ± 1.5	43.5 ± 1.5
550	68.5 ± 2.7	47.0 ± 2.0

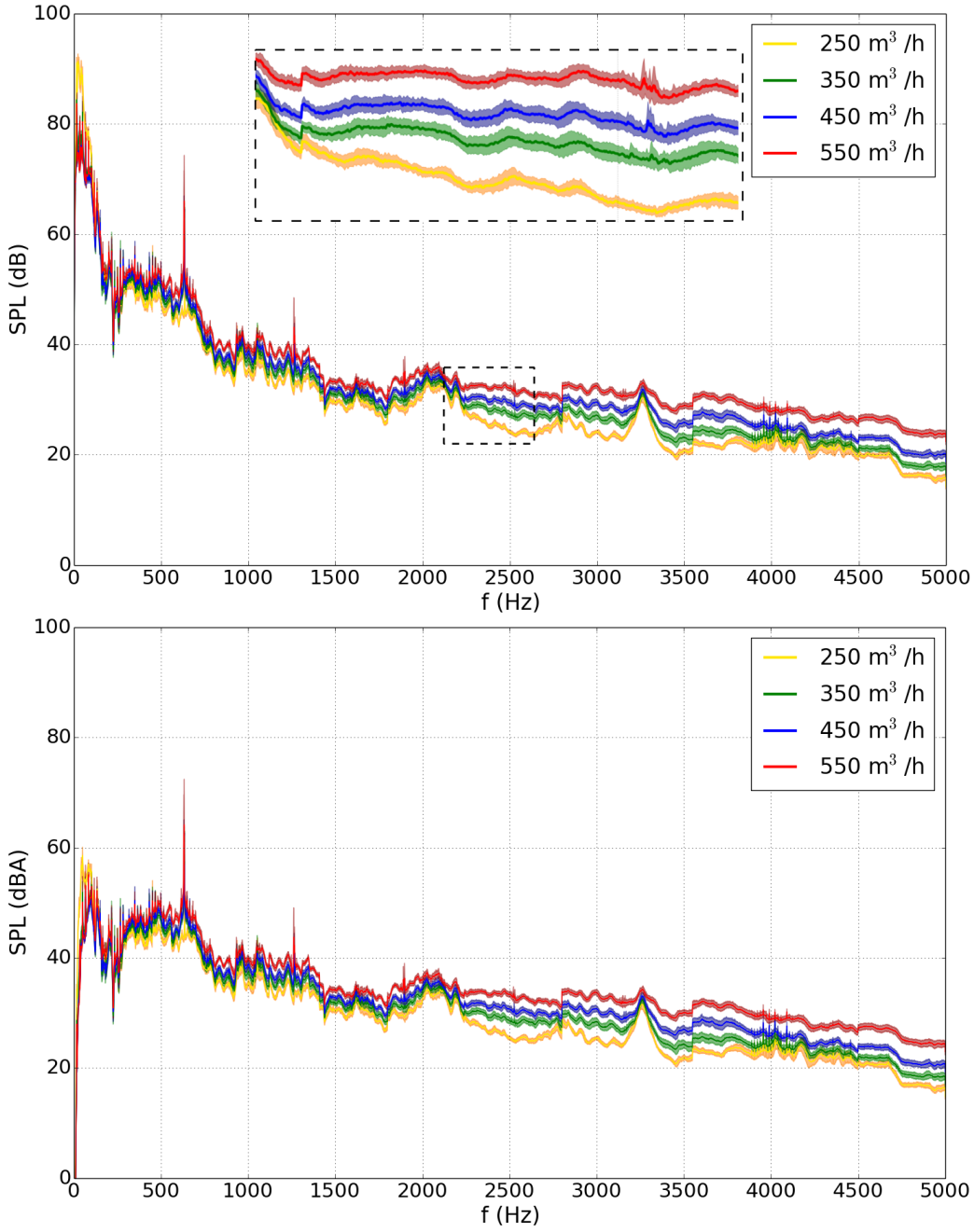

Figure 4.2: The experimental sound pressure level results of the reference model performed at different operating points. The shaded areas show the standard deviation from the mean.

It is well-known that noise measurement is susceptible to the background noise. Since the fan has been placed in a semi-anechoic room during all of

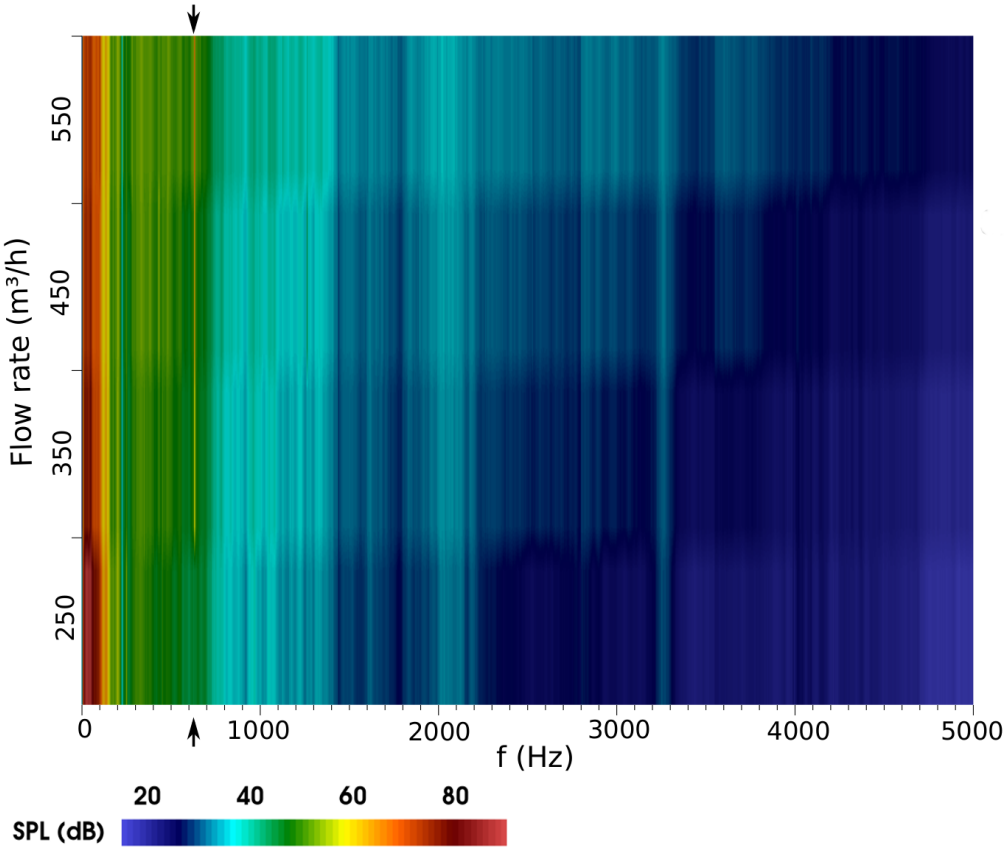

Figure 4.3: Spectrogram of the fan representing its sound pressure level measured at four different flow rates; the arrows indicate the blade passing frequency of the fan.

the experimental measurements performed, it is ensured that the results are not contaminated by any external source except the experimental apparatus itself.
In this context, it is highly probable that the system used to drive the fan causes the corresponding contamination in the spectral results. The fan is connected directly (through a shaft) to the motor, and there is no gearbox in between; hence, the motor itself is the major source of the background noise. Figure 4.5 depicts the sound pressure levels of the fan measured at two operating points in comparison to the motor noise level. The direct motor noise is measured by means of a microphone that was placed near the motor, while the indirect motor noise is recorded by the slit-tube microphones used for the sound measurements (installed in the measurement duct as shown in Fig 2.9).

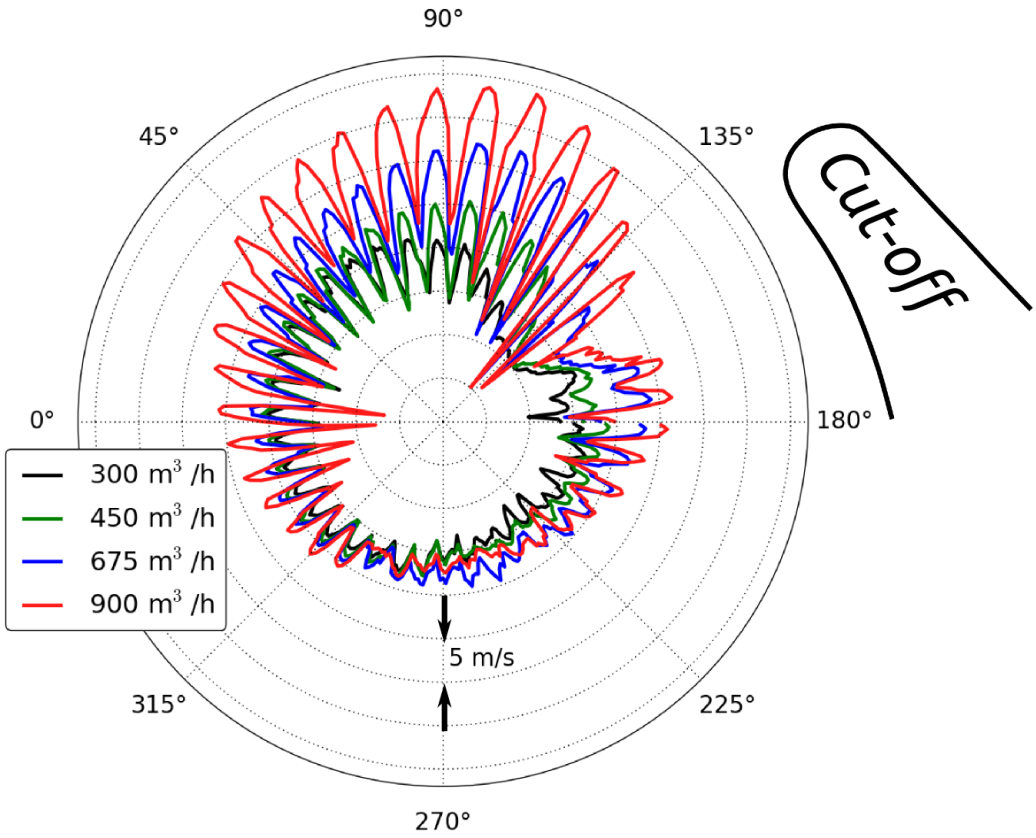

Figure 4.4: Velocity magnitude of the fan captured 2 mm above the blades at different flow rates. Results from a RANS simulation.

During the indirect motor noise measurement the impeller was not installed on the shaft. Figure 4.5 reveals that at least some of the spurious peaks are correlated to the motor noise. Figure 4.6 shows the same comparison with the focus on the range 0-400 Hz. The interval between the vertical dashed lines is equal to the shaft speed frequency, i.e. 16.667 Hz. It can be clearly seen that the excitement of the peaks are exactly coherent with the shaft frequency and its harmonics. Moreover, the spurious peaks are always present at the mentioned frequencies and this trend is independent of the motor noise level.

It is also noticeable that the amplitude of the peaks are dependent on the operating point of the fan, for instance at 283 Hz and at 350 Hz, the curve showing the noise level at 250 m^3/h, despite its lower noise level, is not affected as strongly as the other curve is (i.e, 450 m^3/h).

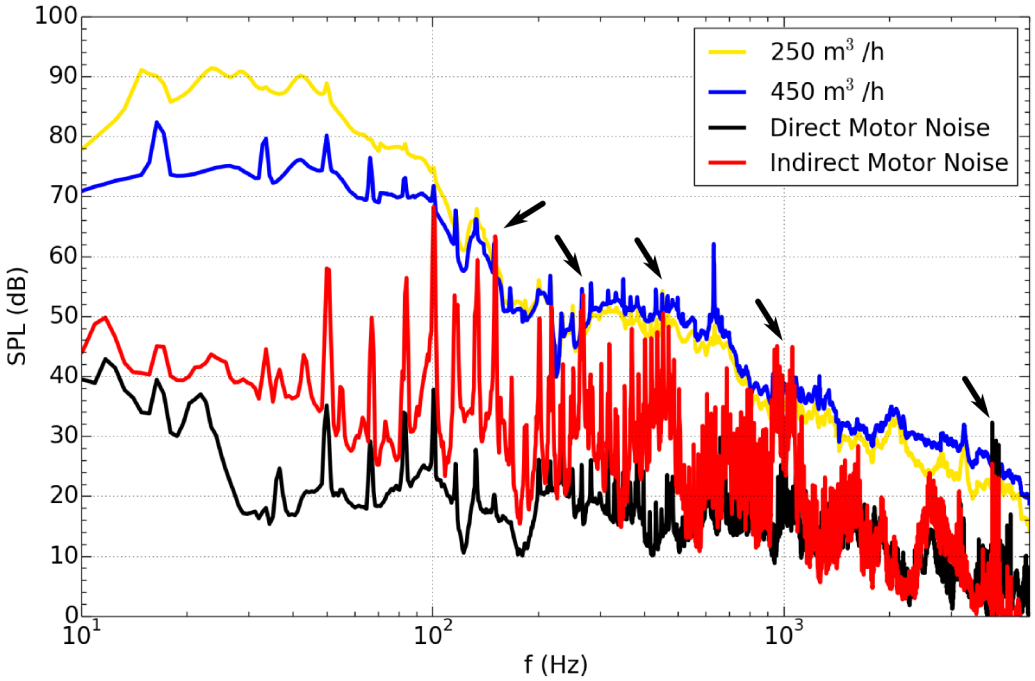

Figure 4.5: Comparison between motor noise level and sound of the fan measured at 250 & 450 m^3/h. The arrows indicate where the motor noise is high enough to contaminate the measurement results.

Two other measurements are performed to make sure that the spikes are not caused by friction between impeller and inlet nozzle or stator wall on the inlet side. For the first measurement the inlet nozzle is completely disconnected from the fan, while in the second measurement a 25% narrower impeller is used. Except the impeller width all other geometrical proportions are the same as the reference impeller. The measurements are performed near the BEP condition of the reference model; however, due to the inherent uncertainties, deviation in the operating point should be expected.

The spikes can be clearly identified at most of the anticipated frequencies Fig. 4.7. The narrow impeller exhibits a relatively smoother trend in the last 200 Hz, which can be due to its higher sound pressure level. Moreover, it is interesting to observe that the SPL curve of the nozzle-less fan is not excited at 100 Hz.
The low-frequency acoustic signature has been verified for other turbomachines by some researchers. Turbomachines operating with supersonic fan tip speeds are known to generate a tonal sound spectrum spread over a range of harmonics of the motor shaft rotation frequency. These harmonics are

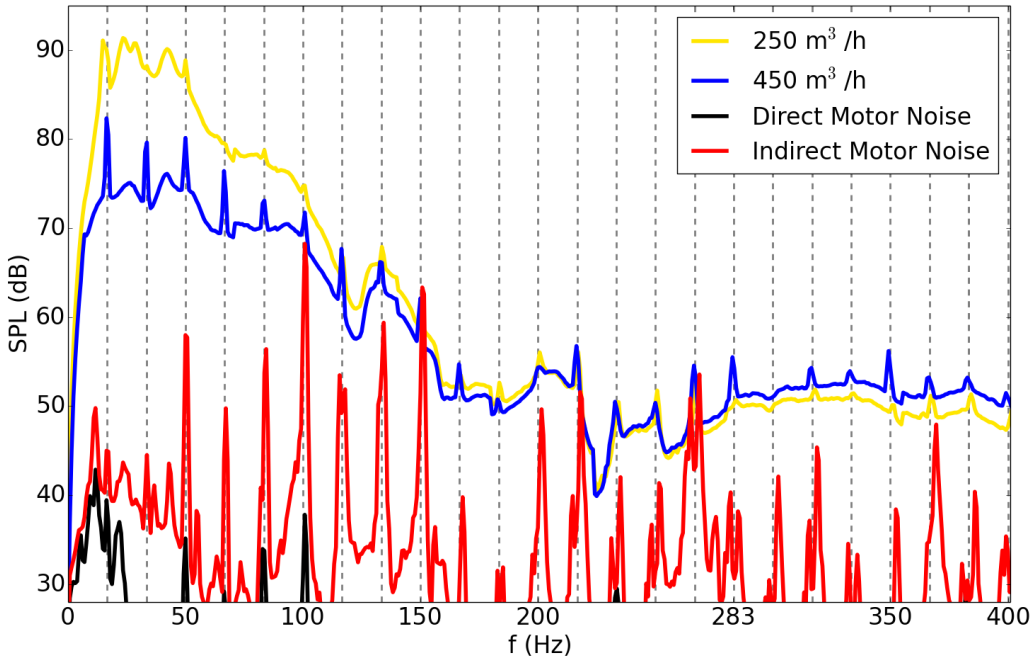

Figure 4.6: Comparison between motor noise level and sound of the fan, measured at 250 & 450 m^3/h, in the range of 0-400 Hz. The interval between the vertical dashed lines is equal to the shaft rotating frequency, i.e. 16.667 Hz.

commonly termed "buzz-saw" noise, and the phenomenon is prevailing in machines with shock waves in the rotating blade channels [150].

At lower rotor speeds narrow-band noise components might appear at about half the blade passing frequency and increase with the speed. In radial compressors these narrow-band components are produced by the secondary flow through the gap between the compressor casing and the impeller blade tips. In axial turbomachines, the source of the mentioned spectral components is the secondary flow at the blade tips. The strength of the peaks are directly related to the gap between the blade tips and the casing wall, hence the expression "tip clearance noise" (TCN) is coined for these narrow-band spectral components [150, 151].

The aerodynamic interaction between the blades and the rotating stall is the cause of low frequency noise production in the most of the radial and axial impellers. The rotating stall is a flow instability more prevailing when the machine is operating in the part-load range, and its typical frequency ranges from 60% to 80% of the blade passing frequency [152, 153].

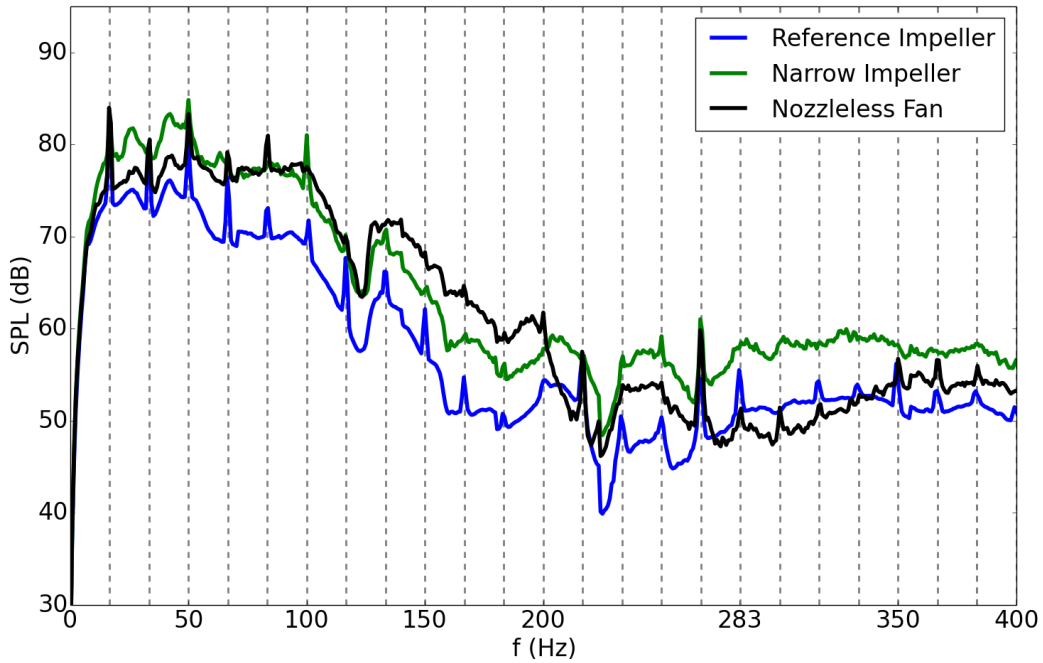

Figure 4.7: Sound pressure level spectra of the reference model with and without the inlet nozzle and a narrower impeller geometry. The interval between the vertical dashed lines is equal to the shaft rotating frequency, i.e. 16.667 Hz.

The correlation between the corresponding phenomena emerging as the dominant noise generation mechanisms in the lower frequency range, and the noise characteristics of the FC fan under investigation, is not close enough to relate any of them to the spikes in the measurement results. However, due to the coherence between the interval of the peaks and the shaft speed frequency, it is probable that mechanical vibrations of the motor are the source of the considered contamination. It is also possible that the corresponding contamination is caused by an electrical source, e.g. from the frequency converter involved with the driving motor. Therefore, in order to make a rigorous judgment about the source of the low-frequency spikes, it is necessary to conduct more experimental measurements including a different driving system.

4.2 Numerical Results

4.2.1 Validation of Different Models

The numerical simulations performed can be divided into three categories, i.e. RANS (steady and unsteady), DES, and LES. The steady RANS simulations are used throughout the study to predict the characteristic curves of the fan and also to investigate the effects of geometrical modifications on aerodynamic performance of the fan. The time-accurate (unsteady) simulations are performed to predict the noise characteristics of the fan.

The URANS simulations are conducted on the 12.5 million (12.5M) as well as the 26.5 million (26.5M) cell models. Detached eddy simulations (DES) are performed on all of the available grids, while the large eddy simulations (LES) are conducted on the 26.5M, and 102M cell models. All of the transient simulations are started from a completely converged and stable condition provided by the RANS simulation performed in advance. The performance predictions obtained from transient simulations are the average of the last four rotations (4320 samples) while the noise predictions are based on the results of the last two rotations of the impeller (2880 samples). The simulations are performed on a 64-core (2.3 GHz) server, and modeling one rotation of impeller takes on average 3840 CPU-hours using the 12.5M model. The required simulation time increases approximately by a factor of 2.5 on the 26.5M model and 7 on the 102M model respectively.

Table 4.2 summarizes the operating values of the fan near its BEP predicted by different models in comparison to the experimental results. Apparently, the pressure rise predictions derived from the RANS simulations are in better agreement with the experimental results, and there is a steady variation in the agreement level from RANS toward LES. The only exception of this trend is the LES_26.5M, whose pressure rise prediction is less accurate than the subsequent model (i.e, LES_102M). This might be an indicator that the 26.5 million cell model is still relatively coarse to be used for performing pure LES.

There is an underestimation in the torque predictions of all of the models listed in Tab. 4.2. This can be explained with respect to the mechanical losses, e.g. bearing losses, in the experimental measurements. Considering the fact that the corresponding mechanical losses do not exist in CFD simulations, it is well justified that the numerically predicted torque values are lower than the experimental data.

Table 4.2: Comparison between experimental and numerical operating values of the fan near its BEP at 1000 rpm.

	Flow rate in m^3/h	Pressure rise in Pa	Torque in N.m	Static Efficiency in %
Experiment	470.0± 4.7	139.8 ± 0.7	0.310 ± 0.004	56.2 ± 2.4
RANS_12.5M	471.0	139.2	0.295	58.9
URANS_12.5M	470.8	145.8	0.292	62.4
URANS_26.5M	469.5	143.2	0.290	61.5
DES_12.5M	470.7	145.9	0.294	61.9
DES_26.5M	468.3	149.3	0.294	63.1
DES_102M	467.6	149.5	0.291	63.7
LES_26.5M	468.0	155.2	0.291	66.2
LES_102M	467.5	151.6	0.291	64.6

Figures 4.8-4.10 depict the noise spectra predicted by different models, and Tab. 4.3 summarizes the tonal noise predictions of the corresponding models at the blade passing frequency of the fan as well as its first harmonic. As can be seen, both of the URANS simulations are capable of predicting the tonal noise accurately. The ability of the URANS simulations to capture the tonal noise component has already been acknowledged in some of the previous studies (e.g. [154, 155]). There is a relatively large deviation between the broadband noise level predicted by URANS 12.5M and the experimental result. On the other hand, URANS_26.5M provides a favorable result up to approximately 1 kHz. Generally, URANS simulations function like a low-pass filter as remarked in [155], and their predictions only cover the low frequency range.

Interpreting Detached and Large Eddy Simulation results are not as straightforward as for URANS. The first difficulty arises from the fact that in complex flows the response of these methods to grid refinement is not as limpid as it is in URANS simulations. In other words, the general idea that the grid refinements do not harm is not necessarily true in DES and LES [132]. According to Fig 4.9, DES_12.5M can accurately predict noise of the fan up to 1 kHz. With respect to the numerical mesh and its refinement level, it seems reasonable to assume that a great part of the domain should be dominated by the RANS mode in DES_12.5M. However, comparing the results obtained to the experimental measurement, it is evident that DES_12.5M result covers a broader frequency range than URANS_26.5M result does. It is also visible that the SPL curve of DES_12.5M remains close to the experimental trend

for approximately another 1 kHz, unlike the SPL curve of URANS_26.5M which tails-off suddenly at approximately 900 Hz. This clearly indicates that detached eddy simulation, even on a coarser grid, is able to capture more flow structures than URANS.

The results obtained from pressure-monitors do not show a considerable improvement when comparing DES_12.5M with DES_26.5M, but there is a closer agreement between the experimental data and the FW-H result obtained from DES_26.5M. However, as can be seen in Tab. 4.2, DES_26.5M fails to accurately predict the tonal noise neither with pressure-monitors nor with the FW-H method.

The noise predictions derived from pressure-monitors in DES_102M show a considerable enhancement in the quality of the results. In fact, pressure-monitors can reliably predict the experimental trend across the whole range up to the upper frequency bound (i.e., herein 5 kHz). The effect of grid refinement on the FW-H prediction is also evident in Fig. 4.9 when comparing DES_102M with the other DES models. However, despite a close correlation in the lower frequency range, FW-H prediction of DES_102M is still limited to the same frequency as the other DES models. This limitation will be further discussed below when interpreting the LES results. The tonal noise component predicted by DES_102M is slightly better than DES_26.5M, yet considerably underestimated in comparison to the experimental data. The most accurate tonal noise prediction belong to the DES_12.5M model, which can reasonably be traced back to the more pronounced role of the URANS mode in it.

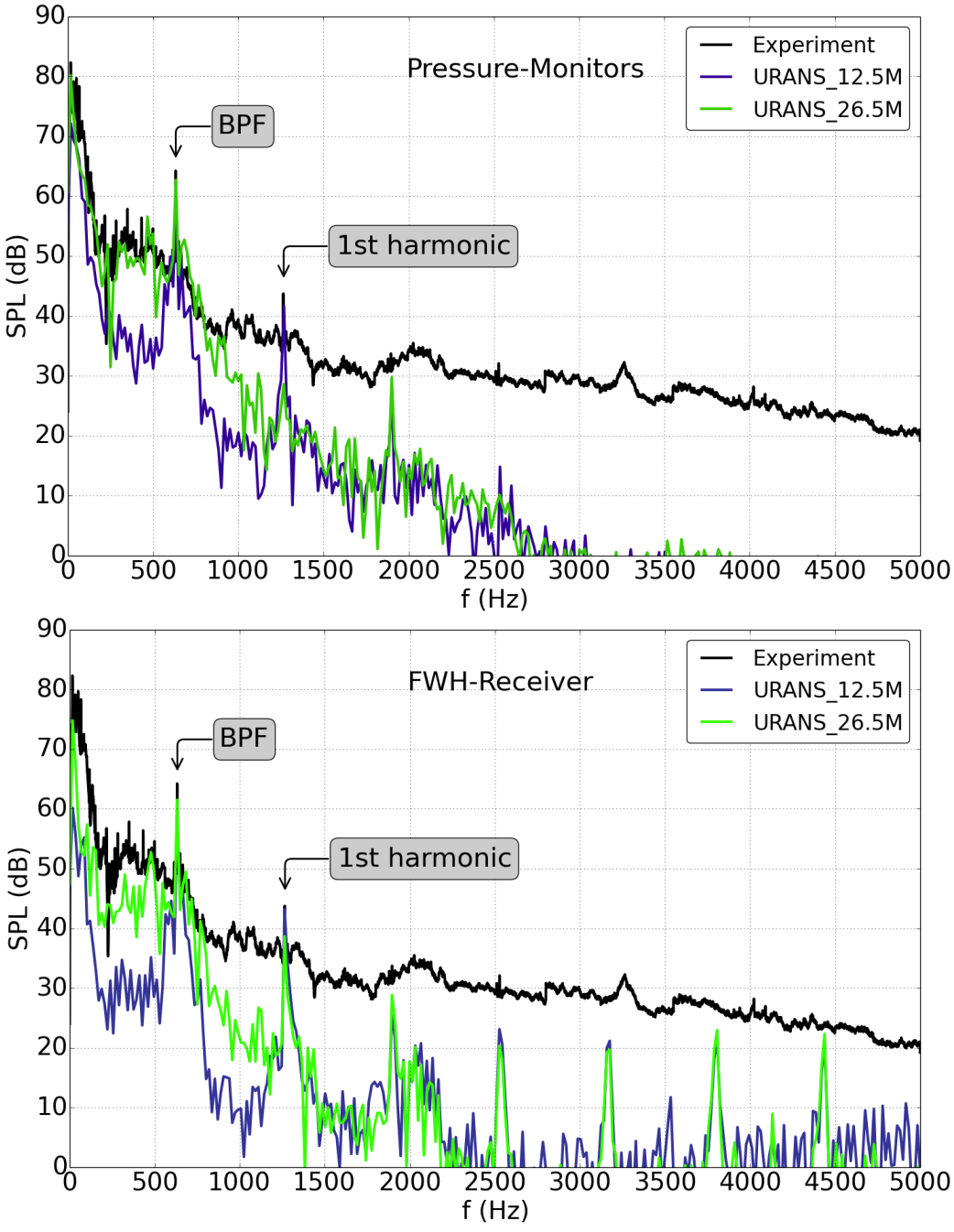

Figure 4.8: Sound pressure level obtained from URANS simulations performed on the numerical grids with 12.5 and 26.5 million cells.

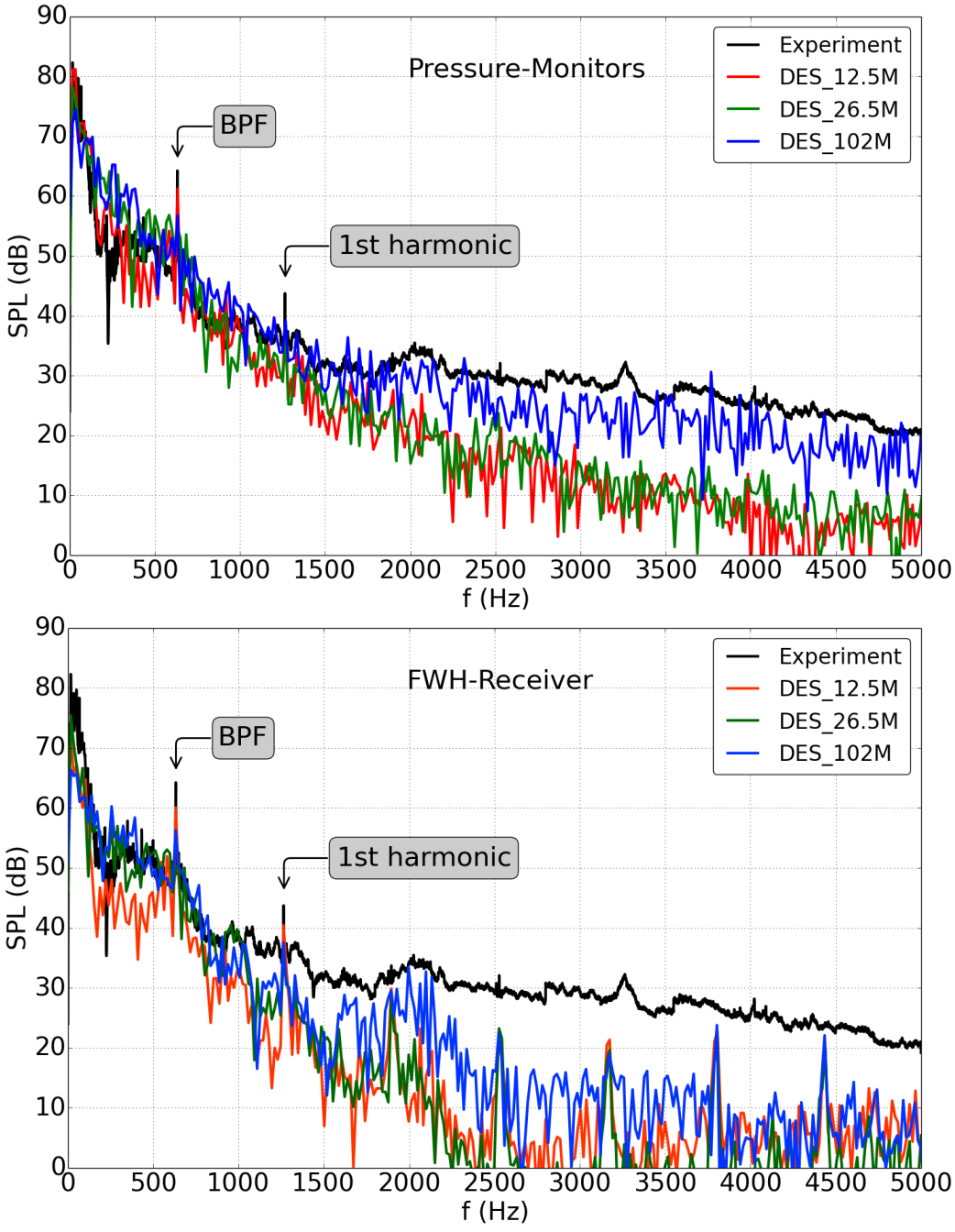

Figure 4.9: Sound pressure level predicted by Detached Eddy Simulations (DES) on the numerical grids with 12.5, 26.5, and 102 million cells.

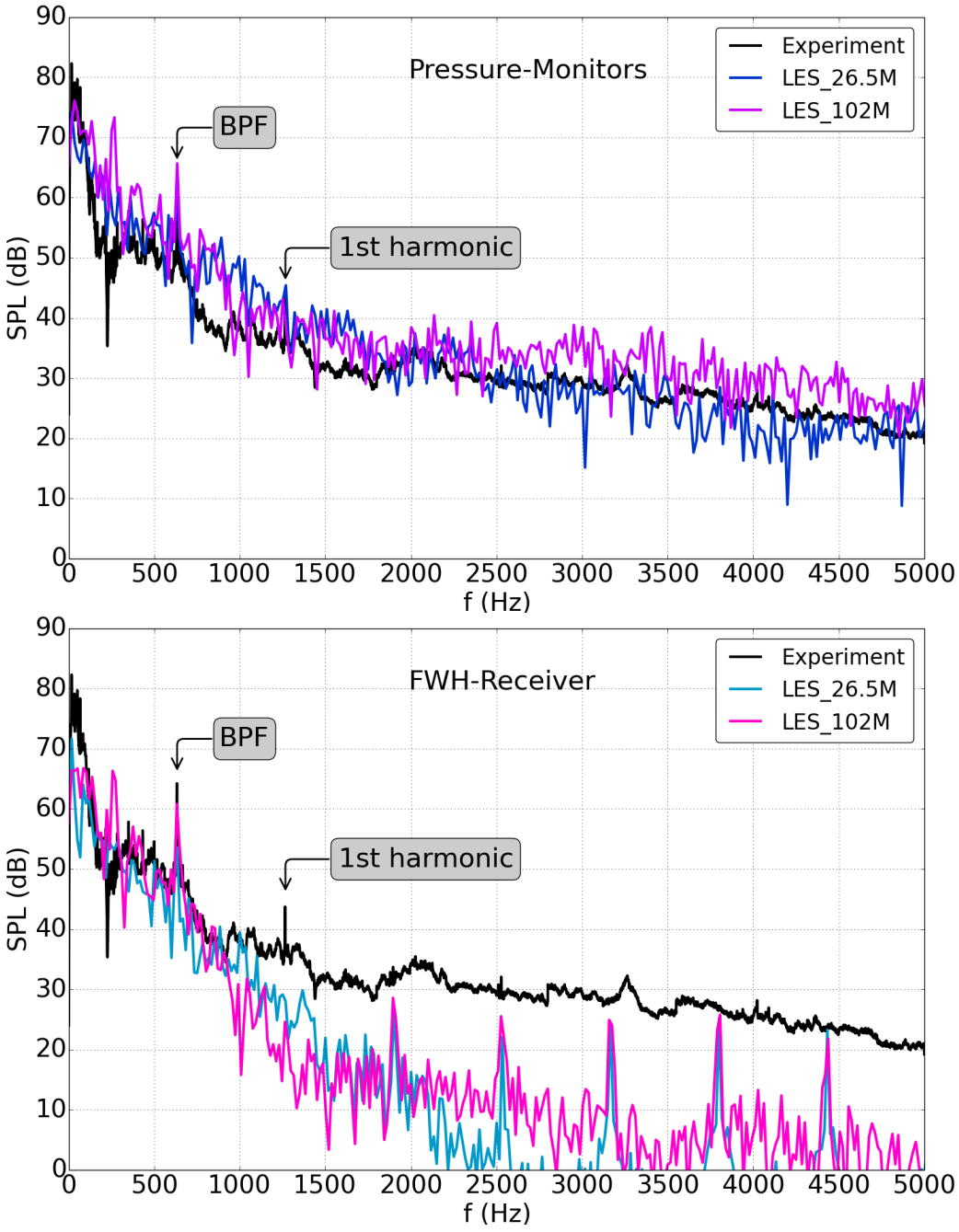

Figure 4.10: Sound pressure level predicted by Large Eddy Simulations (LES) on the numerical grids with 26.5 and 102 million cells.

Table 4.3: Sound pressure level (SPL) at the blade passing frequency (BPF) and its first harmonic predicted by different numerical simulations.

Model		**SPL (dB) 633 Hz**	**SPL (dB) 1266 Hz**
URANS_12.5M	Pressure-Monitor	60.9	41.7
	FW-H	59.2	43.2
URANS_26.5M	Pressure-Monitor	61.9	27.8
	FW-H	60.7	37.8
DES_12.5M	Pressure-Monitor	61.2	37.9
	FW-H	60.1	40.4
DES_26.5M	Pressure-Monitor	54.5	37.1
	FW-H	49.8	34.5
DES_102M	Pressure-Monitor	56.7	39.2
	FW-H	56.2	37.6
LES_26.5M	Pressure-Monitor	58.5	45.4
	FW-H	53.6	28.0
LES_102M	Pressure-Monitor	65.7	38.9
	FW-H	60.8	24.6
Experiment		64.5 ±1.5	43.5 ± 1.5

Large eddy simulation is the last method in this comparison; and its predictions are shown in Fig. 4.10. As can be seen, both LES_26.5M and LES_102M are capable of predicting the experimental trend up to 5 kHz. This clearly shows the effectiveness of pure LES when it comes to the broadband noise prediction. Figure 4.11 helps to shed some light on this topic and find out the reason why LES prediction range, even on the 26.5M mesh, easily extends to higher frequencies.
The isosurfaces shown in this figure represent the velocity magnitude of 20 m/s and are colored with vorticity magnitude. This figure reveals that LES captures considerably more amount of detail than DES on an identical grid. The mentioned fact simply justifies the broader prediction range of LES when comparing it with the other methods. It is quite unexpected, yet interesting that LES_26.5M shows a generous amount of detail that neither DES_26.5M nor DES_102M are capable of providing.
It is also necessary to note that although performing LES on coarse grids, which is refereed to as VLES in some literature, is attractive in view of the computational expenses, there is a school of thought that considers VLES as

an inaccurate and error-prone approach which should be prohibited as much as possible (refer to [126] for more information). As already explained in Section 3.3, it is not always clear whether a simulation is of LES type or VLES. One of the effective methods to verify a large eddy simulations is to calculate the ratio of the resolved to the total turbulent kinetic energy [126, 129]. The corresponding ratio can be determined using the following equation, while the resulting value would be $0 \leq M(x,t) \leq 1$.

$$M(x,t) = \frac{k(x,t)}{k(x,t) + k_{SGS}(x,t)} \tag{4.1}$$

where $k(x,t)$ is the resolved turbulent kinetic energy that is based on the fluctuating parts of the velocities and should be calculated according to Eq. 3.33, $k_{SGS}(x,t)$ is the subgrid-scale (SGS) turbulent kinetic energy that is a predefined function in STAR-CCM+. For a sufficiently resolved LES, $M(x,t)$ should be equal to or greater than 0.8, which means 80% of the turbulent kinetic energy is resolved, while the remaining 20% is provided by the SGS model [156].
Figure 4.12 depicts the corresponding ratio between the resolved and total turbulent kinetic energy for LES_26.5M and LES_102M on two planar cuts through the impeller center. As can be seen, the turbulent kinetic energy is properly resolved in a large part of the domain in both of the simulations. However, in both simulations, it is the SGS model that to a great extent dominates the flow through the inlet nozzle. Furthermore, the flow through the impeller eye is also extensively modeled in the LES_26.5M, while it is the contrary in the case of LES_102M.

The tonal noise predicted by LES 26.5M is on average 4 dB higher than DES_26.5M; however, it still is underestimated comparing with the experimental data. According to Tab. 4.3, only URANS is able to provide an accurate tonal noise on the 26.5 million cell model, while the predictions of both detached and large eddy simulations are considerably underestimated. LES_102M can also accurately predict the tonal noise (contrary to LES_26.5M). The combination of the FW-H method and LES_102M also provides a favorable tonal noise result. However, it can be seen that in all of the presented models the FW-H prediction range is limited to 1.2 kHz. The changes in the numerical grid or turbulence modeling approach could not help towards extending the mentioned limit. This might an indication that in the higher frequency range, the volume or flow based sources become more dominant and play a leading role. Consequently the impermeable FW-H approach employed, which does not include volumetric sources (or permeable surfaces), fails to accurately predict the noise in the higher frequency range.

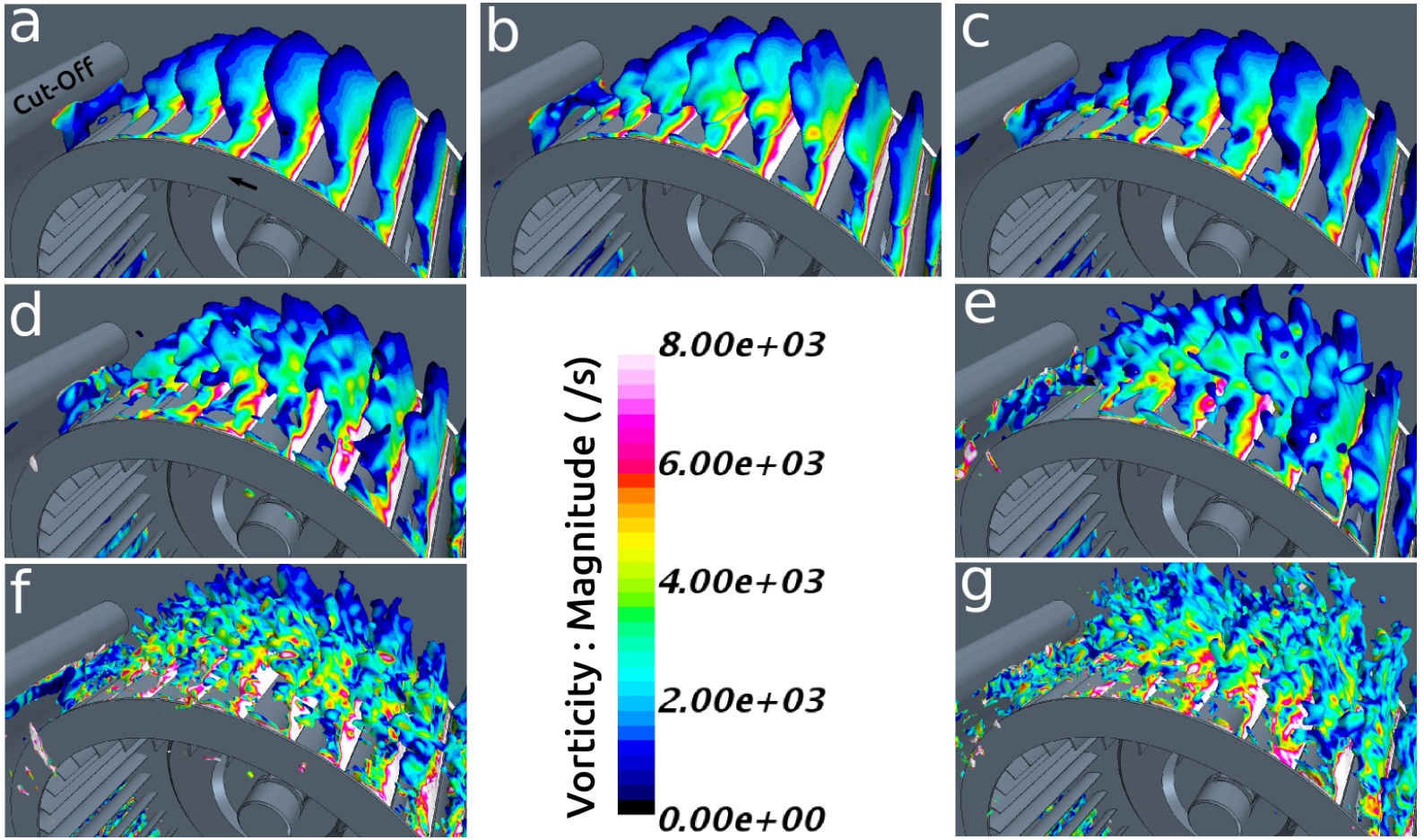

Figure 4.11: Comparison between the velocity magnitude isosurfaces captured by different models at 20 m/s and colored with vorticity magnitude. (a) URANS_12.5M, (b) URANS_26.5M, (c) DES_12.5M, (d) DES_26.5M, (e) DES_102M, (f) LES_26.5M, and (g) LES_102M.

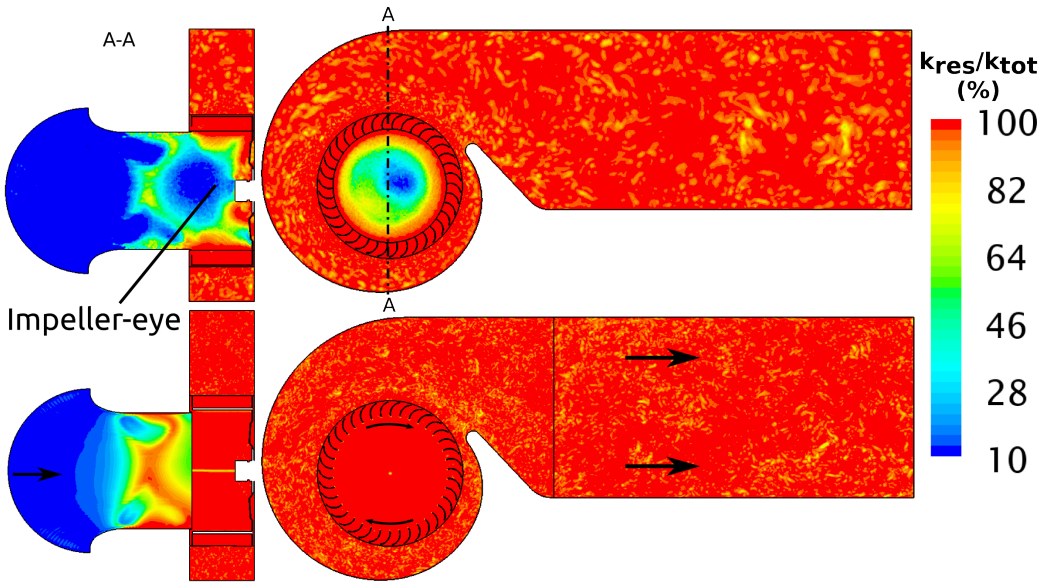

Figure 4.12: The ratio between the resolved and the total turbulent kinetic energy in LES_26.5M (top) and LES_102M (bottom).

LES_102M predictions include a strong peak at approximately 265 Hz. Since the mentioned peak is also evident in the FW-H result, it can be inferred that it is from a dipole source and is based on the flow interaction with a surface. Inspecting the transient surface data representing the sound pressure level at different frequencies reveals that the contribution of the cut-off toward noise generation is not merely limited to the blade passing frequency of the fan. As can be seen in Fig 4.13, the cut-off surface is perpetually involved in noise generation, nevertheless, at the blade passing frequency the cut-off plays its most significant role. Therefore, the mentioned spike at 265 Hz might be related to the interaction between the cut-off surface and a secondary flow forming near the impeller tips. Moreover, the comparatively higher level of vorticity around the impeller in LES_102M (shown in Fig. 4.11) justifies the reason why only LES_102M is able to capture the mentioned peak. It is also probable that the peak mentioned originates from the limited number of impeller rotations modeled in this study. However, continuing the simulation for one more impeller rotation could not affect the level of the spike. It remains unanswered whether or not proceeding the simulation for some more impeller rotations can partly or even completely diminish the corresponding spike at 265 Hz.

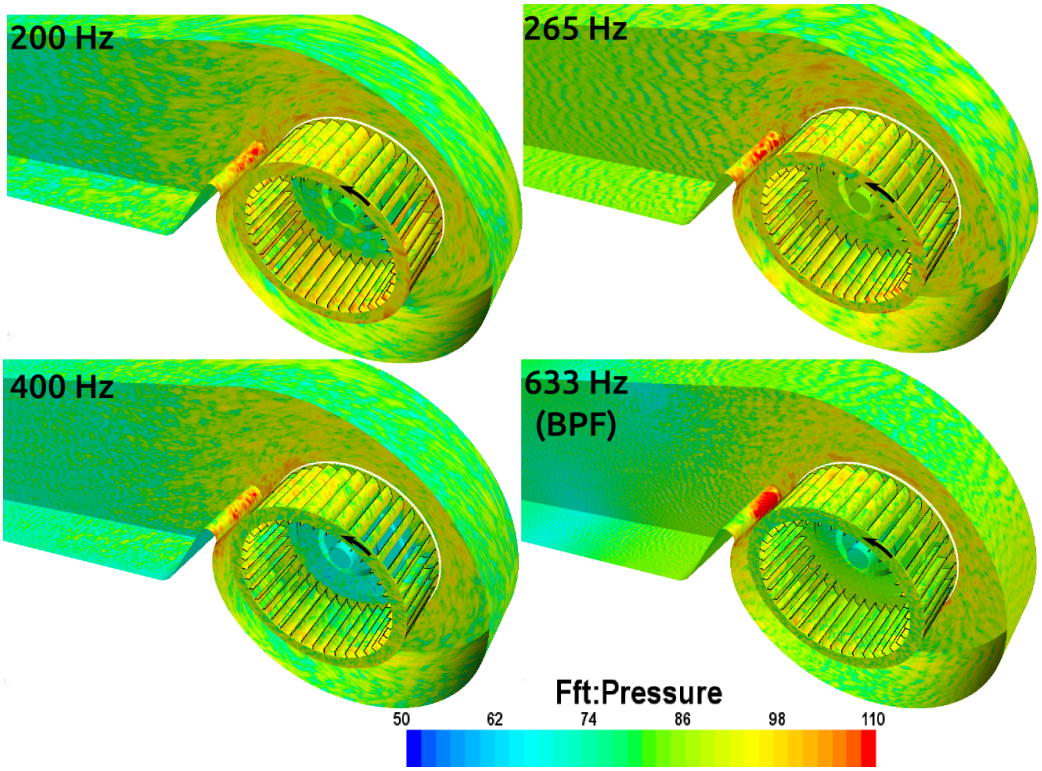

Figure 4.13: Sound pressure level radiated from different boundaries in LES_102M at various frequencies.

4.2.2 Near-Field Effects

An extended model that includes also the measurement duct (approximately 2 m long) is simulated to verify the previous simulation results and investigate the near-field effects on the sound pressure levels (see Figure 4.14). In order to do so, in addition to the reference virtual microphones (shown in Fig. 3.5), new virtual microphones are defined in the measurement duct. The in-duct virtual microphones are exactly at the same positions as the actual microphones are installed in the experimental setup.
The extended model is simulated using DES turbulence model, and except the measurement duct itself, there is no difference between DES_12.5M and the extended simulations. The measurement duct is spatially discretized following the same parameters used in the stationary region. It should be noted that including the measurement duct in the simulation adds 6 million extra cells to the total count as well as 10 more days to the required simulation time. The in-duct microphones consist of both pressure-monitors and FW-H receivers.

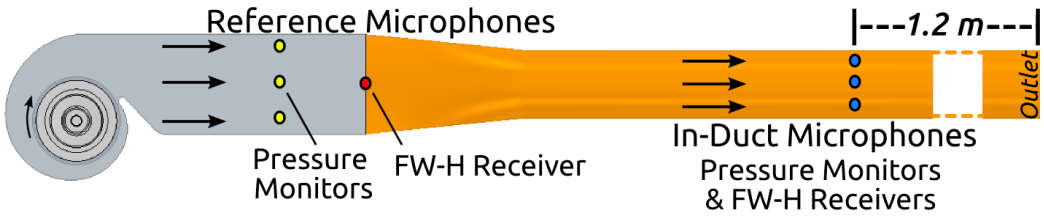

Figure 4.14: In the extended model the measurement duct is incorporated into the reference numerical simulation (i.e, DES_12.5M), and additional numerical results are obtained from the in-duct microphones.

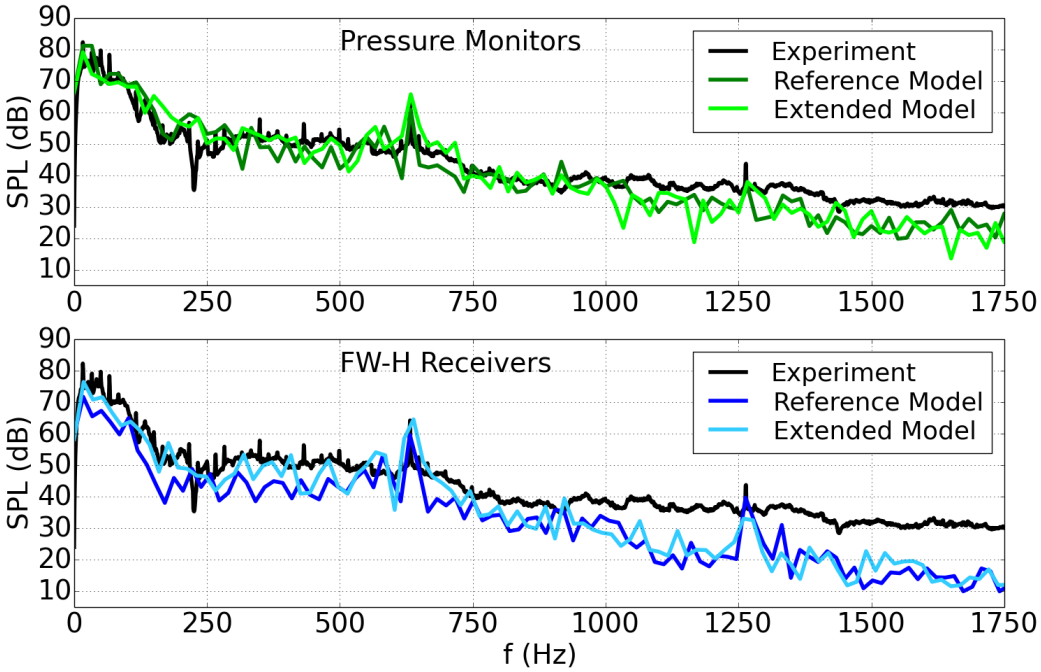

Figure 4.15: Comparison between the results obtained from the reference (DES_12.5M) and the extended model at the reference microphone/receiver positions.

Figure 4.15 shows the first comparison between the results obtained from the reference model (i.e., DES_12.5M) and the extended model. The results in this figure belong to the reference microphone/receiver positions. As can be seen, incorporating the measurement duct into the simulation has only negligible effects on the pressure-monitors and does not change the trend or the level of the predictions. On the other hand, the FW-H result obtained from the extended model shows a trend closer to the experimental curve. This is more pronounced in the lower frequency range and it appears that

including the measurement duct has a positive effect on the FW-H result. It is probable that the FW-H receiver in the reference model is affected by the constraints dictated by the free-stream outlet boundary condition, whereas in the extended model, the FW-H receiver is far from the outlet, therefore not exposed to the corresponding effects.

Comparison between the sound pressure levels predicted by the reference and the in-duct virtual microphones is shown in Fig. 4.16. It is observable that up to approximately 1 kHz, the sound pressure levels predicted are rather comparable, but the agreement level varies in the higher frequency range. In both methods, a notable difference between the spectra is only evident beyond approximately 1.4 kHz. This comparison indicates that the over-estimation of the LES results in the previous section might be related to the position of the virtual microphones in the reference model. This topic deserves some more investigation, and making a conclusive judgment about the near-field effects is only possible after performing large eddy simulation on the extended model using a more refined grid whose result reliably covers the higher frequency range as well.

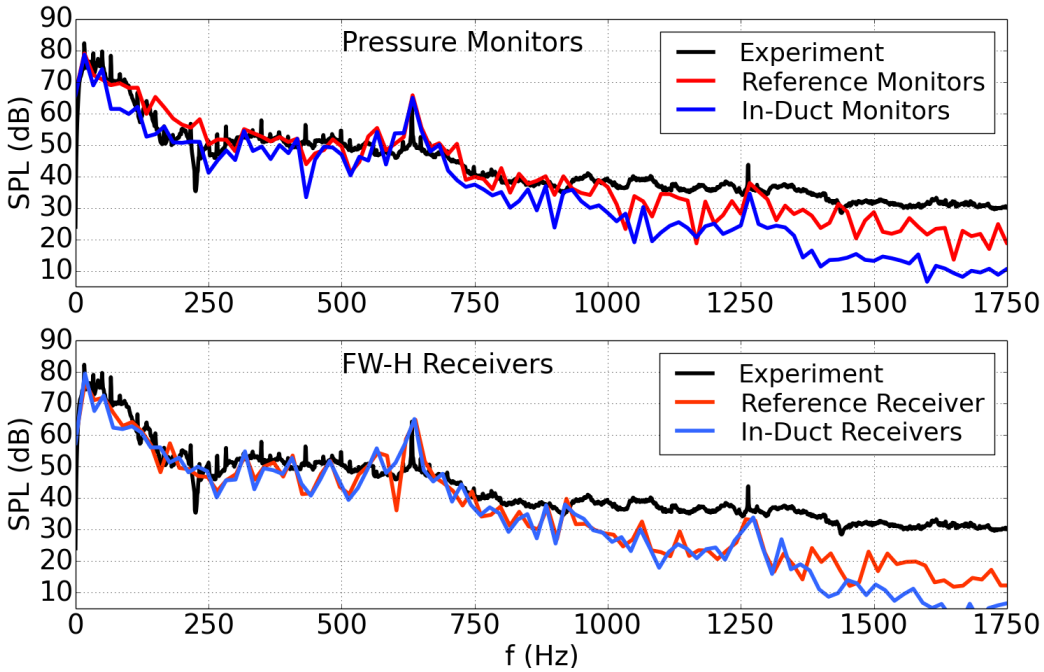

Figure 4.16: Comparison between the numerical sound pressure level spectra obtained from the reference and the in-duct microphones in the extended model.

4.3 Geometrical Modification of the Reference Model

4.3.1 Different Number of Blades

The effect of changing the number of impeller blades on the noise and performance characteristics of the fan is investigated by performing numerical simulations on the mesh with approximately 12.5 million polyhedral cells. The numerical investigations comprise noise and performance predictions of the impellers with 30, 38 (the reference model), 48, and 52 blades. The inlet and outlet blade angles are identical in all of the impeller models and equal to $\beta_1 \approx 77°$, $\beta_2 \approx 165°$. The performance curves are obtained from RANS simulation while the noise predictions are achieved by means of detached eddy simulation.

Figure 4.17 depicts the influence of changing the number of blades on static pressure, torque and static efficiency of the fan. It is observable that reducing the number of blades considerably deteriorate the pressure rise and the efficiency of the fan. On the other hand, increasing the number of blades boosts the aerodynamic performance of the fan, especially at high flow rates.

Increasing the number of impeller blades is known to increase torque which in some cases deteriorates the performance of the fan. However, for the fan under investigation the gain in the pressure rise is large enough to compensate the increment of torque and enhance the efficiency. Figure 4.17 also shows that this trend is only valid up to a definite number of blades and a further increment is likely to reduce the performance of the fan. Accordingly, around $675\,\mathrm{m}^3/\mathrm{h}$, the static efficiency of the fan with 38 blades (the reference model) is slightly higher than the other impellers. According to the numerical results obtained, increasing the number of blades makes the velocity profile above the blade tips more uniform (see Fig. 4.18). As previously mentioned, the discrete noise component (tonal noise) of the fan is a result of the interaction between the unsteady flow leaving the blade channels and the cut-off (volute tongue). Therefore, the trend shown in Fig. 4.18 is a favorable outcome that in turn leads to the reduction of the turbulent kinetic energy above the blades which in the vicinity of the cut-off is likely to reduce the tonal noise component.

The numerical noise predictions obtained from transient simulations are shown in Fig. 4.19. These results depict the sound pressure level of the fans with different blade numbers versus the Strouhal (St) number; while St=1

corresponds to the blade passing frequency. It is observable that there is a considerable tonal noise reduction predicted by both methods for the impellers with the higher number of blades. Conversely, reducing the number of blades not only leads to the increment of the tonal noise, but it also increases the broadband noise across the whole range of the shown Strouhal numbers.

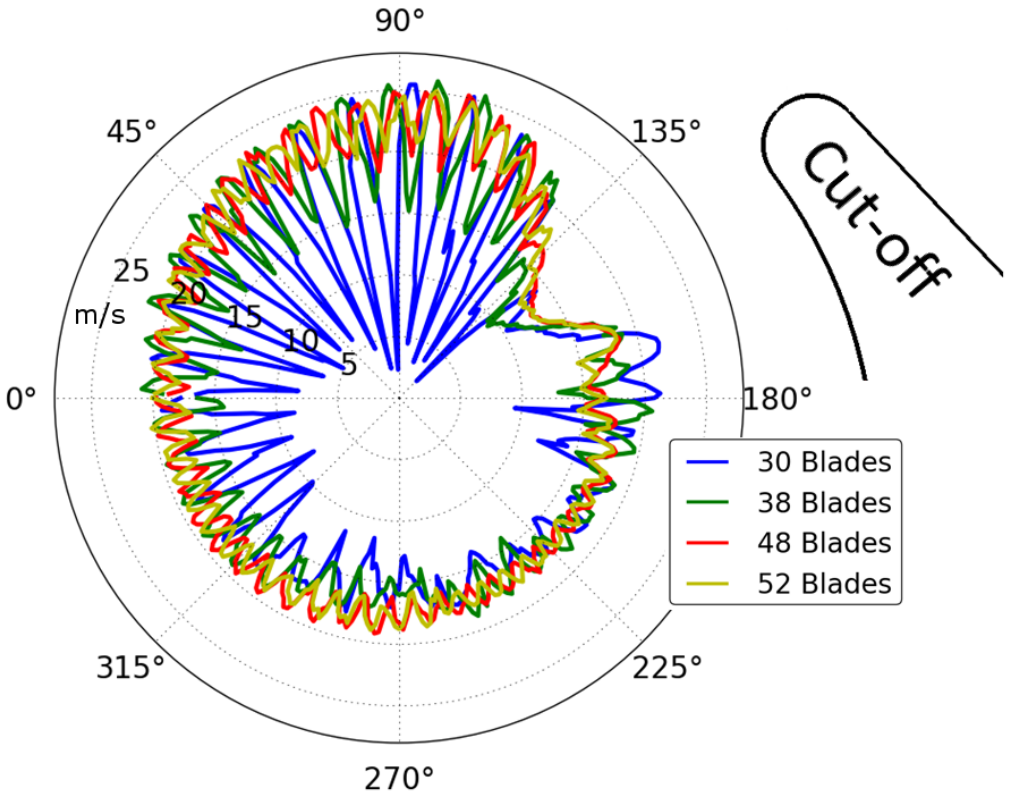

Figure 4.18: Velocity profiles 2 mm above the blade tips of the impellers with different blade numbers obtained from numerical simulations. Increasing the number of blades makes the velocity profile smoother. Figure was first published in [157].

The numerical results also indicate that ultimately the broadband noise level becomes insensible to the number of blades, and adding further blades to the impeller only leads to imperceptible changes in the broadband noise level. The trend observed in the numerical results are in excellent agreement with the experimental results from [5].
Transient surface data helps to visualize the sound pressure level radiated from different components of the fan, and therefore provides a better understanding of the modifications carried out. Figure 4.20 depicts the sound pressure level

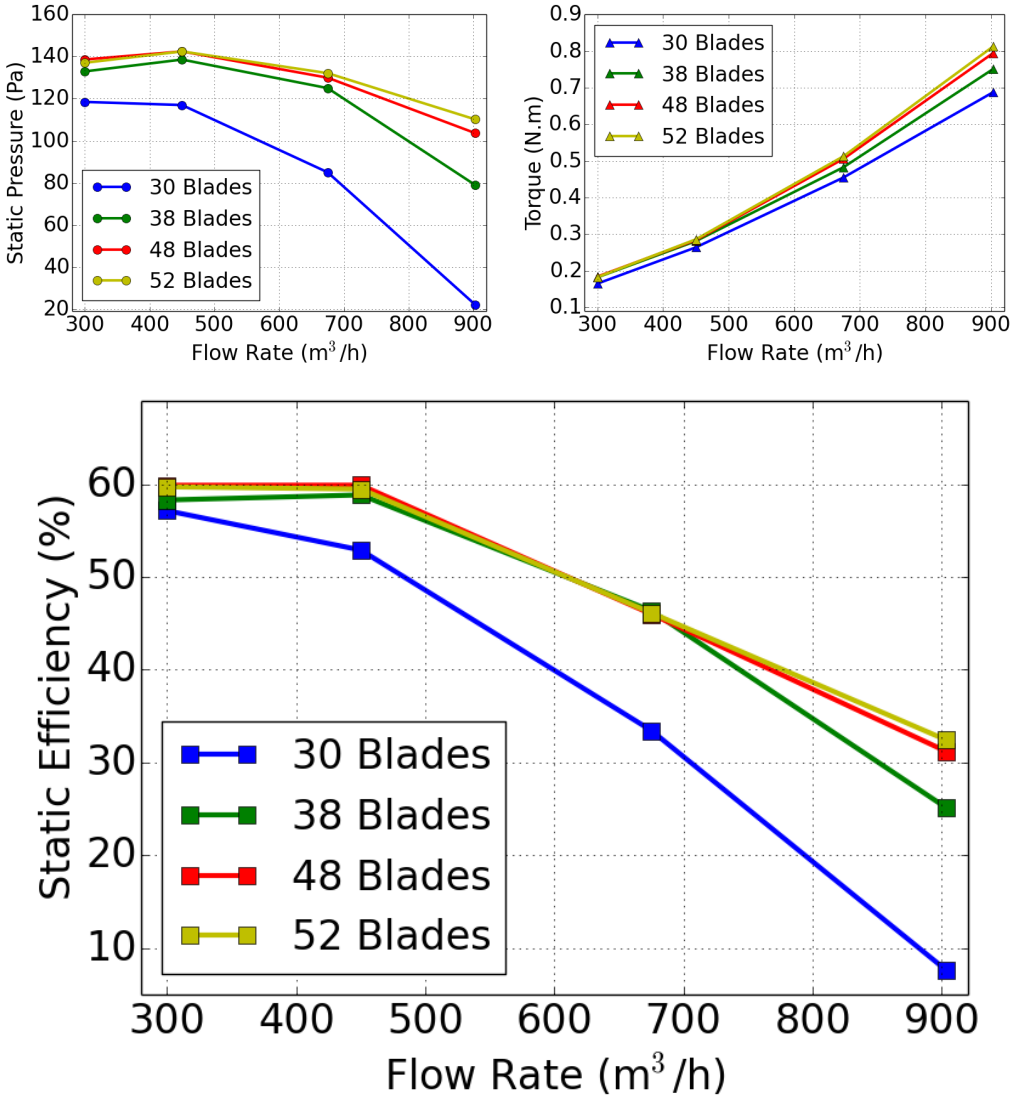

Figure 4.17: The effect of changing the number of impeller blades on static pressure (left), torque (right) and static efficiency (bottom) of the fan. Results are obtained from RANS simulations on numerical grids with cell counts ranging from approximately 11 million (30 blade impeller) to 14 million (52 blade impeller) cells.

radiated from the suction side as well as the pressure side of the blades for different impellers. Accordingly, the suction side of the blades are on average louder than the pressure side. This might be the effect of the flow separation occupying the area near the suction side of the blades (as shown in Fig. 1.7).

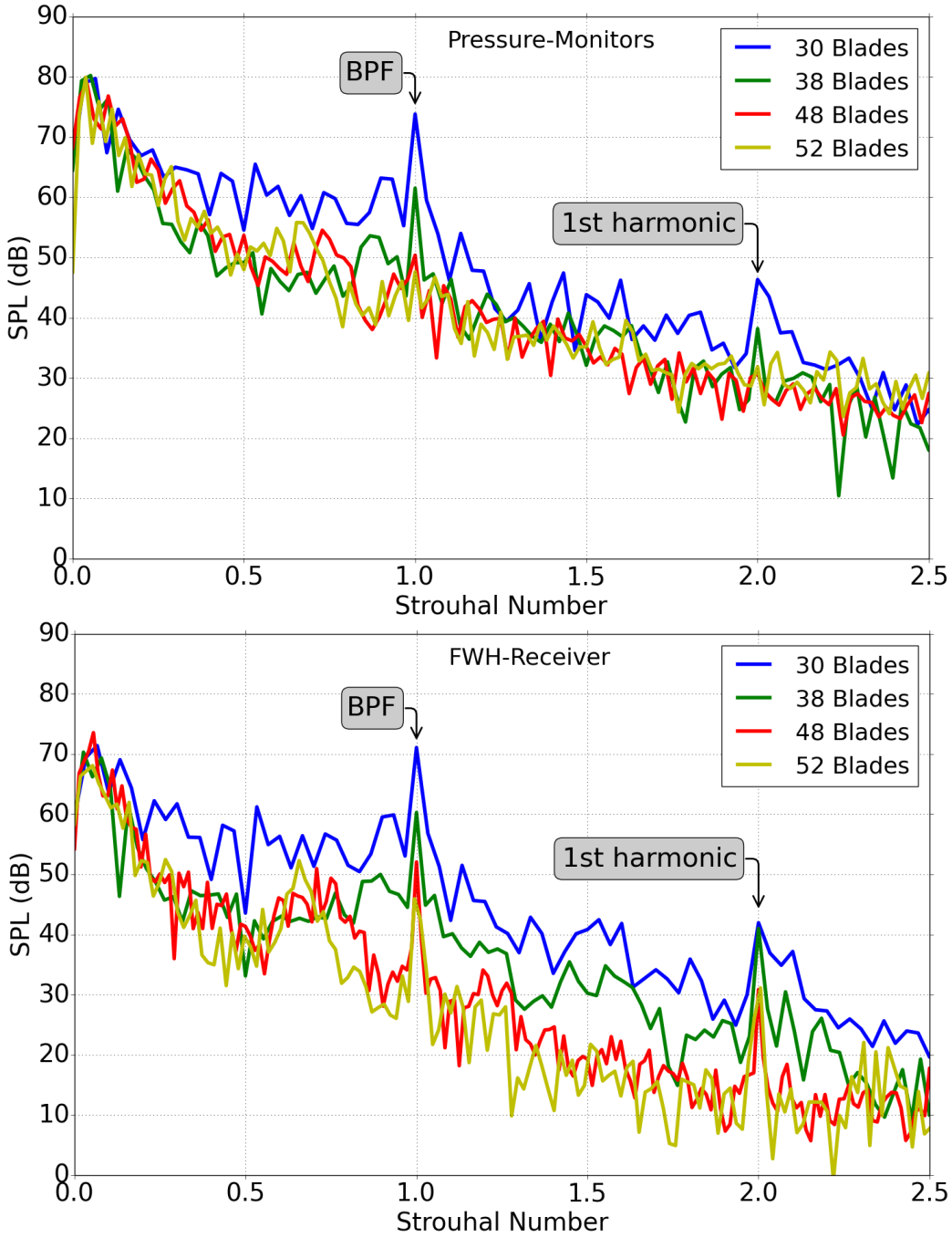

Figure 4.19: Spectral noise analysis of the impellers with various blade numbers; St=1 corresponds to the blade passing frequency. Results are obtained from DES on numerical grids with cell counts ranging from approximately 11 million (30 blade impeller) to 14 million (52 blade impeller) cells.

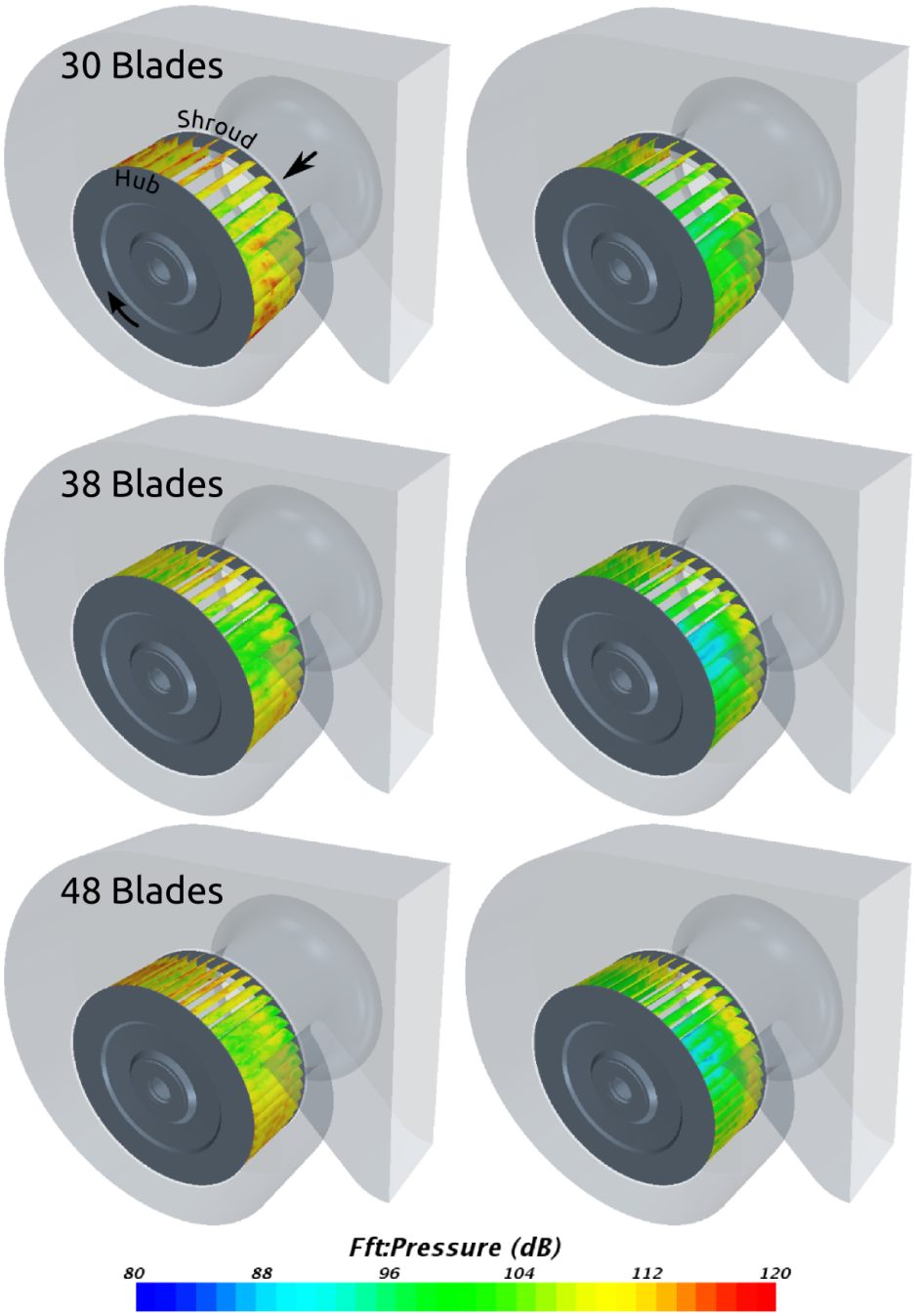

Figure 4.20: Sound pressure level radiated in the range of 100-1000 Hz from the blades suction side (left) and the pressure side (right) of the impellers with different total number of blades. Results are obtained from DES on numerical grids with cell counts ranging from approximately 11 million (30 blade impeller) to 13 million (48 blade impeller) cells.

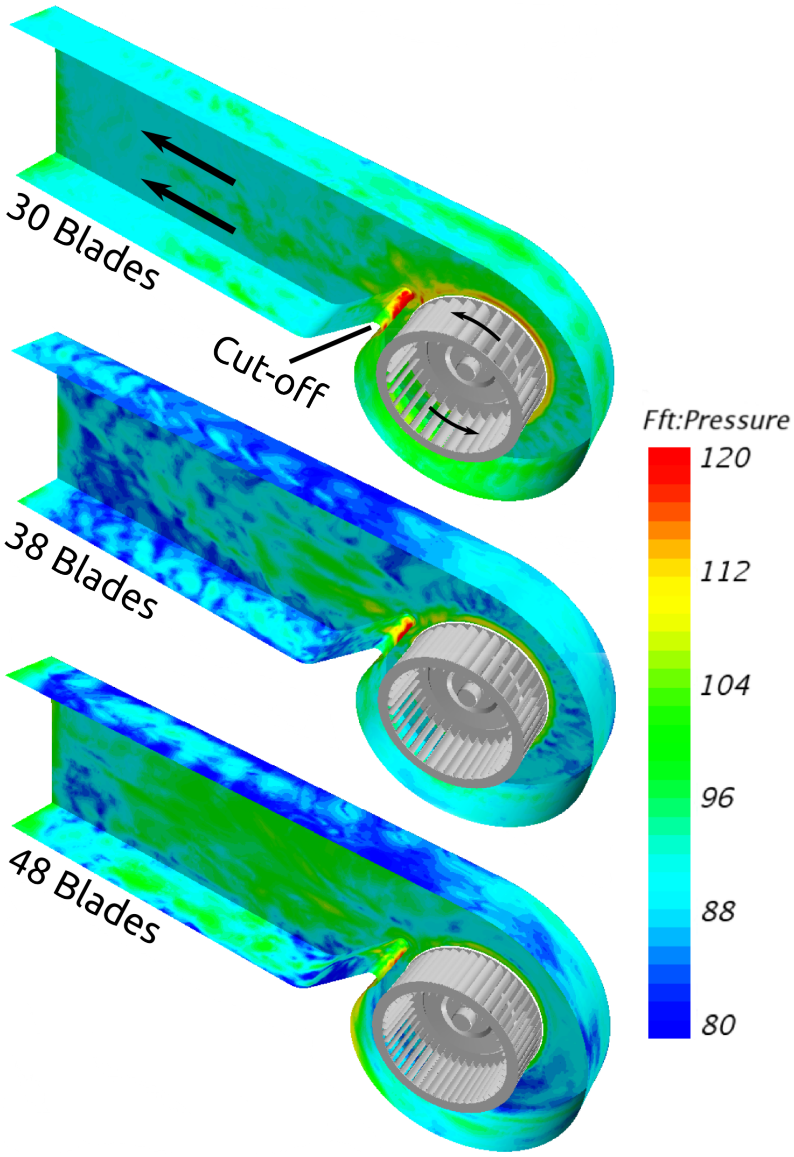

Figure 4.21: Sound pressure level radiated in the range of 100-1000 Hz from the housing of the fans with various impellers. Results are obtained from DES on numerical grids ranging from approximately 11 million (30 blade impeller) to 13 million (48 blade impeller) cells.

The noise radiated from the pressure side of the blades should be mainly due to the interaction between this side of the blades and the incoming flow. It is observable that this interaction is more intensive near the shroud and increases with the number of blades. Figure 4.21 depicts the sound pressure level radiated from the housing of the fan.

According to the SPL spectra shown in Fig. 4.19, increasing the number of blades reduces the tonal noise of the fan. This trend is clearly observable when comparing the SPL distribution on the cut-off surface of different models. Figure 4.21 reveals also that among the configurations shown, the housing of the reference model (i.e., with 38 blades) has on average the lowest level of broadband noise.

4.3.2 Different Blade Outlet Angles

Changing the outlet angle of the impeller blades is the second modification investigated in this study. All the impellers have 38 blades and a blade inlet angle of $\beta_1 \approx 77°$. Figure 4.22 shows the effect of this modification on the aerodynamic performance of the fan. It appears that the effect of changing the outlet angle is similar to those of changing the number of blades. The trend is quite straightforward: increasing the outlet angle leads to a higher pressure rise and torque across the whole operating range, and vice versa.
In the low to mid-range flow rates changing the outlet angle does not considerably affect the static efficiency of the fan, whereas the ensuing effects in the higher range are significant, and the impellers with larger outlet angles show a better performance. Moreover, according to Fig 4.23, which depicts the magnitude of the relative velocity in the channels of the corresponding impellers at the BEP of the fan, it is observable that the flow separation zones, whose formations in the impeller channels are completely unavoidable, become contracted as the the blade outlet angle becomes larger. This is essentially a favorable trend from both aerodynamics and aeroacoustics points of view, and presumably one the reasons that the impellers with wider outlet angles demonstrate a better performance.
Modifying the blade's outlet angle changes the angle of attack at which the flow impinges the cut-off surface, and affects the tonal noise generation of the fan. The sound spectra predicted by numerical simulations are shown in Fig. 4.24. Apparently, the effects of changing the outlet angle is not as significant as changing the number of blades. However, it is interesting to see that there is one outlet angle (i.e., β_2=160°) which produces a louder tonal noise. According to the results obtained making the outlet angle larger or smaller than 160° reduces the tonal noise of the fan. Nonetheless, this trend is only valid in the limited range of the angles investigated here, and it is reasonable to expect that making the outlet angle much smaller, either makes the fan significantly louder or has a double-edged effect, noise reduces negligibly but the aerodynamic performance considerably.

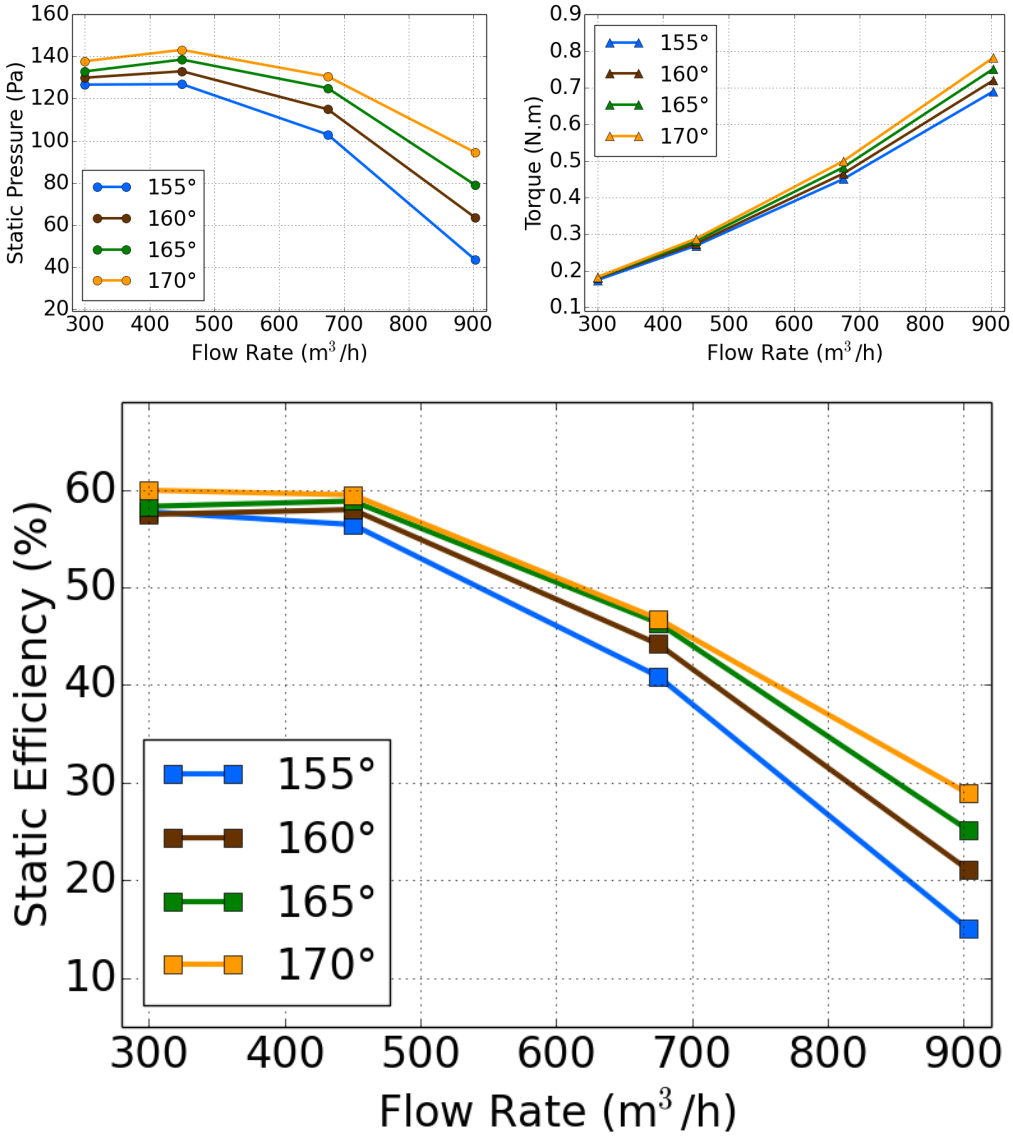

Figure 4.22: The effect of changing the outlet angle of the impeller blades on static pressure (left), torque (right) and static efficiency (bottom) of the fan. Results are obtained from RANS simulations on a numerical grid with approximately 12.5 million cells.

Although varying the blades outlet angle does not appear to be very advantageous herein, it certainly shows the potential benefits of such a modification, specially in cases where the fan design is not optimal and demands vigorous enhancements. The transient surface of the models with different outlet angles can be found in Appendix A.12.

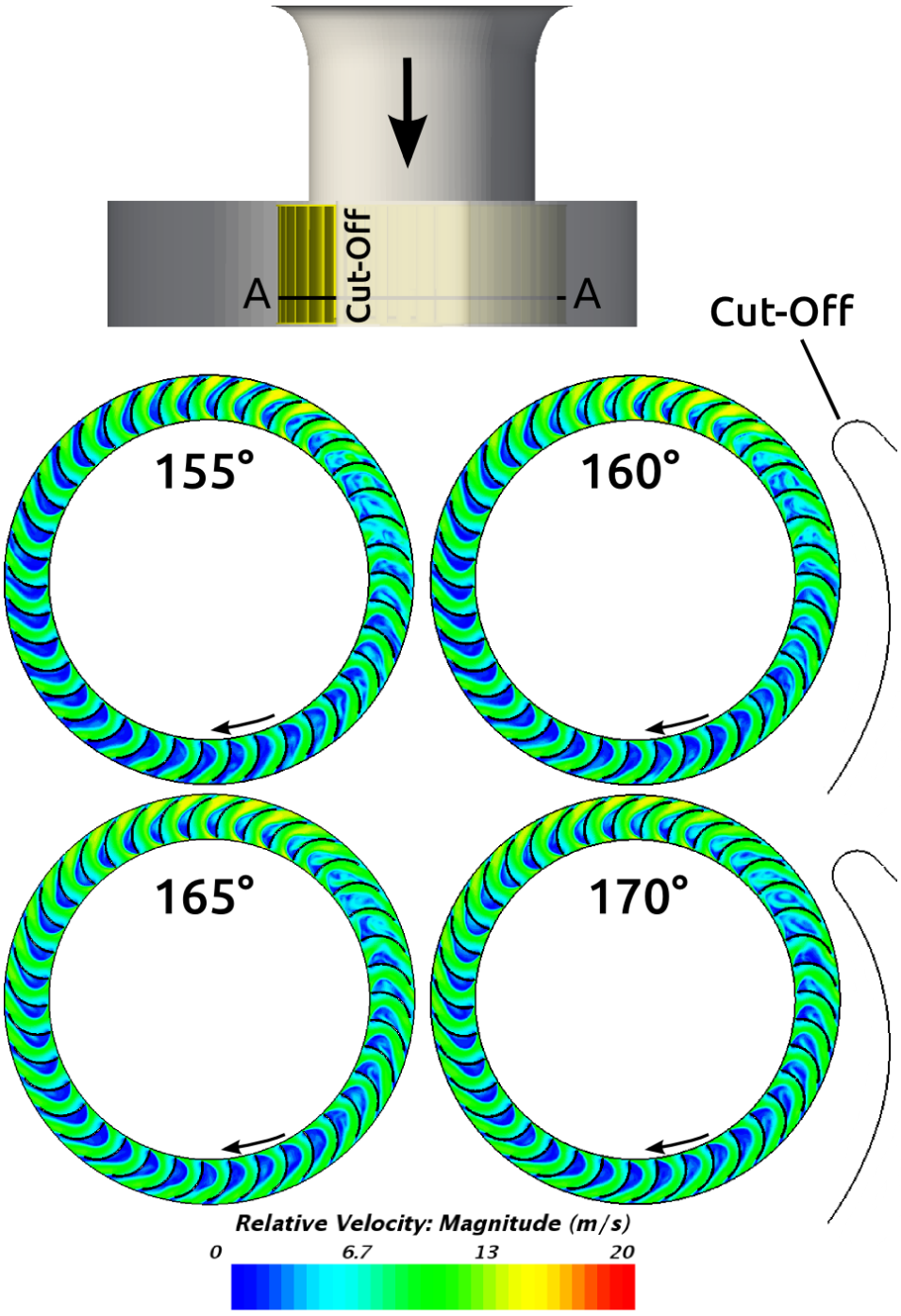

Figure 4.23: Relative velocity in the channels of the impellers with different outlet angles. The size of the flow separation between the blades becomes smaller as the outlet angle becomes larger. Results are obtained from DES simulations performed at the BEP of the fan on a numerical grid with approximately 12.5 million cells (i.e., DES_12.5M).

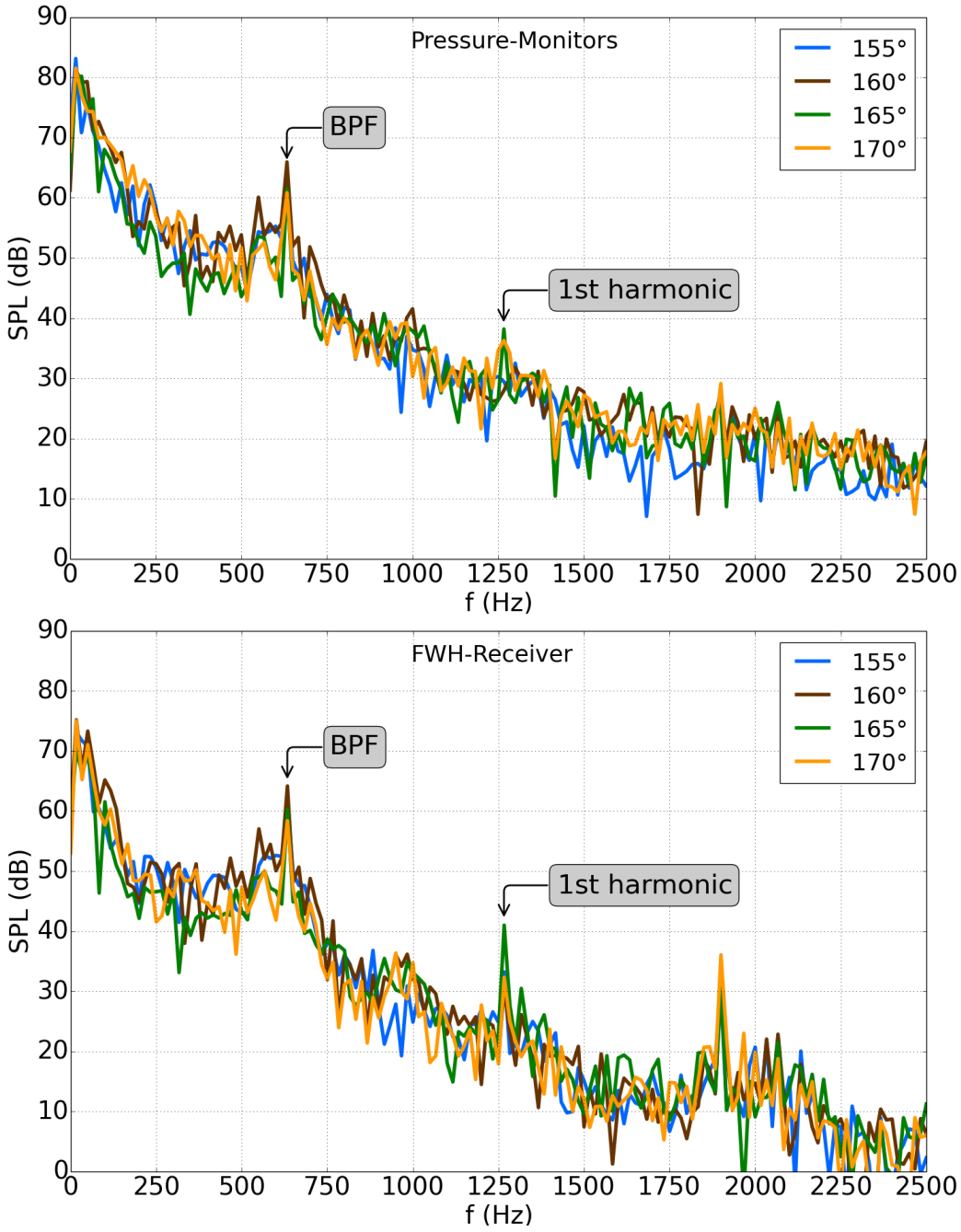

Figure 4.24: Spectral noise analysis of the impellers with various blade outlet angles. The impellers have 38 blades and f=633 Hz is the blade passing frequency. Results are obtained from DES simulations performed at the BEP of the fan on a numerical grid with approximately 12.5 million cells (i.e., DES_12.5M).

4.3.3 Different Cut-Off Shapes

In order to study the effects of different cut-off (volute tongue) shapes on the noise and performance of the fan, experimental measurements and numerical simulations are performed for various geometries. According to the non-uniform distribution of sound pressure level at the cut-off obtained from numerical transient surface data at the blade passing frequency of the fan (shown in Fig. 4.13 and 4.29), it is hypothesized that changing the cut-off geometry can be an effective method to reduce the tonal noise component of the fan.

In the interest of investigating the hypothesis mentioned, the volute tongue (cut-off) geometry is split into different segments with various heights. These geometries are termed *"stepped tongues"* and designated according to the description given in Section 2.1 (see Fig. 2.2 & 2.3). The abbreviation LHLH for instance, denotes the relative position of each segment, from the hub side toward the shroud side (L stands for low and H for high).

In a single-stepped tongue, in the form of LHHH for instance, only one segment has a different height comparing to the reference cut-off, while in a double-stepped tongue, e.g. LHLH, the heights of two segments differ from the reference height. In the patterns obtained from monitors installed on the reference cut-off geometry (Fig. 4.25), it can be observed that the curves are in-phase condition. This is due to the fact that first, the entire cut-off is parallel to the blade passing by, and second, the trailing edge of the corresponding blade has entirely the same view of the cut-off. Therefore, any modification that changes the phase of the corresponding pressure curves, conceptually has the potential to affect the tonal noise of the fan.

Although clear, it should be emphasized that not all of the phase-shifts yield a noise reduction. In fact, only a destructive phase-shift is capable of providing noise cancellation effects, whereas an improper phase-shift may increase the noise level.
It should also be noted that a modification can only be considered as "effective", only if it yields changes in the sound pressure level that are beyond the measurement uncertainties. This makes evaluating the effectiveness of stepped-tongues quite difficult, since in many cases, as subsequently will be seen, the resulting changes in the sound pressure level do not exceed the measurement uncertainty range.

Different standing combinations of the cut-off segments are comprehensively investigated to find out whether it is feasible or not to generate a phase-shift

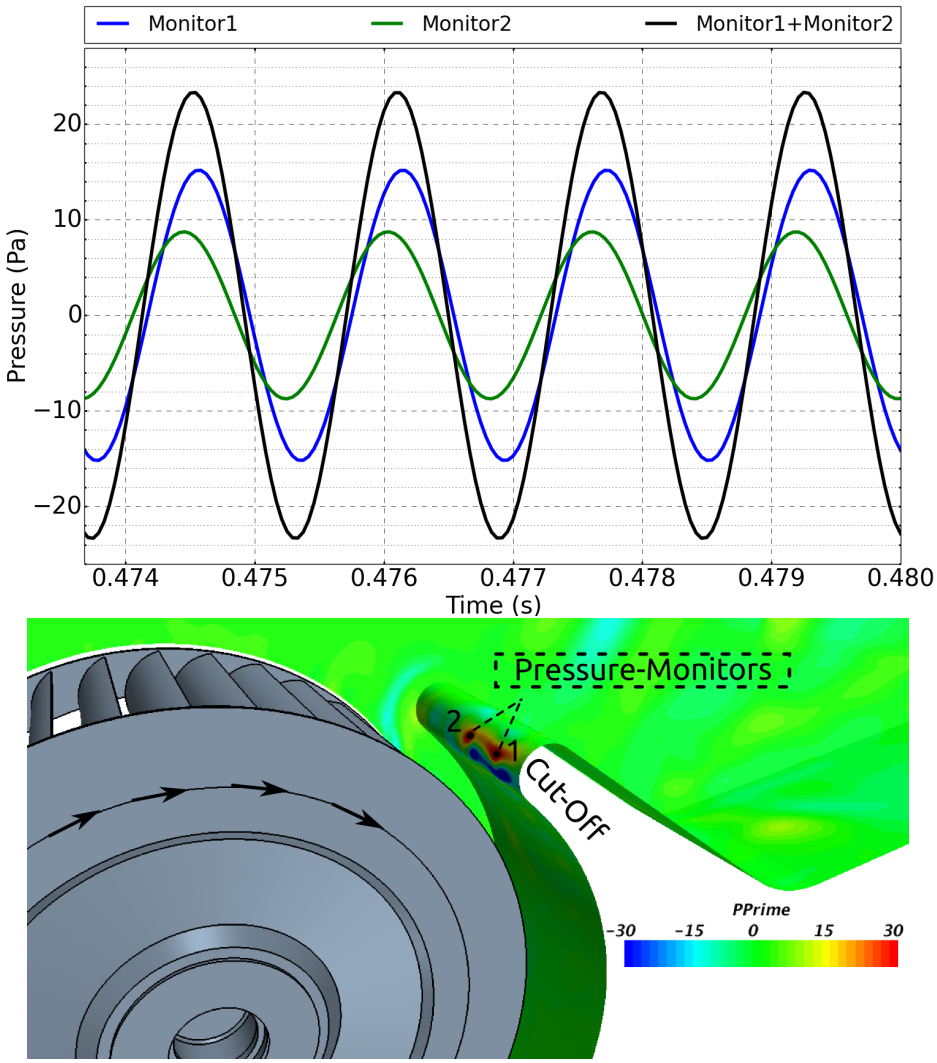

Figure 4.25: The pressure patterns (top) obtained from the monitors installed on the reference cut-off at the positions displayed (bottom). It is evident that the curves are "in-phase" condition. Results are obtained from DES on a numerical gird with approximately 12.5 million cells (i.e., DES_12.5M).

between the adjoining segments and reduce the tonal noise. The heights of the cut-off segments correspond to the circumferential distance between the impeller blades. Accordingly, the height difference in the 8.25 mm stepped tongues (e.g., LHLH_8.25_10_16) is equal to half a blade-to-blade spacing, while the 16.5 mm tongues have a height difference that equals exactly the space of one impeller channel or blade pitch (i.e., $\pi D_2/z$).

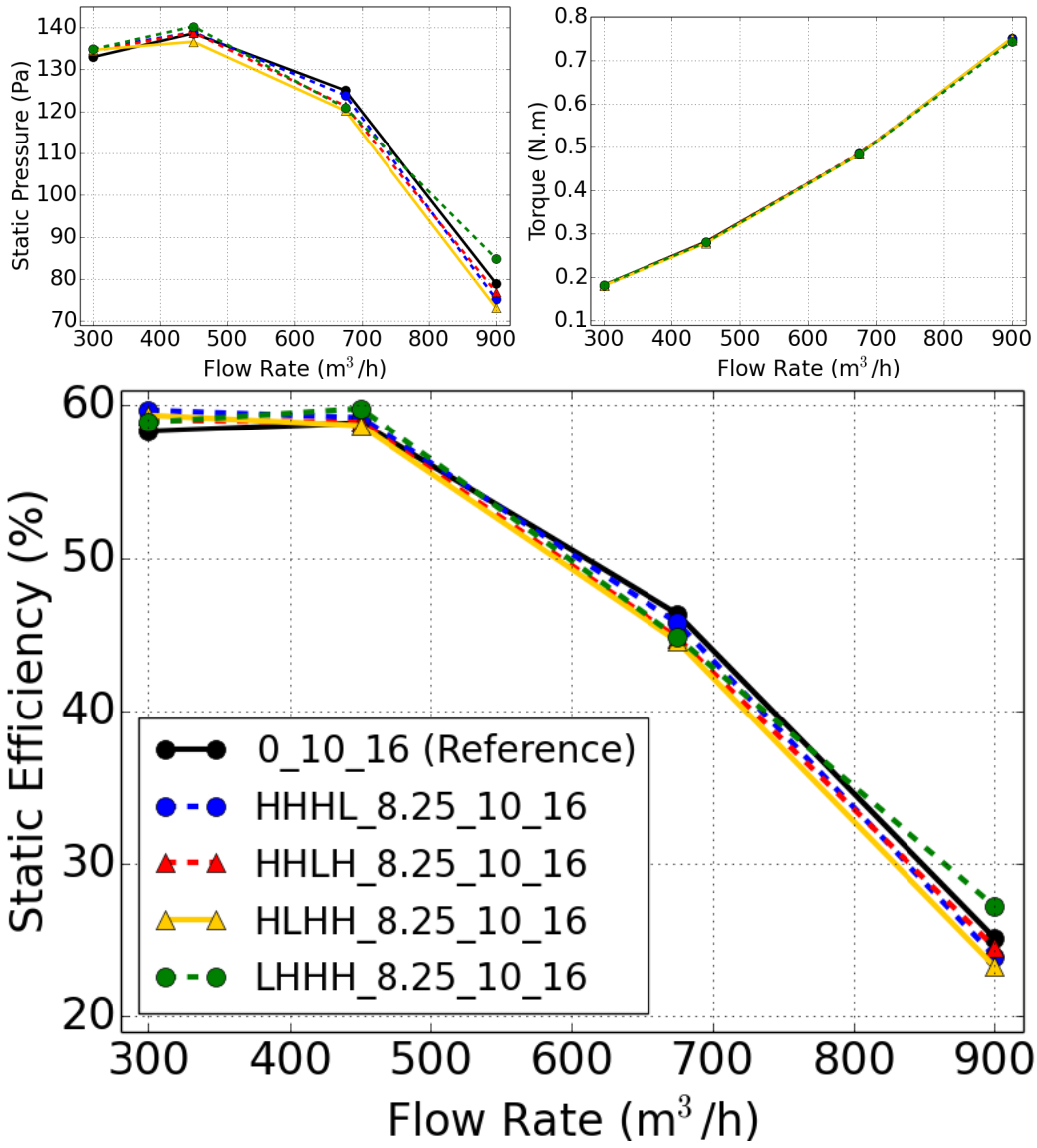

Figure 4.26: Comparison between the performance characteristics of the single stepped tongues and the reference model. Results from RANS simulations on a numerical grid with approximately 12.5 million cells.

The clearance between impeller and volute tongue, i.e. approximately 16 mm, remains deliberately unchanged throughout the study.
Figure 4.26 shows the comparison between the performance curves of the reference model and the single stepped tongues obtained from RANS_12.5M simulations. It is noticeable that the single stepped arrangements have performance characteristics comparable to the reference model.

Torque remains nearly unchanged for various models, and the curves are apparently superimposed at most of the operating points. The HLHH and LHHH arrangements produce a lower pressure rise and consequently have a lower static efficiency at most of the operating points. The maximum efficiency loss of the HLLL arrangement is approximately 7% at 900 m^3/h. However, at the same flow rate the LHHH arrangement demonstrate a better performance comparing to the reference model.

The cumulative A-weighted sound pressure levels of the single stepped tongues are depicted in Fig. 4.27. The corresponding results show the sum of the sound pressure levels measured at four different operating points of the fan, i.e. 250, 350, 450, and 550 m^3/h. Remarkable differences are observable in the broadband noise levels of different cut-off configurations. Most of the 8.25 mm stepped tongues have a higher broadband noise level comparing with the reference cut-off. The only exception is HHHL_8.25_10_16 configuration that demonstrates a lower level across the entire frequency range. On contrary, the highest noise level belongs to the LHHH_8.25_10_16 arrangement, indicating that stepping the cut-off on the shroud-side has a positive effect on the broadband noise level, whereas the same modification on the hub-side increases the noise. The 16.5 mm single stepped tongues follow the same pattern as the 8.25 mm tongues. The only notable difference is in the noise level of the HHHL_16.5_10_16 cut-off, which is accordingly very close to the reference cut-off model.

Figure 4.28 depicts the sum of A-weighted sound pressure levels at the blade passing frequency (i.e, 633 Hz) and its first harmonic (i.e., 1266 Hz) of the single stepped cut-off configurations. The black horizontal line in each bar indicates the sound pressure level at 1266 Hz. The level of each bar, to a great extent, is dominated by the the sound pressure level at the blade passing frequency, due to its considerably higher level, and the SPL at the first harmonic does not change the general trend of the results. However, since the changes in the sound pressure level at the first harmonic are significant for some of the cut-off configurations, the corresponding levels are also explicitly shown.

According to Fig. 4.28, at 250 m^3/h, all of the single stepped tongues increase the tonal noise level at both the BPF and its first harmonic. The increase in the noise level is more prevailing in the case of the 16.5 mm tongues.

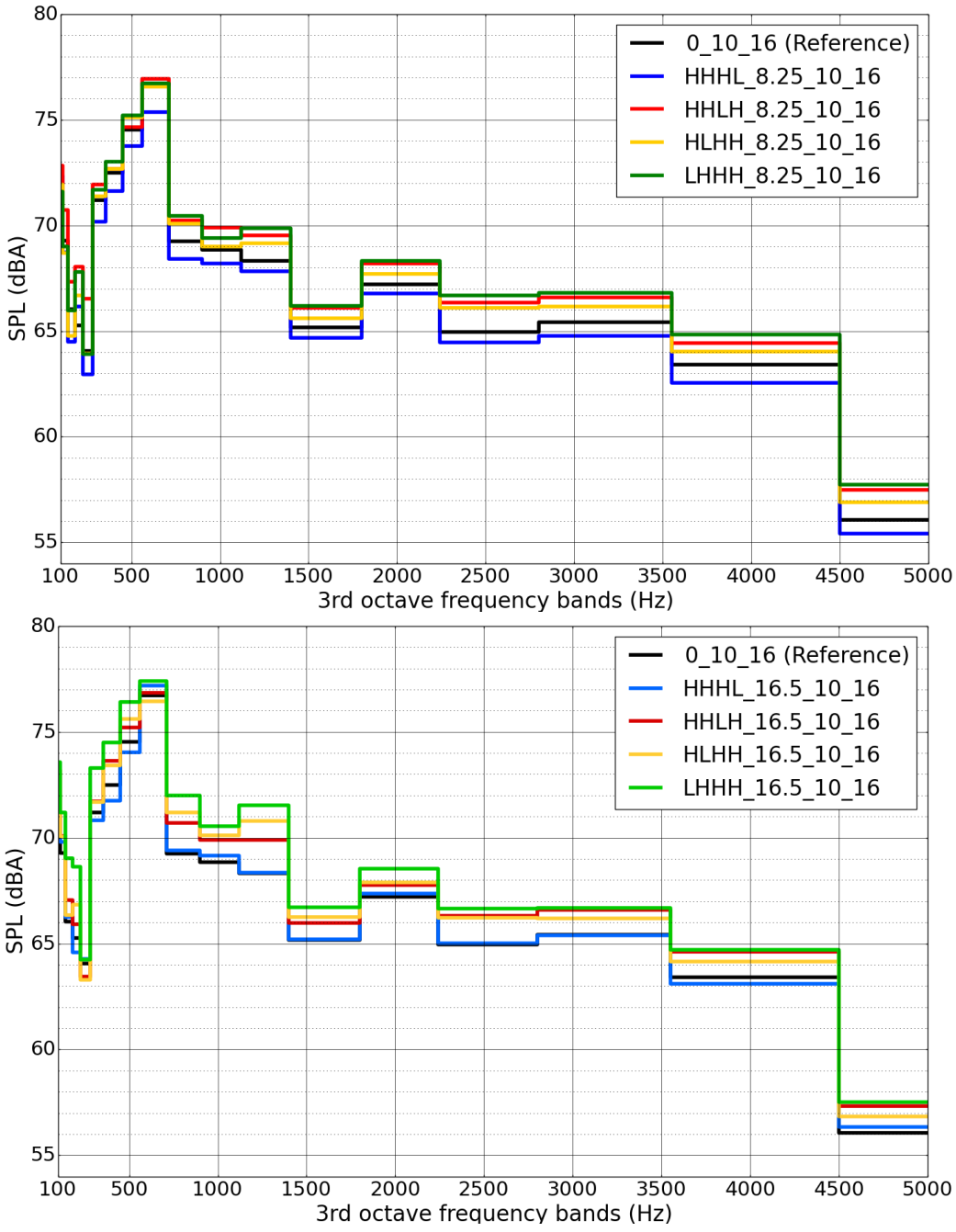

Figure 4.27: The cumulative A-weighted sound pressure levels of the single stepped volute tongues with half a blade-to-blade height difference (top) as well as one blade passage height difference (bottom). Results are obtained from experimental measurements using the in-duct method.

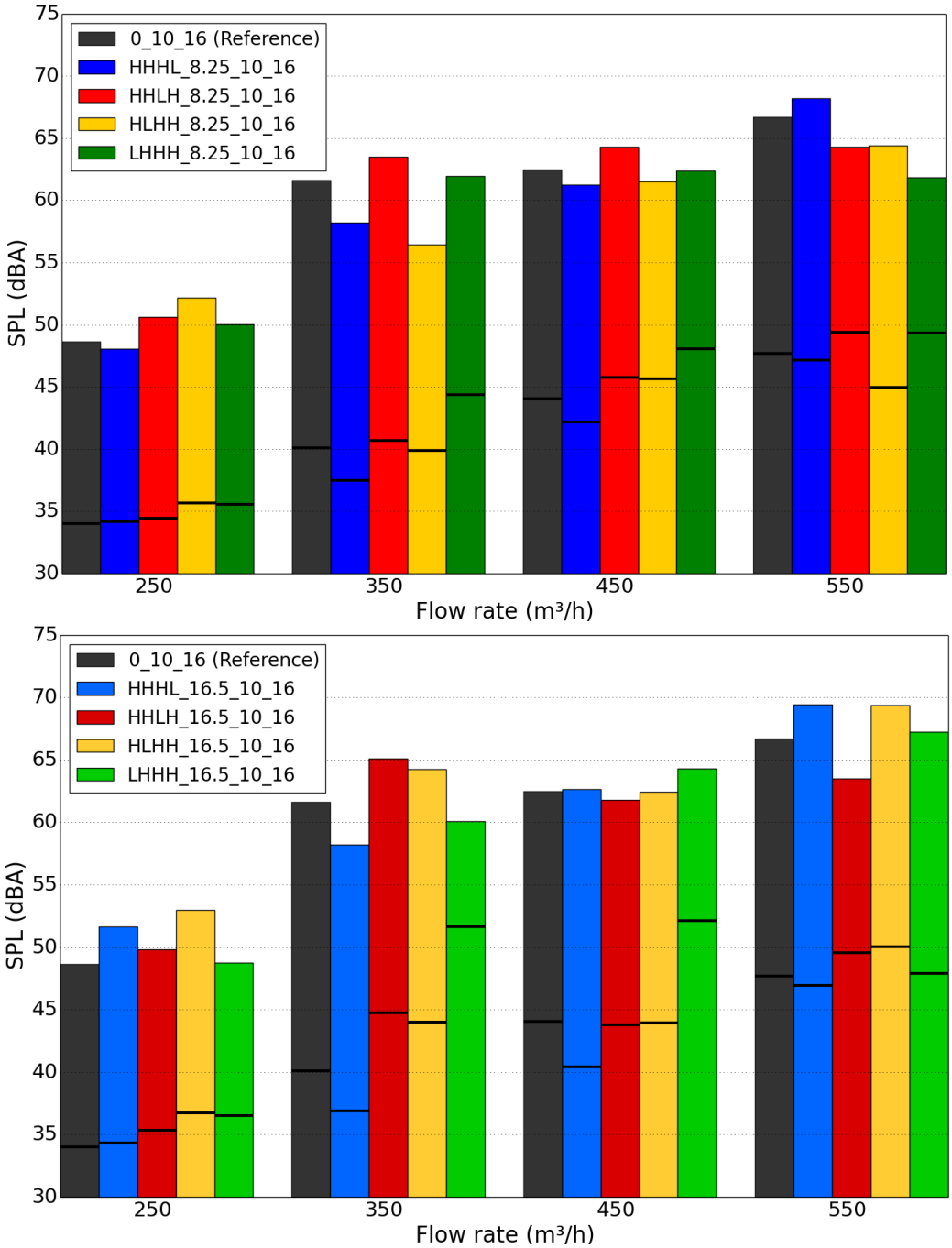

Figure 4.28: The sum of the sound pressure levels at the blade passing frequency and its first harmonic of the single stepped tongues at different operating points. The black horizontal line in each bar indicates the sound pressure level at the first harmonic of the BPF. Results are obtained from experimental measurements using the in-duct method.

The HHHL is the arrangement which effectively reduces the tonal noise level at the BPF and its first harmonic at 350 & 450 m^3/h. Moreover, at the same flow rates, it is the only arrangement that does not increase the noise level at 1266 Hz (i.e., the first harmonic of the BPF). The effectiveness of the HHHL tongue in reducing the noise level is not fully understood, since based on the numerical results shown in Fig. 4.29, near the best efficiency point of the fan, the pressure fluctuation on the hub-side is considerably higher than on the shroud-side. Moreover, at the same operating point, the last portion of the cut-off surface, i.e. on the shroud side, is in front of the in-active region of the impeller that means the flow rate on the corresponding side is considerably lower than the other side. Consequently, the reduction in the noise level of the HHHL arrangement might be related to the measurement uncertainties.

The HHLH arrangement, in its both forms, does not appear to be effective, and its tonal noise levels are either higher than or approximately equal to the reference model. The only operating point at which this arrangement shows some reduction in the tonal noise level is 550 m^3/h. This effectiveness is due to the fact that at higher flow rates, a greater portion of the cut-off surface contributes to tonal noise generation. The same reason is true for the effectiveness of the LHHH_8.25_10_16, and the HLHH_8.25_10_16 at 550 m^3/h. A comparison of the transient surface data of the reference model obtained at the BEP of the fan with an operating point in the overload range is shown in Appendix A.13.

At 250 m^3/h, the HLHH arrangement increases the tonal noise level more than the other arrangements. However, at the other operating points, the 8.25 mm form of the HLHH tongue reduces the tonal noise level, and its effect is more pronounced at 350 & 550 m^3/h, while at the same operating points its 16.5 mm configuration increases the tonal noise level.

The LHHH_8.25_10_16 results only show a notable reduction in the noise level at 550 m^3/h, while the changes at the other operating points are within the uncertainty range of the measurements. Although there is a small reduction in the total noise level of the LHHH_16.5_10_16 arrangement at 350 m^3/h, there is a considerable increase in the SPL at the first harmonic. The same is true at the best efficiency point of the fan (i.e., 450 m^3/h) except the reduction in the total noise level.

In addition to the experimental measurements, numerical simulations are performed for the HLHH_8.25_10_16 as well as the LHHH_8.25_10_16 arrange-

ments. According to the simulation results summarized in Tab. 4.4, the tonal noise of the corresponding arrangements are approximately 6 dB lower than the reference model. However, due to several reasons, the corresponding noise reduction is not reasonable. First, the experimental results do not approve such an effective noise cancellation. Second, the results obtained from pressure monitors installed on each segment of the cut-off (see Fig. 4.30) indicate that at the blade passing frequency, it is the LHHH arrangement that is capable of generating a more destructive phase-shift. There is also a phase-shift evident in the HLLL pressure patterns, yet it is not as effective as the corresponding LHHH arrangement. This means, if the noise reduction should be related to the phase-shift generation, the tonal noise of the LHHH should be lower than HLLL, which is not the case. Third, from comparing the transient surface data of the corresponding arrangements with the reference cut-off (see Fig. 4.29), it can be inferred that the noise level of the LHHH arrangement is comparable to the reference model and there is no indication of noise reduction.

In order to make sure that the turbulence modeling approach used for the simulations of the single stepped tongues (i.e., DES_12.5M) is not the source of the difference between the numerical and experimental results, a URANS_12.5M simulation is performed for the LHHH_8.25_10_16 arrangement. The tonal noise predicted by the corresponding URANS simulation is approximately 3 dB lower than the reference URANS simulation. This confirms the effectiveness of the LHHH_8.25_10_16 as predicted by DES_12.5M. The reason why the performed numerical simulations overestimate the noise cancellation ability of the single stepped tongues remains unclear. However, in the case of the double stepped tongues, as subsequently will be seen, the numerical simulations can predict the experimental trend.

Table 4.4: Comparison of the tonal noise levels (in dBA) at the BEP of the fan obtained from the numerical simulations (DES_12.5M) and the experimental measurements for the single stepped cut-off arrangements.

Cut-Off	**Experimental Result**	**Numerical Results**	
		Pressure Monitors	FW-H
0_10_16 (Reference)	62.7	59.4	58.3
HLHH_8.25_10_16	61.5	53.3	51.9
LHHH_8.25_10_16	62.2	52.7	51.7

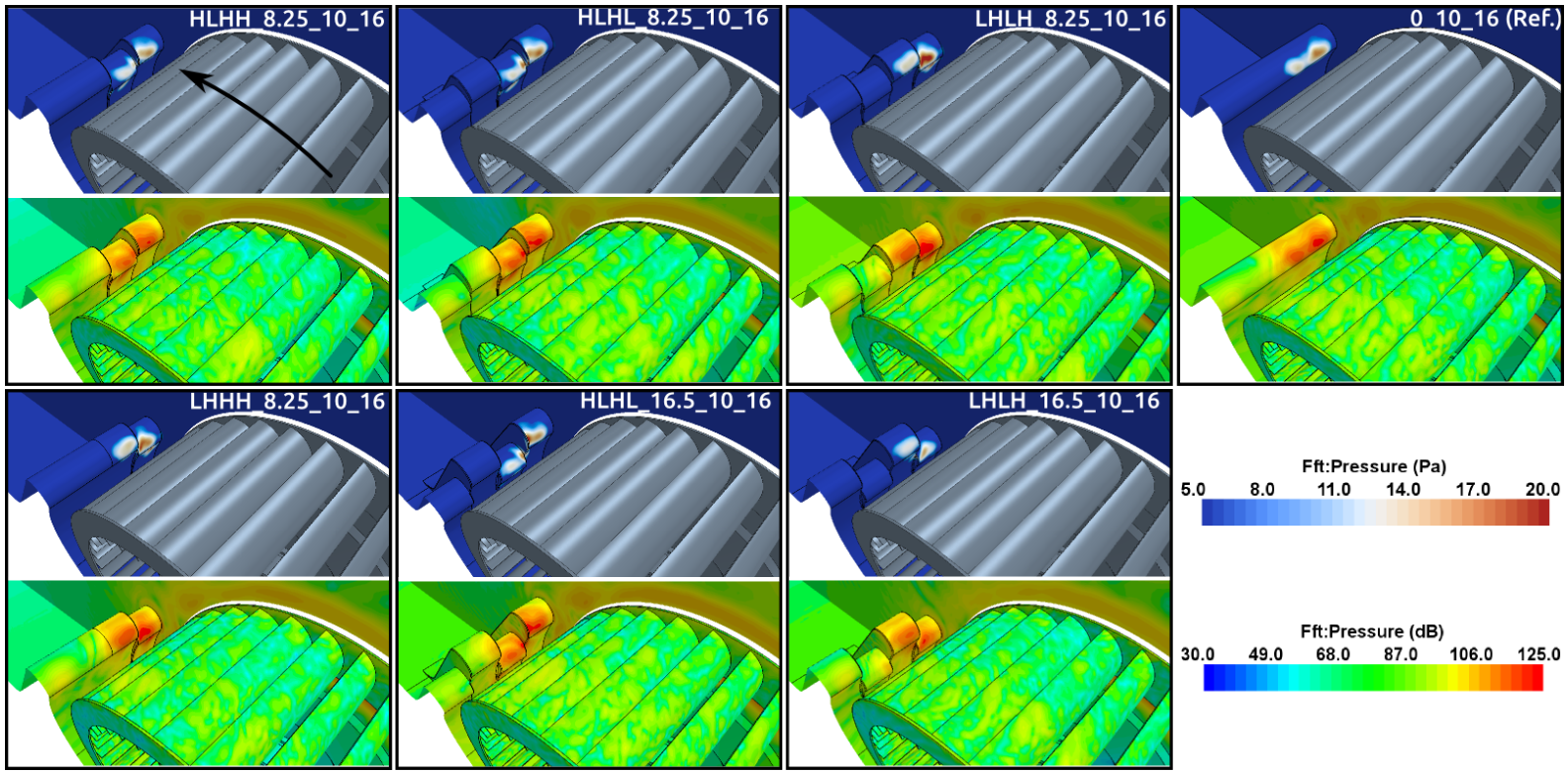

Figure 4.29: Transient surface data representing the pressure fluctuations and the sound pressure levels of different cut-off configurations at the blade passing frequency (i.e., 633 Hz) obtained from DES_12.5M simulations performed at the BEP.

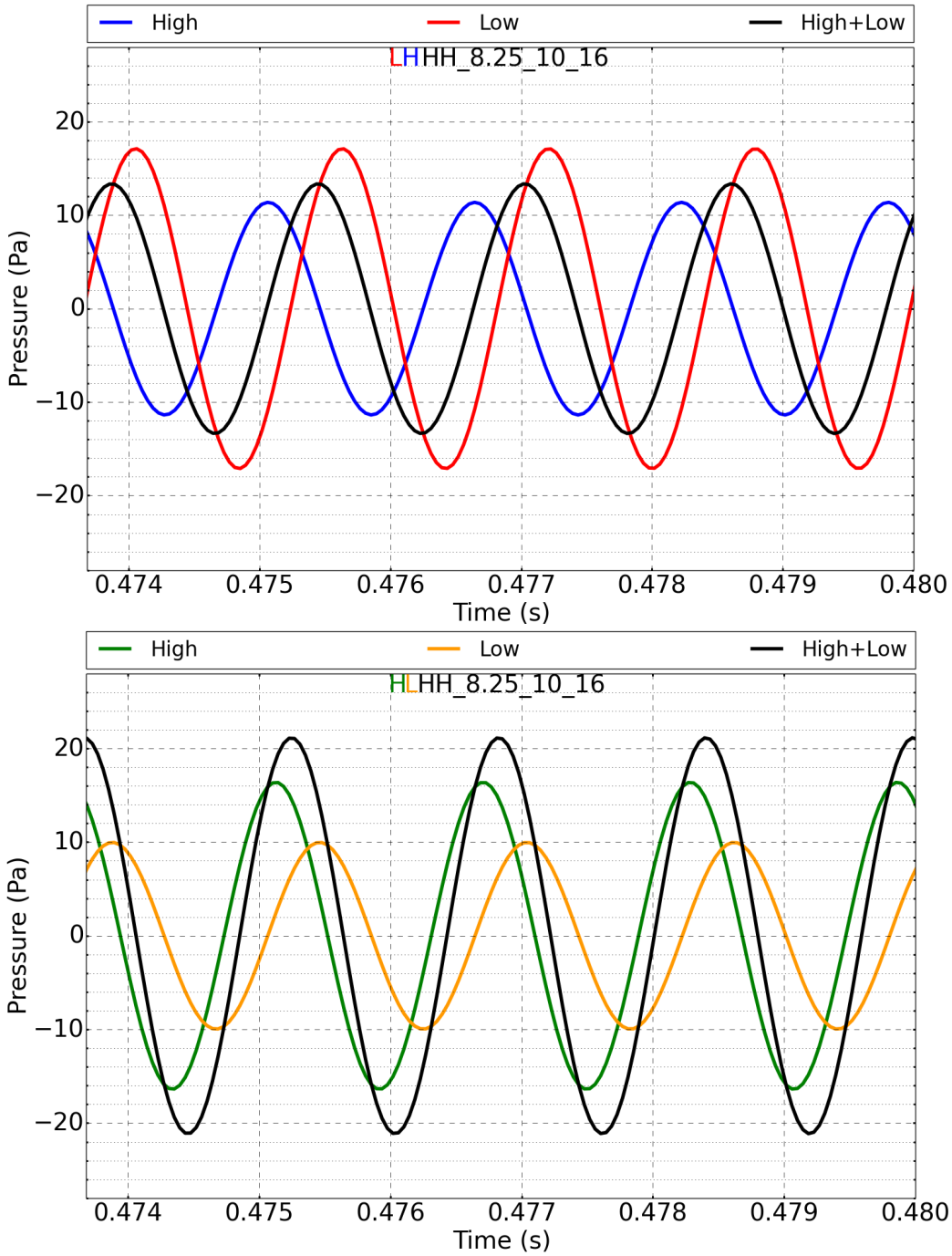

Figure 4.30: The patterns obtained from pressure monitors installed on the hub-side segments of the LHHH_8.25_10_16 (top) and HLHH_8.25_10_16 (bottom) configurations. It is evident that the LHHH arrangement is more competent in generating a destructive phase-shift. Results are obtained from DES performed on a numerical grid with 12.5 million cells (i.e. DES_12.5M).

The stepped tongues featuring a different height in two segments (namely double stepped-tongues) are also investigated in this study. The comparison between the characteristic curves of the LHLH and HLHL arrangements and the reference cut-off is shown in Fig. 4.31. As can be seen, the pressure rise of the fan is more likely to be influenced by double stepping the cut-off, whereas the changes in the torque are negligible. It is also evident that the LHLH tongues have a stronger influence (i.e., negative at most of the operating points) on the performance characteristics of the fan.

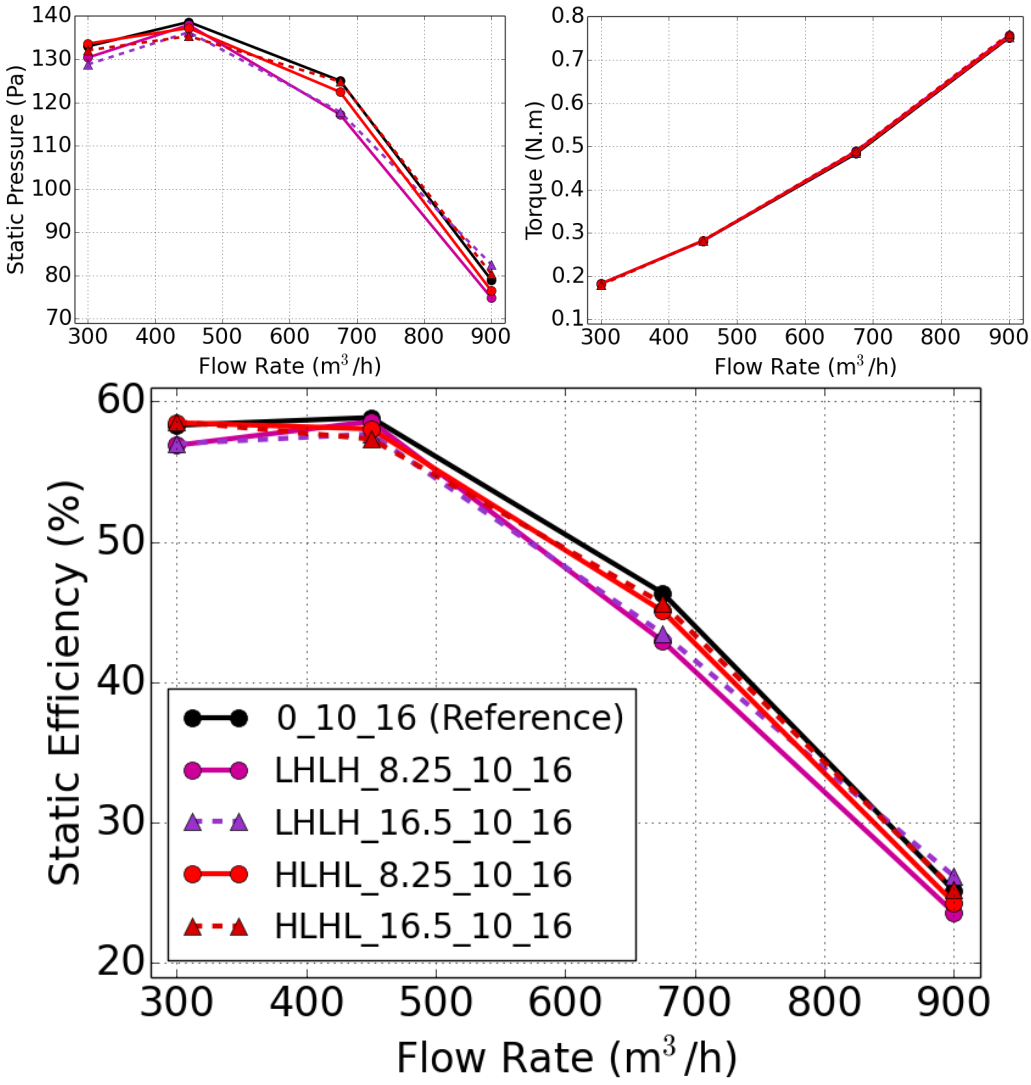

Figure 4.31: Performance characteristics of the LHLH and HLHL arrangements in comparison with the reference cut-off. Results are obtained from RANS simulation on a numerical grid with approximately 12.5 million cells.

Figure 4.32 depicts the cumulative A-weighted sound pressure levels of the double-stepped tongues in comparison with the reference cut-off. There is one possible arrangement, i.e. LLHH_16.5_10_16, which is not included in the comparison; the reason is the significant performance loss caused by the corresponding arrangement. In fact, the effect of this cut-off arrangement is so significant on the performance of the fan, that with a fully open throttle, only a maximum flow rate of 350 m^3/h is obtainable.

According to Fig. 4.32 all of the double-stepped tongues increase the broad-band noise level . However, this increment is more evident in the case of the 16.5 mm tongues. It is also interesting to note that across the whole frequency range, the HLHL_8.25_10_16 tongue has a coherent trend comparing to the reference tongue, while its mirrored arrangement, i.e. LHLH_8.25_10_16, has the highest noise level in most of the frequency bands.

In the case of the 16.5 mm tongues, the HHLL result remains comparatively closer to the reference SPL in most of the frequency bands, while the deviation level is higher in the case of the other arrangements.

The sum of the noise levels of each tongue at the blade passing frequency and its first harmonic is shown in Fig. 4.33. As can be seen, at 250 m^3/h the levels are comparable to the level of the reference cut-off, and none is able to effectively reduce the tonal noise of the fan. The HLLH_8.25_10_16, and the LHLH_16.5_10_16 are the arrangements which demonstrate the highest tonal noise levels at the corresponding flow rate.

At 350 m^3/h, the only arrangements showing a notable change in the noise level are LHHL_8.25_10_16 and HLHL_8.25_10_16. The former increases the noise level, while the latter considerably reduces it. At the same flow rate, most of the 16.5 mm tongues increase the sound pressure level. At the best efficiency point of the fan (i.e. 450 m^3/h), only the HHLL_8.25_10_16 and HLHL_8.25_10_16 arrangements are capable of to effectively reducing the tonal noise level. Moreover, it is an interesting observation that the HLHL arrangement, which is helpful in its 8.25 mm form, has completely the counter effects in its 16.5 mm form and increases the tonal noise level.

The LHHL_16.5_10_16 tongue considerably increases the noise level at 1266 Hz; this is completely in agreement with the previously observed trend of its single stepped analogous tongue, i.e. LHHH_16.5_10_16. Apparently, making a 8.25 mm step on the hub-side leads to a SPL increment at the first harmonic when the fan operates near the best efficiency point.

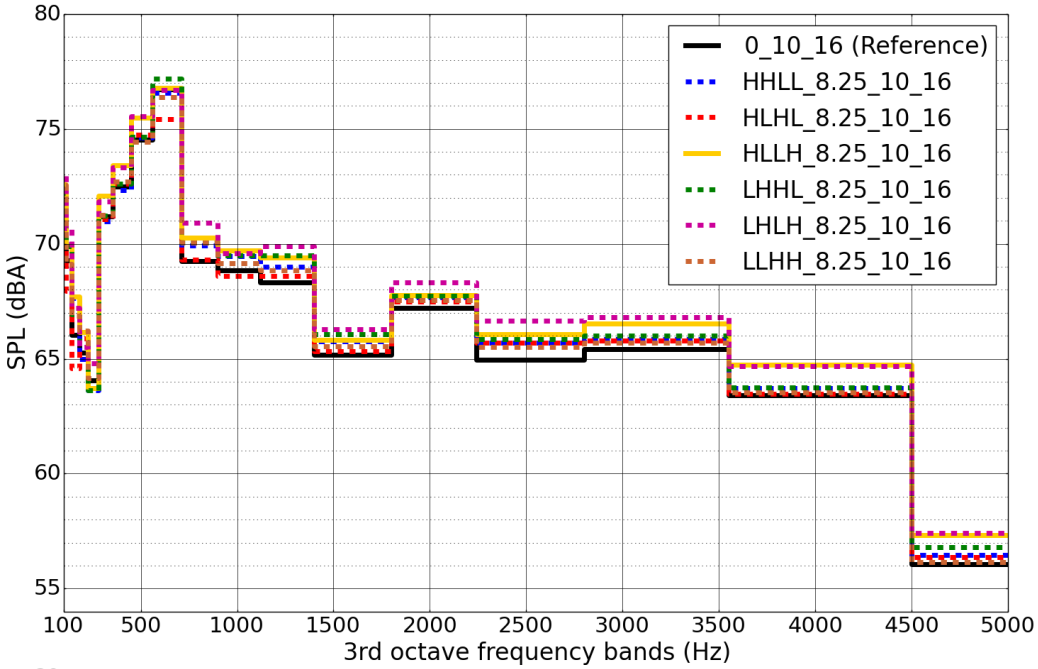

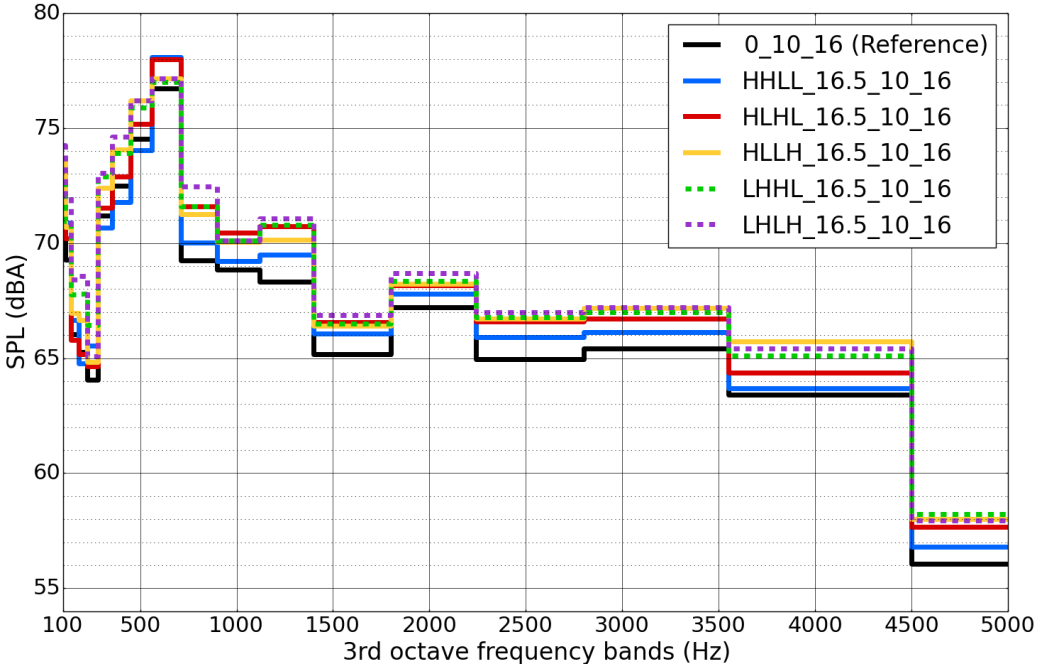

Figure 4.32: Comparison of the cumulative A-weighted sound pressure levels of the double-stepped volute tongues with half a blade-to-blade height difference (top) as well as one blade passage height difference (bottom). Results are obtained from DES performed on a numerical grid with 12.5 million cells (i.e. DES_12.5M).

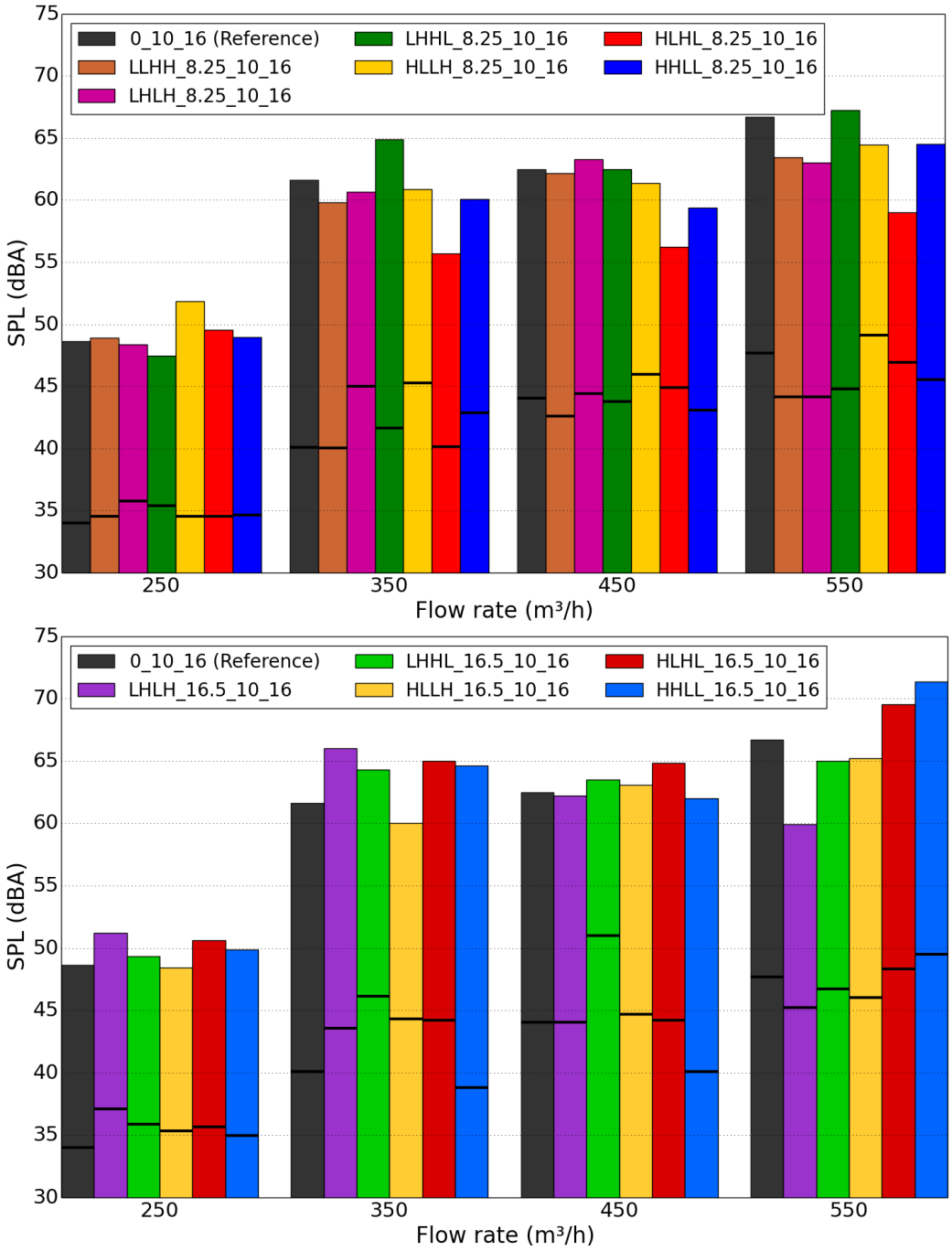

Figure 4.33: The ability of the double stepped cut-off arrangements in reducing the tonal noise of the fan. Each bar shows the sum of the noise level at the blade passing frequency and its first harmonic, and the black line in each bar shows the noise level at 1266 Hz. Results are obtained from DES performed on a numerical grid with 12.5 million cells (i.e. DES_12.5M).

Two double-stepped arrangements appear to be effective at 550 m^3/h, namely the HLHL_8.25_10_16, and the LHLH_16.5_10_16, while the other arrangements are either louder than the reference level, or their corresponding changes are within the measurements uncertainty range. Altogether, the HLHL_8.25_10_16 is the double-stepped arrangement which remains effective at most of the flow rates and reduces the tonal noise level.

Nevertheless, it should be acknowledged that according to Fig. 4.33, except at 250 m^3/h, the noise levels of the HHLL_8.25_10_16 are always lower than the reference sound pressure levels. This arrangement divides the cut-off geometry into two halves that are separated by half a blade-to-blade difference in height. According to the literature survey of Neise [28], Yeow [36] postulated that using a similar cut-off arrangement should be effective in reducing the tonal noise level. However, this suggestion was never experimentally substantiated. Although the measurement results in this study acknowledge the effectiveness of the HHLL_8.25_10_16 arrangement in reducing the tonal noise level, due to several reasons this observation is perplexing. The first reason is also the keystone of the current section, which is several times addressed in the text: according to the numerical results (see Fig. 4.29), near the best efficiency point of the fan, the amplitude of the pressure fluctuations on the hub-side of the cut-off is considerably higher than those on the shroud-side. As a result, at the blade passing frequency, the hub-side of the cut-off is considerably louder than the other side. Keeping this in mind, for an effective tonal noise reduction through local pressure cancellation, the focus should be on the hub-side of the cut-off. Therefore, it is not justified how an arrangement in the form of HHLL can help to reduce the tonal noise of the fan, while its both segments on the hub-side have the same height as the reference cut-off. The second point that makes the behavior of the HHLL_8.25_10_16 arrangement confusing is the inability of its similar single stepped tongue, i.e. HHLH_8.25_10_16, in reducing the tonal noise level. Making a conclusive judgment about the HHLL_8.25_10_16 arrangement demands performing additional experimental measurements and numerical simulations.

Table 4.5 summarizes the results of DES_12.5M simulations performed for some of the double-stepped tongues. It can be seen that the numerical simulations can provide favorable results and reliably predict the trend of the experimental measurements. In general, the results obtained from pressure monitors are more accurate than FW-H predictions. However, both methods accurately predict the noise reduction of the HLHL_8.25_10_16 tongue.

Table 4.5: Comparison of the tonal noise levels (in dBA) at the BEP of the fan obtained from the numerical simulations (DES_12.5M) and the experimental measurements for the double stepped cut-off arrangements.

Cut-Off	**Experimental Results**	**Numerical Results**	
		Pressure Monitors	FW-H
0_10_16 (Reference)	62.7	59.4	58.3
HLHL_8.25_10_16	55.9	51.8	50.4
HLHL_16.5_10_16	64.8	59.4	55.6
LHLH_8.25_10_16	63.3	64.5	63.0
LHLH_16.5_10_16	62.2	59.8	56.3

Figures 4.34 & 4.35 depict the pressure patterns recorded by the pressure monitors installed on the cut-off in the numerical simulations (DES_12.5M). As can be seen in both figures, the double-stepped tongues with half a blade-to-blade height difference (8.25 mm) are capable of generating the desired phase shift effects, whereas the tongues with one blade passage height difference (16.5 mm) do not demonstrate a destructive phase-shift pattern. As a result, the pressure amplitude of the resulting wave in the 16.5 mm tongues is higher than the 8.25 mm tongues. There is an overestimation in the tonal noise level predicted by the numerical simulation of the LHLH_8.25_10_16 arrangement. According to Fig. 4.29, the excessive pressure fluctuations on the first segment of the cut-off (i.e. on the hub-side) is the major source of tonal noise in the corresponding arrangement. The pressure patterns recorded by the monitors installed at the cut-off help to further explain the underlying cause of the increase in the tonal noise level of the LHLH_8.25_10_16 tongue. In Fig. 4.34 & 4.35 it is noticeable that the LHLH arrangement is more capable than the HLHL arrangement in generating the desired phase-shift effects. However, both the experimental results and the sound pressure levels obtained from the transient surface data indicate that the HLHL arrangement has a lower tonal noise level. This suggests that generating a phase-shift between the cut-off segments is a useful method, yet not sufficient. In particular, when stepping the cut-off increases the pressure-fluctuations, as is the case for example in LHLH_8.25_10_16 arrangement, the tonal noise may become even higher, and the existing phase-shift between the segments cannot help to reduce it.

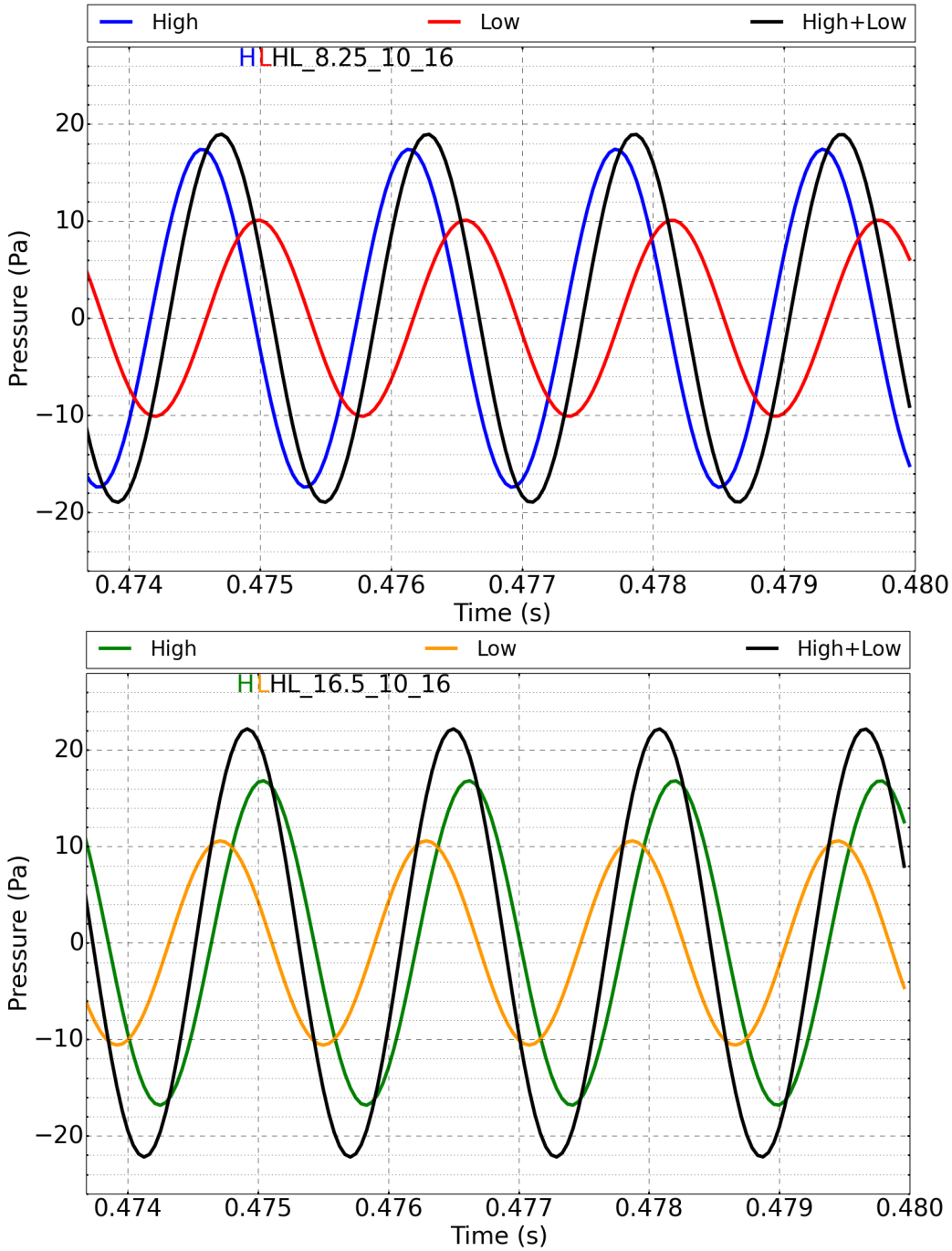

Figure 4.34: The pressure patterns obtained from the monitors installed on different cut-off segments of the HLHL_8.25_10_16 (top) and the HLHL_16.5_10_16 (bottom) at the blade passing frequency (i.e., 633 Hz). There is an evident phase-shift between the segments of the 8.25 mm arrangement. Results are obtained from DES performed on a numerical grid with approximately 12.5 million cells.

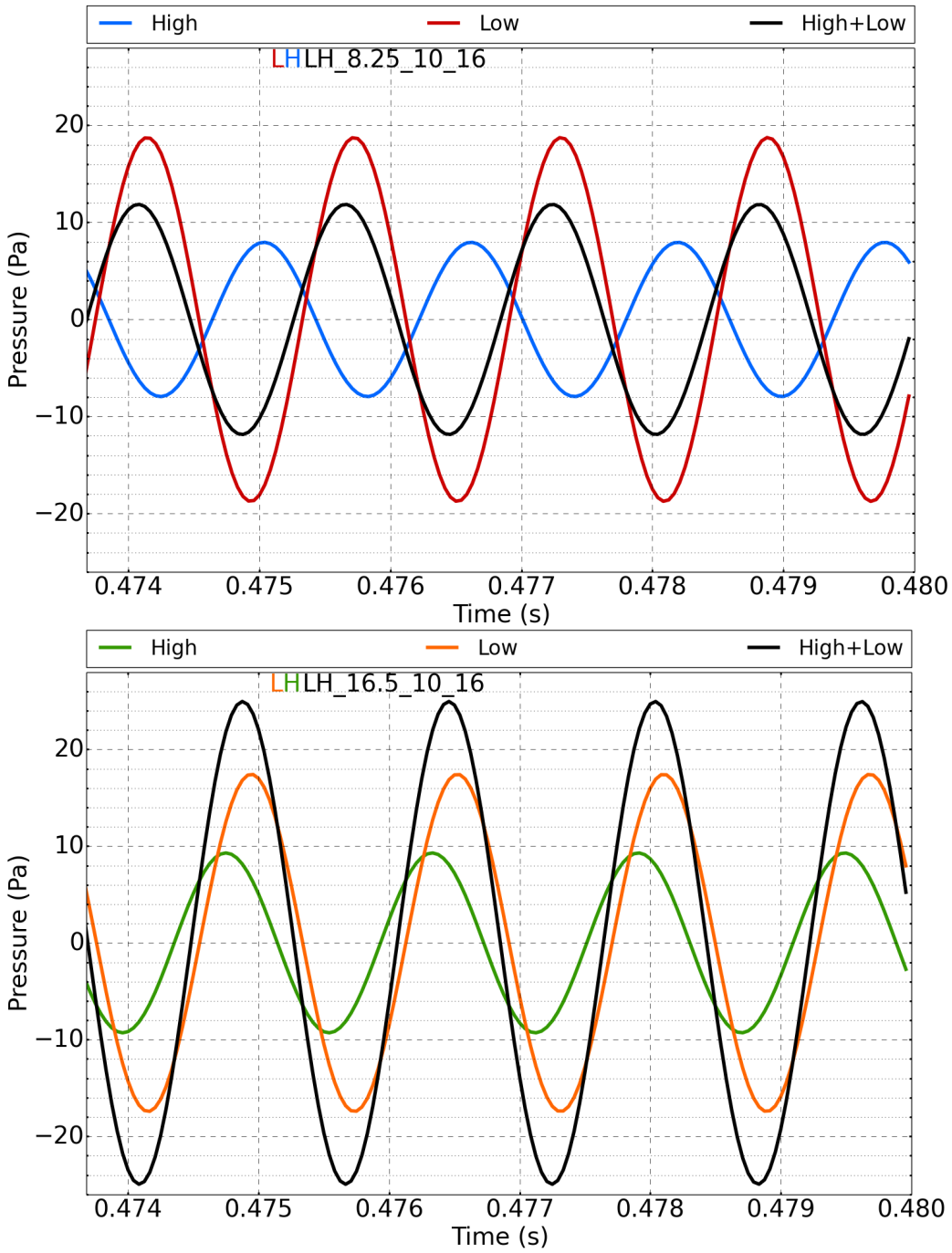

Figure 4.35: The pressure patterns obtained from the monitors installed on different cut-off segments of the LHLH_8.25_10_16 (top) and the LHLH_16.5_10_16 (bottom) at the blade passing frequency (i.e., 633 Hz). There is an evident phase-shift between the segments of the 8.25 mm arrangement. Results are obtained from DES performed on a numerical grid with approximately 12.5 million cells.

Stepping the cut-off geometry is not the only way to generate phase-shift. Inclining either the cut-off or the impeller blades is also known to be effective and capable of generating phase-shift [28, 30]. Inclined cut-off models are also investigated on the FC fan of this study. The angles by which the cut-off is inclined are similar to the height differences used in the stepped tongues herein, i.e. half a blade-to-blade spacing as well as one complete blade passage. However, there is not a considerable noise reduction evident in the SPL spectra of the inclined tongues. The inability of the corresponding tongues is related to their moderate levels of inclination (The reader is referred to [140] for more information). It is probable that increasing the angle at which the cut-off is inclined helps to generate a more successful phase-shift.

It is also worth mentioning that the effects of the stepped-tongues and the inclined tongues are both numerically and experimentally investigated for a sharp tongue model with a radius of 2 mm, and a very small impeller-tongue clearance (i.e. 3 mm). The clearance in this model is deliberately chosen so small to excite particularly the tonal noise of the fan. It is found out that both modifications are able to effectively reduce the tonal noise of the fan by up to 6 dB [140, 158]. This suggests that the corresponding modifications can be more useful in the case of a poorly designed FC fan.

Chapter 5

Concluding Remarks

The radial fan with forward-curved (FC) blades is used extensively in the automotive industry, and in heating, ventilation and air conditioning (HVAC) applications as well as in household dryers. Despite its broad range of applications, the characteristics of this fan type are not known in detail and questions still remain unanswered after more than a century of its invention. This thesis is an attempt to shed some light onto the noise and performance characteristics of FC fans through experimental and numerical investigations. The performance curves of the fan are obtained from chamber test-rig measurements in accordance with DIN/ISO 5801, while the noise measurements have been taken by using the in-duct method in accordance with DIN/ISO 5136. The noise measurements are performed at four various operating points of the fan at a rotating speed of 1000 rpm by using high-precision microphones equipped with wind shields. The numerical simulations are performed at the best efficiency point (BEP) of the fan. A commercially available computational fluid dynamics (CFD) package STAR-CCM+ has been employed for the numerical simulations including both performance and noise predictions. A wide range of the available turbulence modeling approaches has been investigated on different numerical grids in this thesis. This includes Reynolds Averaged Navier-Stokes (RANS), Improved Delayed Detached Eddy Simulation (IDDES), and Large Eddy Simulation (LES) on unstructured CFD grids ranging from approximately 12 to 100 million cells. The noise of the fan is numerically predicted by means of pressure-monitors installed in the fan outlet as well as a Ffowcs Williams and Hawkings (FW-H) monitor installed near the outlet. The FW-H predictions are based on the radiation from the impermeable surfaces and consist of thickness and loading noises. The reliability of the performed simulations is assessed by comparing numerical predictions against experimental measurements. It has been concluded that

the unsteady (U)RANS simulations can accurately predict the tonal noise of the fan that emerges at the blade passing frequency (BPF). Moreover, the URANS simulation performed on the grid with 26.5 million can properly cover the lower frequency range, i.e. up to 1 kHz. Detached eddy simulations are performed on all of the numerical grids generated, i.e. 12.5M, 26.5M, and 102M cell models. The tremendous ability of DES on the coarsest grid is a striking observation; in fact, DES results on the 12.5M model can reliably predict the radiated noise of the fan up to approximately 1.2 kHz. It can be concluded that DES on a coarser grid (e.g., 12.5M) can capture more flow structures than URANS does on a more refined grid (e.g., 26.5M). In terms of the broadband noise prediction, there is a constant improvement in the quality of the DES predictions as the resolution of the numerical grid increases. Consequently, DES on the 102-million cell model (DES_102M) is reliably capable of predicting the experimental trend up to 5 kHz. Nonetheless, the most accurate tonal noise prediction is obtained from DES_12.5M, while the other models, i.e. DES_26.5M and DES_102M, underestimate the discrete (tonal) noise of the fan.

The comparison of the performed Detached and Large Eddy Simulations helped to gain a better insight into the essence of the corresponding approaches. It has been concluded that the LES on an identical or even on a coarser grid is capable of capturing considerably more flow structures than DES. Owing to the generous amount of LES content in the flow field of the LES_26.5M, this model has also been able to predict the experimental trend up to 5 kHz, while DES_26.5M prediction is limited to approximately 1.5 kHz. The overestimation of the pressure rise in the LES_26.5M gave the initial impression that this model suffers from the lack of adequate grid resolution. However, estimating the total turbulent kinetic energy helped to calculate the ratio between resolved and total turbulent kinetic energy. It is surprising to observe that more than 80% of the turbulent kinetic energy has been properly resolved in the LES_26.5M, although the LES_102M is definitely the more superior model in fulfilling the mentioned requirement.

Compared to DES_26.5M, the tonal noise predicted by LES_26.5M is closer to the experimental measurement, although this model also underpredicts the mentioned noise component. On the other hand, LES_102M can reliably capture the discrete noise component. This model shows great effectiveness in predicting the broadband noise of the fan. Despite the accurate trends obtained from LES_102M, its predictions are slightly overestimated. The comparison of the reference numerical model with an extended model that also includes the measurement duct, suggests that the mentioned overestimation

might be related to the near field effects and the place where the pressure monitors are installed.

The FW-H method has succeeded in providing favorable results in the lower frequency range. However, unlike the results obtained from the pressure monitors, employing a more sophisticated turbulence modeling approach failed to extend the prediction range of the FW-H approach. This deficiency is caused by the absence of the volume sources in the FW-H method in this study. The volume sources (permeable surfaces) are not included in the FW-H model, since the flow inside the fan is completely subsonic, and dipole sources are dominant in such a case. However, the results obtained indicate that this simplification has negatively affected the accuracy of the FW-H predictions in the higher frequency range. Including the permeable surfaces (volume sources) is expected to enhance the quality of the FW-H results as well as extending its prediction range.

In addition to the turbulence modeling approach, the numerical grid plays a cardinal role in the accuracy of a simulation, specially when predicting the noise is the purpose of the simulation. In this study the domains are spatially discretized by means of the polyhedral and trimmed cells. It is concluded that both of the cell shapes mentioned are suitable for use in the simulation of FC fans. However, trimmed cells appear to be more reflective than polyhedral cells [159], which means that grid resolution should be increased when using the trimmed cells to avoid the spurious pressure reflections.
It is considered good practice to refine the numerical grid so that resolving at least 20 cells in the smallest wavelength of interest becomes feasible. The results obtained in this thesis also support the mentioned guideline; however, it should be emphasized that this refinement strategy should be considered as a starting point, and following it does not necessarily guarantee accurate results. As a matter of fact, even the 12.5M mesh model in this study fulfills the mentioned requirement and resolves 20 cells per the wavelength of 5 kHz, but its prediction range is limited to approximately 1.2 kHz. Moreover, it has been observed that the LES_26.5M is simply capable of predicting the broadband noise up to the higher frequencies, but in the case of the DES_26.5M the predictions are limited to 1.5 kHz. It can therefore be inferred that not only the smallest wavelength of interest, but also the chosen turbulence modeling approach, should be taken into account when generating a grid. Generally speaking, DES demands a higher grid resolution to be able to cover the same frequency range as LES. Therefore, 20 cells per the maximum wavelength might be a useful guideline when considering the LES approach, but the same might be insufficient for DES.

Time-step is another parameter upon which the accuracy of an unsteady (transient) numerical simulation depends. The best practice guideline suggests resolving 10 points per maximum frequency of interest. The smallest time-step used in this study for the last two rotations of the impeller resolves 10 points per approximately 2.4 kHz. However, according to results obtained the predictions of the LES_26.5M, DES_102M, and the LES_102M simply cover the frequency range beyond the mentioned cut-off frequency. Therefore, at least in the case of the FC fan under investigation, the mentioned guideline can be considered as "stringent", and resolving 5 points per the maximum frequency appears to be sufficient.

The effects of different geometrical modifications on the noise and performance of the fan have been investigated in this thesis. On the impeller side, the effects of the blade's outlet angle, as well as the number of blades, are studied by performing the numerical simulations. It is concluded that increasing the number of blades as well as their outlet angle both have the potential to enhance the aerodynamic performance of the fan, especially at high flow rates. The numerical results reveal that increasing the number of blades leads to an effective tonal noise reduction, as experimentally proved in [5]. It can be concluded that the number of blades is the most important parameter governing both the aerodynamic performance and the tonal noise level of the fan. Changing the blade's outlet angle appears to have insignificant effects on tonal noise generation. However, the numerical results show that the fan generates the highest tonal noise level when the impeller has a definite outlet angle (i.e., 160° in this study). Making the outlet angle either greater or smaller than the corresponding value leads to reduction of the tonal noise level. The numerical results also indicate that the recirculation zones between the impeller blades become smaller as the outlet angle increases. This has the potential to reduce the broadband noise level of the fan, although the predicted acoustic spectra do not show a notable change in the corresponding noise component. It would be interesting to continue the numerical simulation of the impellers with various outlet angles for some more rotations to increase the frequency resolution and obtain an enhanced representation of the broadband noise levels.

On the stator side, the most important parameter governing the tonal noise level is the distance between the impeller blades and the volute tongue (cut-off). Increasing the impeller-tongue clearance results in an effective tonal noise reduction as well as aerodynamic performance deterioration [159]. On the other hand, reducing the distance between the impeller and the cut-off

significantly amplifies the tonal noise of the fan [140, 158]. A large portion of this thesis is devoted to investigation of the stepped tongues with the aim of finding to what extent it is feasible to generate a destructive phase-shift between different cut-off segments and consequently reduce the tonal noise of the fan. The numerical and experimental results obtained acknowledge the ability of the stepped tongues in reducing the tonal noise of the fan. Based on the results, it is concluded that there are specifically two parameters which affect the ability of a step tongue. The first is the height difference between the neighboring cut-off segments, and the second is the arrangement of the corresponding segments. The results obtained reveal that making half a blade-to-blade circumferential difference between the heights of the adjoining portions helps to generate a destructive phase-shift and reduce the tonal noise. Moreover, the arrangement of the cut-off portions has a strong influence on the tonal noise generation.

This study can be continued considering different aspects:

- An impeller with uneven blade spacings should be able to spread the sound spectrum over a wider range of frequencies without negating the aerodynamic performance of the fan. The effectiveness of this method in reducing the tonal noise of the fan has already been approved in the case of a radial fan with backward-curved blades [160]. It would be interesting to apply this method to the FC fan under investigation.

- In order to study the effectiveness of the stepped-tongue geometries, the heights of the cut-off segments are decreased in comparison to the reference cut-off position. As a result of this modification, some of the cut-off arrangements have caused undesirable efficiency losses. Therefore, it would be also interesting to investigate the stepped tongues whose segments stand higher than the reference cut-off position. Such a configuration should still be able to generate the desired phase-shift effects without negating the aerodynamic performance of the fan.

- The pressure trends obtained from the monitors installed on the cut-off surface testify the ability of the stepped tongues to generate a destructive phase-shift. However, it is not fully understood why such a destructive phase-shift does not always lead to a tonal noise reduction. Therefore, it would be of great interest to conduct additional experimental measurements using surface mounted pressure transducers and further investigate the essence of the phase-shift between the cut-off segments.

Bibliography

[1] F. J. Ferris. Heritage group of the chartered institution of building services engineers. Technical report, Chartered Institution of Building Services Engineers (CIBSE), September 2011.

[2] The Sirocco Fan. The Lancet, 198(5106):90, July 1921.

[3] B. Eck. Ventilatoren. Springer Verlag, 1962.

[4] B. Eck. Fans: Design and Operation of Centrifugal Axial Flow and Cross Flow Fans. Pergamon Press Limited, 1973.

[5] H. W. Roth, H. Leist, and J. Zierep. Untersuchungen an Trommelläufer-Ventilatoren. Technical report, Institut für Strömungslehre und Strömungsmaschinen der Technischen Hochschule Karlsruhe, October 1979.

[6] D. Raj and W. B. Swim. Measurements of the Mean Flow Velocity and Velocity Fluctuations at the Exit of an FC Centrifugal Fan Rotor. Journal of Engineering for Gas Turbines and Power, pages 393–399, 1981.

[7] N. Montazerin, A. Damangir, and S. Mirian. A new concept for squirrel-cage fan inlet. Journal of Power and Energy, 212:343–349, 1998.

[8] N. Montazerin, A. Damangir, and H. Mirzaie. Inlet induced flow in squirrel-cage fans. Journal of Power and Energy, 214:243–253, 2000.

[9] N.N. Bayomi, A. Abdel Hafiz, and A.M. Osman. Effect of inlet straighteners on centrifugal fan performance. Energy Conversion and Management, 47:3307–3318, 2006.

[10] N. Montazerin, A. Damangir, and K. Fard. A study of slip factor and velocity components at the rotor exit of forward-curved squirrel cage fans, using laser doppler anemometry. Journal of Power and Energy, 215:453–463, 2001.

[11] E-M. Guo and K-Y. Kim. Three-dimensional flow analysis and improvement of slip factor model for forward-curved blades centrifugal fan. pages 1203–1211. ASME/JSME 2003 4th Joint Fluids Engineering Conference, July 2003.

[12] G. R. Denger, M. W. Mcbride, and G. C. Lauchle. An Experimental Evaluation of the Internal Flow Field of an Automotive Heating, Ventilating and Air Conditioning System. Technical Report TR 90-011, Penn State University, July 1990.

[13] H. Tsurusaki, Y. Tsujimoto, Y. Yoshida, and K. Kitagawa. Visualization Measurement and Numerical Analysis of Internal Flow in Cross-Flow Fan. Journal of Fluids Engineering, 119:633–638, September 1997.

[14] T. Klemm and M. Gabi. Using PIV and CFD to investigate the effect of casing design on cross flow fan performance. Proceedings of Pacific Symposium on Flow Visualization and Image Processing 4 (PSFVIP4), June 2003.

[15] T. Klemm and M. Gabi. Investigations of fans for ventilation systems in automobiles. Proceedings of the 11th International Symposium on Transport Phenomena and Dynamics of Rotating Machinery, ISROMAC-11, February 2006.

[16] S. V. Suárez, R. B. Tajadura, and J. G. Pérez. Numerical Simulation of the Unsteady Flow Patterns in a Small Squirrel-Cage fan. ASME Joint U.S.-European Fluids Engineering Summer Meeting, July 2006.

[17] S. M. Rezaei Niya, N. Montazerin, A. Damangir, and A. H. Dehkordi. Performance and laser doppler anemometry experimental investigation of squirrel cage fans with half-cone rotors. Journal of Power and Energy, 220:753–763, November 2006.

[18] M. Kitadume, M. Kawahashi, H. Hirahara, T. Uchida, and H. Yanagawa. Experimental Analysis of 3D Flow in Scroll Casing of Multi-Blade Fan for Air-Conditioner. Journal of Fluid Science and Technology, 2:302–310, 2007.

[19] Y. Jung and J. Baek. A numerical study on the unsteady flow behavior and the performance of an automative sirocco fan. Journal of Mechanical Science and Technology, 22:1889–1895, 2008.

[20] J. Fukutomi, T. Shigemitsu, and T. Yasunobu. Performance and internal flow of sirocco fan using contra-rotating rotors. Journal of Thermal Science, 17:35–41, 2008.

[21] A. Stuchlik, S. Frank, and P.-U. Thamsen. Performance Investigations of Sirocco Fans by means of Computational Fluid Dynamics. ISROMAC-13-2010-012, April 2010.

[22] A. Stuchlik and S. Frank. Numerische Berechnung und Auslegung von Trommelläufer-Ventilatoren bei idealer und gestörter Zu- und Abströmung (NUBAT). Technical report, Hochschule für Technik und Wirtschaft HTW Berlin, Mai 2011.

[23] S. Frank, M. Darvish, B. Tietjen, and A. Stuchlik. Design Improvements of Sirocco Type Fans By Means Of Computational Fluid Dynamics And Stereoscopic Particle Image Velocimetry. Fan 2012, April 2012.

[24] M. Darvish and S. Frank. Toward the CFD Simulation of Sirocco Fans: From Selecting a Turbulence Model to the Role of Cell Shapes. Fan 2012, April 2012.

[25] A. Stuchlik. Berechnung und Optimierung von Trommelläufer-Ventilatoren. PhD thesis, Technische Universität Berlin, 2013.

[26] J. B. Moreland. Housing Effects on Centrifugal Blower Noise. Journal of Sound and Vibration, 36(2):191–205, 1974.

[27] W. Neise. Comments on housing Effects on Centrifugal Blower Noise. Journal of Sound and Vibration, 46(2):299–301, 1976.

[28] W. Neise. Noise reduction in centrifugal fans: A literature survey. Journal of Sound and Vibration, 45(3):375–403, 1976.

[29] F.P. Bleier. Fan handbook: selection, application and design. McGraw-Hill, 1998.

[30] T. Carolus. Ventilatoren: Aerodynamischer Entwurf, Schallvorhersage, Konstruktion. Springer Vieweg, 2012.

[31] F.Holste and W. Neise. Experimental Comparison of Standardized Sound Power Measurement Procedures for Fans. Journal of Sound and Vibration, 152:1–26, 1992.

[32] S. Velarde-Suárez, R. Ballesteros-Tajadura, C. Santolaria-Morros, and Br. Pereiras-Garcia. Reduction of the aerodynamic tonal noise of a forward-curved centrifugal fan by modification of the volute tongue geometry. Applied Acoustics, 69:225–232, 2008.

[33] T. F. W. Embleton. Experimental study of noise reduction in centrifugal blowers. Journal of the Acoustical Society of America, 35:700–705, 1963.

[34] L. A. Lyons and S. Platter. Effect of cutoff configuration on pure tones generated by small centrifugal blowers. Journal of the Acoustical Society of America, 35:1455–1456, 1963.

[35] Q. Datong, M. Yijun, L. Xiaoliang, and Y. Minjian. Experimental study on the noise reduction of an industrial forward-curved blades centrifugal fan. Applied Acoustics, 70:1041–1050, 2009.

[36] K. W. Yeow. Centrifugal fan noise research: A brief survey of previous literature. Institute of Sound and Vibration Research, Southampton, Memorandum No. 143, 1966.

[37] Y. I. Petrov, G. A. Khoroshev, and S. Y. Novoshilov. Reduction of the noise level in centrifugal fans by means of transition meshes. Sudostroenie, 5:22–25, 1970.

[38] G. A. Khoroshev and Yu. I. Petrov. Some new methods of fan noise reduction. Proceedings of the 7th International Congress on Acoustics, Budapest, 1971.

[39] Y. I. Petrov and G. A. Khoroshev. Improving the noise level of centrifugal fans. Russian Engineering Journal, 51:42–44, 1971.

[40] N. Saeki, K. Kamiyama, M. Uomoto, and Y. Ishihara. Development of low noise blower fan. SAE Technical Paper 971842, 1997.

[41] W. Neise and G. H. Koopmann. Reduction of centrifugal fan noise by use of resonators. Journal of Sound and Vibration, 73:297–308, 1980.

[42] G. H. Koopmann, D. J. Fox, and W. Neise. Active source cancellation of the blade tone fundamental and harmonics in centrifugal fans. Journal of Sound and Vibration, 126:209–220, 1988.

[43] G. H. Koopmann and W. Neise. The use of resonators to silence centrifugal blowers. Journal of Sound and Vibration, 82:17–27, 1982.

[44] A. Gérard, M. Besombes, A. Berry, P. Masson, and S. Moreau. Tonal Noise Control from Centrifugal Fans Using Flow Control Obstructions. Fan 2012, April 2012.

[45] W. H. Jeon. A numerical study on the effects of design parameters on the performance and noise of a centrifugal fan. Journal of Sound and Vibration, 265:221–230, 2003.

[46] S. Caro, P. Ploumhans, X. Gallez, R. Sandboge, F. Shakib, and M. Matthes. A New CAA Formulation based on Lighthill's Analogy applied to an Idealized Automotive HVAC Blower using AcuSolve and Actran/LA. 11th AIAA/CEAS Aeroacoustics Conference, May 2005.

[47] E. Sorguven, Y. Dogan, F. Bayraktar, and E. Arslan. Computational noise prediction of a centrifugal fan. Proceedings of the ASME International Mechanical Engineering Congress and Exposition, November 2007.

[48] E. Sorguven, Y. Dogan, F. Bayraktar, and K.Y. Sanliturk. Noise prediction via large eddy simulation: Application to radial fans. Noise Control Engineering Journal, 57:169–178, 2009.

[49] S. Velarde-Suárez, R. Ballesteros-Tajadura, and J. G. Peŕez. Pressure fluctuation pattern and tonal noise generation in a squirrel-cage fan. Fan Noise 2007, September 2007.

[50] S. Khelladi, S. Kouidri, F. Bakir, and R. Rey. Predicting tonal noise from a high rotational speed centrifugal fan. Journal of Sound and Vibration, 313:113–133, 2008.

[51] Y. Mao, D. Qi, X. Liu, and H. Tang. Numerical prediction of aerodynamic tonal noise radiated from a centrifugal fan. Journal of Power and Energy, 222:831–842, 2008.

[52] S. Lee, S. Heo, and C. Cheong. Prediction and reduction of internal blade-passing frequency noise of the centrifugal fan in a refrigerator. International Journal of Refrigeration, 33:1129–1141, 2010.

[53] S. Heo, C. Cheong, and T.-H. Kim. Development of low-noise centrifugal fans for a refrigerator using inclined S-shaped trailing edge. International Journal of Refrigeration, 34:2076–2091, 2011.

[54] D. J. Gingery. How to Design and Build Centrifugal Fans for the Home Shop. Lindsay Publications, Inc., 1987.

[55] O. Cordier. Ähnlichkeitsbedingungen für Strömungsmaschinen. Brennstoff-Wärme-Kraft, Zeitschrift für Energiewirtschaft und technische Überwachung, 5(10), October 1953.

[56] G. T. Csanady. Theory of Turbomachines. McGraw-Hill, 1964.

[57] S.L. Dixon and C.A. Hall. Fluid Mechanics and Thermodynamics of Turbomachinery. Elsevier, sixth edition, 2006.

[58] D. M. Driver and H. L. Seegmiller. Features of a Reattaching Turbulent Shear Layer in Divergent Channel Flow. AIAA Journal, 23:163–171, February 1985.

[59] D.R. Raichel. The Science and Applications of Acoustics. Springer, second edition, 2006.

[60] T. Wright. Fluid Machinery: Performance, Analysis, and Design. CRC Press LLC, 1999.

[61] A. Gérard and M. Besombes. Psychoacoustic impact of tonal noise control from fans. Automobile and railroad comfort congress, November 2008.

[62] N. Curle. The Influence of Solid Boundaries upon Aerodynamic Sound. Proceedings of the Royal Society of London. Series A. Mathematical and Physical Sciences, 231(1187):505–514, 1955.

[63] B. R. Munson, D. F. Young, T. H. Okiishi, and W. W. Huebsch. Fundamentals of Fluid Mechanics. John Wiley & Sons, Inc., sixth edition, 2009.

[64] F. Fahy. Foundations of Engineering Acoustics. Elsevier, 2001.

[65] M. Möser. Engineering Acoustics: An Introduction to Noise Control. Springer, second edition, 2009.

[66] M. P. Norton and D. G. Karczub. Fundamentals of Noise and Vibration Analysis for Engineers. Cambridge University Press, second edition, 2003.

[67] J. Whitaker and K.B. Benson. Standard Handbook of Audio and Radio Engineering. McGraw-Hill, 2002.

[68] F.A. Everest and K.C. Pohlmann. Master Handbook of Acoustics. McGraw-Hill, fifth edition, 2009.

[69] T.D. Rossing. Springer Handbook of Acoustics. Springer, 2007.

[70] L. L. Beranek. Acoustics. American Institute of Physics, Inc., 1986.

[71] M. Bruneau and T. Scelo. Fundamentals of Acoustics. ISTE Ltd, 2006.

[72] L.E. Kinsler, A.R. Frey, A.B. Coppens, and J.V. Sanders. Fundamentals of Acoustics. John Wiley & Sons, Inc., fourth edition, 2000.

[73] DIN 61672-1 Electroacoustics - Sound level meters - part 1: Specifications (IEC 61672-1:2013). International Organisation for Standardization, 2013.

[74] DIN 226 Acoustics - Normal equal-loudness-level contours. International Organisation for Standardization, 2003.

[75] Punker technical Data Sheets for Model $TLR\,200 \times 82 - L$. Punker GmbH: http://www.punker.de.

[76] DIN 5801 Industrial fans- Performance testing using standardized airways. International Organisation for Standardization, 2011.

[77] DIN 5136 Acoustics - Determination of sound power radiated into a duct by fans and other air-moving devices - In-duct method. International Organisation for Standardization, 2003.

[78] W. Neise and F. Arnold. On Sound Power Determination In Flow Ducts. Journal of Sound and Vibration, 244(3):481–503, 2001.

[79] A. N. Bolton and E. J. Margetts. Anechoic Terminations for In-Duct Fan Noise Measurement. International Conference on Fan Design & Applications, September 1982.

[80] K. Ehrenfried. Strömungsakustik. Mensch & Buch Verlag, 2004.

[81] R. Streuber. Untersuchungen zur Aero-Akustik von Trommelläufer-Ventilatoren. Master's thesis, Hochschule für Technik und Wirtschaft HTW Berlin, 2013.

[82] F. Khan. Konstruktion, Fertigung und akustische Abnahme eines reflexionsarmen Abschlusskanals für Trommelläufer-Ventilatoren. Master's thesis, Hochschule für Technik und Wirtschaft HTW Berlin, 2011.

[83] Microtech Gefell GmbH. http://www.microtechgefell.de.

[84] Product Data Sound Calibrator Type 4231. Brüel & Kjær: http://www.bksv.com/.

[85] T. J. Mueller. Aeroacoustic Measurements. Springer, 2002.

[86] W. Neise and B. Stahl. The Flow Noise Level At Microphones In Flow Ducts. Journal of Sound and Vibration, 63:561–579, 1979.

[87] U. Bolleter, R. Cohen, and J.Wang. Design Considerations For An In-Duct Soundpower Measuring System. Journal of Sound and Vibration, 28:669–685, 1973.

[88] DIN 3744 Acoustics-Determination of sound power levels of noise sources using sound pressure- Engineering method in an essentially free-field over a reflecting plane. International Organisation for Standardization, 2010.

[89] DIN 3743-1 Acoustics-Determination of sound power levels of noise sources-engineering methods for small, movable sources in reverberant fields-Part 1: Comparison method in hard-walled test rooms. International Organisation for Standardization, 2010.

[90] DIN 3743-2 Acoustics-Determination of sound power levels of noise sources-Engineering methods for small, movable sources in reverberant fields-Part 2: Methods for special reverberation test rooms. International Organisation for Standardization, 2009.

[91] SAMURAI Basic Version manual 2.0. SINUS Messtechnik GmbH: http://www.soundbook.de/.

[92] C. Wagner, T. Huettl, and P. Sagaut. Large-Eddy Simulation for Acoustics. Cambridge University Press, 2007.

[93] J. F. Wendt. Computational Fluid Dynamics An Introduction. Springer, third edition, 2009.

[94] J. D. Anderson. Computational Fluid Dynamics, The Basics with Applications. Mc-Graw-Hill, Inc., 1995.

[95] J. Blazek. Computational Fluid Dynamics: Principles and Applications. Elsevier, first edition, 2001.

[96] J .C. Tannehill, D. A. Anderosn, and R. H. Pletcher. Computational Fluid Mechanics and Heat Transfer. Taylor & Francis, second edition, 1997.

[97] H. K. Versteeg and W. Malalasekera. An Introduction to Computational Fluid Dynamics. Pearson Education Limited, second edition, 2007.

[98] W. W. Seto. Schaum's Outline of Theory and Problems of Acoustics. Mc-Graw-Hill, Inc., 1971.

[99] M. J. Lighthill. On Sound Generated Aerodynamically. I. General Theory. Proceedings of the Royal Society of London. Series A. Mathematical and Physical Sciences, 211(1107):564–587, 1952.

[100] T. J. Chung. Computational Fluid Dynamics. Cambridge University Press, 2002.

[101] F. Farassat. The Acoustic Analogy as a Tool of Computational Aeroacoustics. In J. C. Hardin and M.Y. Hussaini, editors, Computational Aeroacoustics, pages 133–155. Springer Verlag, 1993.

[102] USER GUIDE STAR-CCM+ Version 09.02.007. CD-Adapco, 2014.

[103] K. S. Brentner and F. Farassat. An Analytical Comparison of the Acoustic Analogy and Kirchhoff Formulation for Moving Surfaces. AIAA Journal, 36, 1998.

[104] K. S. Brentner and F. Farassat. Modeling Aerodynamically Generated Sound of Helicopter Rotors. Progress in Aerospace Sciences, 39:83–120, 2003.

[105] J. E. Ffowcs Williams and D. L. Hawkings. Sound Generation by Turbulence and Surfaces in Arbitrary Motion. Philosophical Transactions of the Royal Society of London. Series A, Mathematical and Physical Sciences, 264(1151):321–342, May 1961.

[106] F. Farassat. Derivation of Formulations 1 and 1A of Farassat. National Aeronautics and Space Administration, Langley Research Center, Hampton, Virginia, March 2007.

[107] F. Farassat. Open Rotor Noise Prediction at NASA Langley-Capabilities, Research and Development. National Aeronautics and Space Administration, Langley Research Center, Hampton, Virginia, January 2010.

[108] D .C. Wilcox. Turbulence Modeling for CFD. DCW Industries, Inc., 1994.

[109] T. Cebeci. Turbulence Models and Their Application. Springer, 2004.

[110] P. Bradshaw. Turbulence: the chief outstanding difficulty of our subject. Experiments in Fluids, 16, February 1994.

[111] P. Bradshaw. The understanding and prediction of turbulent flow. Aeronautical Journal, pages 403–418, July 1972.

[112] J. H. Ferziger and M. Perić. Computational Methods for Fluid Dynamics. Springer, third edition, 2002.

[113] S. B. Pope. Turbulent Flows. Cambridge University Press, 2000.

[114] P. Moin and K. Mahesh. Direct numerical simulation: A tool in turbulence research. Annual Review of Fluid Mechanics, pages 539–578, 1998.

[115] W.P. Jones and B.E. Launder. The prediction of laminarization with a two-equation model of turbulence. International Journal of Heat and Mass Transfer, 15:301–314, February 1972.

[116] T.H. Shih. An Improved $k - \epsilon$ Model for Near-Wall Turbulence and Comparison With Direct Numerical Simulation. Institute for Computational Lewis Research Center Cleveland, Mechanics in Propulsion Ohio, NASA Technical Memorandum 103221, August 1990.

[117] C. O. Paschereit. Vorlesungsskript: Turbulenz und Strömungskontrolle. Technische Universität Berlin, May 2013.

[118] S. V. Patankar. Numerical Heat Transfer and Fluid Flow. McGraw-Hill, 1980.

[119] H. Schlichting. Boundary Layer Theory. McGraw-Hill, seventh edition, 1978.

[120] P. R. Spalart and S. R. Allmaras. A one-equation turbulence model for aerodynamic flows. AIAA-92-0439, January 1992.

[121] J. E. Bardina, P. G. Huang, and T. J. Coakley. Turbulence Modeling Validation, Testing, and Development. NASA Technical Memorandum 110446, Ames Research Center Moffett Field, California 94035-1000, April 1997.

[122] S. R. Allmaras, F. T. Johnson, and P. R. Spalart. Modifications and Clarifications for the Implementation of the Spalart-Allmaras Turbulence Model. Seventh International Conference on Computational Fluid Dynamics (ICCFD7), July 2012.

[123] T.H. Shih, W. W. Liou, A. Shabbir, Z. Yang, and J. Zhu. A new $k - \epsilon$ eddy viscosity model for high reynolds number turbulent flows. Compurers Fluids, 24(3):227–238, 1995.

[124] F. R. Menter. Two-Equation Eddy-Viscosity Turbulence Models for Engineering Applications. AIAA Journal, 32(8):1598–1605, August 1994.

[125] M. Darvish. Numerical Investigations on the Performance Characteristic of Radial Fans with forward curved blades by means of CFD. Master's thesis, Hochschule für Technik und Wirtschaft Berlin, 2010.

[126] J. Fröhlich and D. von Terzi. Hybrid LES/RANS methods for the simulation of turbulent flows. Progress in Aerospace Sciences, pages 349–377, 2008.

[127] H. Tennekes and J.L. Lumley. A First Course in Turbulence. The MIT Press, 1972.

[128] N. J. Georgiadis, D. P. Rizzetta, and C. Fureby. Large-Eddy Simulation: Current Capabilities, Recommended Practices, and Future Research. AIAA Journal, 48(8):1772–1784, August 2010.

[129] V. Armenio, B. Geurts, and J. Fröhlich. Direct and Large-Eddy Simulation VII. Proceedings of the Seventh International ERCOFTAC Workshop on Direct and Large-Eddy Simulation, held at the University of Trieste, September 8-10, 2008. Springer, 2010.

[130] P. R. Spalart, W.-H. Jou, M. Stretlets, and S. R Allmaras. Comments on the Feasibility of LES for Wings and on the Hybrid RANS/LES Approach. Advances in DNS/LES, Proceedings of the First AFOSR International Conference on DNS/LES, August 1997.

[131] Squires K. D. Detached-Eddy Simulation of Turbulent Flows. von Kármán Institute for Fluid Dynamics Lecture series on "Large Eddy Simulation and Related Techniques: Theory and Applications", February 2010.

[132] P. H. Spalart. Detached-Eddy Simulation. Annual Review of Fluid Mechanics, 41:181–202, 2009.

[133] C. Mockett, M. Fuchs, and F. Thiele. Progress in DES for wall-modelled LES of complex internal flows. Computers & Fluids, 65:44–55, July 2012.

[134] F.R. Menter and M.Kuntz. Adaptation of Eddy-Viscosity Turbulence Models to Unsteady Separated Flow Behind Vehicles. The Aerodynamics of Heavy Vehicles: Trucks, Buses, and Trains, pages 339–352, 2004.

[135] P. R. Spalart. Young-Person's Guide to Detached-Eddy Simulation Grids. National Aeronautics and Space Administration, Langley Research Center, Hampton, Virginia, July 2001.

[136] P. R. Spalart, S. Deck, M. L. Shur, K. D. Squires, M. Kh. Strelets, and A. Travin. A new version of detached-eddy simulation, resistant to ambiguous grid densities. Theoretical and Computational Fluid Dynamics, 20:181–195, July 2006.

[137] M. L. Shur, P. R. Spalart, M. Kh. Strelets, and A. K. Travin. A hybrid RANS-LES approach with delayed-DES and wall-modelled LES capabilities. International Journal of Heat and Fluid Flow, 29:1638–1649, December 2008.

[138] T. Van de Ven, J. Louis, D. Palfreyman, and F. Mendonça. Computational Aeroacoustic Analysis of a 1/4 Scale G550 Nose Landing Gear and Comparison to NASA and UFL Wind Tunnel Data. AIAA/CEAS Aeroacoustics Conference (30th AIAA Aeroacoustics Conference), 2009.

[139] F. Mendonça, A. Read, S. Caro, K. Debatin, and B. Caruelle. Aeroacoustic Simulation of Double Diaphragm Orifices in an Aircraft Climate Control System. 11th AIAA/CEAS Aeroacoustics Conference, May 2005.

[140] M. Darvish and S. Frank. Numerische und Experimentelle Geräusch-Optimierung von Trommelläufer-Ventilatoren (NEGOT). Technical report, Hochschule für Technik und Wirtschaft HTW Berlin, April 2014.

[141] V. K. Garg. Applied Computational Fluid Dynamics. Marcel Dekker, Inc., 1998.

[142] C. H. Tan, K. S. Voo, W. L. Siauw, J. Alderton, A. Boudjir, and F. Mendonça. CFD Analysis of the Aerodynamics and Aeroacoustics of the NASA SR2 Propeller. Proceedings of ASME Turbo Expo 2014: Turbine Technical Conference and Exposition GT2014, June 2014.

[143] O. Baris and F. Mendonça. Automotive Turbocharger Compressor CFD and Extension Towards Incorporating Installation Effects. Proceedings of ASME Turbo Expo 2011: Power for Land, Sea and Air GT2011, June 2011.

[144] L. Tan and J. Jiang. Digital Signal Processing Fundamentals and Applications. Academic Press of Elsevier, second edition, 2013.

[145] V. K. Madisetti. The Digital Signal Processing Handbook. CRC Press, second edition, 2010.

[146] S. W. Smith. Digital Signal Processing: A Practical Guide for Engineers and Scientists. Newnes of Elsevier, 2003.

[147] D. Havelock, S. Kuwano, and M. Vorländer. Handbook of Signal Processing in Acoustics Volume 1. Springer, 2008.

[148] L. F. Chaparro. Signals and Systems Using MATLAB. Academic Press of Elsevier, 2011.

[149] B. Tietjen, M. Benz, M. Darvish, and S. Frank. Untersuchung der Doppelwirbel-Strömung im Gehäuse eines Trommelläufer-Ventilators mit Stereo Particle Image Velocimetry. Proceedings der 21. GALA-Fachtagung Lasermethoden in der Strömungsmesstechnik, September 2013.

[150] T. Raitor and W. Neise. Sound generation in centrifugal compressors. Journal of Sound and Vibration, 314:738–756, July 2008.

[151] F. Kameier and W. Neise. Rotating Blade Flow Instability as a Source of Noise in Axial Turbomachines. Journal of Sound and Vibration, 203:833–853, June 1997.

[152] L. Mongeau, D.E. Thompson, and D.K. McLaughlin. Sound generation by rotating stall in centrifugal turbomachines. Journal of Sound and Vibration, 163:1–30, May 1993.

[153] D. Wolfram and T. H. Carolus. Experimental and numerical investigation of the unsteady flow field and tone generation in an isolated

centrifugal fan impeller. Journal of Sound and Vibration, 329:4380–4397, October 2010.

[154] D. Casalino, S. Moreau, and M. Roger. One, no one and one hundred thousand methods for low-speed fan noise prediction. International Journal of Aeroacoustics, 9(3):307–327, 2010.

[155] H. Reese, T. Carolus, and C. Kato. Numerical Prediction of the Aeroacoustic Sound Sources in a Low Pressure Axial Fan with Inflow Distortions. Fan 2007, September 2007.

[156] S. B. Pope. Ten questions concerning the large-eddy simulation of turbulent flows. New Journal of Physics, 6, March 2004.

[157] M. Darvish, B. Tietjen, D. Beck, and S. Frank. Tonal Noise Reduction in a Radial Fan with Forward-Curved Blades.

[158] D. Beck. Beitrag zur aeroskustischen Untersuchung an Lüftern radialer Bauweise mit vorwärtsgekrümmten Schaufeln. Master's thesis, Hochschule für Technik und Wirtschaft Berlin, 2013.

[159] B. Tietjen. A Numerical Study of Various Volute Cut-Offs and the Influence on the Aeroacoustics and Aerodynamics of a Forward Curved Fan. Master's thesis, Hochschule für Technik und Wirtschaft Berlin, 2013.

[160] M. Boltezar, M. Mesaric, and A. Kuhelj. The influence of uneven blade spacing on the SPL and noise spectra radiated from radial fans. Journal of Sound and Vibration, 216:697–711, 1998.

Appendices

A.1 Conversion of Sound Levels from Flat Response to A, B, C Weightings

Frequency (Hz)	A weighting (dB)	B weighting (dB)	C weighting (dB)
10	-70.4	-38.2	-14.3
12.5	-63.4	-33.2	-11.2
16	-56.7	-28.5	-8.5
20	-50.5	-24.2	-6.2
25	-44.7	-20.4	-4.4
31.5	-39.4	-17.1	-3.0
40	-34.6	-14.2	-2.0
50	-30.2	-11.6	-1.3
63	-26.2	-9.3	-0.8
80	-22.5	-7.4	-0.5
100	-19.1	-5.6	-0.3
125	-16.1	-4.2	-0.2
160	-13.4	-3.0	-0.1
200	-10.9	-2.0	0
250	-8.6	-1.3	0
315	-6.6	-0.8	0
400	-4.8	-0.5	0
500	-3.2	-0.3	0
630	-1.9	-0.1	0
800	-0.8	0	0
1000	0	0	0
1250	0.6	0	0
1600	1	0	-0.1
2000	1.2	-0.1	-0.2
2500	1.3	-0.2	-0.3
3150	1.2	-0.4	-0.5
4000	1	-0.7	-0.8
5000	0.5	-1.2	-1.3
6300	-0.1	-1.9	-2.0
8000	-1.1	-2.9	-3.0
10000	-2.5	-4.3	-4.4
12500	-4.3	-6.1	-6.2
16000	-6.6	-8.4	-8.5
20000	-9.3	-11.1	-11.2

A.2 One-third Octave Bands

Lower Band Limit f_L (Hz)	Center Frequency f_C (Hz)	Upper Band Limit f_U (Hz)
18	20	22.4
22.4*	25	28
28	31.5*	35.5
35.5	40	45*
45*	50	56
56	63*	71
71	80	90*
90*	100	112
112	125*	140
140	160	180*
180*	200	224
224	250*	280
280	315	355*
355*	400	450
450	500*	560
560	630	710*
710*	800	900
900	1000*	1120
1120	1250	1400*
1400*	1600	1800
1800	2000*	2240
2240	2500	2800*
2800*	3150	3550
3550	4000*	4500
4500	5000	5600*
5600*	6300	7100
7100	8000*	9000
9000	10000	11200*
11200*	12500	14000
14000	16000*	18000
18000	20000	22400*

* Octave marking points

A.3 Detailed Geometrical Dimensions of the FC Fan Investigated in this Study

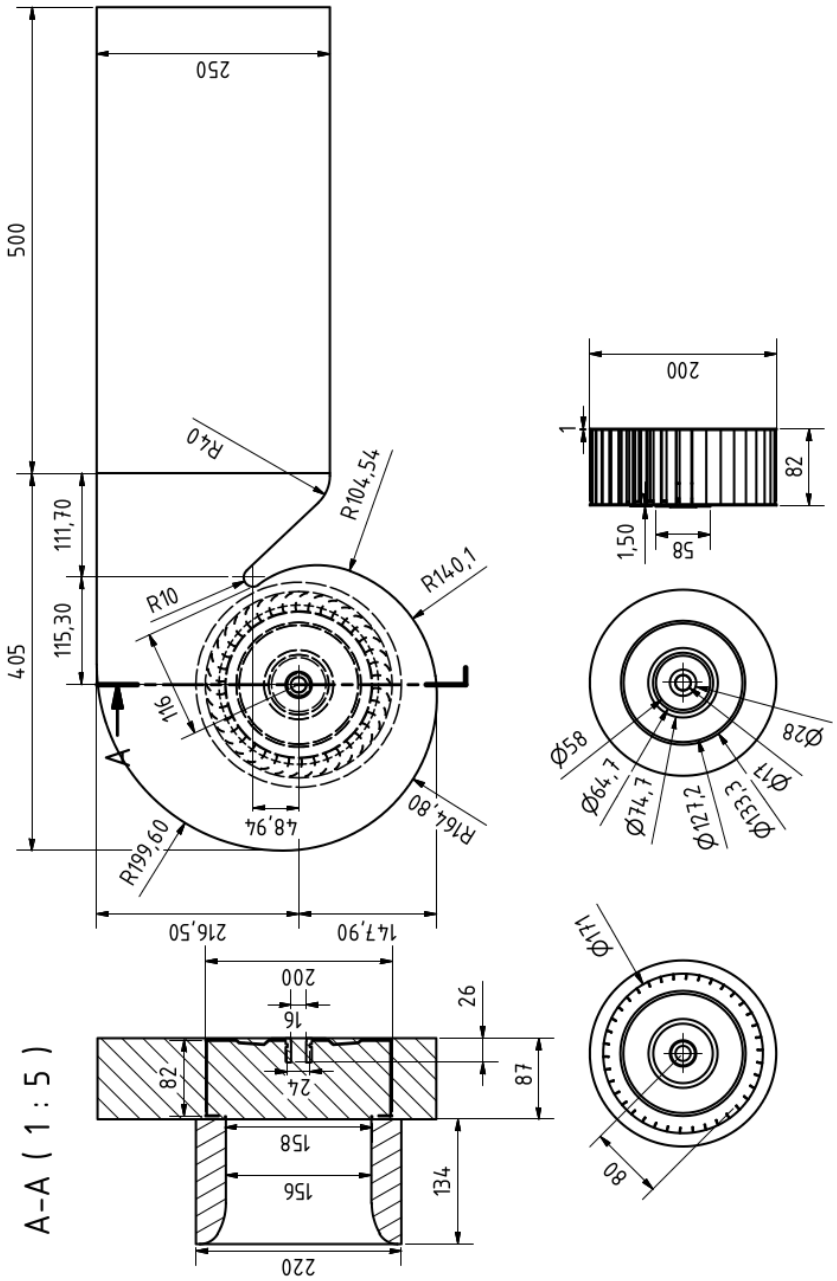

A.4 Detailed Impeller Dimensions

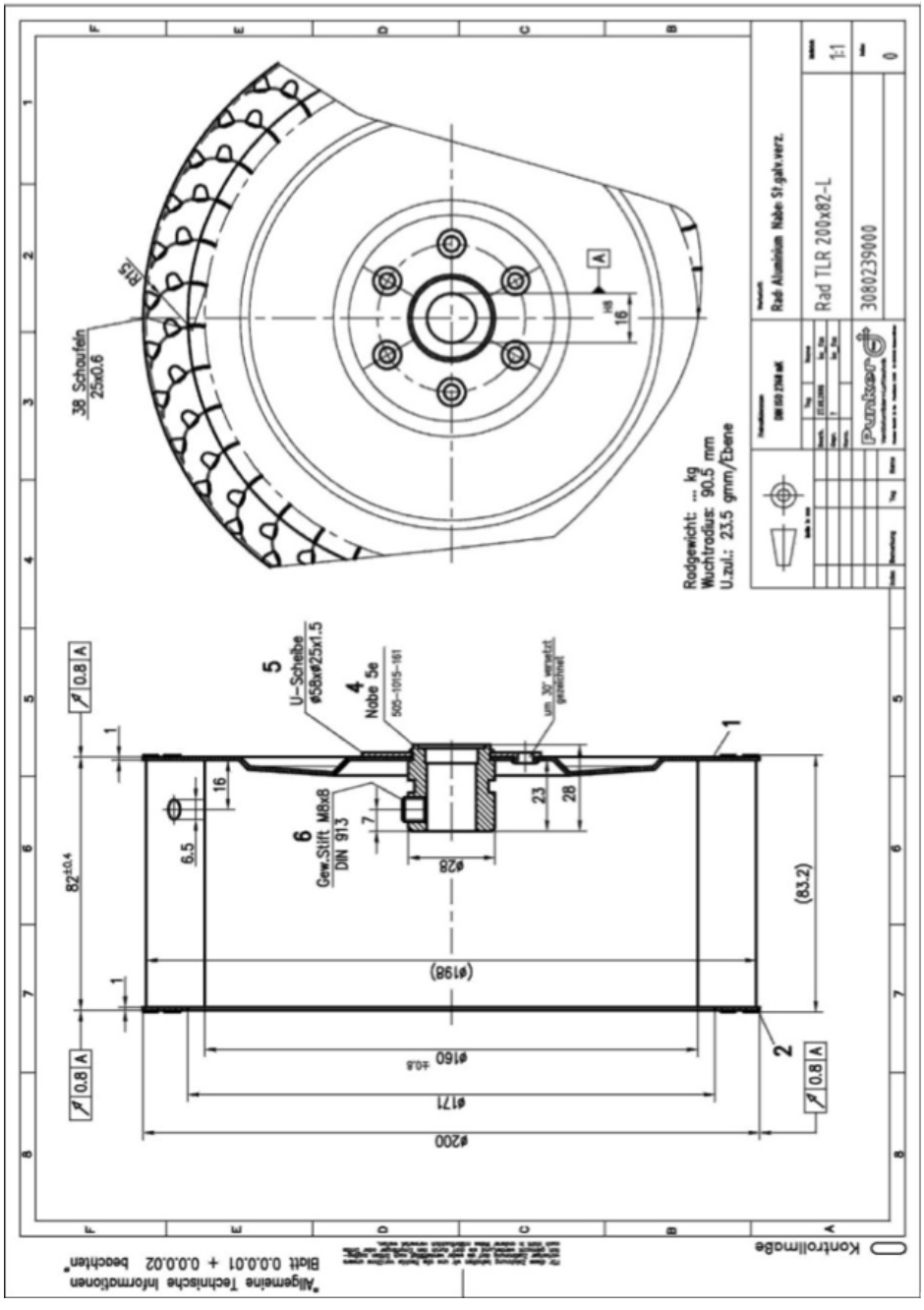

Impeller model *TLR* 200 × 82-*L* manufactured by Punker GmbH [75].

A.5 Detailed Housing Dimensions

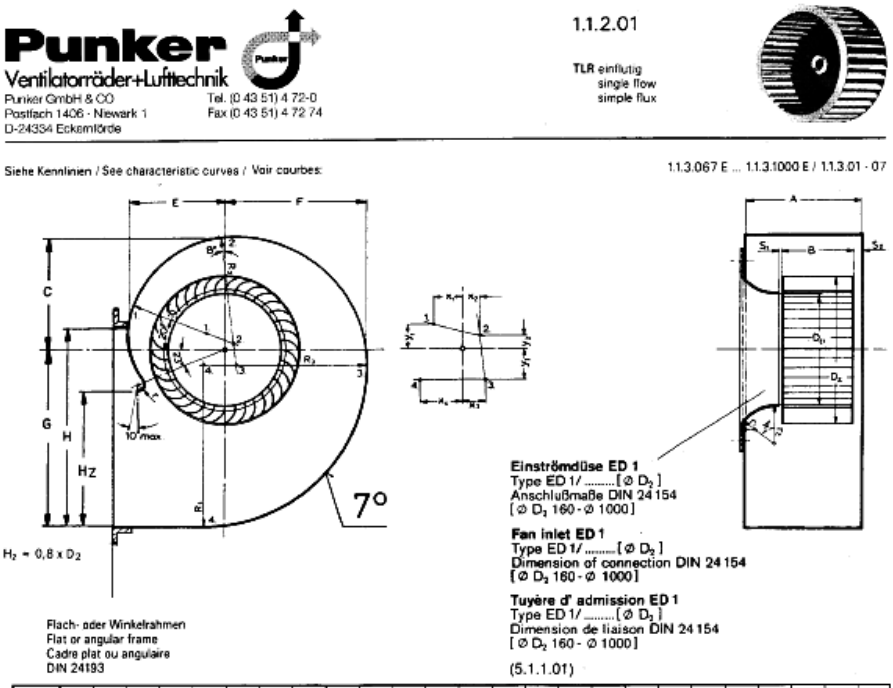

Type	67	76	85	97	108	120	133	146	160	180	200	225	250	280	315	355	400	450	500	560	630	710	800	900	1000
Ø D_2	67	76	85	97	108	120	133	146	160	180	200	225	250	280	315	355	400	450	500	560	630	710	800	900	990
B	27	34	34	42	42	52	52	62	62	74	82	92	102	114	128	143	163	183	204	229	254	284	319	359	404
A	40	45	50	63	67	71	80	90	100	112	125	140	160	180	200	224	250	280	315	355	400	450	500	560	630
H	75	85	95	110	120	135	150	165	200	224	250	280	315	355	400	450	500	560	630	710	800	900	1000	1120	1250
C	49	56	63	72	80	89	98	108	118	133	148	166	185	207	233	262	295	332	369	413	465	524	591	664	739
E	43	49	54	62	69	77	85	94	103	115	128	144	160	179	202	228	256	288	320	359	404	455	513	577	641
F	60	68	76	86	96	107	118	130	142	160	178	200	222	249	280	316	356	400	445	498	561	632	712	801	890
G	73	82	92	105	117	130	144	159	173	195	216	244	271	303	341	384	433	487	541	606	682	769	866	974	1082
R_1	35	39,7	44,5	50,7	56,5	62,8	69,6	76,3	83,7	94,1	104,6	117,7	130,7	146,4	164,7	185,6	209,2	235,3	261,5	292,8	329,4	371,3	418,3	470,6	522,9
R_2	46,9	53,2	59,5	67,9	75,6	84	93,1	102,2	112	126,1	140	157,6	175,1	196,1	220,6	248,6	280,1	315,1	350,1	392,1	441,1	497,2	560,2	630,2	700,2
R_3	55,2	62,6	70	79,9	89	98,9	109,6	120,3	131,8	148,3	164,8	185,4	206	230,7	259,5	292,5	329,6	370,8	412	461,4	519,1	585	659,1	741,5	823,9
R_4	66,9	75,9	84,8	96,8	107,8	119,8	132,7	145,7	159,7	179,8	199,6	224,5	249,5	279,4	314,4	354,3	399,2	449,1	499	558,8	628,7	708,5	798,3	898,1	997,9
r	3,6	4	4,5	5	5,6	6	6,7	7,1	8	9	10	11,2	12,5	14	16	18	20	22,4	25	28	31,5	35,5	40	45	50
x_1	7,9	9	10	11,5	12,7	14,2	15,7	17,2	18,9	21,2	23,6	26,6	29,5	33	37,2	41,9	47,2	53,1	59	66,1	74,3	83,8	94,4	106,2	118
x_2	3,3	3,7	4,1	4,7	5,3	5,9	6,5	7,1	7,8	8,8	9,8	11	12,2	13,7	15,4	17,3	19,5	21,9	24,4	27,3	30,7	34,6	39	43,9	48,8
x_3	4,4	5	5,6	6,4	7,1	7,9	8,8	9,6	10,6	11,9	13,2	14,9	16,5	18,5	20,8	23,4	26,4	29,7	33	37	41,8	46,9	52,8	59,4	66
x_4	7,2	8,2	9,2	10,5	11,7	13	14,4	15,8	17,3	19,4	21,6	24,3	27	30,2	34	38,3	43,2	48,6	54	60,5	68	76,7	86,4	97,2	108
y_1	6,6	7,5	8,4	9,5	10,6	11,8	13,1	14,3	15,7	17,7	19,7	22,1	24,6	27,5	31	34,9	39,3	44,2	49,1	55	61,9	69,8	78,6	88,4	98,3
y_2	2,6	2,9	3,3	3,7	4,1	4,6	5,1	5,6	6,1	6,8	7,6	8,6	9,5	10,6	12	13,5	15,2	17,1	19	21,3	23,9	27	30,4	34,2	38
y_3	5,7	6,4	7,2	8,2	9,1	10,1	11,3	12,3	13,5	15,2	16,9	19	21,1	23,7	26,6	30	33,8	38	42,3	47,3	53,2	60	67,6	76,1	84,5
S_1	2	2	2	2	2	2	2	2	2	2	2	2	2,3	2,3	2,8	3,3	3,5	3,5	4,5	4,5	5	5	6	6	6
S_2	2	2	2	2	2	2	2	2	3,5	3,5	3,5	3,5	3,5	6	6	6	6	6	6	6	6	6	8	8	8
ED1	67	76	85	97	108	120	133	146	160	180	200	225	250	280	315	355	400	450	500	560	630	710	800	900	1000
$ØD_{E1}$	47	56	64	76	82	94	107	115	127	143	161	180	203	228	257	289	325	365	410	460	516	581	652	733	823
r_1	8	9	14	16	18	16	14,5	22	16,7	19,5	22	22,8	21,5	24,5	25	29	34	38	37	40,5	43,5	47	57	65,6	65
r_2	–	–	–	–	–	–	30,5	70	44,2	40	47	55	75	81	91,5	100	105	120	146,5	169	201,5	234,5	243	272	313
									Ø D_2 DIN ≙ 323/R 20																

Detailed housing dimensions provided by Punker GmbH [75].

A.6 Microphones Technical Specifications

SEIT 1928 KONDENSATORMIKROFONE FÜR STUDIO - UND MESSTECHNIK

MICROTECH GEFELL

Kondensator-Messmikrofonkapsel MK 202

Die 1/2" Messmikrofonkapsel MK 202 ist für akustische Messungen in Forschung, Entwicklung und Industrie konzipiert und wird unter anderem auch in der Bauakustik und der Audiologie eingesetzt.

■ Frequenzbereich 10 Hz bis 40 kHz, Freifeld ■ Schalldruckpegel bis 158 dB

Der sorgfältige Aufbau und das konstruktive Konzept der Mikrofonkapseln garantieren eine hohe zeitliche Konstanz der elektroakustischen Parameter. Alle wichtigen Teile, einschließlich der in einem speziellen galvanischen Verfahren hergestellten und befestigten Membran, bestehen aus Nickel. Die Gegenelektrode ist durch eine Quarzglasscheibe vom Kapselgehäuse isoliert. Die Membran ist durch eine Schutzkappe, in die ein isoliertes Eichgitter integriert ist, vor mechanischen Beschädigungen geschützt. Eine einfache Kontrolle des Mikrofonfrequenzganges ist mit Hilfe des integrierten Eichgitters möglich. Ein definiertes elektrostatisches Feld (200 V/DC, 30 V/AC) kann ohne Entfernen der Schutzkappe und ohne spezielle Abstandshalter angelegt werden. Der statische Druckausgleich zwischen dem inneren Hohlraum und der Atmosphäre wird über eine Kapillare zum nachfolgenden Vorverstärker gewährleistet. Das ermöglicht die Verwendung des Trockenadapters TA 202.
Der international übliche Gewindetyp (60 UNS) für den Anschluss der Mikrofonkapsel gestattet die Austauschbarkeit mit anderen 1/2" Mikrofonkapseln und ermöglicht den Anschluss an alle geeigneten Kalibrier- und Messgeräte.
Messmikrofonkapsel MK 202 und Messmikrofonvorverstärker MV 203 sind als Mikrofonglied eichfähig und für Schallpegelmesser der **Klasse 1 nach IEC 651** geeignet.
Beim Einsatz in extrem feuchter Atmosphäre kann zur Erhöhung der Betriebssicherheit der Trockenadapter TA 202 zwischen Mikrofonkapsel und Vorverstärker geschraubt werden.
Auf Kundenwunsch wird dieser Kapseltyp mit einer seitlichen Druckausgleichsöffnung als Messmikrofonkapsel MK 201 gefertigt.

Condenser Measuring Microphone Cartridge Type MK 202

The 1/2" measuring microphone cartridge MK 202 is designed for acoustical measurements in research and development and also for industrial use. Some applications include audiology, the measurement of building acoustics and noise levels.

■ Frequency range 10 Hz to 40 kHz, free-field ■ Sound pressure levels up to 158 dB

The microphone cartridge is designed and very carefully constructed to ensure excellent long-time stability of the electroacoustical parameters. All essential components including the diaphragm are made of nickel and the diaphragm is bonded by a special galvanic process. The rear electrode is insulated from the cartridge housing by a quartz glass plate. The diaphragm ist protected against mechanical damage by a protection grid in which an insulated calibration grid is integrated.
This allows convenient measurement of each cartridge's frequency response curve by applying a well-defined electrostatic field (200 volts/dc, 30 volts/ac) without removing the protection grid or requiring special spacers.
The equalization of the static air pressure between the inside and outside of the MK 202 cartridge is by means of a capillary tube rear-vented into the preamplifier. This enables the use of the optional TA 202 dehumidifier.
The cartridge uses the international standard thread 60 UNS which ensures compatibility with a wide range of calibration equipment and measurement devices available from many manufacturers.
Microphone cartridge MK 202 and measurement microphone preamplifier MV 203 can be calibrated and are designed for sound level meters of **IEC Type 1 according to IEC 651**.
The TA 202 dehumidifier can be screwed between cartridge and preamplifier to increase the reliability for operation in an extremely humid atmosphere.
Alternatively, this cartridge is available as the side-vented type MK 201 on special order.

Lieferumfang/Delivery

Messmikrofonkapsel Measuring Microphone Cartridge	MK 202 im Holzetui MK 202 in wooden case	Best.-Nr./Order-No. 311102

MICROTECH GEFELL GMBH MÜHLBERG 18 D-07926 GEFELL TEL. ++49 (0)36649 / 882-0 FAX ++49 (0)36649 / 882 11
INTERNET http://www.microtechgefell.de e-mail info@microtechgefell.de

Technische Daten/Specifications MK 202

21.31 PTB-Zulassung-Nr.
96.121 zur amtlichen Eichung CE

Wandlertyp Transducer type	Kapazitiver Druckempfänger Capacitive pressure transducer
* Frequenzbereich des Freifeldübertragungsmaßes * Frequency range free-field response	10 Hz ... 35 kHz (± 1,5 dB) 40 kHz (0...-3 dB)
* Feld-Leerlauf-Übertragungsfaktor/Sensitivity	14 mV/Pa
Grenzschalldruckpegel für 3 % Klirrfaktor bei 1 kHz Max. SPL for THD ≤ 3 % at 1 kHz	158 dB
Eigenrauschen mit Vorverstärker MV 203 Inherent noise with preamplifier MV 203	22 dBA
Polarisationsspannung/Polarization voltage	200 V
* Kapazität mit Polarisationsspannung bei 1 kHz * Polarized cartridge capacitance at 1 kHz	25 pF
Arbeitstemperaturbereich Operating temperature range	-50 ... +100 °C
Temperaturkoeffizient Main ambient temperature coefficient	≤ 0,01 dB/K
Statischer Druckkoeffizient Main ambient pressure coefficient	$-1x10^{-5}$ dB/Pa
Durchmesser/Diameter	
mit Schutzkappe/with protection grid	13,2 ± 0,02 mm
ohne Schutzkappe/without protection grid	13,2 ± 0,02 mm
Höhe/Height	14,2 mm
Gewicht/Weight	8,5 g
Gewinde für Vorverstärker/Preamplifier thread	11,7 mm 60 UNS
Gewinde für Schutzkappe/Protection grid thread	12,7 mm 60 UNS

Wartung und Instandhaltung

Zur Gewährleistung der Funktionstüchtigkeit ist die Messmikrofonkapsel vor mechanischen Beschädigungen zu schützen und in Abhängigkeit von den Einsatzbedingungen in festzulegenden Intervallen im betriebsspannungsfreien Zustand allseitig auf Verschmutzung zu überprüfen.
Nach Entfernen der Schutzkappe sind die Verunreinigungen in deren Innenraum sowie auf der Membran äußerst vorsichtig mit einem weichen Pinsel oder Tuch zu entfernen.
Die Messmikrofonkapsel ist nicht für den Einsatz in chemisch aggressiven Medien und leitendem Staub geeignet. Kondensatbildung ist auszuschließen.

Maintenance and upkeep

In order to maintain its functioning the measurement microphone cartridge should be protected against mechanical damage. It should be disconnected from its power source and completely checked for any pollution in regular intervals that have to be defined depending on the operating conditions.
After removal of the protection grid the pollution within the grid and on the diaphragm should be cleaned very carefully with a soft clean cloth or brush.
The measurement microphone cartridge is not suitable for use in chemical aggressive conditions and in conductible dust. Condensation must be avoided.

Polardiagramme/Polar patterns

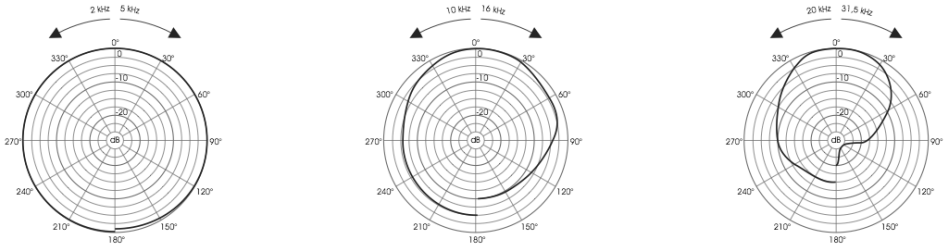

Frequenzgänge/Frequency responses

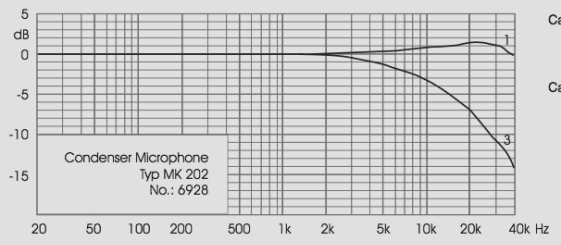

Calibration Chart

Sensitivity S_o:	-37,1 dB re 1 V/Pa
equivalent to:	14,0 mV/Pa
Cartridge Capacitance:	23,0 pF

Calibration Conditions

Polarization Voltage:	200 V
Ambient Static Pressure:	95,5 kPa
Ambient Temperature:	22 °C
Relative Humidity:	63 %

1 Zero Degree Incidence
Random Incidence
3 Actuator Pressure Response

Date: 22.01.92 Signature:

*individuell kalibriert/individually calibrated

MICROTECH GEFELL

MICROTECH GEFELL GMBH MÜHLBERG 18 D-07926 GEFELL TEL. ++49 (0)36649 / 882-0 FAX ++49 (0)36649 / 882 11
INTERNET http://www.microtechgefell.de e-mail info@microtechgefell.de

Technische Daten/Specifications MV 203 / MV 204

CE

Betriebsspannung/Power supply	28 ... 130 V
Stromaufnahme/Current consumption	≤ 2,3 mA
Verstärkung/Gain	0 ± 0,05 dB
Frequenzbereich/Frequency range	
± 0,5 dB; 18 pF; Kleinsignal/small signal	1 Hz ... 1 MHz
± 3 dB; 18 pF; Kleinsignal/small signal	0,8 Hz ... 4,5 MHz
Eingangsimpedanz/Input impedance	20 GΩ; 0,2 pF
Ausgangsimpedanz/Output impedance	≤ 80 Ω
Maximale Ausgangsspannung/Max. RMS output	7 ... 33 V_{eff}
Eigenrauschen/Inherent noise	
A - bewertet/A - weighted 20 pF	≤ 2,5 µV
linear 20 pF	≤ 10 µV
Umgebungsbedingungen/Ambient conditions:	
Temperatur/Temperature:	
Arbeitsbereich/Operating	-10 °C ... +50 °C
Lagerbereich/Storage	-20 °C ... +70 °C
Feuchte, Betauung unzulässig/Humidity, non condensing:	
Arbeitsbereich/Operating	bis/to 90 % RF/RH
Lagerbereich/Storage	bis/to 95 % RF/RH
Steckverbinder/Plug	7 pin LEMO FGG 1 B 307 CNAD 62
Kapselanschlussgewinde/Capsule thread	11,7 mm 60 UNS
Abmessungen/Dimensions	∅ 12,7 x 90 mm
Gewicht/ Weight, kompl.	165 g

MV 203

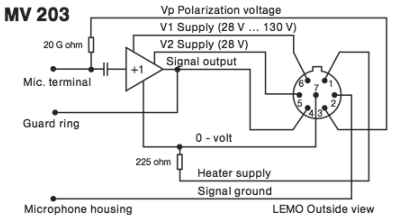

MV 204

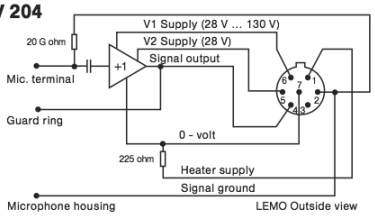

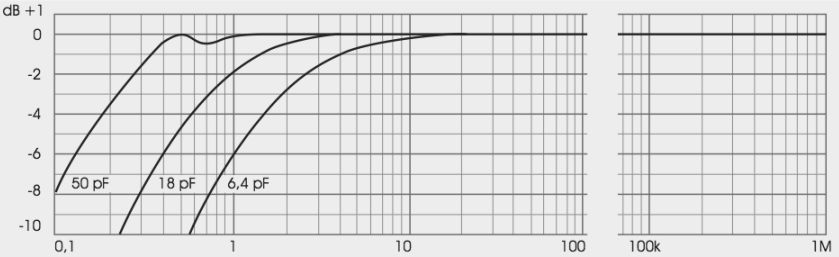

Frequenzgänge/Frequency responses

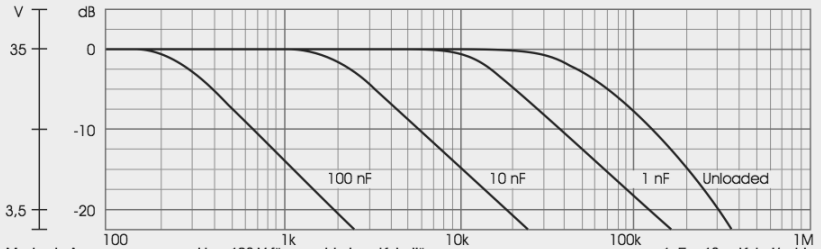

Maximale Ausgangsspannung U_B= 120 V für verschiedene Kabellängen
Maximum RMS levels for sinusoidal signals with 120 V supply for different cable loads

1nF = 10 m Kabel/cable

MICROTECH GEFELL GMBH GEORG-NEUMANN-PLATZ D-07926 GEFELL TEL. +49 (0)36649 / 882-0 FAX +49 (0)36649 / 882 11
INTERNET http://www.microtechgefell.de e-mail info@microtechgefell.de

A.7 Sound Calibrator Technical Data

PRODUCT DATA

Sound Calibrator Type 4231

Sound Calibrator Type 4231 is a handy, portable sound source for calibration of sound level meters and other sound measurement equipment. The calibrator is very robust and stable, and conforms to EN/IEC 60942 (2003) Class LS and Class 1, and ANSI S1.40–2006.

Uses and Features

Uses
- Calibration of sound level meters and other sound measurement equipment

Features
- Conforms to EN/IEC 60942 (2003) Class LS and Class 1, and ANSI S1.40–2006
- Robust, pocket-sized design with highly stable level and frequency
- Calibration accuracy ±0.2 dB
- 94 dB SPL or 114 dB SPL for calibration in noisy environments
- Extremely small influence of static pressure and temperature
- Sound pressure independent of microphone equivalent volume
- 1 kHz calibration frequency for correct calibration level independent of weighting network
- Fits Brüel & Kjær 1″ microphones (1/2″, 1/4″ and 1/8″ microphones with adaptor)
- Switches off automatically when removed from the microphone

Brüel & Kjær

Brüel & Kjær sound calibrator (Type 4231) [84]

A.8 Coefficients for the Determination of $C_{3,4}$

Values of coefficients a_i up to 5000 Hz for the determination of the combined mean flow velocity and modal correction $C_{3,4}$ in decibels of the sampling tube for duct diameters $0.15\,\mathrm{m} < d < 0.2\,\mathrm{m}$

$a_i(\mathrm{dB})\cdot s^i \cdot m^{-i}$					
f (Hz)	a_0	a_1	a_2	a_3	a_4
$\lvert U\rvert \leq 60\,\mathrm{m/s}$					
≤ 630	$-5\,e^{-2}$	$2.7\,e^{-2}$			
800		$2.97\,e^{-2}$			
1000	$-2.09\,e^{-2}$	$2.85\,e^{-2}$	$1.18\,e^{-4}$		
1250	$8.41\,e^{-1}$	$3.61\,e^{-2}$	$9.34\,e^{-5}$		
1600	$7.79\,e^{-1}$	$5.01\,e^{-2}$	$1.38\,e^{-4}$		
2000	$7.67\,e^{-1}$	$5.45\,e^{-2}$	$3.77\,e^{-4}$		
2500	1.59	$6.12\,e^{-2}$	$5.06\,e^{-4}$		
3150	2.4	$8.26\,e^{-2}$	$7.45\,e^{-4}$	$-3.02\,e^{-6}$	
4000	3.43	$9.99\,e^{-2}$	$9.61\,e^{-4}$	$-3.29\,e^{-6}$	
5000	3.98	$1.29\,e^{-1}$	$2.21\,e^{-3}$	$-8.88\,e^{-6}$	$-2.32\,e^{-7}$

A.9 Total Correction of the Microphone Shield

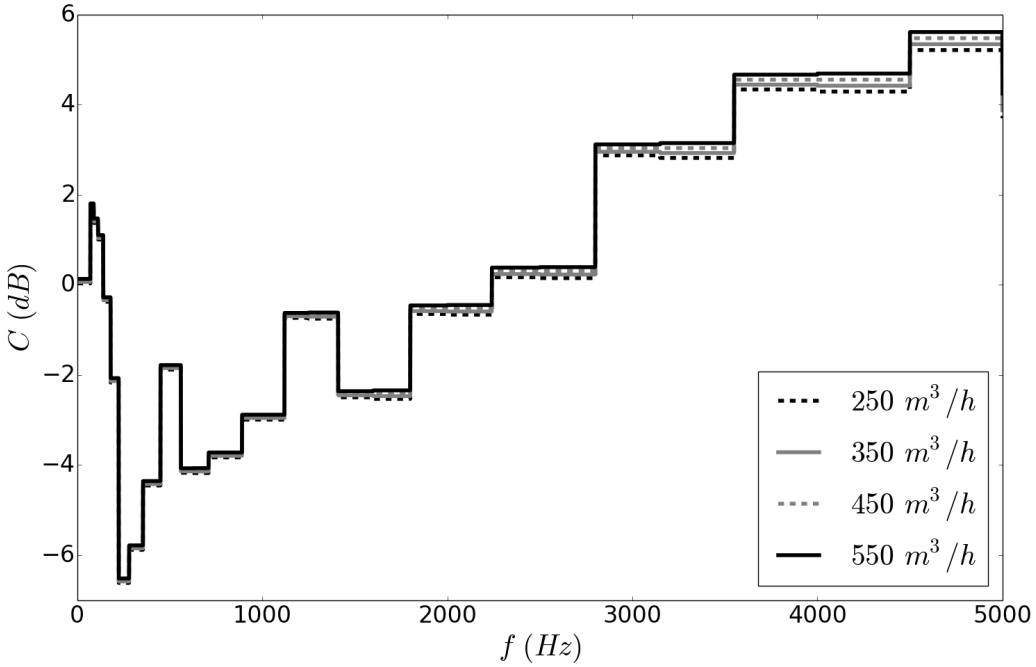

Total correction factor C of the microphone shield calculated for different flow rates.

A.10 Averaging Methods

$$\text{Time averaging:} \quad \overline{\phi_T}(x_i) = \lim_{T\to\infty} \frac{1}{T} \int_t^{t+T} \phi(x_i, t)\, dt$$

$$\text{Spatial averaging:} \quad \overline{\phi_V}(t) = \lim_{V\to\infty} \frac{1}{V} \int_V \phi(x_i, t)\, dV$$

$$\text{Ensemble averaging:} \quad \overline{\phi_E}(x_i, t) = \lim_{N\to\infty} \frac{1}{N} \sum_{n=1}^{N} \phi(x_i, t)$$

$$\text{Favre averaging:} \quad \overline{\phi_F}(x_i) = \frac{1}{\overline{\rho}} \lim_{T\to\infty} \frac{1}{T} \int_t^{t+T} \rho\, \phi(x_i, t)\, dt$$

A.11 WALE Subgrid Scale Formulation

According to STAR-CCM+ user guide [102], the following equations are valid for the WALE Subgrid Scale model:

$$\mu_t = \rho\,\Delta^2\,S_W$$
$$\Delta = min(\kappa\,d,\, C_W\,V_{cell}^{1/3})$$
$$S_W = \frac{S_d : S_d^{3/2}}{S_d : S_d^{5/4} + S : S^{5/2}}$$
$$S = \frac{1}{2}(\nabla\overrightarrow{v} + \nabla\overrightarrow{v}^T)$$
$$S_d = \frac{1}{2}[\nabla\overrightarrow{v}\cdot\nabla\overrightarrow{v} + (\nabla\overrightarrow{v}\cdot\nabla\overrightarrow{v})^T]$$
$$t = \frac{C_t}{S}$$
$$k_{SGS} = C_t\nu_t S$$
$$l = \frac{C_t^{3/2}\nu_t^{1/2}}{S^{1/2}}$$

μ_t: Subgrid scale viscosity
Δ: Grid filter width
V_{cell}: Cell volume
κ: Von Karman constant (= 0.41)
S: Strain-rate tensor
S_d: Deformation tensor
S_W: Deformation parameter
d: Wall distance
C_W: Model coefficient (=0.544)
t: Turbulent time-scale
l: Turbulent length-scale
k_{SGS}: Subgrid scale turbulent kinetic energy
C_t: Model constant (=1.25 in version 7 and =3.5 in version 9)

Scalar (inner,double-dot) product of two tensors, whose result is a scalar:
$S : T = S_{ij}T_{ji}$

A.12 Tranient Surface Data for Models with Different Rotor Outlet Angles

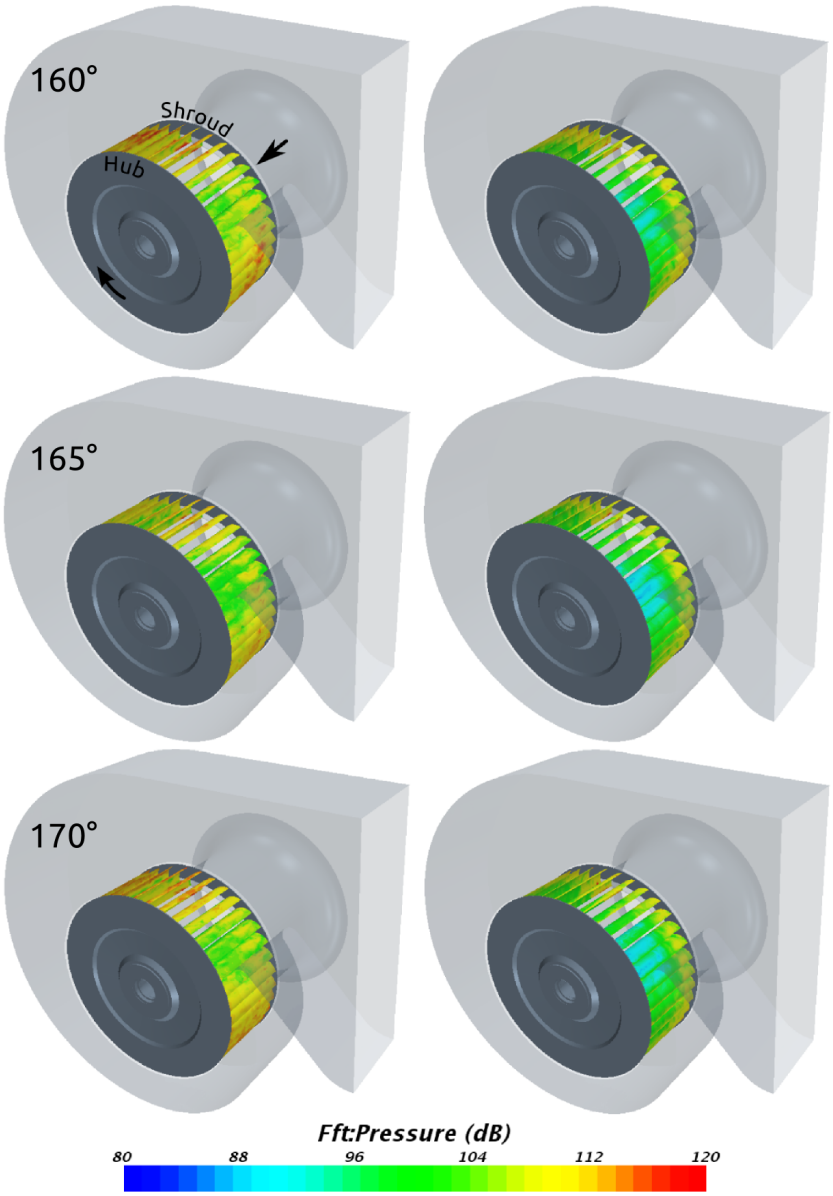

Sound pressure level radiated in the range of 100-1000 Hz from the blade's suction side (left) and the pressure side (right) of the impellers with different outlet angles. Results are obtained from DES on a numerical grid with approximately 12.5 million cells.

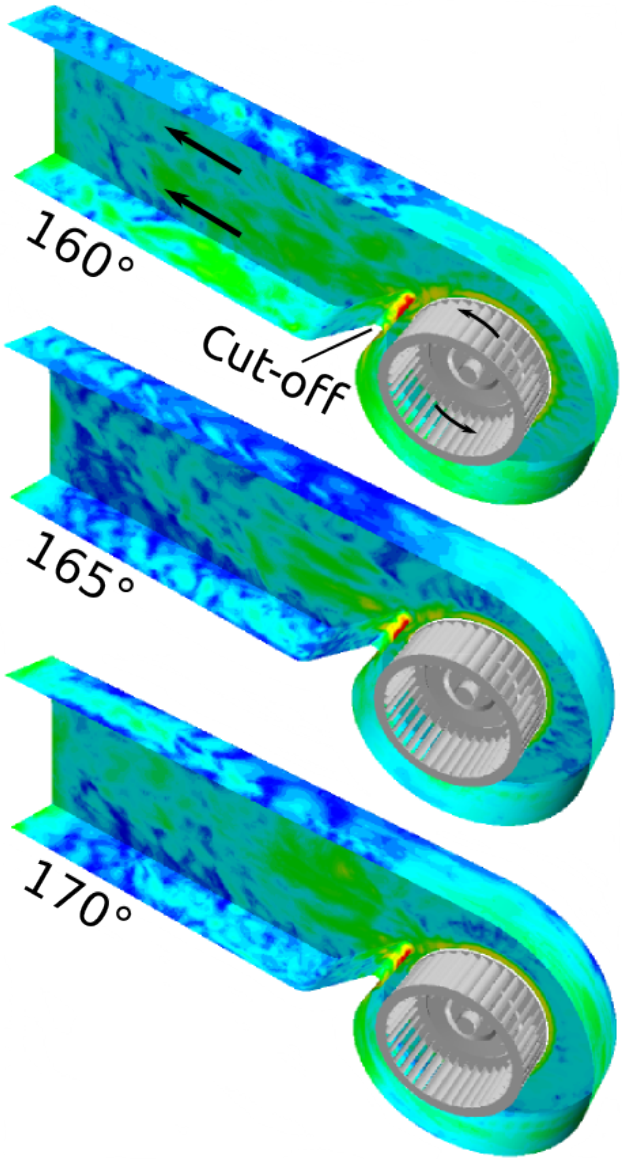

Sound pressure level radiated in the range of 100-1000 Hz from the housing of the fans with various rotor outlet angles ; Colorbar is the same as in the previous figure. Results are obtained from DES on a numerical grid with approximately 12.5 million cells.

A.13 Tranient Surface Data Of the Reference Model at Different Operating Points

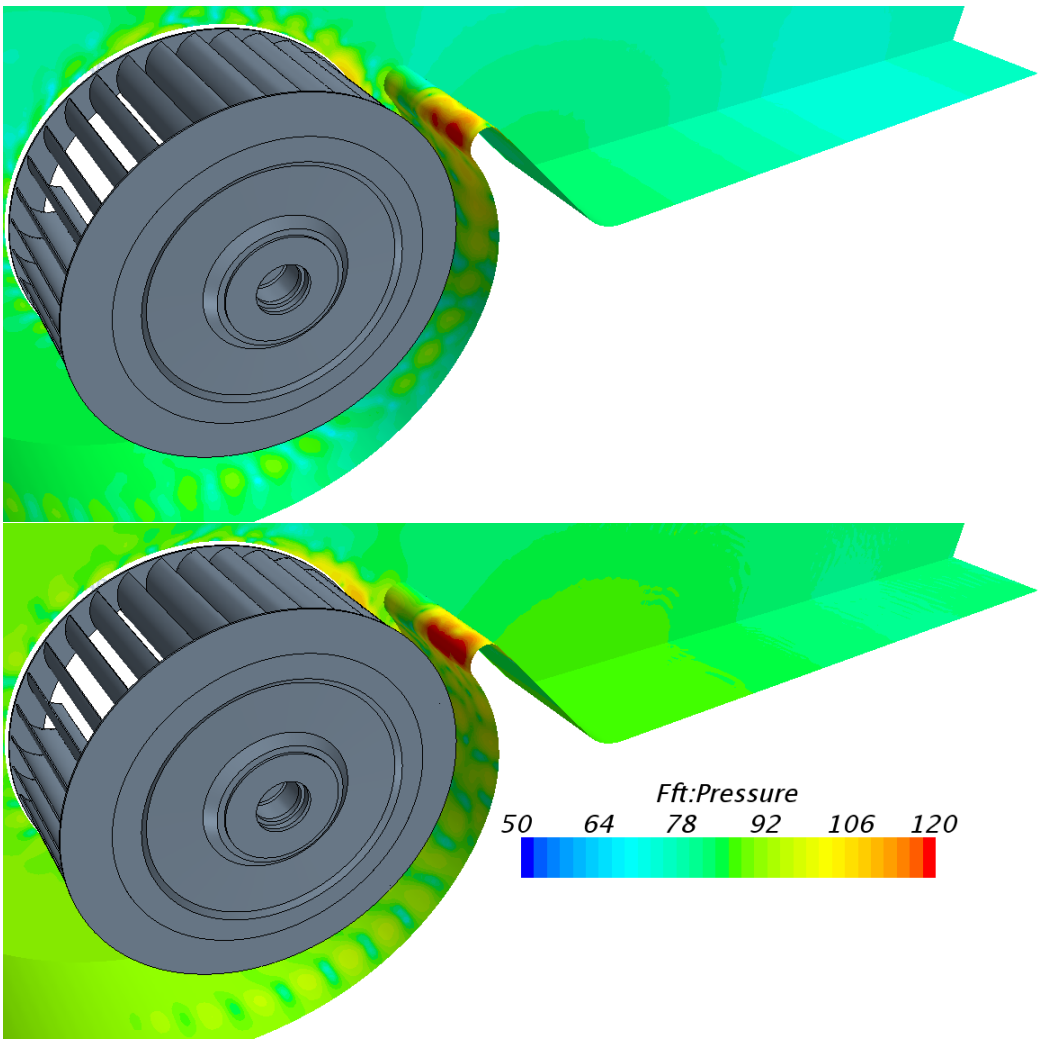

Comparasion between the transient surface data of the reference fan operating at 450 m^3/h (top) and 675 m^3/h (bottom).